

# Digitally Assisted Transmitter Enhancement Techniques for Millimeter Wave Radio Systems

Prasidh Ramabadran

2020

Dissertation submitted in fulfilment of the requirements for  
candidature for degree of

Doctor of Philosophy



NUI MAYNOOTH

Ollscoil na hÉireann Má Nuad

National University of Ireland Maynooth  
Department of Electronic Engineering

**Supervisors:** Dr. John Dooley, Prof. Ronan Farrell

**Head of Department:** Prof. Ronan Farrell

**Date of submission**

31 Oct 2019

“An investment in knowledge always pays the best interest.”  
— Benjamin Franklin



# Contents

<b>Abstract</b>	<b>1</b>
<b>1. Introduction</b>	<b>11</b>
1.1. Key Parameters, Channel Capacity and Resource Sharing Schemes in Wireless Communications . . . . .	12
1.1.1. Channel Parameters . . . . .	12
1.1.2. Channel Capacity . . . . .	12
1.1.3. Resource Sharing Schemes . . . . .	13
1.2. Features of Next Generation Wireless Communication Systems . . . . .	14
1.3. Challenges In The Design For Next Generation Wireless Communi- cations That Motivated This Work . . . . .	17
<b>2. Overview of a Wireless Transceiver and Signal Distortion Effects in Wireless Communications</b>	<b>21</b>
2.1. A Modern Wireless Transceiver . . . . .	21
2.2. Key Performance Indicators of SISO Transceivers . . . . .	23
2.2.1. Key Performance Indices of an RF transmitter . . . . .	23
2.2.2. Key Performance Indices of an RF receiver . . . . .	27
2.3. Non-Ideal Characteristics of hardware blocks in a SISO transceiver and their impacts. . . . .	31
2.3.1. Transmitter . . . . .	33
2.3.2. Receiver . . . . .	42
2.4. Active Antenna Arrays for 5G Communications . . . . .	47
2.5. Conclusion . . . . .	49
<b>3. Calibration of RF Signal Paths in Transmitters</b>	<b>51</b>
3.1. Introduction . . . . .	51
3.2. Prior Art Techniques for calibration of Impairments . . . . .	52
3.2.1. Iterative calibration of LO Leak . . . . .	55
3.2.2. Calibration of IQ gain imbalance, quadrature phase error and timing offsets. . . . .	55
3.2.3. Review of prior arts . . . . .	57
3.3. Novel Non-Iterative Procedures to Perform Wideband Calibration . . . . .	59
3.3.1. Time Interleaved stimuli to signal paths . . . . .	60
3.3.2. Calibration by Constellation Mapping . . . . .	83
3.4. Conclusions: . . . . .	89

<b>4. RF Power Amplifiers: Key Parameters, Classes, Topologies and Behavioral Modelling</b>	<b>91</b>
4.1. Introduction . . . . .	91
4.2. Key Parameters of an RF Power Amplifier . . . . .	92
4.3. Behavioural Modelling and Digital Pre Distortion . . . . .	100
4.3.1. Behavioural Modelling . . . . .	100
4.3.2. Digital Pre-distortion . . . . .	101
4.4. Power Amplifier Classes . . . . .	103
4.5. Power Amplifier Topologies . . . . .	109
4.5.1. Introduction to Outphasing Amplifiers . . . . .	109
4.5.2. Introduction to Doherty Power Amplifier . . . . .	114
4.6. Novel Contributions in the area of RF Power Amplifiers . . . . .	116
4.6.1. Primary Contribution: Calibration Of RF Signal Paths In Outphasing Amplifiers . . . . .	116
4.6.2. Secondary Contributions: . . . . .	120
4.6.3. Behavioral Modelling of Asymmetric Doherty PAs . . . . .	120
4.6.4. Nonlinearity Modeling of Chireix Outphasing PowerCombiner Under Amplitude Imbalance . . . . .	121
4.6.5. Phase only Pre Distortion of Outphasing Amplifiers . . . . .	122
4.7. Conclusions . . . . .	123
<b>5. Combined Physical Layer Security and PAPR Reduction in Wideband Transmitters</b>	<b>125</b>
5.1. Introduction: . . . . .	125
5.2. Physical Layer Security Techniques . . . . .	126
5.3. PAPR Reduction Techniques . . . . .	129
5.4. Physical Layer Authentication and PAPR Reduction . . . . .	133
5.4.1. System Design . . . . .	135
5.4.2. Key Generation scheme in TDD systems . . . . .	136
5.4.3. Encrypting Single Carrier Modulated Signals . . . . .	144
5.5. Experimental Validation . . . . .	147
5.5.1. Validation of the constellation encryption scheme: . . . . .	147
5.5.2. Experimental Validation of symmetric key generation, encryption and PAPR reduction . . . . .	150
5.5.3. Modulation Encryption Key Generation . . . . .	150
5.5.4. Encryption of an OFDM signal . . . . .	155
5.5.5. PAPR Reduction . . . . .	158
5.5.6. Encryption of Single Carrier Modulated Signals . . . . .	161
5.6. Conclusion . . . . .	163
<b>6. Bandwidth Interleaved Modulators and Transmitters</b>	<b>165</b>
6.1. Introduction: . . . . .	165
6.2. Prior Art Techniques to mitigate the problems . . . . .	170
6.2.1. Digital to Analogue Converters: . . . . .	170

6.3. A novel system level design approach for wideband modulators and transmitters . . . . .	176
6.3.1. Bandwidth Interleaved Modulators: . . . . .	178
6.4. Experimental Validation of Bandwidth Interleaved Modulators . . . .	186
6.4.1. Spatially Combined Bandwidth Interleaved Transmitters . . . .	190
6.5. Experimental Validation of spatially combined bandwidth interleaved transmitters . . . . .	193
6.6. Conclusions . . . . .	200
<b>7. Conclusions and future work</b>	<b>203</b>
7.1. Summary . . . . .	203
7.2. Contributions . . . . .	204
7.2.1. Primary Contributions . . . . .	204
7.2.2. Contributions As Co-author . . . . .	206
7.3. Future Work . . . . .	207
7.4. Conclusions . . . . .	207
<b>Acknowledgments</b>	<b>209</b>
<b>A. Appendix Impact of oscillator phase noise on SNR, timing jitter.</b>	<b>211</b>
A.1. Timing Jitter and Phase Noise . . . . .	213
<b>B. Impairments in data converters</b>	<b>215</b>
<b>Bibliography</b>	<b>219</b>



# Abstract

Wireless communication has become an integral part of life in a modern society. The data to be transmitted is modulated on radio frequency carrier signals for transmission where the bandwidth of the signal to be transmitted increases proportional to the speed at which the data is intended to be transmitted.

The present generation cellular wireless communication systems employ channel bandwidths as wide as 20 MHz in multipole bands between 800 MHz and 3.5 GHz with digitally modulated multi-carrier transmission schemes and hybrid access schemes in time, frequency and spatial domains. The radio spectrum has stretched to occupy multiple bands below to meet the demand for volume and speed of the data to be communicated. Indoor short range wireless communications of present generation employ channel bandwidths as wide as 160 MHz and transmit at powers lesser than a tenth of that transmitted by cellular systems and employ similar access schemes as cellular wireless systems. There has been a similar evolution in the area of wireless communications through satellites. Next generation wireless communication systems such as 5G and High-Throughput-Satellite systems in the millimetre wave bands have promised a step increase in data rates in the order of several gigabits per second operating multiple frequency bands over and above those in use at present. This necessitates design of state of the art mm-wave transceivers capable of operating in millimetre wave bands with instantaneous bandwidths of several hundreds of MHz. The cost and complexity of implementation of the radio transmission system increases rapidly as the bandwidths increase.

This work investigates digital enhancement techniques to enhance performance of wideband radio frequency transmitters. A section of the work focusses on characterizing wideband impairments in radio frequency hardware and mitigating them through digital signal processing. Another section devises digital signal processing operations to jointly enhance power efficiency in radio frequency transmitters along with providing an additional tier of security to the information being transmitted. The third section focusses on methods of transmission of wideband modulated signals by seamlessly interleaving multiple radio frequency transceivers of relatively narrow bandwidths in the frequency domain thereby presenting an architecture for scalable bandwidth transmitters. Overall this thesis presents innovative techniques to mitigate limitations in radio frequency hardware that hinder wideband operation and schemes to construct scalable bandwidth transceivers with scope to reuse legacy radio frequency hardware for next generation communication systems in part or whole.



# List of Publications

1. Ramabadran, P., Dooley, J., & Farrell, R. (2017), Frequency Interleaved Modulators to Support Channel Bonding in Satellite Communications. *18th Research Colloquium on Radio Science and Communications for a Smarter World Presented at Royal Irish Academy (RIA) on 08 Mar 2017*.
2. Ramabadran, P., Madhuwantha, S., Afanasyev, P., Farrell, R., Marco, L., Pires, S., & Dooley, J. (2018). Digitally Assisted Wideband Compensation of Parallel RF Signal Paths in a Transmitter. *2018 91st ARFTG Microwave Measurement Conference (ARFTG)*, 1–4. <https://doi.org/10.1109/ARFTG.2018.8423839>.
3. International Patent Publication WO/2019/145565: CHARACTERISING RADIO FREQUENCY SIGNAL PROCESSING PATHS.
4. Ramabadran, P., Madhuwantha, S., Afanasyev, P., Farrell, R., & Dooley, J. (2018). Wideband Interleaved Vector Modulators for 5G Wireless Communications. *2018 IEEE MTT-S International Microwave Workshop Series on 5G Hardware and System Technologies, IMWS-5G 2018*, 1–3. <https://doi.org/10.1109/IMWS-5G.2018.8484496>.
5. Madhuwantha, S., Ramabadran, P., Farrell, R., & Dooley, J. (2018). N-way Digitally Driven Doherty Power Amplifier Design and Analysis for Ku band Applications. *29th Irish Signals and Systems Conference, ISSC 2018*, (13), 1–6. <https://doi.org/10.1109/ISSC.2018.8585370>
6. Madhuwantha, S., Dooley, J., Ramabadran, P., Byrne, D., Niotaki, K., Doyle, J., & Farrell, R. (2018). Behavioural Models for Distributed Arrays of High Performance Doherty Power Amplifiers. *29th Irish Signals and Systems Conference, ISSC 2018*, (13), 1–6. <https://doi.org/10.1109/ISSC.2018.8585367>
7. Madhuwantha, S., Ramabadran, P., Farrell, R., & Dooley, J. (2019). Novel Calibration Technique for Wideband Transmitters Using Constellation Mapping. *2019 92nd ARFTG Microwave Measurement Conference: Next Generation Microwave and Millimeter-Wave Measurement Techniques and Systems, ARFTG 2019*, (1), 1–4. <https://doi.org/10.1109/ARFTG.2019.8637231>
8. Ramabadran, P., Malone, D., Madhuwantha, S., Afanasyev, P., Farrell, R., Dooley, J., & O'Brien, B. (2018). A Novel Physical Layer Encryption Scheme

to Counter Eavesdroppers in Wireless Communications. 2018 25th IEEE International Conference on Electronics, Circuits and Systems (ICECS), 69–72. <https://doi.org/10.1109/ICECS.2018.8617993>

9. Ramabadran, P., Afanasyev, P., Hesami, S., McCarthy, D., Farrell, R., Dooley, J., & O'Brien, B. (2019). Spatially Combined Wideband Interleaved Transmitter. *2019 European Conference on Networks and Communications (EuCNC)*, (13), 230–234. <https://doi.org/10.1109/eucnc.2019.8802059>
10. Ramabadran, P., Afanasyev, P., Leiser, M., Malone, D., McCarthy, D., Farrell, R., Dooley, J., & O'Brien, B. (2019). Novel Physical Layer Authentication with PAPR Reduction based on Channel and Hardware Frequency Responses. (2019) Accepted for publication in *IEEE Transactions on Circuits and Systems-1 (TCAS-1)*
11. 10. UK Patent Application No. 1817117.3 RF Encryption Scheme.
12. P. Afanasyev, P. Ramabadran, S. Mohammady, R. Farrell and J. Dooley, "Phase-Only Digital Predistortion Technique for Class-E Outphasing Power Amplifiers," 2019 European Microwave Conference in Central Europe (EuMCE), Prague, Czech Republic, 2019, pp. 14-17.
13. Afanasyev, P., Ramabadran, Farrell, R., Dooley, J. (2019), Nonlinearity Modeling of Chireix Outphasing Power Combiner Under Amplitude Imbalance. *2019 17th IEEE International New Circuits and Systems Conference (NEW-CAS 2019)*, In Press

# List of Figures

1.1. Network Protocol Stack . . . . .	11
1.2. Functional Block Diagram of a Radio Frequency Transceiver . . . . .	17
2.1. Block Diagram of Wireless Transceiver . . . . .	21
2.2. Time Division Duplex . . . . .	22
2.3. Frequency Division Duplex . . . . .	23
2.4. Ideal and Non-Ideal Constellation Comparison . . . . .	24
2.5. Spurious Emissions . . . . .	25
2.6. LO Leak . . . . .	26
2.7. IQ Imbalance and skew . . . . .	27
2.8. Non Linear Amplitude Response . . . . .	29
2.9. Spurious Free Dynamic Range . . . . .	30
2.10. Image Rejection . . . . .	31
2.11. Constellation Rotation . . . . .	32
2.12. Heterodyne Transceiver . . . . .	32
2.13. Generalised Transmitter Block Diagram . . . . .	33
2.14. DAC Settling Errors . . . . .	34
2.15. Ka Band sub-harmonic mixer . . . . .	37
2.16. Mixer conversion gain vs freq . . . . .	37
2.17. Mixer phase vs signal power . . . . .	38
2.18. Nonlinear transfer function of a mixer . . . . .	38
2.19. Phase vs Frequency in a quadrature RF power splitter . . . . .	39
2.20. Edge Coupled RF bandpass filter designed for Ka Band operation . . . . .	40
2.21. Gain characteristics of edge coupled Ka Band BPF . . . . .	40
2.22. Phase characteristics of edge coupled Ka Band BPF . . . . .	41
2.23. Generalised Receiver Block Diagram . . . . .	42
2.24. S Parameters and Noise Figure of a HBT . . . . .	43
2.25. $S_{11}$ , $S_{22}$ and $G_{opt}$ of a HBT . . . . .	44
2.26. Circuit schematic of an LNA using a HBT . . . . .	44
2.27. Beam forming with two transmitters . . . . .	48
2.28. 8PSK demodulated constellation received from beamforming transmitters without path calibration . . . . .	48
2.29. 8PSK demodulated constellation received from beamforming transmitters with path calibration . . . . .	49
3.1. Modulator Output with DC Offset and Image . . . . .	53
3.2. Spectrum of LO Leak . . . . .	56

3.3. Modulator and up-converter of a super heterodyne satellite uplink transmitter. . . . .	60
3.4. Truncated Sinc pulse generated using Hamming window kernel . . . .	62
3.5. Frequency domain characteristics of the proposed truncated Sinc pulse test signal . . . . .	63
3.6. Chirp Waveform . . . . .	63
3.7. Chirp Spectrum . . . . .	64
3.8. Single Path Test Setup . . . . .	65
3.9. Spectrum of response to Sinc stimulus . . . . .	66
3.10. Single Path Reference Receiver . . . . .	67
3.11. Amplitude plot of FFT of the single path response . . . . .	67
3.12. Amplitude response of the single path post calibration. Trace1 (Blue):Before Calibration. Trace 2 (Black): After Calibration. . . . .	68
3.13. In-band group delay of single path . . . . .	68
3.14. Single path calibration process . . . . .	69
3.15. RF Transmitter with multiple signal paths . . . . .	70
3.16. Stimulus for calibration of two paths in a transmitter . . . . .	70
3.17. Correlated stimuli and responses . . . . .	71
3.18. Time aligned magnitudes of paths 1 and 2. . . . .	72
3.19. FFT plots of wideband amplitude responses of two paths . . . . .	72
3.21. Calibration of multiple RF signal paths. . . . .	72
3.20. Response of IQ paths to Sinc stimulus post calibration . . . . .	73
3.22. Work Bench with DAC, IF up-converter and RF test instruments . .	74
3.23. Four Signal Paths Test Apparatus . . . . .	75
3.24. Four paths of LINC Transmitter calibrated with chirp stimulus . . . .	76
3.25. Comparison of spectrum of a 64-QAM modulated signal . . . . .	77
3.26. Comparison of constellations of 64-QAM signal post calibration . . .	77
3.27. Ku-Band test bench . . . . .	78
3.28. Comparison of spectrum of a DVB-S2 8PSK modulated signal at Ku Band before and after calibration . . . . .	78
3.29. Comparison of 8PSK constellation before and after calibration of the double heterodyne Ku Band modulator . . . . .	79
3.30. Modulation parameters reported by Vector Signal Analyser 'FSQ-40' of R&S at 14.23GHz . . . . .	79
3.31. Calibration of a wideband receiver with scalar RF down-converter . .	80
3.32. Calibration of a wideband receiver with vector RF down-converter . .	81
3.33. DC offset in ADCs of a receiver observed in response to chirp stimuli	81
3.34. Frequency domain spectra of magnitude and phase of stimulus . . . .	84
3.35. Constellation is mapped on a polar plot with 64-QAM modulation symbols. . . . .	84
3.36. Identification of AM-AM and AM-PM distortions . . . . .	85
3.37. Comparison of constellations of a 256-QAM modulated signal before and after calibration by constellation mapping technique. . . . .	86

3.38. Comparison of constellations of an 8PSK modulated signal before and after calibration by constellation mapping technique. . . . .	87
3.39. Comparison of QAM64 constellation before and after calibration of the single heterodyne Ku Band modulator . . . . .	88
3.40. Comparison of QAM64 constellation before and after calibration of the transmitter with a Doherty Amplifier . . . . .	89
4.1. Typical Single Transistor RF Power Amplifier Circuit . . . . .	92
4.2. Power Amplifier's RF Output Spectrum . . . . .	94
4.3. Impact of AM AM conversion on the amplitude of an OFDM signal subject to amplification by a non-linear amplifier . . . . .	95
4.4. Impact of AM AM conversion on the amplitude of an OFDM signal subject to amplification by a non-linear amplifier. . . . .	96
4.5. OFDM Envelope . . . . .	98
4.6. RF Transmitter with Power Amplifier and Receiver for DPD . . . . .	102
4.7. Adaptive Learning . . . . .	102
4.8. Typical DC bias characteristics of RF power transistor . . . . .	104
4.9. Waveforms of RF voltage and current in a Class A Amplifier . . . . .	105
4.10. Waveforms of RF gate voltage and drain current in a Class B Amplifier	105
4.11. Waveforms of RF gate voltage and drain current in a Class AB Amplifier	106
4.12. Waveforms of RF gate voltage and drain current in a Class C Amplifier	107
4.13. Class E Amplifier Schematic . . . . .	108
4.14. Typical Class E Drain-Source Voltage and Current Waveforms . . . . .	108
4.15. Block Diagram of Outphasing Amplifier . . . . .	111
4.16. Spectrum of Original WCDMA signal . . . . .	112
4.17. Spectrum of outphasing signals generated for the WCDMA signal . . . . .	112
4.18. Outphasing Constellation . . . . .	113
4.19. Spectrum of the ideally re-combined outphasing signals . . . . .	113
4.20. Structure of nonisolated Chireix combiner. . . . .	114
4.21. Doherty Amplifier Block Diagram . . . . .	114
4.22. Doherty Amplifier Efficiency curve . . . . .	116
4.23. Outphasing Modulator Calibration Setup . . . . .	117
4.24. Work Bench with DAC, IF up-converter and RF test instruments . . . . .	118
4.25. Outphasing transmitter Spectrum before and after calibration with Chirp stimulus . . . . .	119
4.26. Outphasing transmitter Spectrum before and after calibration with Sinc stimulus . . . . .	119
5.1. Channel probing model between legitimate wireless nodes in the presence of an eavesdropper. . . . .	127
5.2. CCDF plot of a 2048 point OFDM signal with 1664 QPSK modulated sub-carriers exceeding threshold PAPR values . . . . .	129
5.3. PAPR reduction by clipping. . . . .	130
5.4. Selective Mapping . . . . .	131

5.5. Scheme of Partial Transmit Sequence . . . . .	132
5.6. Diffie Hellman Key Agreement . . . . .	134
5.7. Fig. 5.7 Practical Channel Probing Model. . . . .	136
5.8. Channel Probing Procedure . . . . .	138
5.9. Normalised Convolved Channel and Hardware Frequency Responses .	140
5.10. Encrypting OFDM Modulated Signals . . . . .	142
5.11. Frequency Response of Hamming Windowed FIR Filter . . . . .	145
5.12. Proposed Physical Layer Encryption Scheme with Encryption Filter .	147
5.13. Ku-Band test bench . . . . .	148
5.14. Original Constellation . . . . .	148
5.15. Encrypted Constellation . . . . .	149
5.16. Recovered Constellation Re-modulated . . . . .	149
5.17. Spectrum Comparison . . . . .	149
5.18. Gerber screenshot of the antenna designed and its simulated gain pattern (dBi) in azimuth plane. . . . .	150
5.19. Test Bench used for validation. Node 1 is on the left. Node 2 and Node 3 are on the right. Node 3 is connected to a Vector Signal Analyzer. . . . .	151
5.20. Frequency Responses of Node 1 and Node 2 at 28.9 GHz . . . . .	151
5.21. Screenshot of measured channel responses between legitimate nodes and the eavesdropper . . . . .	152
5.22. Apparatus used for symmetric key generation . . . . .	153
5.23. Key generation information consisting of convolved channel and hard- ware responses evaluated at each node. . . . .	154
5.24. Phase encrypted OFDM sub-carriers received over the 28.9GHz wire- less link. . . . .	157
5.25. Recovered QPSK constellation of OFDM sub-carriers received over the 28.9 GHz wireless link. . . . .	158
5.26. CCDF of PAPR of Original and Encrypted 2048 point QPSK-OFDM modulated signals with 1664 active sub-carriers . . . . .	159
5.27. CCDF of PAPR of Original and Encrypted 2048 point QAM64-OFDM modulated signals with 1664 active sub-carriers . . . . .	159
5.28. Comparison of amplitudes of the original and encrypted signals . . .	160
5.29. PAPR comparison over 10000 simulation cycles . . . . .	160
5.30. First 1000 symbols of he received encrypted 8PSK signal before de- cryption and equalization. . . . .	162
5.31. Recovered 8PSK constellation after decryption filtering and equaliza- tion. . . . .	162
6.1. Generic block diagram of a wireless transmitter . . . . .	166
6.2. DAC slewing and settling times. . . . .	167
6.3. Response of Anti-Alias Filter . . . . .	168
6.4. Transmitter with feedback for DPD . . . . .	169
6.5. DAC Multiplexing . . . . .	170

6.6. DAC Time Interleaving . . . . .	172
6.7. .Interleaving DACs in frequency domain . . . . .	174
6.8. Practical frequency domain interleaving DACs with images . . . . .	175
6.9. Switched band feedback receiver for DPD . . . . .	177
6.10. Wideband signal generated in parts and combined at 2.4 GHz . . . . .	178
6.11. Bandwidth Interleaved Modulator . . . . .	179
6.12. Complex baseband FFT and its output modulation spectrum . . . . .	180
6.13. . Digital up-conversion of the desired baseband to digital IFs in quadrature. The chosen digital IF is centred at $F_s/4$ . . . . .	181
6.14. Single sideband up-conversion and combination of the interleaved basebands. . . . .	182
6.15. Spectrum screenshots of 96MHz DVB-S2 8PSK signal generated at 2.29 GHz with BW interleaved modulators. . . . .	183
6.16. 8-PSK modulated signal generated with single wideband modulator using DACs operating at 200 MSPS . . . . .	187
6.17. 8-PSK modulated signal generated with bandwidth interleaved modulator using DACs operating at 100 MSPS. . . . .	188
6.18. Phase noise of 600 MHz clock . . . . .	189
6.19. Phase noise of 300 MHz clock . . . . .	190
6.20. LO phase noise profile at Ku Band . . . . .	190
6.21. Spatially Combined Bandwidth Interleaved . . . . .	191
6.22. Two transmitters spatially combined . . . . .	192
6.23. Gerber screenshot of the antenna designed and its simulated gain pattern (dBi) in azimuth plane. . . . .	194
6.24. Test Bench used for validation. Receiver is on the left. The transmitters are on the right. . . . .	194
6.25. Antenna placement (Left: Receiving Antenna) (Right: Transmitting Antennas) . . . . .	195
6.26. Received Spectrum of Bandwidth interleaved transmission . . . . .	196
6.27. Comparison of constellations demodulated by VSA at 28.9GHz. . . . .	196
6.28. Spectrum of 400MSPS 8PSK signal received from interleaved transmitters centered at 28.9GHz . . . . .	197
6.29. Demodulated 8PSK constellation at 400MSPS . . . . .	197
6.30. Uncalibrated case with bandwidth interleaved transmitters . . . . .	198
6.31. Spectrum of 355.2 MHz wide QAM64 modulated OFDM signal . . . . .	199
6.32. Demodulated constellation of QAM64 OFDM signal of bandwidth 355.2MHz . . . . .	199
6.33. Comparison of PAPR of Bandwidth Interleaved Signals against that of the original wideband signal. . . . .	200
A.1. Phase Locked Loop based Local Oscillator . . . . .	211
A.2. VCO schematic . . . . .	212
A.3. LO phase noise profile at Ku Band . . . . .	213

B.1. Sinc Roll-off . . . . .	216
B.2. Constellation Dispersion due to Noise and Jitter . . . . .	217

# 1. Introduction

In modern wireless communications, digital data in a communicating node is processed by several computing stages through software and hardware modules in accordance with a pre-defined protocol. The processed data is transmitted over wideband complex envelope modulated radio frequency (RF) carriers. The different processing stages are abstracted in the form of a network protocol stack. The protocol stack of Wireless Local Area Network (WLAN) system is shown in Fig. 1.1. The data to be communicated is generated in the upper most layer i.e. the application layer and then encapsulated in the form of packets, framed, formatted, encoded in the next four layers of the stack with each layer accomplishing a distinct objective and adding its header to the data to be transmitted. The physical layer (PHY) is tasked with the actual connectivity of the transmitting or receiving node to the peer node through the communication channel. This layer defines the transmitter-receiver (transceiver) hardware and air interface specifications such as carrier frequency ( $F_c$ ), modulation standard, signal bandwidth (BW), effective isotropic radiated power (EIRP), RF pulse width, etc. The focus of the work presented in this thesis is on enhancing the PHY performance for transmission of wideband modulated signals.

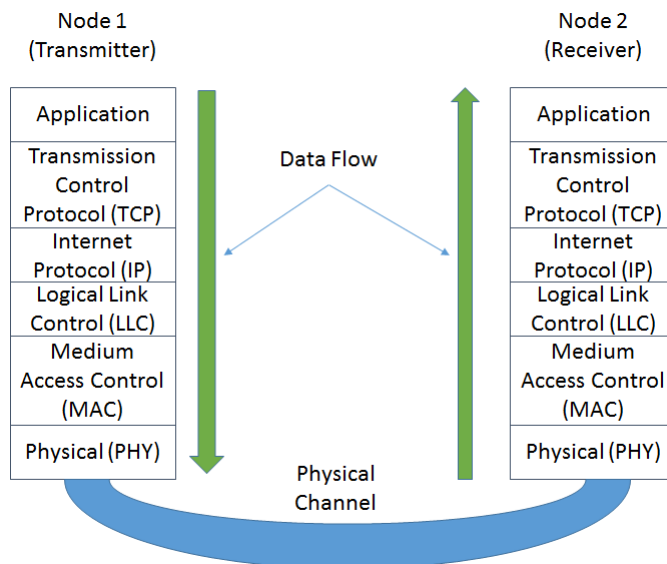


Fig. 1.1.: Network Protocol Stack

## 1.1. Key Parameters, Channel Capacity and Resource Sharing Schemes in Wireless Communications

Wireless communications take place over the microwave and millimetre wave bands of the electromagnetic spectrum which are allocated to network operators in accordance with legal and commercial agreements governed by national and international authorities. The available band of spectrum is divided into channels which are in-turn allocated to users of the network by the operator/communications controller. Some of the key parameters of the channel are introduced in this sub-section.

### 1.1.1. Channel Parameters

Carrier Frequency ( $F_c$ ): This refers to the frequency of a radio carrier around which data is centred for wireless communications.

Bandwidth (BW): The length of the band or range of frequencies occupied around the carrier by the data intended to be transmitted/received.

Modulation: A process of varying some parameter of a radio carrier in accordance with the data to be transmitted.

a) Amplitude modulation (AM): The amplitude of the carrier signal is varied in accordance with the data to be transmitted.

b) Frequency modulation (FM): The frequency of the carrier signal is varied in accordance with the data to be transmitted

c) Phase Modulation (PM): The phase of the carrier signal is varied in accordance with the data to be transmitted

d) Vector Modulation: A modulation scheme involving radio signals at the same frequency but at orthogonal phases where each point in the modulation space is defined by a magnitude and phase.

Eg: Phase Shift Keying (PSK), Quadrature Amplitude Modulation (QAM).

Signal to Noise Ratio (SNR): Ratio of the power of the signal of interest to the power of noise in the channel.

### 1.1.2. Channel Capacity

Channel capacity ( $\{C_c\}$ ): This refers to the amount of information that can be carried on a channel as a function of SNR. The channel capacity in bits per second is provided by Shannon's formula:

$$C_c = BW \log_2(1 + SNR) \quad (1.1)$$

### 1.1.3. Resource Sharing Schemes

The most valuable resource in wireless communications is the electromagnetic spectrum over which transmission and reception take place. It is therefore imperative to share the available spectrum between several users, their data sources and several communicating nodes.

**Multiplexing:** The process of distributing parts of a resource to multiple data sources/entities.

a) **Time Division Multiplexing (TDM):** A multiplexing scheme where a given spectrum or bandwidth for communication is allotted to different data streams/entities at fixed time slots.

b) **Frequency Division Multiplexing (FDM):** A multiplexing scheme where the available frequency spectrum is divided into smaller parts and allocated to different data streams/entities.

c) **Orthogonal Frequency Division Multiplexing (OFDM):** A scheme where the bandwidth available around a radio carrier is divided into orthogonal sub-carriers which are modulated in accordance to the data to be transmitted. A block of data is split into parallel streams with the number of streams equal to the number of sub-carriers chosen in the available channel bandwidth. Each sub-carrier is modulated at a data rate equal to the intended data rate divided by the number of sub-carriers. Each sub-carrier is orthogonal to the other sub-carriers in the channel and hence the name. This task is popularly accomplished with the use of Fast Fourier Transforms (FFT).

**Multiple Access Scheme:** The scheme of allocating the access of wireless channels to multiple users/clients.

a) **Time Division Multiple Access (TDMA):** A multiplexing scheme where a given spectrum or radio channel for communication is allotted to different users/clients at fixed time slots. Every user in the scheme can access the entire radio spectrum in his/her time slot.

b) **Frequency Division Multiple Access (FDMA):** A multiplexing scheme where the overall available frequency spectrum is divided into smaller parts and allocated to different users/clients. Every user can access his/her portion of the spectrum all the time.

c) **Code Division Multiple Access (CDMA):** A spread spectrum scheme where several nodes communicate over the same carrier frequency and band using different pseudorandom spreading codes.

d) **Hybrid Multiple Access Schemes:** Schemes were combinations of the above access schemes are involved.

e) **Orthogonal Frequency Division Multiple Access (OFDMA):** A scheme where the overall spectrum available is divided into channels and each channel is divided in

to sub-carriers and the users/clients are allocated a subset of sub-carriers either in the same or multiple channels. The modulation on each sub-carrier may be same or different depending upon the available Signal to Noise Ratios.

f) Spatial Division Multiple Access (SDMA): A scheme where directional properties of radiated RF signals are exploited to reuse a set of frequencies at multiple geographical regions. Two or more regions can use the same set of frequencies if they are separated to an extent such that the transmissions don't interfere mutually. SDMA is used in conjunction with other multiple access schemes mentioned above.

## 1.2. Features of Next Generation Wireless Communication Systems

The process in a radio transmitter involves generation of the carrier, modulating one or more of its parameters namely amplitude, phase and frequency by the data intended to be transmitted, boosting the signal strength to cover the required communication range and transmitting it through a designated RF channel by means of an antenna. The modulation schemes adopted in present day wireless systems involve vectors where the digital data to be transmitted is grouped in terms of number of bits and each bit pattern is assigned a magnitude and a phase (angle) thereby generating a vector symbol. In other words, each pattern of 'n' bits of digital data is assigned a vector symbol where 'n' is the number of bits per symbol. For example in a general Offset Quadrature Phase Shift Keying (O-QPSK) modulation scheme, the digital data is grouped in the form of symbols of two bits each with the possible patterns 00, 01, 10, 11 and each of these symbols is represented by a magnitude and phase as shown in Tab. 1.1.

**Tab. 1.1.:** QPSK symbols, real and imaginary parts

Bit Pattern/Symbol	Magnitude	Phase/Angle in degrees	Complex representation	Real Part (I)	Imaginary (Q)
00	1	45	$0.707+j0.707$	0.707	0.707
01	1	135	$-0.707+j0.707$	-0.707	0.707
11	1	225	$-0.707-j0.707$	-0.707	-0.707
10	1	315	$0.707-j0.707$	0.707	-0.707

The digitally generated vector baseband symbols representing each bit pattern are also represented in the form of complex numbers. The real part of the complex symbol thus generated is designated as the 'In-Phase' (I) component and the imaginary part of the complex symbol is designated as the 'Quadrature' (Q) component. The 'I' and 'Q' components of the modulation symbols are orthogonal to one another i.e. exhibit a phase difference of 90 degrees between one another. In the QPSK case, the modulated signal carries two bits of information per Hz of bandwidth.

Next generation wireless communications such as Fifth Generation or 5G Wireless and Next Generation High Throughput Satellite have promised a step increase in the rates at which data can be communicated. The technical objective of Mobile and wireless communications Enablers for the Twenty-twenty Information Society (METIS) [1][2] that reflects the 5G requirements is to develop technical solutions towards a system concept that supports 1000 times higher mobile data volume per area, 10 to 100 times higher number of connected devices and 10 to 100 times higher user data rate. Spectrum in wireless communications is limited in availability and licensed by regulatory bodies. With increasing demands for speed of wireless connectivity, it is imperative to maximize the utilization of the available spectrum by transmitting as many bits as possible per Hz using schemes such as Quadrature Amplitude Modulation with 256 constellation points (QAM 256) where 8 bits of data are transmitted per Hz of bandwidth. However, scaling up the order of modulation i.e. number of bits per Hz is not an easy task. An increase in the channel capacity by a bit per Hz requires an increase in the signal to noise ratio (SNR) by a factor of 2 as can be inferred from eq. 1.1. The available SNR is limited by several factors such as fading, channel noise, noise figures of the RF hardware involved in generation, transmission and reception of the modulated signal. It is also equally necessary for a wireless service provider to allocate the available spectrum to clients using efficient sharing mechanisms or multiple access schemes where each client gets a fair share of the spectrum for the data at his/her end to be communicated whenever needed. Some of the key enablers to accomplish the objective of seamless wireless communication at data rates in the order of multiple gigabits per second are:

1. Wider Channel Bandwidths and Carrier Aggregation
2. Advanced waveforms and adaptive modulation schemes.
3. Multi-Band Operation
4. Spatial division multiple access, MIMO

The term MIMO refers to Multi-Input Multi-Output schemes where the wireless communications between two nodes take place over multiple propagation paths traversed by the RF signals between them. If the signal propagation paths are uncorrelated, the data rate can be scaled up by the number of paths despite using the same carrier frequency and bandwidth i.e. same spectrum. Orthogonal Frequency Division Multiplexing (OFDM) is a scheme where the bandwidth available around a radio carrier is divided into orthogonal sub-carriers which are modulated in accordance to the data to be transmitted. A block of data is split into parallel streams with the number of streams equal to the number of sub-carriers chosen in the available channel bandwidth. Each sub-carrier is modulated at a data rate equal to the intended data rate divided by the number of sub-carriers. Each sub-carrier is orthogonal to the other sub-carriers in the channel and hence the name. This task is popularly accomplished with the use of Discrete Fourier Transforms (DFT). An

OFDM signal may be mathematically represented in the form eq. 1.2

$$s(t) = \frac{1}{\sqrt{N}} \sum_{k=1}^N X(k)e^{j2\pi kt/T_s} \quad (1.2)$$

where  $s(t)$  is the instantaneous time domain value of the OFDM signal at time  $t$   $N$  is the number of points in the FFT is the sampling interval in seconds  $X(k)$  is the  $k$ th complex modulated symbol OFDM based modulation schemes have been deployed in a number of present day state of the art wireless communication systems such as Long Term Evolution (LTE), WLAN, Digital Video Broadcast – Terrestrial (DVB-T/T2), etc. Carrier aggregation refers to transmission of the intended data on more than one carrier frequency simultaneously. The carrier frequencies could be in the same frequency band (intra-band) or in different frequency bands (inter-band). Similarly if the aggregated carriers are contiguous in frequency, the scheme is termed Contiguous Carrier Aggregation. European Telecommunications Standards Institute (ETSI) has published extension of licensed spectrum for commercial wireless networks to millimetre wave bands up to 145 GHz for back haul radio links [3] with channel bandwidths up to 800 MHz supporting data rates in the range 5 to 10 Gbps with 4L multi input multi output (MIMO) configuration and carrier aggregation in November 2018. Qualcomm Technologies Incorporation (QTI) has published commercially viable schemes in [4] for mobile communications where the commercial spectrum extends to 28 GHz with channel bandwidths up to 400 MHz. The air interface features modulation schemes in accordance with 5G New Radio (5G NR) standard where scalable OFDM modulated carriers are employed with carrier and time slot aggregations. Time Slot aggregation refers to transmission of the intended data in more than one time slot.

Some of the salient features of Next Generation High Throughput Satellite Communications [5, 6]:

- a) Wideband, High-Capacity Waveform Q Scalable from 1 to 225 Msps/32APSK
- b) Higher orders of modulation and wideband carriers that enable higher efficiencies and throughputs with bandwidths up to 500 MHz per beam.
- c) Very high density, up to 2 Gbps capacity per transceiver.
- d) Readily scalable from 100 to 100,000s of sites with the use of spot beams.
- e) Adaptive coding and modulation schemes.

Wireless standards for low power indoor short [4, 7] distance communications in unlicensed bands such as IEEE 802.11ad have evolved which feature channel bandwidths of 2.16GHz at carrier frequencies operating in the 60GHz band.

Work has also been in progress to integrate satellite communications in 5G networks [8, 9].

### 1.3. Challenges In The Design For Next Generation Wireless Communications That Motivated This Work

A radio transceiver is the fundamental block of a wireless communication node. The high level functional block diagram of a typical radio transceiver for wireless communications is shown in Fig. 1.2 where the transmitter section consists of a vector modulator where an RF carrier generated by the local oscillator LO-1 is subject to complex envelope modulation. The power of the modulated signal is then boosted in accordance with the distance over which communication needs to be performed. The receiver section consists of a low noise amplifier (LNA) tasked with increasing the strength of the received signal to a level compatible with the vector demodulator. The vector demodulator recovers the transmitted bit stream for further processing and interpretation by the computing device. The transmitter and the receiver are connected to a common antenna through a duplexer whose architecture depends on the type of duplexing scheme.

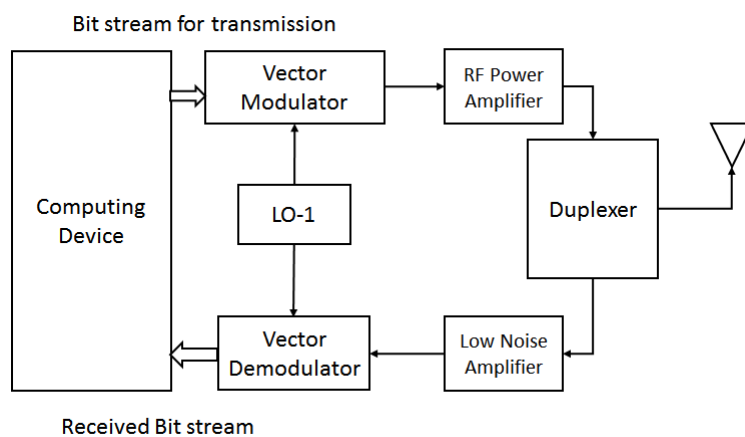


**Fig. 1.2.:** Functional Block Diagram of a Radio Frequency Transceiver

The quality of the modulated signal generated and transmitted depends on the quality of the modulator, oscillator and the RF power amplifier. Their performance over the operating bandwidth and dynamic range of the signal encountered impose limits on the range, speed and reliability of the wireless communication system. The system level design challenges that motivated this research are

1) Bandwidth dependent performance of the functional modules in a transmitter: The modulator in the transmitter is made up of Digital to Analogue Converters (DACs), RF mixers, RF filters and associated circuits whose transfer functions vary as a function of the frequency of operation and its modulation bandwidth. This is particularly significant when it is required to design systems to support the data rates in the order of multiple gigabits per second discussed in the previous section.

Similarly, the modules present in the demodulator such as RF mixers, baseband filters, Analogue to Digital Converters (ADCs) present significant challenges in reception and detection of wideband complex modulated signals. These parameters and associated distortions are described in Chapter 2. This thesis is focussed on enhancing the wideband performance of transmitters providing seamless bandwidth scalability next generation wireless communications.

2) Peak to Average Power Ratio (PAPR): This is the ratio of the peak power in a modulated signal to its average power. The present generation wireless standards specify OFDM modulated schemes due to their obvious benefits of immunity against fading, resilience to interference and simpler channel equalisation. But OFDM modulated signals possess high PAPR values [10]. This may be visualized in the form of Inverse Fourier Transform of a rectangular function. For example, if the magnitude of  $X(k)$  in eq. 1.2 remains the same at all active sub-carriers at value '1', it results in a rectangular function in frequency domain. It may be inferred that the inverse Fourier Transform of a rectangular function would yield a sinc function exhibiting a high PAPR. 5G wireless communication standard features flexible bandwidth and numerology configurations. An example of a 5G OFDM configuration at 28 GHz with sub-carrier spacing (SCS) of 120 kHz and bandwidth 400 MHz in [4]. The RF power amplifier (PA), which is a power hungry and an expensive part in the transmitter would need to be operated in a linear manner to adhere with the amplitude swings encountered with present day and next generation modulation schemes. Linear operation of a PA results in power inefficiency leading to high operating costs and thermal dissipations and it is hence preferred to operate the PA close to saturation region of its transfer characteristics. However, the PA would need to be backed off from operating at the saturation point to accommodate swings in the envelope of the signal being amplified. Therefore, signals with high PAPR would imply greater levels of back off for the PA and hence lower efficiency. Published state of the art frequency domain PAPR reduction techniques require extra information to be transmitted to restore the original amplitudes at the receiver for faithful demodulation. One of the objectives of the research work undertaken is to derive techniques to reduce the PAPR of wideband OFDM modulated signals in a manner such that the process can be undone at the receiver prior to demodulation in a predictable manner and without additional information being transmitted.

3) Transmission over parallel RF signal paths: MIMO communications involves transmission of data over parallel signal paths using an array of antennas. Spatial Division Multiple Access (SDMA) schemes require antennas with narrow beam widths. This often requires an array of antennas with appropriate amplitude and phase excitations. Mismatch in amplitudes and phases between the feeding paths over the bandwidth of interest results in undesirable radiation characteristics. Multi-input RF power amplifiers such as Outphasing Amplifiers involve signal amplification in parallel stages whose outputs are combined to yield an amplified version of the signal intended to be transmitted. Signal distortions in any of the paths involved and imbalances between the amplitude and phase responses over the bandwidth of

operation will jeopardize the entire system. An objective of the research work undertaken was to derive novel techniques to identify the imbalances and distortions present in multiple RF signal paths of a transmission system across the bandwidth of interest and mitigate them through digitally assisted means.

4) Security in the Physical Layer: Unlike, wired communication schemes, wireless data transmission is broadcast where the occurrence of transmission is sensed and can be received by multiple receivers including the legitimate nodes and eavesdroppers. The security of the data transmitted depends on the ability to encrypt the data such that only the legitimate receivers are able to interpret the message. This task is conventionally handled in the higher layers of the network protocol stack with techniques such as scrambling, bit and packet encryption. These techniques however do not encrypt the air interface of the wireless network and therefore leave the nodes open for traffic analysis and interception by eavesdroppers and man-in-the-middle platforms [11, 12]. One of the ways to reduce the probability of interception by an unauthorized node is to provide a degree of security in the physical layer (PHY) independent of the network protocols and infrastructure. Physical layer security has been gaining interest among researchers in recent years. One of the methodologies developed in the research work undertaken was to encrypt the modulated constellation of the signal being transmitted so as to impair the ability of eavesdroppers from demodulating it.

Overall, this thesis presents innovative techniques to mitigate limitations in radio frequency hardware that hinder wideband operation and schemes to construct scalable bandwidth transceivers with scope to reuse legacy radio frequency hardware for next generation communication systems in part or whole. The remainder of this thesis is organized as follows:

Chapter 2: A block level description of a radio transceiver, key performance indices of its transmitting and receiving sections and bandwidth dependent signal distortions in them are presented.

Chapter 3: The work in this chapter focusses on characterizing wideband impairments in radio frequency hardware described in Chapter 2 and mitigating them through digital signal processing. Novel techniques that were developed by the author to calibrate multiple RF signal paths in a single iteration are presented. These correspond to items 2, 3 and 7 in the list of publications.

Chapter 4: An introduction to RF Power Amplifiers (PAs), their classes, topologies, behavioural modelling and digital pre-distortion (DPD) are discussed. The novel techniques developed by the author and presented in Chapter 3 are applied to calibrate the RF signal paths in a multi-way Doherty power amplifier and to linearize an outphasing power amplifier in collaboration with co-researchers. These correspond to items 5, 6, 12 and 13 in the list of publications.

Chapter 5: Schemes to provide security in physical layer of wireless communications and techniques for reduction of PAPR in OFDM signals are discussed. A novel scheme for encrypting wideband signals to jointly provide security in the physical

layer and reduce PAPR is presented where the key for encryption is generated using the unique hardware and channel responses between two legitimate nodes is presented over the operating bandwidth. These correspond items 8, 10 and 11 in the list of publications.

Chapter 6: System design techniques to generate and transmit wideband complex modulated signals in parts using multiple modulators and transmitters and combining them in a seamless manner are presented. The techniques presented enable mitigation of bandwidth limitations in the baseband and RF hardware at system level, enable construction of scalable bandwidth transmitters and also enable reuse of legacy equipment for next generation wireless communications in part or whole. These correspond items 8, 10 and 11 in the list of publications. 1, 4 and 9 in the list of publications.

Chapter 7: The conclusions derived from this work are summarized.

## 2. Overview of a Wireless Transceiver and Signal Distortion Effects in Wireless Communications

Enablers for next generation wireless communications present significant engineering challenges to mitigate in each stage of the wireless transceiver owing to practical limitations caused by bandwidth and frequency dependent impairments. In this chapter, the functional block diagram of a radio transceiver for wireless communications is introduced. This is followed by an introduction to key performance indices of the transmitter and the receiver sections. The impairments caused by linear and weakly non-linear modules in the RF chain with focus on factors that affect bandwidth are discussed in the third part.

### 2.1. A Modern Wireless Transceiver

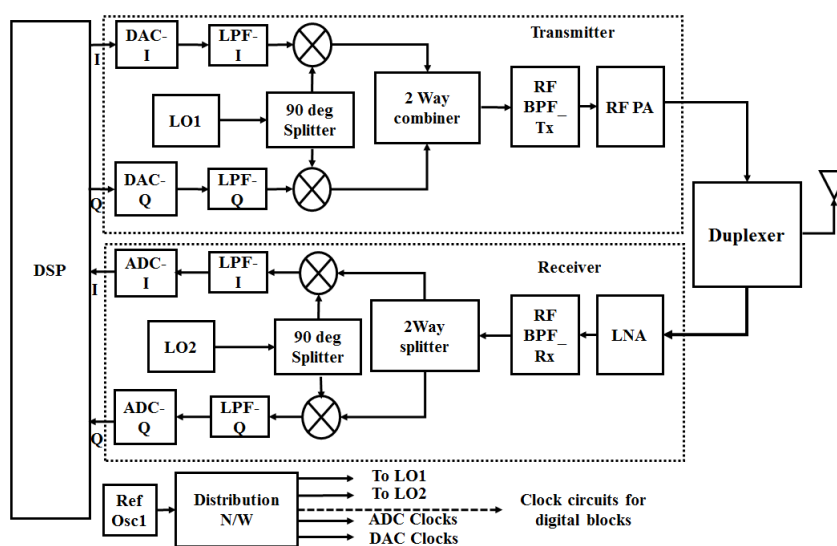
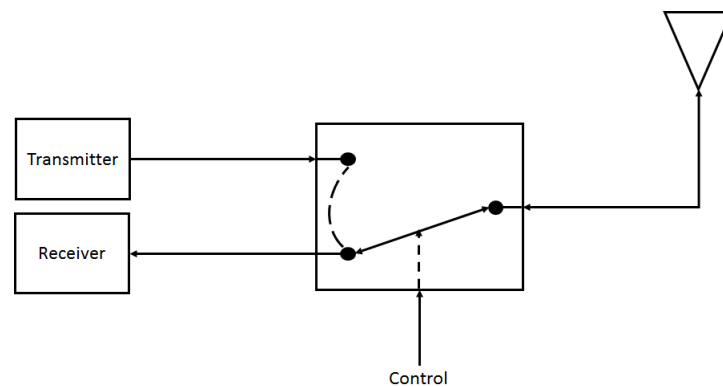


Fig. 2.1.: Block Diagram of Wireless Transceiver

The functional block diagram of a radio frequency transceiver was described in Chapter 1. A more detailed block diagram of a typical present day wireless transceiver is shown in Fig. 2.1. The transmitter consists of a digital signal processor (DSP) that generates the vector modulated symbols consisting of quantized amplitudes and phases in response to the digital data intended to be transmitted. The Digital to Analogue Converters (DACs) in the I and Q signal paths generate the equivalent analogue baseband signals. The outputs from the DACs are translated to the intended radio frequency (RF) through mixers in each path by multiplication with the intended RF carrier signal. The LO signal is injected in the I and Q signal paths at quadrature to one another to accomplish vector up-conversion. This yields a complex envelope modulated signal at the intended carrier frequency. The vector up-converted signal is filtered to suppress frequency components outside the band of interest by means of an RF band pass filter (BPF). The bandwidth of the modulated carrier is proportional to the rate at which the intended data modulates the carrier i.e. the faster the data, higher is the bandwidth needed. For example, an ideal wireless transmission system where the input bits change at a rate of 200 megabits per second (Mbps) employing a QPSK modulation scheme where each symbol represents two bits with require a bandwidth of 100 megahertz (MHz ). The filtered output is then amplified to the required power in the RF power amplifier (PA). The output of the PA is transmitted through the duplexer and the antenna. The duplexer is a block that separates the signal being received from that being transmitted.

**a) Time Division Duplex (TDD):** In this scheme, the transmitter and the receiver are connected to the antenna at different timeslots and operate at the same carrier frequency and bandwidth. An RF Single Pole Double Throw (SPDT) switch is used to connect the antenna to the transmitter or the receiver at the appropriate timeslot. A block diagram of this scheme is shown in Fig. 2.2.



**Fig. 2.2.:** Time Division Duplex

**b) Frequency Division Duplex (FDD):** In this scheme, the transmitter and the receiver operate at different frequencies and can hence operate simultaneously

all the time. The signals for transmission and reception paths are separated by means of band-pass filters (BPF) in each signal path to reject the signals from the other signal path. Fig. 2.3 Frequency Division Duplex.

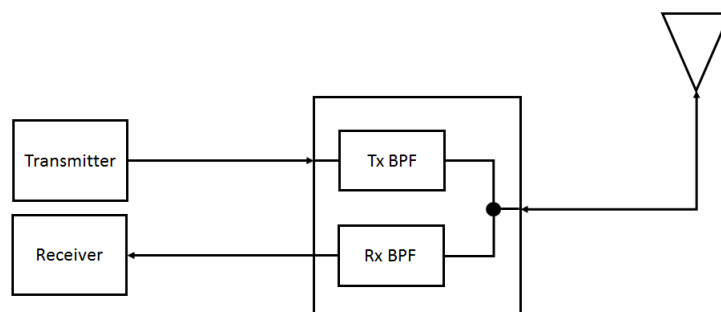


**Fig. 2.3.:** Frequency Division Duplex

## 2.2. Key Performance Indicators of SISO Transceivers

The radio frequency (RF) transceiver is the most critical part of the physical layer in a wireless communication system. The quality of service depends upon the extent of achievable performance of wireless transceivers deployed in the wireless network for the intended application. The key performance indicators of the transmitter and the receiver sections in a transceiver are summarized below.

### 2.2.1. Key Performance Indices of an RF transmitter

**Centre frequency stability and accuracy:** This is a measure of the extent to which the carrier frequency deviates from its ideal value. The deviation is measured in parts per million (ppm). This parameter is dependent upon the design of the local oscillator (LO). The deviation in ppm is mathematically expressed as  $\delta f$ .

$$\delta f = \frac{f_{\text{actual}} - f_{\text{ideal}}}{f_{\text{ideal}}} \times 10^6 \quad (2.1)$$

where  $f_{\text{actual}}$  is the actual frequency of the signal generated by the LO and  $f_{\text{ideal}}$  is the ideal frequency of LO's output signal.

**Error Vector Magnitude (EVM):** This is a measure of the deviation of the values of modulated signal vectors from the ideal values. A comparison of ideal and measured modulation constellation of a transmitter is shown in Fig. 2.4. It may be

noticed that the actual modulated amplitudes and phases deviate from the ideal values. EVM is a measure of the extent of this deviation and an indicator of the integrity of the transmitter. The mathematical expression for EVM measured over N modulated symbols is

$$\text{EVM} = \sqrt{\frac{\text{RMS}(|I_{\text{ideal}}(n) - I_{\text{actual}}(n)|^2 + |Q_{\text{ideal}}(n) - Q_{\text{actual}}(n)|^2)}{(\text{RMS}(I_{\text{ideal}}(n) + jQ_{\text{ideal}}(n)))^2}} \quad (2.2)$$

where  $I_{\text{ideal}}(n) + jQ_{\text{ideal}}(n)$  value of nth modulated symbol.  $I_{\text{actual}}(n) + jQ_{\text{actual}}(n)$  is the actual measured value of nth modulated symbol. EVM in eq. 2.2 is expressed as root mean squared (RMS) value in percentage. It can also be expressed as a mean value and in decibel (dB) scale.

Higher order modulation schemes require low EVM. The lowest value of EVM is ‘0’ which implies no deviation from ideal value.

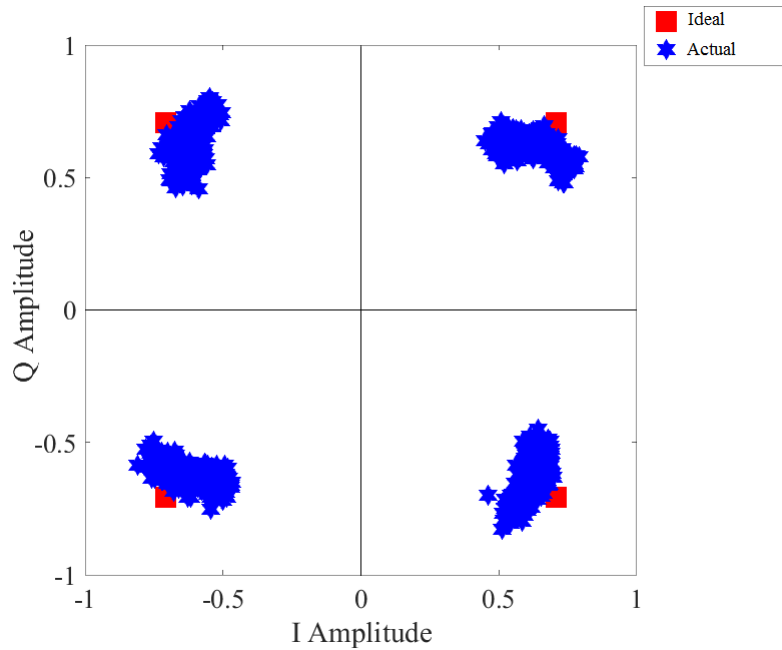


**Fig. 2.4.:** Ideal and Non-Ideal Constellation Comparison

**RF output power:** The modulation schemes used in modern wireless communications employ complex envelope modulated carriers and hence the power content in the signal being transmitted has peak and average values. Average power is derived from the RMS value of the amplitudes of the signal being transmitted. Peak power is derived from the maximum amplitude of the signal being transmitted. The RF power amplifier needs to maintain the PAPR to maintain the integrity of the modulated content. This will be elaborated further in Chapter 4.

**Power Amplifier Drain Efficiency ‘ $\eta$ ’:** This figure is an indicator of the extent of DC power consumed to produce the measured output RF power.

$$\eta = \frac{P_{\text{RF}}}{P_{\text{DC}}} \tag{2.3}$$

where  $P_{\text{RF}}$  is the output power and  $P_{\text{DC}}$  is the supplied DC bias power.

**Adjacent Channel Power Ratio (ACPR):** ACPR is a large signal parameter referring to the amount of power emitted by the transmitter outside its allocated channel that leaks into the adjacent channel. This parameter has a legal implication and its limit is set by the applicable wireless communication standard.

**Spurious Emissions:** These are RF emissions outside the allocated band of operation. The power of these emissions are required to be well below the power in the signal intended signal being transmitted. A typical pictorial description of spurious emissions in the output spectrum of a transmitter is shown in Fig. 2.5.

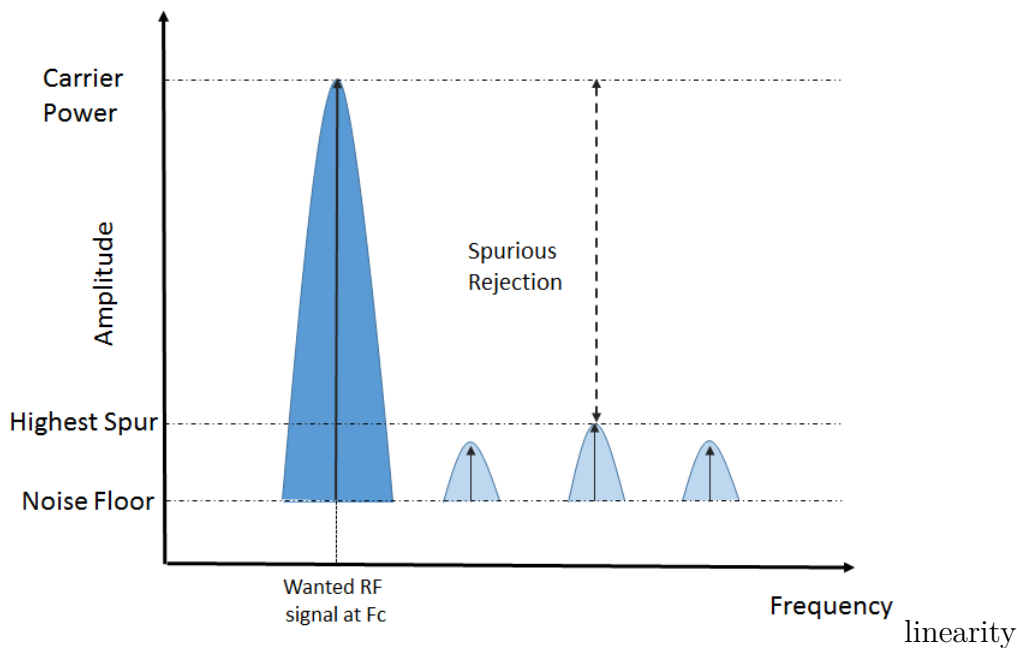


**Fig. 2.5.:** Spurious Emissions

**LO signal leakage:** This refers to the extent of leakage of un-modulated signal from the LO coupling with the RF output of the transmitter. This is particularly a problem encountered with zero-IF or direct conversion transmitters. The leakage causes power inefficiency and errors in the modulated constellation.

**Spectral Flatness:** This characteristic is a measure of extent of uniformity of RF gain across the channel bandwidth. This is particularly a critical parameter in

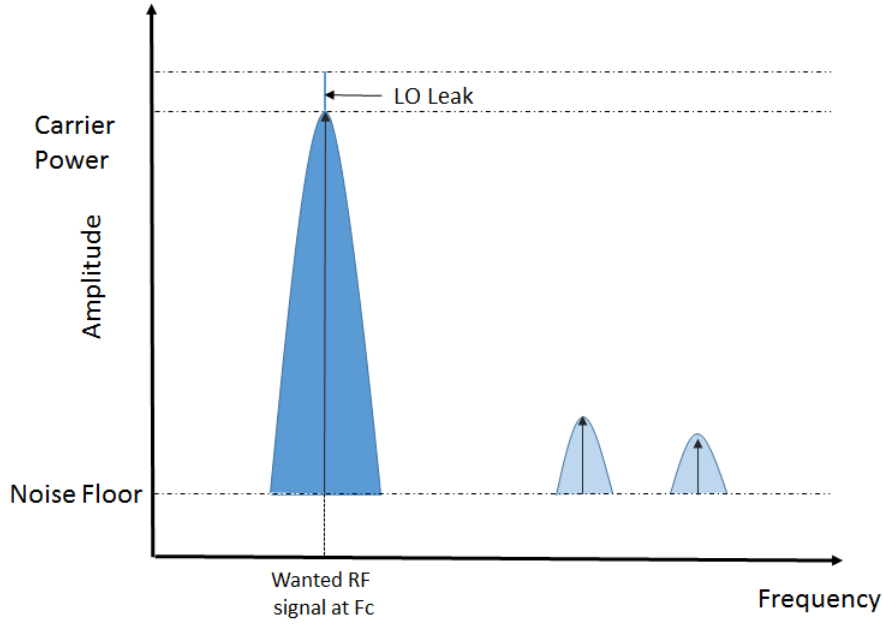


**Fig. 2.6.:** LO Leak

OFDM modulated systems since a droop or ripple in pass band gain can reduce the amplitude of a modulated sub-carrier relative to other sub-carriers leading to a misinterpretation of the transmitted symbol at the receiver.

**Power On and Power Down Ramp:** These parameters refer to the amount of time involved in the output of RF power to rise from 0 to 90% and from 100 % to 10% of the of final value respectively. These parameters are critical in TDD systems and are specified in the applicable wireless standards. For example, the maximum power on and power down ramp times allowed in WLAN transceivers is  $2\mu\text{sec}$ . RF power output vs time: These parameters are measures of stability of the RF output power of a transmitter and are affected by thermal factors.

**Output Voltage Standing Wave Ratio (VSWR ):** This is a sub-system parameter and refers to the extent to which the impedance at the RF output port of the transmitter is matched with the specified load. Impedance mismatches result in standing waves owing to reflections and large standing waves can cause permanent damage to RF power transistors. The relations between the output impedance, system's characteristic impedance (also load impedance), output reflection co-efficient and output VSWR are provided in equations eq. 2.4 and eq. 2.5.

$$\Gamma = \frac{Z_{\text{out}} - Z_o}{Z_{\text{out}} + Z_o} \tag{2.4}$$

$$VSWR = \frac{1 + \Gamma}{1 - \Gamma} \tag{2.5}$$

**Quadrature skew:** The ideal difference in phase between I and Q parts of the baseband signals should be 90 degrees. The extent of deviation from this figure is termed as quadrature skew. This skew affects EVM as shown in Fig. 2.7b. This is a measure of the quality of the modulator stage in the transmitter and the maximum acceptable limits are specified in the applicable wireless standards. Higher modulation schemes have lower tolerance to quadrature skew.

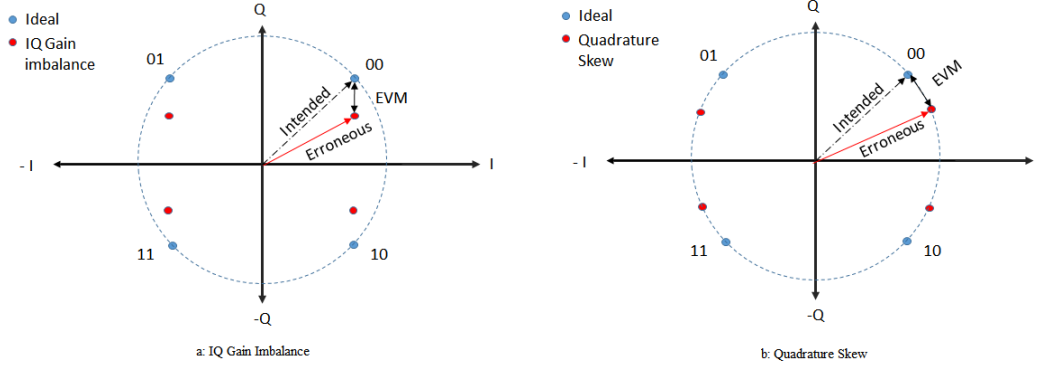


Fig. 2.7.: IQ Imbalance and skew

**I-Q gain imbalance:** This refers to an imbalance in gain between the I and Q signal paths in the transmitter. This imbalance affects EVM as shown in Fig. 2.7a.

### 2.2.2. Key Performance Indices of an RF receiver

**Sensitivity:** This refers to the minimum signal power needed at the radio receiver’s input port to be able to demodulate it to recover the transmitted data without errors. This parameter is a primary figure of merit of a receiver and indicates how far it can be located from the transmitter. The sensitivity of the receiver is determined by calculating the minimum detectable signal level with a given SNR, at a given signal bandwidth with a finite noise figure (NF).

**Noise Figure (NF):** This refers to the extent of noise added by the RF blocks in a receiver to the received signal and is popularly expressed in dB scale. It is also the ratio of SNR at the input to the receiver to the SNR at the output of the receiver. Noise Figure in linear scale (dimensionless) is designated as noise factor. In a receiver consisting of ‘N’ RF stages, the overall cascaded factor ‘NF<sub>N</sub>’ is given by the mathematical relation eq. 2.7.

$$F_{\text{total}} = F_1 + \frac{F_2 - 1}{G_1} + \dots + \frac{F_N - 1}{G_1 G_2 \dots G_{N-1}} \quad (2.6)$$

$$NF_N = 10 \text{Log}_{10} F_{\text{total}} \quad (2.7)$$

The thermal noise floor dependent on operating bandwidth and temperature is given by the mathematical relation eq. 2.8.

$$N_{\text{thermal}} = kTB \quad (2.8)$$

Where  $k$  is the Boltzmann constant equal to  $1.38 \times 10^{-23}$  J/K,  $T$  is the absolute temperature in Kelvin (K),  $B$  is the bandwidth in Hz. The sensitivity  $P_{\text{sens}}$  of the receiver in dBm may be calculated from  $N_{\text{thermal}}$  the thermal noise floor expressed in dBm, noise figure in dB, the required signal to noise ratio in dB  $SNR_{\text{dB}}$  using the mathematical relation given in equation eq. 2.9.

$$P_{\text{sens}} = N_{\text{thermal}} + SNR_{\text{dB}} + NF \quad (2.9)$$

**$P_{1\text{dB}}$  compression point:** This is the input power level at which the overall system gain of the receiver reduces by a dB.

**Dynamic Range:** This parameter refers to the range of input RF signal powers over which the receiver is able to demodulate the signal of interest without errors. The lower limit of this range is the sensitivity level and the higher limit is the input This is shown graphically in Fig. 2.8. This parameter is a measure of linearity in the receiver and indicates how close a receiver can be located relative to the transmitter to demodulate the signal of interest without errors.

**Intermodulation and Spurious Free Dynamic Range (SFDR):** Intermodulation refers to the process of two or more signals with frequencies in the band of interest mixing (multiplying) with one another to yield parasitic signals. The parasitic signals thus generated are termed as intermodulation products. This is caused by non-linear characteristics of the gain blocks in the receiver .

The parasitic signal components thus generated in the receiver due to non-linear transfer function of the gain block in the receiver are designated as intermodulation spurs. The intercept point for a given order of intermodulation is defined as the signal power level at which the gain presented to the fundamental (intended) frequency signal components would equal that of the intermodulation components.

**Output third order intercept point  $OIP_3$ :** This is defined as the signal power level at which the gain presented to the fundamental (intended) frequency signal components would equal that of the third order intermodulation components.  $OIP_3$  in dBm for an RF sub-system may be evaluated mathematically as given in

$$OIP_3 = P_{\text{fundamental}} + \frac{P_{\text{fundamental}} - P_{\text{IM3}}}{2} \quad (2.10)$$

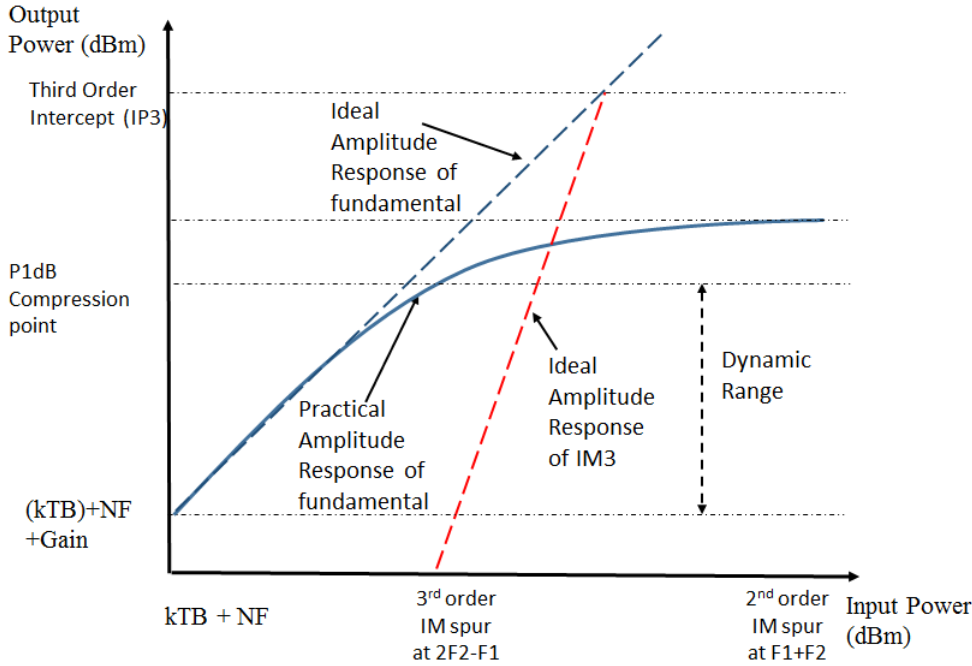


Fig. 2.8.: Non Linear Amplitude Response

where  $P_{\text{fundamental}}$  is the signal power level of the intended (fundamental) signal in dBm and  $P_{\text{IM3}}$  is the power level of the third order intermodulation signal components in dBm. It may be inferred mathematically that the third order intermodulation components increase by 3dB for every dB increase in the fundamental signal power. If the overall cascaded linear gain of the receiver has a magnitude ‘G’, the input third order Intercept point IIP3 may be obtained by dividing by G.

**Spurious Free Dynamic Range (SFDR):** This refers to the range of input power levels over which the receiver can operate while keeping the intermodulation spurs below the noise floor. SFDR depends on the intercept points for the order of intermodulation. The overall spurious free dynamic range SFDR in dB is mathematically given by eq. 2.11 and is shown graphically in Fig. 2.9.

$$SFDR = 2/3(IIP3_{\text{dBm}} - NF) \tag{2.11}$$

**Adjacent channel immunity:** This refers to the selectivity of the receiver i.e. the ability to receive the signal in the band of interest in the presence of a strong signal in the adjacent channel.

**Minimum SNR:** This is the minimum SNR required by the receiver to demodulate the signal of interest without errors. This parameter depends on the bandwidth and modulation scheme. The ideal value is given by Shannon’s equation of channel capacity mentioned in eq. 1.1 . The practical values of SNR needed for faithful

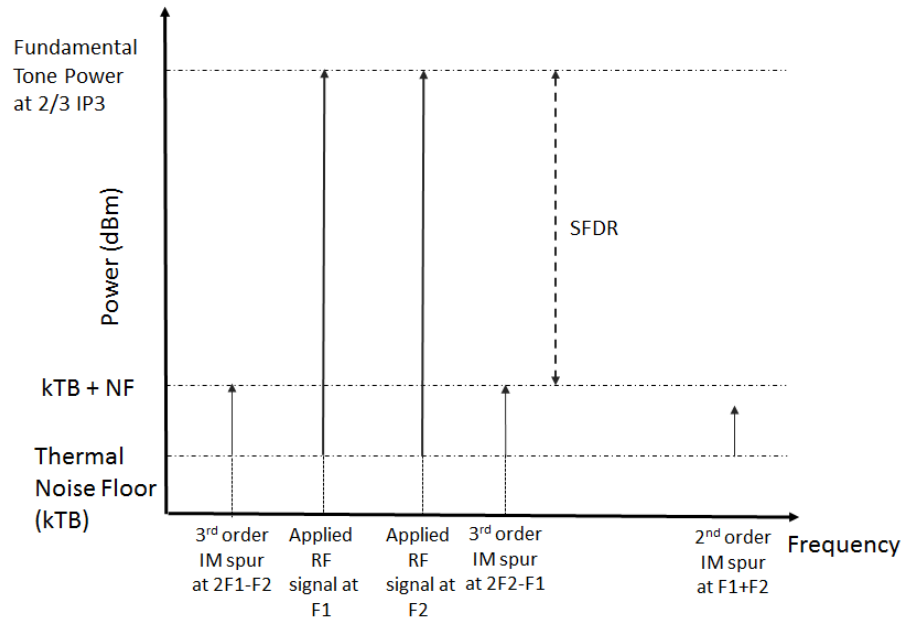


**Fig. 2.9.:** Spurious Free Dynamic Range

demodulation would exceed that in equation owing to implementation losses involved in the receiver’s RF hardware and ADC.

**Image rejection:** This is a measure of selectivity of the receiver and is critical especially in super heterodyne architectures. The extent to which the image signal is rejected is termed as image rejection factor as shown in Fig. 2.10. The image rejection factor needs to be well above the minimum SNR needed to demodulate the signal being received. The image frequencies in case of zero IF or homodyne receivers fall at harmonics of the frequency of the signal being received.

**Input Amplitude Ripple and Tilt Tolerance:** This refers to the extent of in-band variation of the input signal’s spectrum that can be tolerated by the receiver for faithful demodulation of the signal. This parameter also indicates the effectiveness of equalizing filters in the demodulator.

**Input IQ Imbalance tolerance:** This refers to the extent of imbalance in I and Q components of the modulated RF input signal that can be tolerated by the receiver for faithful demodulation. This parameter also indicates the effectiveness of equalizing filters in the demodulator. Higher modulation schemes have lower tolerance to IQ imbalance. The impact of IQ gain imbalance on the modulated constellation is shown in Fig. 2.7.a.

**Input Quadrature skew tolerance:** The ideal difference in phase between I and Q parts of the modulated RF input should be 90 degrees. The extent of tolerable deviation from this figure is as quadrature skew tolerance. This parameter also indicates the effectiveness of equalizing filters in the demodulator. Higher modulation

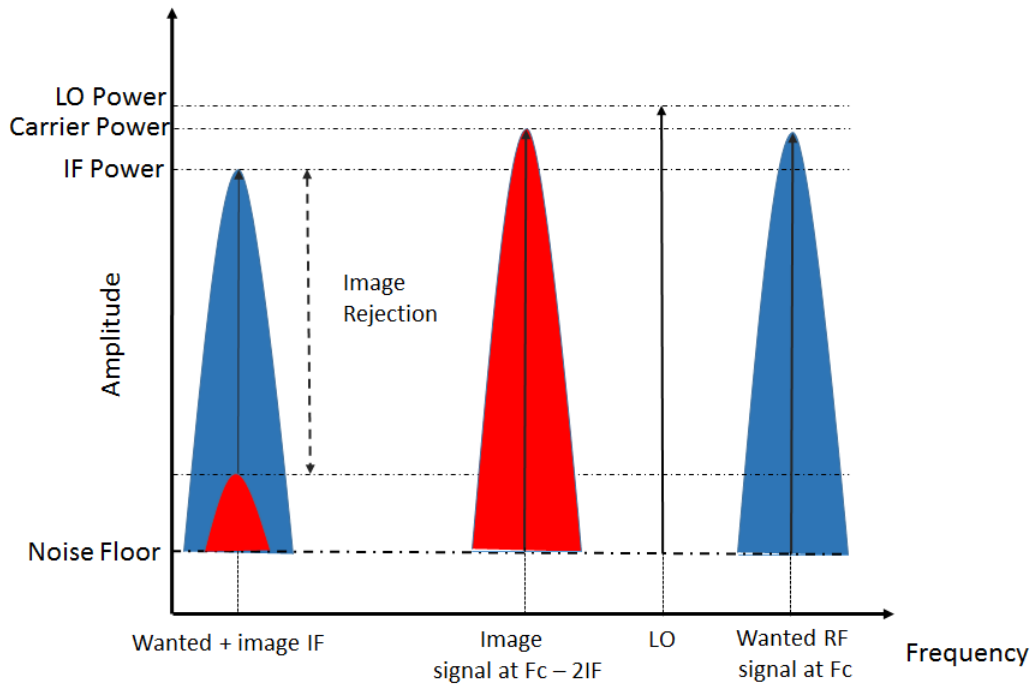


Fig. 2.10.: Image Rejection

schemes have lower tolerance to quadrature skew. The impact of quadrature skew on the modulated constellation is shown in Fig. 2.7.b.

**Constellation Rotation:** This is the extent of angular shift in the demodulated constellation from the ideal constellation caused by phase mismatch in the reference oscillator of the receiver relative to that of the transmitter. This problem can be mitigated using carrier phase recovery circuits such as Costal Loop or using pilot signals of pre-set modulation symbols. Constellation rotation affects EVM as shown in Fig. 2.11.

## 2.3. Non-Ideal Characteristics of hardware blocks in a SISO transceiver and their impacts.

Designs for transceivers intended for operation in millimeter wave cellular base stations or their backhaul wireless links and in ground stations for satellite communications are expected to follow super heterodyne architectures where the vector modulated signal is first generated at an intermediate frequency (IF) and then wired to an outdoor unit (ODU) consisting of a millimeterwave RF up/down-converter, RF power amplifier and antennas. This is preferred to minimize the loss of signal power in the feed cable that runs between the indoor transceiver unit and the antenna mounted outdoor. The block diagram of a typical super heterodyne transceiver for

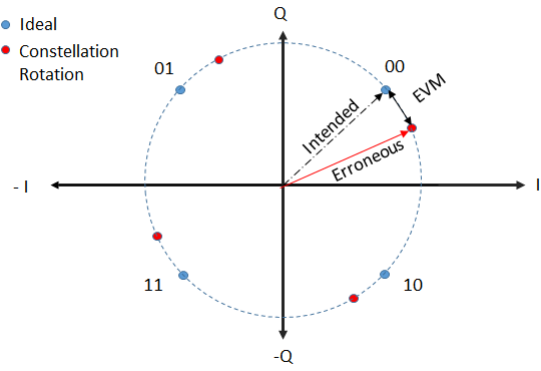


**Fig. 2.11.:** Constellation Rotation

operation at Ka Band (28 GHz to 36 GHz) is shown in Fig. 2.12. The quality of transmission and reception of data in a wireless communication system depends on the quality of the signals transmitted and received which depend upon the channel characteristics and the physical characteristics of the transmitter and the receiver. The limitations are discussed for the transmitter and the receiver sections individually for clarity. Interested readers are redirected to references [13, 14, 15, 16] for more information on the theories and design guidelines on these modules.

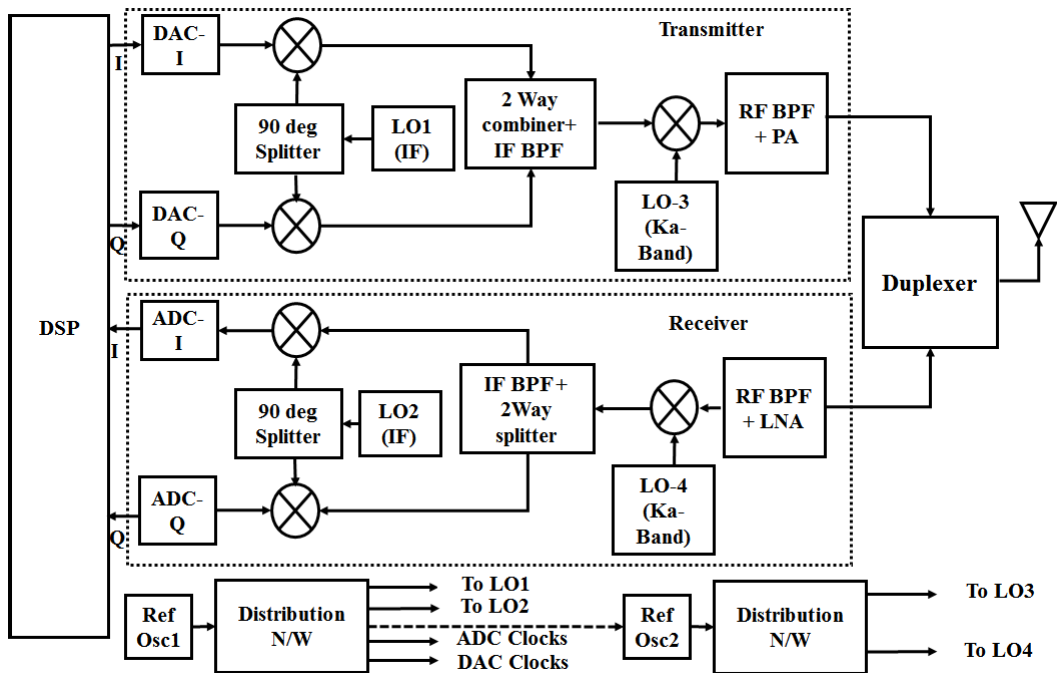


**Fig. 2.12.:** Heterodyne Transceiver

### 2.3.1. Transmitter

This section is intended to provide a concise description of the performance limitations in the critical building blocks of a transmitter except the power amplifier and the consequent impairments in the baseband or RF signal. A separate chapter is dedicated to discuss the performance indicators of the strongly non-linear block i.e. RF Power Amplifier.

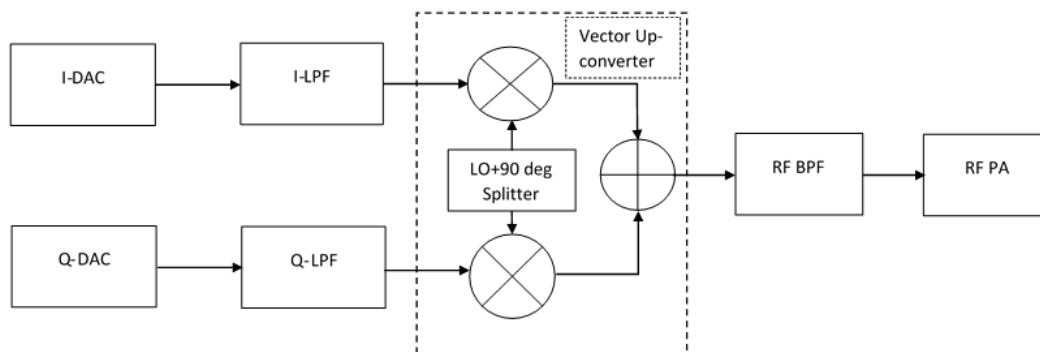


Fig. 2.13.: Generalised Transmitter Block Diagram

#### 2.3.1.1. Bandwidth dependent performance indices of DACs

Most high speed DACs generate the analogue signal by steering currents from binary weighted current sources into a load where the individual current sources are connected or disconnected from the load in accordance with the input digital code. The connection and disconnection of the current sources is achieved by means of switching transistors whose operations are controlled by a sampling clock. By Nyquist theorem, the maximum bandwidth of a signal that can be generated from a DAC operating at a sampling clock frequency  $f_s$  is  $f_s/2$ . The maximum bandwidth of a baseband signal that can be generated thus depends on the maximum clock rate of the DACs which in turn depends upon the achievable switching times of the transistors and slew rates of the baseband amplifiers used in constructing the DACs. Interested readers are redirected to literatures in [13, 14, 15] for detailed information on these aspects.

- **Settling Errors in Data Converters:** If the input to a DAC is varied from a starting value  $X_{\text{start}}$  to the final value  $X_{\text{final}}$ , it takes a finite amount of time for the analogue output voltage to rise and settle to a value close to  $X_{\text{final}}$  for pre-determined accuracy (example within 0.1% of  $X_{\text{final}}$ ). The time taken to settle is termed as settling time  $T_s$ , the time taken to rise is termed as slew time  $T_{\text{slew}}$  and the difference in the final settled value and the desired final

value  $X_{\text{final}}$  is the settling error. A brief graphical description of this error mechanism is shown in Fig. 2.14. This parameter affects the maximum speed at which the DAC can be operated and is affected by the slew rate of the switching transistors involved in driving the binary weighted current sources in the DAC. The impact of settling errors increases with bandwidth of the signal. Difference in settling errors between the data converters used in the I and Q paths affects the EVM of the modulated or demodulated signal by introducing IQ imbalance.

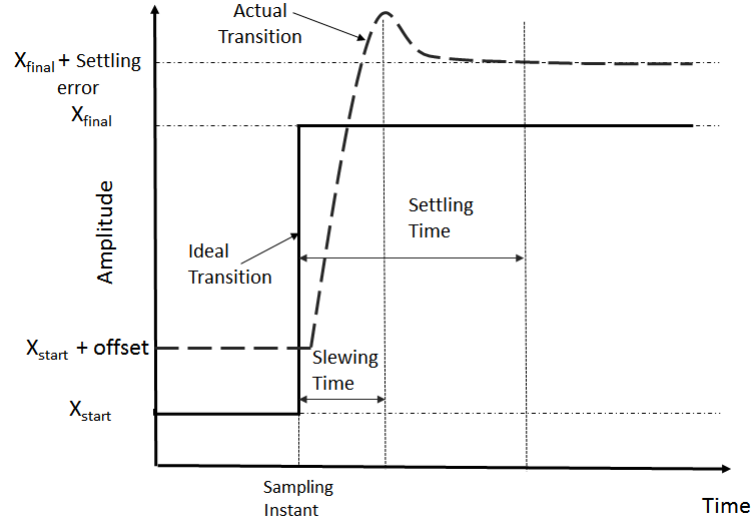


**Fig. 2.14.:** DAC Settling Errors

- **Sampling time uncertainty:** Jitter in the sampling clock causes a variation in the time interval between adjacent samples. Jitter is caused by noise in the oscillator that generates the clock signal. The average power of this error  $P_{\delta}$  caused by timing error  $T_{\delta}$  with intended sampling interval  $T_s$  and step size  $X_{\delta}$  is given by eq. 2.12. Differences in sampling uncertainties between the data converters used in the I and Q paths cause parasitic phase modulation which would corrupt the intended modulation.

$$P_{\delta} = \frac{X_{\delta}}{T_{\delta}} \tag{2.12}$$

- **Sinc Roll off:** The frequency response of a data converter rolls off in the form of Sinc function due to zero order hold characteristic of its analogue circuits. The frequency response of a DAC is of the form

$$H(f) = \frac{\text{Sin}(\pi f T_s)}{(\pi f T_s)} \tag{2.13}$$

This implies that the amplitude of the frequency component at  $0.4/f_s$  in the output of the DAC is reduced to a value of 75.6% of the ideal amplitude. This behaviour

impacts the spectral flatness of the modulated signal generated by the DAC in wideband systems. This is behaviour would specifically affect OFDM based systems since the integrity of the modulation on the sub-carriers would be compromised.

- **Quantization Noise:** The quality of the signal generated by the DAC depends on the number of bits of resolution  $N$  in the DACs. The effective SNR in dB available in the output signal of bandwidth  $B$  in the presence of quantization noise [14] is given by the mathematical relation in eq. B.3. Since DAC's output is actually in discrete steps and not continuous, the extent of error in the output analogue value relative to an ideal analogue signal manifests in the form of noise thereby affecting the SNR of the output signal being generated. This has an impact on the quality of the modulated signal generated in the modulation stage of an RF transmitter. The effective SNR in dB available in the output signal of bandwidth  $BW$  in the presence of quantization noise [14] is given by the mathematical relation

$$SNR_{dB} = 6.02N + 1.76 + 10\text{Log}_{10}(f_s/2BW) \quad (2.14)$$

- **Impact of Peak to Average Ratio on Signal Quality:** The signals encountered in wireless communication applications such as OFDM consist of multiple tones and the time domain envelopes exhibit a high peak to average ratios.

The value of SNR reduces in the presence of PAR to

$$SNR = 6.02N + 4.77 - 20\text{Log}_{10}(PAR\sqrt{2}) + 10\text{Log}_{10}(f_s/2BW) \quad (2.15)$$

$$SNR_{multi} = SNR_{single} - 20\text{Log}_{10}(PAR\sqrt{2}) \quad (2.16)$$

- **Signal to Noise and Distortion Ratio (SNDR):** This is the effective figure of signal quality that can be obtained from a data converter. In addition to the noise mechanisms described above, there also exist distortion mechanisms in DACs such as intermodulation, clock feed through and harmonic distortions which impair the signal being generated and limit the spurious free dynamic range. The effective signal quality is quantified in terms of SNDR mathematically eq. 2.17 where THD is the total harmonic distortion.eq. 2.17

$$SNDR_{dB} = 20\text{Log}_{10}\sqrt{\left(10^{\frac{-SNR}{20}}\right)^2 + \left(10^{\frac{-THD}{20}}\right)^2} \quad (2.17)$$

- **Effective Number of Bits (ENOB):** The resolution of a data converter can be  $N$  bits but its effectiveness reduces due to the combined impact of quantization and distortion. ENOB in the presence of a finite Signal to Noise and Distortion Ratio (SNDR) is mathematically computed as:

$$\text{ENOB} = \frac{\text{SNDR} - 1.76}{6.02} \quad (2.18)$$

- **Effective Resolution Bandwidth (ERB):** It was observed in eq. B.5 and eq. B.4 that SNR of the signal generated or sensed by a data converter is dependent on its frequency and hence the value of ENOB reduces with frequency. The frequency of the tone at which ENOB reduces by 3 dB is termed as the Effective Resolution Bandwidth (ERB). This is a parameter that indicates the usable bandwidth of data-converter for a given SNDR requirement.
- **Timing Jitter  $T_{\text{jitter}}$ :** Another parameter that affects the quality of the signal generated and imposes an upper limit on the operating sample/clock rate is the timing jitter. It is the uncertainty in the rising and falling instants of a clock signal caused by phase noise mechanisms of the oscillator that generates the clock. The relation between phase noise and timing jitter is explained in Appendix 1. Timing jitter increases with frequency of the clock. The rise in noise floor due to jitter is quantified mathematically by eq. 2.19.

$$N_{\text{jitter}} = -20 \text{Log}_{10}(2f_{\text{signal}} T_{\text{jitter}}) \quad (2.19)$$

The impairments described above are not exhaustive but contribute significantly to the quality of modulation or demodulation respectively in the signal generated. Other key parameters involved in selection of DACs for wireless communications such as intermodulation distortion, total harmonic distortion, clock feed through, gain offset, differential and integral non-linearities are explained in detail in literature [13]. The problem complicates further in the presence of non-uniformity in these impairments between the DACs in the I and Q paths of the transmitter.

### 2.3.1.2. Bandwidth and Power Dependent Distortions in Mixers

Active components used in mixers are either Schottky Barrier diodes or Field Effect Transistors whose individual frequency responses affect the spectral flatness of a wideband signal subject to up or down conversion. The ohmic losses in the active and passive components involved in the construction of the mixer reduce the available carrier to noise ratio. A typical circuit schematic of a sub-harmonic mixer used for up-conversion of a sub 1GHz IF input to Ka Band is shown in Fig. 2.15

a) Conversion Gain vs. Frequency: The reactance in the active components leads to frequency dependent conversion gain. A plot of conversion gain vs frequency is shown in Fig. 2.16

### 2.3 Non-Ideal Characteristics of hardware blocks in a SISO transceiver and their impacts.

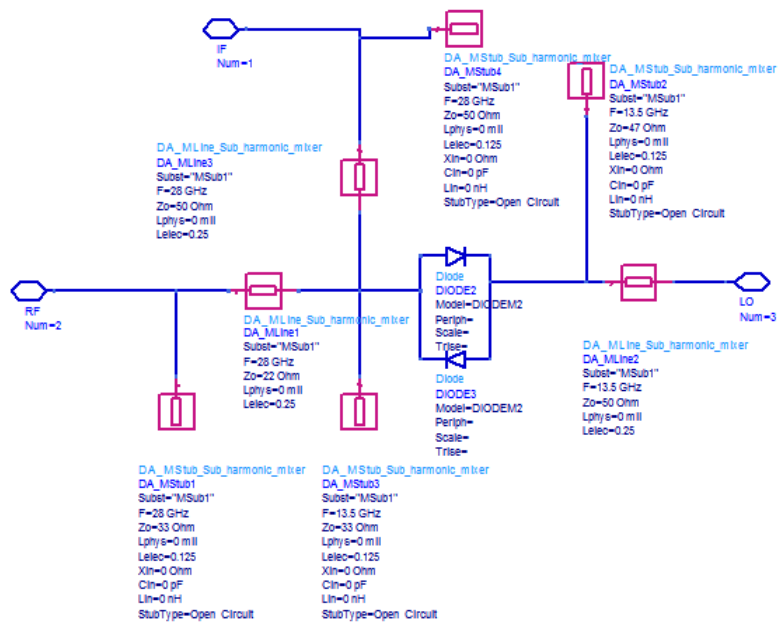


Fig. 2.15.: Ka Band sub-harmonic mixer

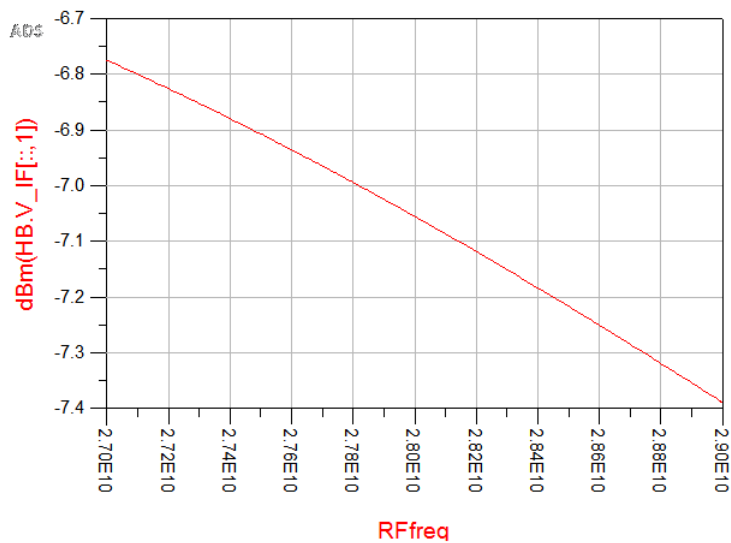
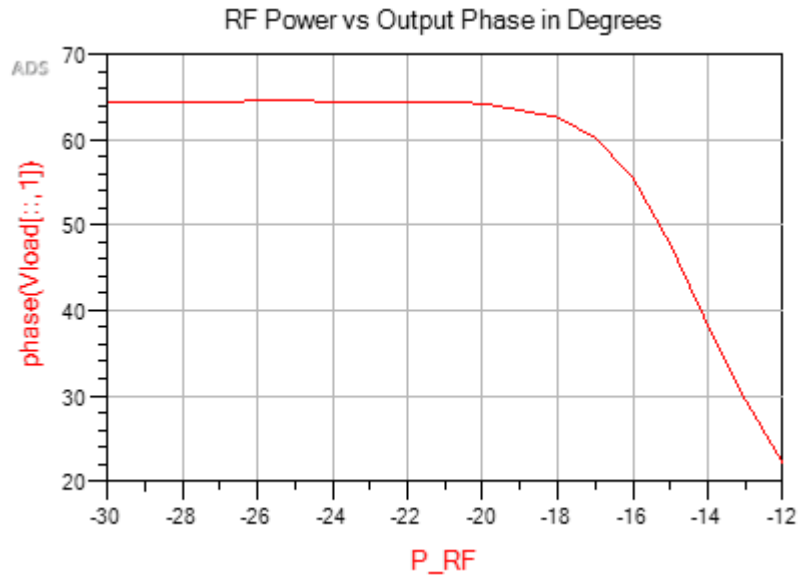
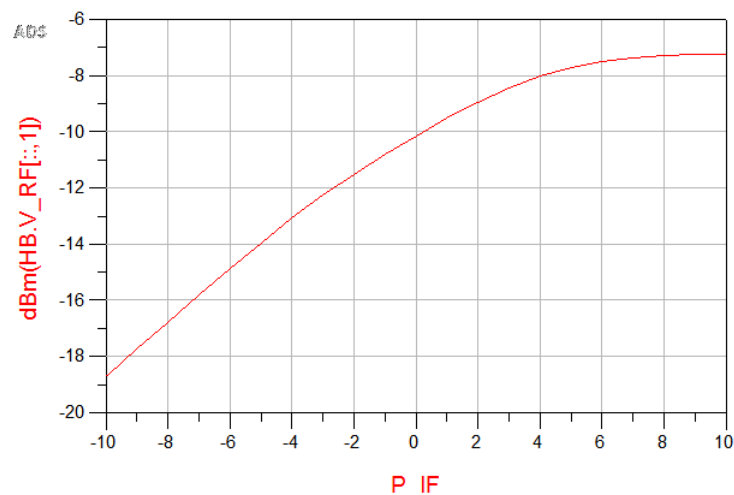


Fig. 2.16.: Mixer conversion gain vs freq

b) Input power dependent phase responses: The effective capacitance in the Schottky diodes have a dependency on the density of charge carriers which in turn depends on the power of the LO signal injected. As the amplitude of the input IF signal increases close to the P1dB compression point of the mixer, the capacitance of the diodes also exhibit signal strength dependent variation as shown in Fig. 2.17.



**Fig. 2.17.:** Mixer phase vs signal power



**Fig. 2.18.:** Nonlinear transfer function of a mixer

c) Mixer Non-linearity: An RF mixer is inherently a non-linear device. The higher the  $P_{1dB}$  compression point of the mixer, the lesser the gain required for the next stage which is usually a driver amplifier to drive the RF power amplifier. Another non-linear parameter is the third order intermodulation intercept point or IP3 which determines the dynamic range of the mixer.

The above parameters of the mixer are not exhaustive but give some insight of bandwidth and power dependent behaviours which need to be mitigated when operating

with high PAPR wideband signals such as 5G NR signals.

d) Frequency dependent phase response of quadrature power splitter: To accomplish complex envelope modulation of a carrier, the baseband needs to be subjected to vector up-conversion where the in-phase component I of the complex baseband mixes with the cosine component of the LO signal and the quadrature component Q mixes with the sine component of the LO. This requires the LO signal to be split at quadrature phases to feed the I and Q sections of a vector up-converter. Practically, perfect quadrature splitting can be achieved only at one frequency and hence the quadrature splitter itself introduces phase errors. Frequency response of a typical branch-line quadrature splitter is shown in Fig. 2.19.

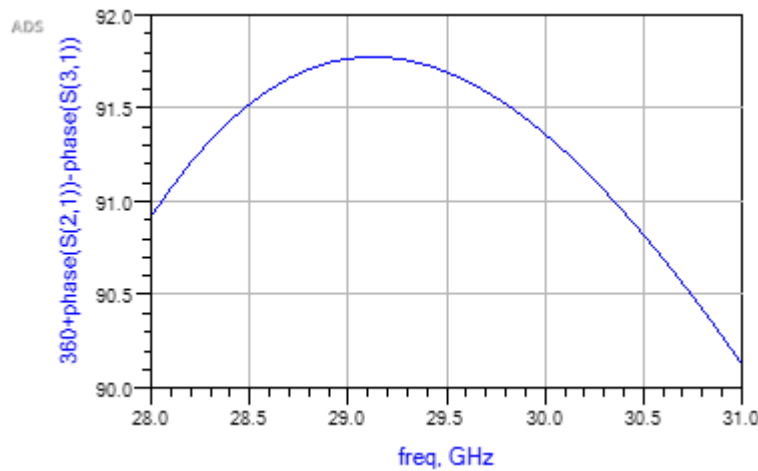


**Fig. 2.19.:** Phase vs Frequency in a quadrature RF power splitter

The system level impacts of key impairments of the other blocks in the transmitter except the PA are tabulated in Tab. 2.1 and Tab. 2.2. The PA aspects are discussed in Chapter 4.

### 2.3.1.3. Bandwidth Dependent Behaviour of RF Filters

The primary task of a filter is to pass a desired band of frequencies and reject the rest. RF filters are made of resonant circuits with an aim to pass frequencies of interest and reflect the rest. A perfect filter where the transition between the pass and stop bands is a perfect brick wall is impossible to build. Practically all filters have a finite transition band between the pass and stop bands. The spectral characteristics of a filter depend upon the poles and zeros of its transfer function. One of the strategies adopted in industry to design an RF filter is to design the locations poles and zeros in accordance with standard polynomials such as Butterworth, Chebyshev, Cauer (elliptic), etc. Butterworth polynomial exhibits the flattest passband of

the three and a slow transition from the passband to the stop band. Cauer (Elliptic) polynomial exhibits the fastest transition from the required pass band to stop band but exhibits high ripples in both pass and stop bands. Chebyshev polynomial exhibits ripples in either pass or stop band and provides more flexibility to the designer. However, with increasing frequency of operation, filters cannot be built with lumped elements and hence circuits with distributed elements such as transmission line based resonators need to be designed. A popular band pass filter topology using planar transmission lines is a microstrip edge coupled filter whose design is shown in Fig. 2.20. The simulated gain characteristics of the filter in Fig. 2.20 are shown in Fig. 2.21. Another parameter of RF filters that can have adverse effects on the integrity of the modulated envelope in wireless communications is the phase response over the operating bandwidth. This characteristic has been exploited in Chapter 5 to provide security in the physical layer of wireless communications. A plot of the simulated phase characteristics of the filter shown in Fig. 2.20 are shown in Fig. 2.22.

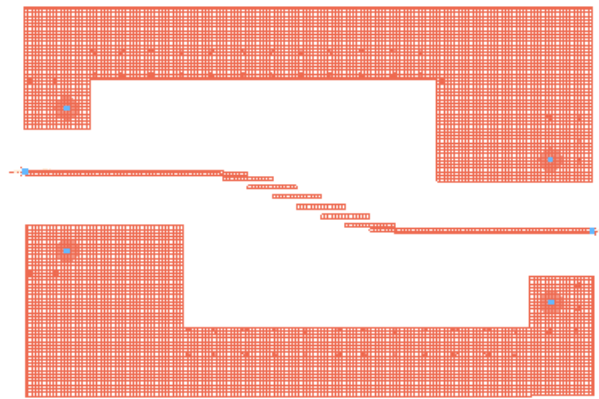


**Fig. 2.20.:** Edge Coupled RF bandpass filter designed for Ka Band operation

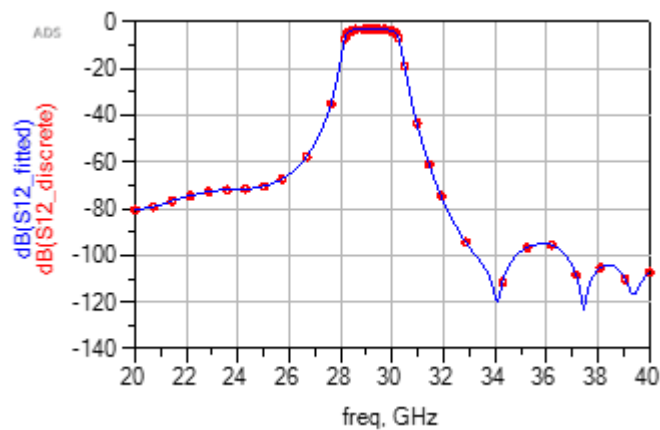


**Fig. 2.21.:** Gain characteristics of edge coupled Ka Band BPF

### 2.3 Non-Ideal Characteristics of hardware blocks in a SISO transceiver and their impacts.

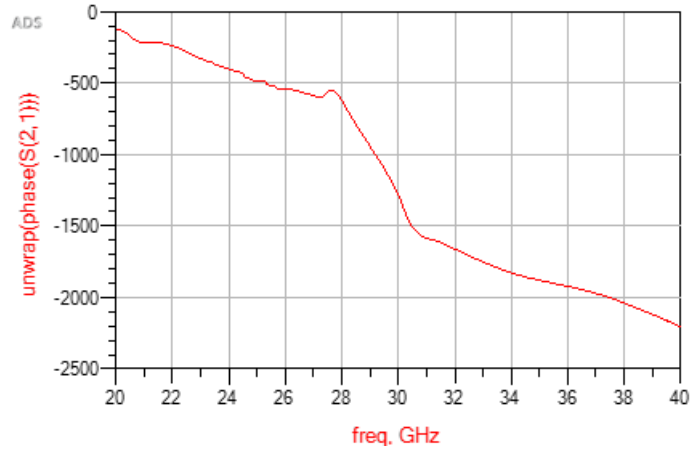


Fig. 2.22.: Phase characteristics of edge coupled Ka Band BPF

#### 2.3.1.4. Summary Of Impairments In A Transmitter

Tab. 2.1.: Impairments in transmitter blocks and their system level impacts

DACs		LPF		Up-converter		RF BPF	
Impairment	System Impact	Impairment	System Impact	Impairment	System Impact	Impairment	System Impact
Gain Error	EVM	In-band Gain Ripple	Spectrum Flatness, EVM	Mixer's In-band Gain Ripple	Spectrum Flatness, EVM	In-band Gain Ripple	Spectrum Flatness, EVM
Differential Non-Linearity	EVM	Group Delay	EVM	Mixer's Group Delay	EVM	Group Delay	EVM, usable signal and system bandwidths
Integral Non-Linearity	EVM	Insertion Loss	Dynamic Range	Mixer's Conversion Loss	Dynamic Range, usable signal and system bandwidths	Insertion Loss	Dynamic Range
Offset Error	LO Leak	Half power bandwidth	Signal Bandwidth, Spectrum Flatness	Mixer's Finite LO to RF Isolation	LO Leak, EVM	Half power bandwidth	Signal Bandwidth, Spectrum Flatness
Harmonic Distortion	SFDR	Finite Stop Band Attenuation	Spurious, ACPR	Mixer's Finite RF to IF isolation	Spurious, power efficiency	Finite Stop Band Attenuation	Spurious, ACPR
Quantization Error	Dynamic Range	Gain Imbalance b/w I and Q LPFs	IQ imbalance, EVM	Mixer's Finite LO to IF isolation	Spurious, power efficiency	Stop Band Ripple	Spurious
Maximum Sample Rate	Signal Bandwidth, Spectrum Flatness, EVM	Group Delay Variation b/w I and Q LPFs	IQ constellation dispersion, EVM	Mixer's P1 dB compression	Dynamic Range, EVM		

**Tab. 2.2.:** Impairments in transmitter blocks and their system level impacts continued

DACs		DACs Continued		Up-converter		Up-converter continued	
Intermodulation intercept points	SFDR	Effective Resolution Bandwidth	Signal Bandwidth, Spectrum Flatness, EVM	Mixer's Intermodulation intercept points IP2 and IP3	SFDR, usable bandwidth	LO Harmonics	Spurious, Image Rejection in Zero IF architectures.
Settling Skew	EVM	Clock timing jitter (Refer to Note 2)	Glitches, SNR, Maximum usable bandwidth	Group Delay Variation b/w I and Q Mixer's	IQ constellation dispersion, EVM	RF Combiner Gain imbalance b/w I and Q ports	IQ gain imbalance, EVM
Clock Feed-Through, Glitches	SFDR			Gain Imbalance b/w I and Q Mixer's	IQ imbalance, EVM	RF Combiner phase imbalance b/w I and Q ports	IQ quadrature skew, EVM
Gain Imbalance b/w I and Q DACs	IQ imbalance, EVM			LO power differences between I and Q Mixer's	IQ gain imbalance, EVM	RF Combiner's finite isolation b/w I and Q ports	IQ quadrature skew, EVM
Clock Phase b/w I and Q DACs	IQ quadrature skew, EVM			LO quadrature injection phase errors between I and Q Mixer's	IQ quadrature skew, EVM	LO Phase Noise (Refer to Appendix 1)	Constellation dispersion, EVM, SNR, ACPR (due to reciprocal mixing)
Timing offset b/w I and Q DACs	IQ quadrature skew, EVM, glitches			LO Frequency stability	EVM, ACPR		

The critical impairments in each block of the transmitter and their impacts on the system performance are summarised in Tab. 2.1 and Tab. 2.2. The in-band impairments caused by linear and weakly non-linear hardware modules mentioned related to gain and phase can be mitigated by wideband calibration techniques discussed in detail in the next chapter.

### 2.3.2. Receiver

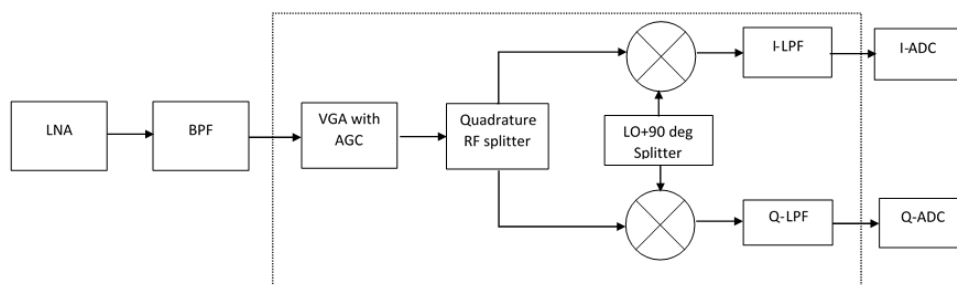


**Fig. 2.23.:** Generalised Receiver Block Diagram

The parameters discussed for the blocks in a transmitter in the previous sub-section are also applicable to receivers with the exception of LNAs and ADCs. The primary difference in the design approach for the RF front end in transmitters and receivers is that the characteristics of the signal being generated and processed are well known in the former case and are only estimated on the basis of channel model and statistics in the latter case. While a transmitter is designed to minimize EVM and maximize EIRP for the bias power consumed, a receiver is designed to maximize sensitivity, adapt its gain in accordance with the strength of the RF signal sensed, equalize the impairments undergone in the wireless channel and demodulate the received signal with minimum bit error rate (BER).

### 2.3.2.1. Bandwidth and Power dependent behaviour of Low Noise Amplifiers (LNAs)

It was shown in eq. 2.7 that the first stage in the receiver and its gain has the highest bearing on the overall noise figure of the system. A low noise amplifier (LNA) is the first amplification stage of a receiver whose task is to amplify a weak signal of captured by the antenna with minimum noise added to it. The ideal noise figure of an LNA is 0 dB. The parameters affecting the noise figure of an LNA are  $F_{min}$ , the minimum noise figure of the active device,  $R_n$  the equivalent noise resistance of the active device and variation in the input reflection co-efficient relative to the optimum input reflection co-efficient for minimum noise figure  $F_{min}$ .  $F_{min}$  of a transistor increases with frequency. The design of an LNA often presents a trade-off between achieving maximum gain and minimum noise figure.

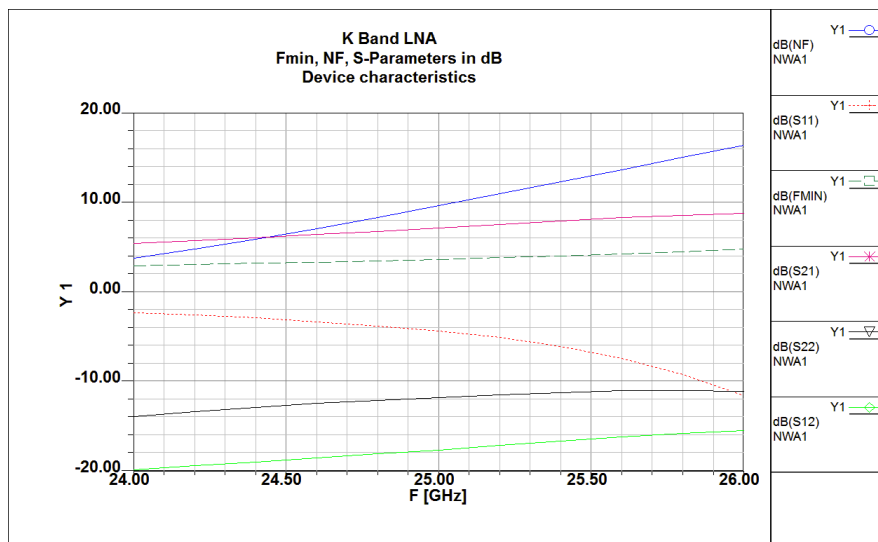


Fig. 2.24.: S Parameters and Noise Figure of a HBT

A plot of S-Parameters and Noise Figure in dB across the frequency range 24 GHz to

26 GHz of a Heterojunction Bipolar Transistor is shown in Fig. 2.24 and the values of the input and output reflection co-efficients  $S_{11}$  and  $S_{22}$  and the optimal input reflection co-efficient  $G_{opt}$  for minimum noise figure are shown on a Smith Chart in Fig. 2.25.

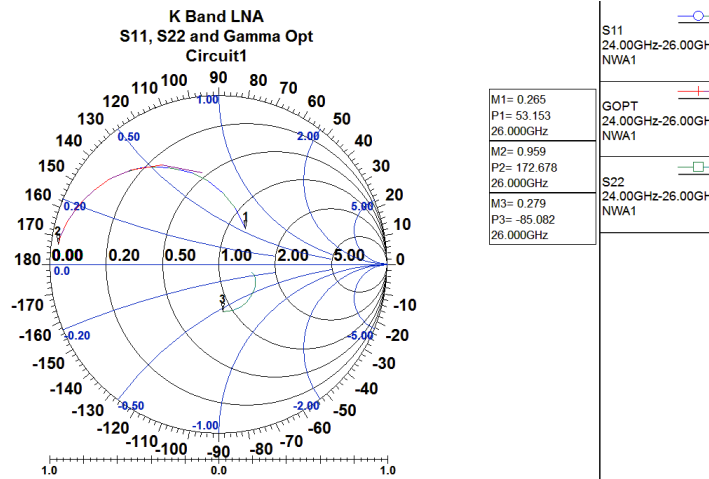


Fig. 2.25.:  $S_{11}$ ,  $S_{22}$  and  $G_{opt}$  of a HBT

The schematic of a typical LNA circuit using a HBT is shown in Fig. 2.26

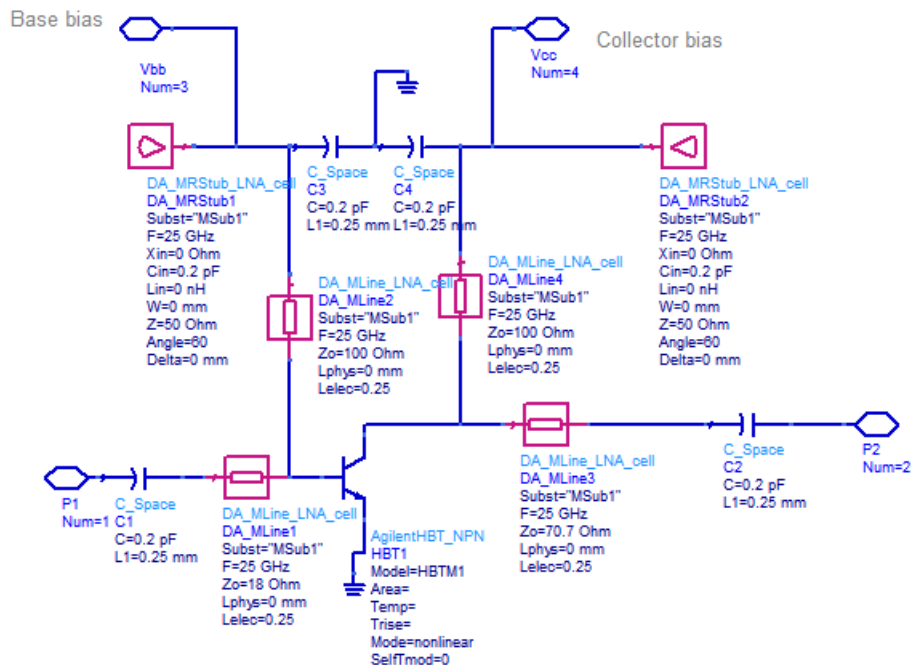


Fig. 2.26.: Circuit schematic of an LNA using a HBT

While it may seem desirable to maximize the gain of the LNA to minimize the system noise figure, it is not always beneficial since it would compromise linearity. Typically wideband receivers are expected to have a dynamic range of at least 50 dB [3].

### **2.3.2.2. Bandwidth and power dependent performance of ADCs**

The maximum demodulation bandwidth of a receiver depends upon the maximum operating bandwidth of an ADC which in turn depends on the maximum sample rate. The maximum sample rate in turn depends on the achievable switching speeds in transistors used in building the ADC and the slew rates and settling times of the sample and hold circuits. The quality of the baseband signal sensed depends on the bit resolution and sample rate as in the DAC's case. The effective resolution bandwidth of the ADC is similar to that of the DAC. The input to the ADC is an analogue voltage waveform consisting of all the frequencies amplified and passed by the LNA and the RF down-converter. It is essential to band-limit the signal being sampled by the ADCs sample and hold circuit to avoid aliasing. This requires a sharp filter at the input to the sample and hold circuit. Wideband transmitters with RF power amplifiers delivering power in the range of tens of watts often require an observation receiver in the form of a feedback to monitor the quality of the output signal and assist in mitigating the impairments through digital pre-distortion. The effectiveness of digital pre-distortion depends on the ability to capture the impairments over the required bandwidth which in-turn depends on the bandwidth and dynamic range of the ADC in the observation receiver.

### **2.3.2.3. Summary Of Impairments In A Receiver**

The system level impacts of key impairments of blocks in the receiver are tabulated in tables Tab.2.3 and Tab.2.4. The in-band impairments caused by linear and weakly non-linear hardware modules mentioned related to gain and phase can be mitigated by wideband calibration techniques discussed in Chapter 3. The techniques are the same as that applicable to the transmitter except for dc offset correction in the ADC. Even though the primary focus of the research undertaken for this thesis is enhancement of transmitters for wideband millimetre wave communications, receivers play a critical part in evaluating the transmitters and hence it is essential to have an insight of the mechanisms and impairments in them. Sophisticated RF test equipment like spectrum analysers, signal analysers, distortion analysers are indeed receivers. Reference receivers were used extensively in the work presented in chapters 3, 5 and 6.

**Tab. 2.3.:** Impairments in salient receiver blocks and their system level impacts

LNA		RF BPF		Down-converter		LPF		ADCs	
Impairment	System Impact	Impairment	System Impact	Impairment	System Impact	Impairment	System Impact	Impairment	System Impact
In-band Gain Ripple and Tilt	Spectrum Flatness, EVM, Sensitivity, Dynamic Range, Usable signal and system bandwidths	In-band Gain Ripple	Spectrum Flatness, EVM	Mixer's In-band Gain Ripple	Spectrum Flatness, EVM	In-band Gain Ripple	Spectrum Flatness, EVM	Gain Error	EVM
Noise Figure	EVM, Sensitivity, Dynamic Range, Usable signal and system bandwidths	Group Delay	EVM, usable signal and system bandwidths	Mixer's Group Delay	EVM	Group Delay	EVM, usable signal and system bandwidths	Differential Non-Linearity	EVM
P1dB Compression Point	EVM, Dynamic Range	Insertion Loss	Dynamic Range	Mixer's Conversion Loss	Dynamic Range, usable signal and system bandwidths	Insertion Loss	Dynamic Range	Integral Non-Linearity	EVM
Intermodulation Intercept Points (IP2 and IP3)	SFDR, Usable signal and system bandwidths	Half power bandwidth	System Bandwidth, image rejection, Spectrum Flatness	Mixer's Finite LO to RF Isolation	LO Leak, EVM	Half power bandwidth	Signal Bandwidth, Spectrum Flatness	Offset Error	Dc offset in sensed signal
Input VSWR	Sensitivity, Dynamic Range	Finite Stop Band Attenuation	Spurious, ACPR	Mixer's Finite RF to IF isolation	Spurious, power inefficiency	Finite Stop Band Attenuation	Spurious, ACPR	Harmonic Distortion	SFDR

**Tab. 2.4.:** Impairments in salient receiver blocks and their system level impacts

Down-converter		Down-converter continued		Down-converter continued		ADCs		ADCs continued	
Mixer's Finite LO to IF isolation	Spurious, power efficiency	LO Phase Noise (Refer to Note 1)	Constellation dispersion, EVM, SNR, ACPR (due to reciprocal mixing)	VGA Gain Ripple and Tilt	EVM, Sensitivity, Dynamic Range, Usable signal and system bandwidth	Quantization Error	Dynamic Range	Timing offset b/w I and Q DACs	IQ quadrature skew, EVM, glitches
Mixer's P1 dB compression	Dynamic Range, EVM	LO Frequency stability	EVM, ACPR	VGA P1dB Compression Point	EVM, Dynamic Range	Maximum Sample Rate	Signal Bandwidth, Spectrum Flatness, EVM	Effective Resolution Bandwidth	Signal Bandwidth, Spectrum Flatness, EVM
Mixer's Intermodulation intercept points IP2 and IP3	SFDR, usable bandwidth	LO Harmonics	Spurious, Image Rejection in Zero IF architectures	VGA Intermodulation Intercept Points (IP2 and IP3)	SFDR, Usable signal and system bandwidths	Intermodulation intercept points	SFDR	Clock timing jitter (Refer to Appendix 1)	Glitches, SNR, Maximum usable bandwidth
Gain Imbalance b/w I and Q Mixer's	IQ imbalance, EVM	RF Quadrature splitter's Gain imbalance b/w I and Q ports	IQ gain imbalance, EVM	VGA Gain Control Slope	EVM, Sensitivity, Dynamic Range	Settling Skew	EVM		
Group Delay Variation b/w I and Q Mixer's	IQ constellation dispersion, EVM	RF Quadrature splitter's imbalance b/w I and Q ports	IQ quadrature skew, EVM	VGA Gain Control Loop Bandwidth	Usable signal and system bandwidths	Clock Feed-Through, Glitches	SFDR		
LO quadrature injection phase errors between I and Q Mixer's	IQ quadrature skew, EVM	RF Quadrature splitter's finite isolation b/w I and Q ports	IQ quadrature skew, EVM	VGA Power detector dynamic range	EVM, Sensitivity, Dynamic Range	Gain Imbalance b/w I and Q DACs	IQ imbalance, EVM		
LO power differences between I and Q Mixer's	IQ gain imbalance, EVM	VGA Noise Figure	EVM, Sensitivity, Dynamic Range, Usable signal and system bandwidth			Clock Phase b/w I and Q DACs	IQ quadrature skew, EVM		

## 2.4. Active Antenna Arrays for 5G Communications

One of the technological enablers proposed for next generation wireless communications in the millimeter wave band is Massive MIMO[17, 4, 2, 1]. This requires active antenna arrays for steering the beam in the designated directions where the RF outputs from multiple RF transmitter chains are combined spatially at the intended point of reception. The integrity of the signal at the intended receiver depends on maintenance of the gains and phase relations between the individual beam forming transmitters across the frequency band of interest. This requires calibration of the I and Q signal paths not only in a transmitter but also the I and Q relations between

the multiple transmitters involved in the beam-forming array. The RF impairments in a beam-forming transmitter are analyzed in detail in references[18], [19] and [20]. A typical scheme of two beamforming transmitters is shown in Fig. 2.27

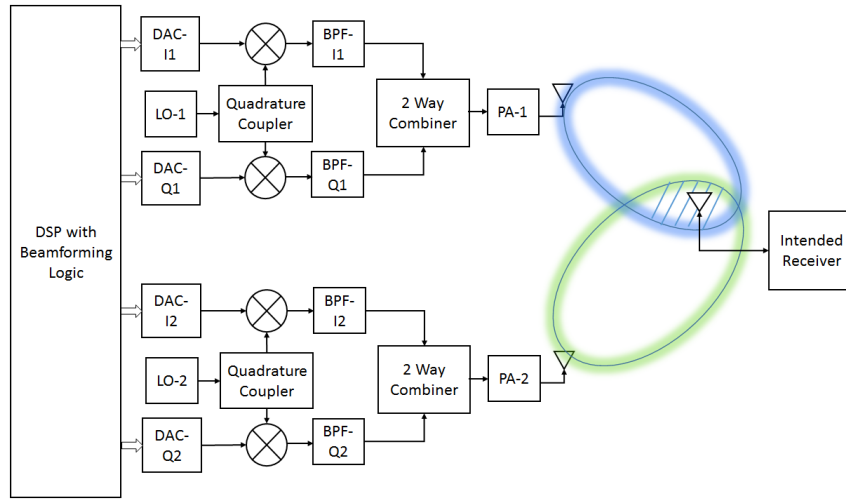


**Fig. 2.27.:** Beam forming with two transmitters

The demodulated constellations of an 8-PSK modulated signal transmitted using beam forming transmitters with and without calibration of the RF signal paths are shown in Fig. 2.28 and Fig. 2.29.

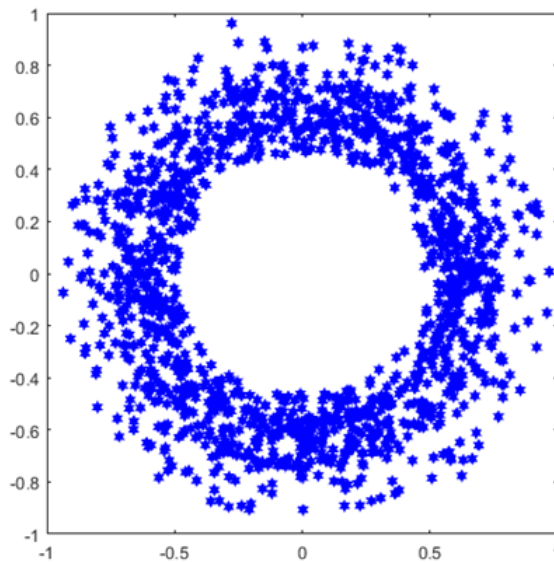


**Fig. 2.28.:** 8PSK demodulated constellation received from beamforming transmitters without path calibration

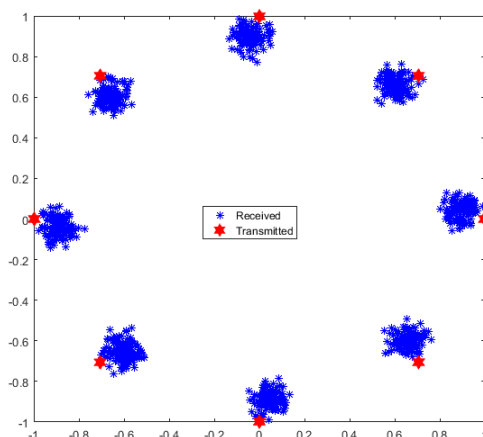


**Fig. 2.29.:** 8PSK demodulated constellation received from beamforming transmitters with path calibration

These impairments in addition to those listed in subsec.2.3.1 are exploited to provide a degree of security in the physical layer in the novel schemes presented in chapters 5 and 6.

## 2.5. Conclusion

Wireless communication systems are affected by the key performance indices of the wireless transceivers which are in turn dependent upon the performance of their building blocks. The impacts of module level impairments on the overall system performance were analysed in this chapter. It is inferred that the frequency and amplitude dependent behaviour of the modules in the wireless transceivers have adverse impacts on wideband modulated signals whose mitigation is necessary for operation in next generation wireless systems.

Modern wireless communication equipment such as outphasing power amplifiers or systems like massive-MIMO rely heavily on parallel signal transmission paths involving multiple wideband transmitters. The quality of the signal generated and transmitted by them depend on the performance of the RF modules in each path, maintenance of gain and phase relations between the signal paths over the operating signal bandwidths. As these signal bandwidths increase, wireless transmitters are more susceptible to amplitude and phase distortions across frequency. The associated effort to compensate for these distortions increases proportionally with the number of transmit paths. It is hence essential to devise novel schemes which can maximize performance of the available RF hardware in a transceiver by mitigating frequency dependent impairments in the band of operation across multiple RF signal paths. The techniques also need to be scalable to accommodate higher or

lower number of RF signal paths. The next chapter is dedicated to the mitigation of these impairments through digitally assisted wideband characterization of the wireless transceiver hardware and pre-compensating the signals to mitigate them.

It is inferred that the performance of data-converters is degraded in the presence of varying envelopes of the modulated signals proportional to their PAR values. This degradation in performance is also applicable to RF power amplifiers as will be seen in Chapter 4. But PAR values are set to increase with increasing number of sub-carriers in OFDM signals and such OFDM based modulation schemes feature in next generation wireless standards such as 5G and beyond as seen in the previous chapter. A similar argument is applicable to massive MIMO transmitters where each transmitter sees an input which is a vector sum of several OFDM signals, each multiplied with a weighing factor related to a specific direction of transmission. This aggravates the problem of PAR further. It is essential to reduce the PAR of OFDM signals at the transmitter prior to power amplification and transmission and restore the original signal envelope at the receiver prior to demodulation. This requires transmission of additional information to the receiver to convey the modifications applied to the original signal. But the additional transmission would require dedicated sub-carriers or an extra narrow band signalling channel. It is therefore essential to derive novel schemes that can reduce the PAPR through modifications which are known to both transmitting and receiving nodes in a wireless network.

The maximum operating bandwidths of modules such as data converters are limited by the physical characteristics of the blocks involved in building them. In order to overcome such physical limitations, it is essential to derive novel schemes that can generate and transmit wideband complex envelope modulated signal in parts using multiple band-limited modules in synergy and combining their outputs in a seamless manner to meet the greater objective of wideband operation. From a system designer's point of view, it is the overall system performance that is visible. It is beneficial to evolve novel schemes where the greater objective of wideband signal transmission can be accomplished by seamlessly combining the outputs of multiple bandwidth interleaved transmitters in an efficient and scalable manner while keeping the efforts on hardware modifications at minimum.

# 3. Calibration of RF Signal Paths in Transmitters

In this chapter, novel schemes are presented to mitigate the frequency dependent impairments in the data converters and RF front end modules through digitally assisted calibration. The work presented in this chapter correspond to items 2, 3 and 7 in the list of publications. The author's contributions to the first novelty presented in this chapter are end to end system design, experimental validation including designing the test apparatus and publications 2 and 3 as the primary author. The author's contributions to the second novelty presented in this chapter are end to end system co-design, experimental validation and co-authoring item 7 in the list of publications.

## 3.1. Introduction

Modern wireless hardware employs digital modulation schemes where the digital data to be transmitted is modulated on RF carrier signals. The impact of non-ideal performance indices of the hardware blocks in an RF transceiver on the overall system performance were discussed in the previous chapter. In modern communication equipment such as beamforming transceivers or massive MIMO transceivers, there are multiple signal paths where the processing for each path takes place in parallel stages. The relative gain and phase relationships between all paths over the desired bandwidth of operation are critical to operation. Another example of a system with parallel complex/vector modulated transmit paths is an outphasing power amplifier in which the real and imaginary parts of a digital baseband are modulated on to RF carrier sinusoids of equal amplitudes and quadrature in phase by means of signal multiplication using an RF mixer in each path. The outputs of the two parallel modulators in quadrature are combined to yield a vector modulated RF signal whose values for amplitude and phase act as identifiers for the digital information/symbol being transmitted. The timing, gain, phase and the imbalances between the two parallel paths and their distortions in each path over the required bandwidth will alter the amplitudes and phases of the modulated RF carrier which critically affect the performance of the final power amplification stage. The components needed to build each hardware block in the transmitter are chosen in accordance with the desired bandwidth but no component is ideal. The imperfections in each component contribute towards the degradation that a modulated RF carrier undergoes as it

traverses through each stage of the transmitter as discussed in the previous chapter. A number of complex RF equipment such as a base station transceiver, satellite terminals, etc are built using line replaceable units (LRUs) procured from different vendors for different stages in the RF chain such as modulator, up-converter, RF power amplifier, harmonics rejection filter, etc. From a system point of view, it is not practical to pin point the exact module or the exact component in the module that caused an impairment. The causes of some of the system level impairments such as LO leakage, IQ imbalance, constellation rotation, constellation dispersion, pass band gain ripple and tilt were discussed in chapter 2. These may be classified as bandwidth dependent and bandwidth independent impairments. One of the ways to mitigate the problem is to estimate the extent of degradation caused at each stage and attempt to pre-compensate the signal for the degradations that it would undergo at various stages. Bandwidth independent impairments such as LO leak, IQ gain offset and IQ phase offset can be corrected with relative ease. Bandwidth dependent impairments require greater efforts to identify and to mitigate. In order to do this, it is necessary to characterize each stage for imperfections across the intended frequency band of operation. This is conventionally done by means of an expensive and sophisticated instrument called the ‘Vector Network Analyzer’. Usage of this instrument is not always practical while dealing with RF hardware of integrated nature where it is impractical to remove each block from the transmitter system, characterize and replace it. The entire RF front end apparatus would be a black box for a system level designer who won’t have an insight into the design. An alternate method to accomplish the task is to generate test signals within the transmitter and sweep them across the frequency band of operation and record the parameters of interest at each frequency. This is a tedious task particularly while the bandwidth of interest is wide where the number of frequency points to be swept would be high. In this chapter, novel calibration techniques are proposed to mitigate the problems of wideband bandwidth dependent impairments in each signal path and also the relative imbalances in gains and phases between two or more signal paths in the RF hardware. The techniques are explained for calibration of the RF signal chain in a transmitter and the same are applicable to a receiver with minor variations.

## 3.2. Prior Art Techniques for calibration of Impairments

The typical spectrum of a vector modulator’s output is shown in Fig. 3.1 where the image of the intended wideband modulated signal and leakage from the LO are visible. These parasitic signals need to be attenuated to the maximum possible extent to avoid interference with other wanted/intended signals at those frequencies. In order to minimize these parasitic signals, it is first necessary to look into the mechanism that generates them in the modulator. Consider for example the generation

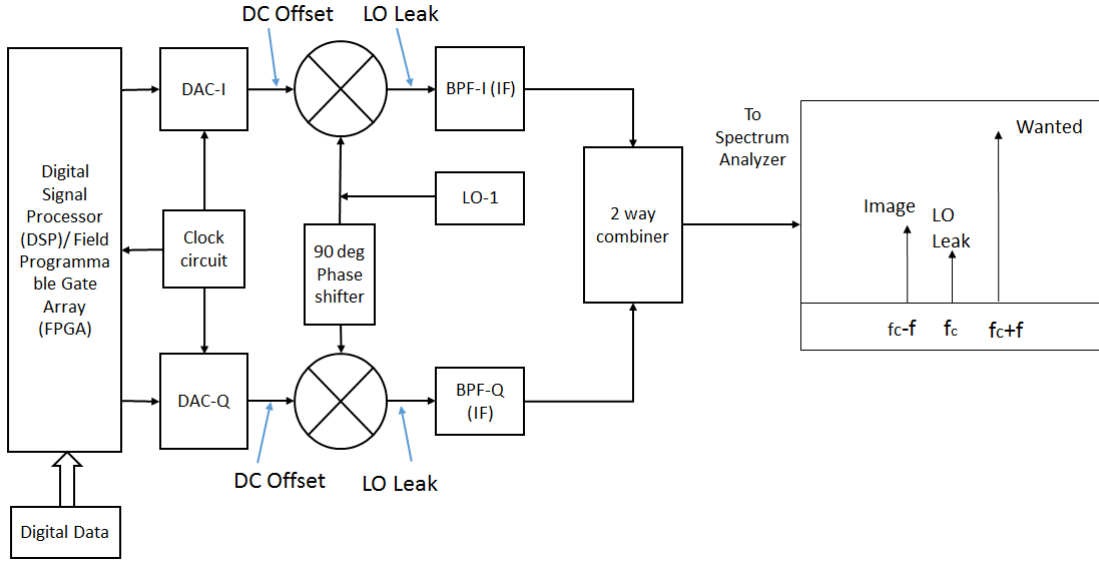


**Fig. 3.1.:** Modulator Output with DC Offset and Image

of a single tone sinusoidal signal at frequency  $f_1$  using the vector signal modulator. Let  $f_1 = f + f_c$  where  $f$  is the frequency of the digital IF at the output of a DAC and  $f_c$  is the output frequency of the LO.

This is done by generating an in-phase tone I and a quadrature tone Q digitally of equal amplitudes and subjecting them to single sideband up-conversion. Let  $I = \cos(2\pi ft)$  and  $Q = \sin(2\pi ft)$ ,  $t$  is the instantaneous time interval equal to  $nT_s$  where  $n$  is the sample number and  $T_s$  is the sampling interval.  $T_s = 1/f_s$ . The sampled signals I and Q are put through the DAC and vector up-converted using an LO at frequency  $f_c$ . In an ideal vector up-converter, the in-phase component i.e. cosine component of the LO would mix with I and the quadrature component i.e. sine component of the LO would mix with Q to yield a single output tone at frequency  $f_1 = f + f_c$  by means of single sideband (SSB) up-conversion. This can be verified mathematically as computed below.

$$\cos(2\pi ft)\cos(2\pi f_c t) = 1/2[\cos 2\pi(f + f_c)t + \cos 2\pi(f - f_c)t] \quad (3.1)$$

$$-\sin(2\pi ft)\sin(2\pi f_c t) = 1/2[\cos 2\pi(f + f_c)t - \cos 2\pi(f - f_c)t] \quad (3.2)$$

Summing the above equations yields

$$\cos(2\pi ft)\cos(2\pi f_c t) - \sin(2\pi ft)\sin(2\pi f_c t) = \cos 2\pi(f + f_c)t \quad (3.3)$$

i) Cause of LO leakage:

Under non-ideal conditions where the output of the DACs in I and Q paths of the modulator have a parasitic dc component, it would cause the LO to leak into the RF output port. This can be verified mathematically as computed below. Let  $I = I_{dc} + \cos(2\pi ft)$  and let  $Q = Q_{dc} + \sin(2\pi ft)$ . Substituting these in eq.3.1, eq.3.2 and summing them yields an output signal  $I_{dc}\cos(2\pi f_c t) - Q_{dc}\sin(2\pi f_c t) + \cos(2\pi(f+f_c)t)$  with the parasitic frequency components at the LO frequency  $f_c$ .

ii) Cause of Image output:

Under non-ideal conditions where the output of the DACs in I and Q paths of the modulator have a difference in gain  $\delta$  and a deviation from quadrature relationship  $\theta$ . Let  $I = I\cos(2\pi ft)$  and let  $Q = (\delta + 1)\sin(2\pi ft + \theta)$ . These offsets in gain and phase would cause parasitic signals to appear at the image frequency  $f_c - f$  when subject to vector up-conversion. This can be verified mathematically as computed below.. Substituting these in eq.3.1,eq.3.2 yields.

$$I\cos(2\pi f_c t) = \cos(2\pi ft)\cos(2\pi f_c t) = 1/2[\cos 2\pi(f + f_c)t + \cos 2\pi(f - f_c)t] \quad (3.4)$$

$$-Q\sin(2\pi f_c t) = (1 + \delta)\sin(2\pi ft + \theta)\sin(2\pi f_c t) \quad (3.5)$$

$$= (1 + \delta)/2[\cos 2\pi(f + f_c)t + \theta - \cos 2\pi(f - f_c)t - \theta] \quad (3.6)$$

summing the above equations yields

$$\begin{aligned} & \cos \{2\pi (f_c + f) t\} \left\{ \frac{1}{2} + \frac{(1 + \delta)\cos(\theta)}{2} \right\} + \sin \{2\pi (f_c + f) t\} \left\{ \frac{(1 + \delta)\sin(\theta)}{2} \right\} \\ & - \sin \{2\pi (f_c - f) t\} \left\{ \frac{(1 + \delta)\sin(\theta)}{2} \right\} + \cos \{2\pi (f_c - f) t\} \left\{ \frac{1}{2} - \frac{(1 + \delta)\cos(\theta)}{2} \right\} \quad (3.7) \end{aligned}$$

The terms in eq.3.7 indicate existence of parasitic products at the image frequency  $f_c - f$  accompanied by a parasitic component in the wanted frequency band  $f_c + f$  whose amplitude is proportional  $\sin(\theta)$  and  $\delta$ .

The inputs to the DAC are quantized numbers in the range 0 to  $2N - 1$ , where  $N$  is the number of bits. The non-linear behaviour of the current sources and switches in DACs lead to intermodulation and harmonics as discussed in chapter 2 and hence it is a standard practice to operate the DACs one bit below the maximum resolution. This also provides flexibility to add constant offsets to the signal being generated or scale the signal up by small fractions if needed. Hence, a 16 bit DAC is operated only up to 15 bits for the sake of headroom to accomplish the tasks describe above.

### 3.2.1. Iterative calibration of LO Leak

One of the well established ways to attenuate the LO leak is by applying fixed amounts of constant offsets to the signals in the I and Q path such that they combine destructively at the modulator's output [21]. This is an iterative process since the exact dc value at the output of the DACs is not known beforehand. This task can be accomplished by observing the RF power at the LO frequency on a spectrum analyser and applying fixed offsets to the I and Q signals iteratively to minimize the power at the LO frequency. The process of LO leak calibration by adding offsets to the signal of interest iteratively is illustrated below.

- i) Maintain the signal in Q path at its original state and add a coarse offset of 50 LSBs to the signal in I path.
- ii) Observe the change in the power of the leaked LO signal. If there is an increase in the power of the leaked LO signal subtract the coarse offset.
- iii) Repeat step ii until the power of the leaked LO signal reaches a minimum value.
- iv) Reduce the step size to 5 LSBs and add a step as offset to the last signal state in step iii.
- v) Repeat ii and iii with the smaller step size. vi) Reduce the step size to 1 LSB and add a step as offset to the last signal state in v.
- vii) Repeat ii and iii with the smaller step size.
- viii) Freeze the state of the signal in I path to that set in vii. Repeat ii to vii with the signal in Q path.

Note: The LO leak can vary depending upon the baseband gain and hence the offset values identified above to minimize the LO leak can change if the baseband gain in the DACs internal amplifier is changed. A minimum attenuation of 60dB for the LO leak relative to the wanted signal is desired by thumb rule. This is particularly required in wireless communication systems using single carrier modulation schemes. Eg. DVB-S2. A comparative plot of the spectrum of a vector modulator's output signal before and after the calibration of LO leak is shown in Fig. 3.2. The power indicated by marker 2 shows a reduction in LO leak by 33 dB after calibration. The up-conversion image is seen on the left side of the spectrum at 2.15 GHz. The next section of this chapter deals with its elimination.

### 3.2.2. Calibration of IQ gain imbalance, quadrature phase error and timing offsets.

The causes and impacts of IQ gain imbalance, quadrature phase and timing offsets were discussed in the previous chapter. IQ imbalance and quadrature phase error may be classified into two types namely bandwidth dependent and bandwidth independent. The bandwidth independent IQ gain imbalance /error is caused by a

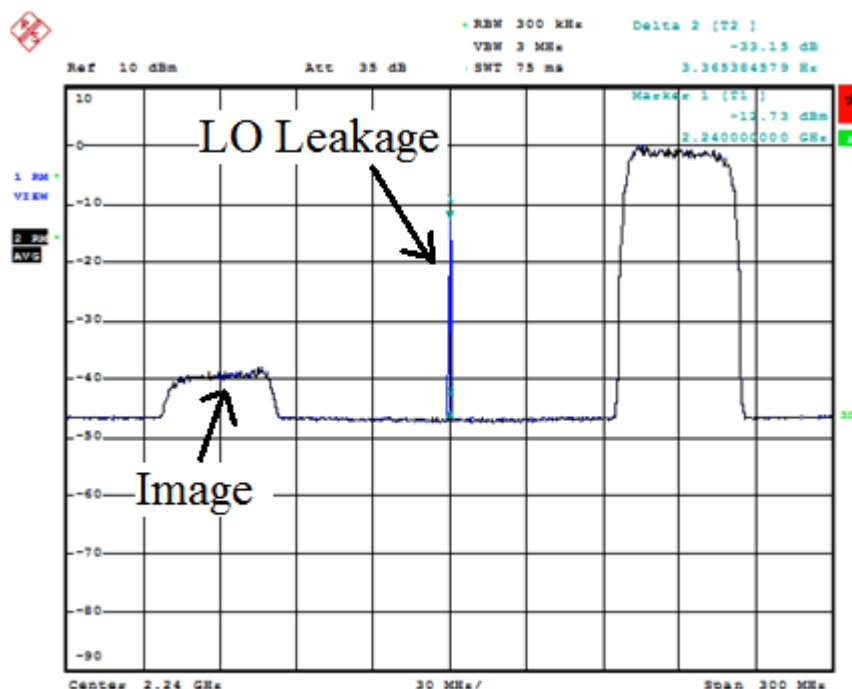


Fig. 3.2.: Spectrum of LO Leak

constant offset in gain of the baseband amplifiers, difference in the powers of the LO feed or tolerance of components in the respective signal paths. Similarly the quadrature phase errors between the I and Q paths are caused by phase of the sampling clock due to differences in electrical lengths of the clock distribution circuits and errors in the quadrature LO feeds. Bandwidth dependent IQ imbalances are caused by impairments such as amplitude ripple and tilt in frequency response and sinc roll off in DACs/ADCs. Similarly bandwidth dependent phase errors are caused by group delay variations in the filters, mixers and AM-PM conversion effects in RF Power Amplifiers (PAs). Referring to eq. 3.1, eq. 3.2 and eq. 3.3, absence of gain and phase imbalance results in perfect single sideband up-conversion. Imbalances in gain and phase between the I and Q paths result in distortion in the wanted frequency band and also result in appearance of image components as observed in eq. 3.5 and eq. 3.7. It can also be observed by inspection of eq. 3.5 and eq. 3.7 that the image can be rejected and the distortion in the wanted frequency band can be eliminated if  $\delta$  and  $\theta$  can be made zero.

A standard method to identify IQ gain and quadrature phase errors is by observing the spectrum of an up-converted baseband signal in the intended carrier band and in the image band. A simple pictorial representation of this is shown in Fig. 3.2. A standard procedure to calibrate the IQ gain and phase offsets is to iteratively vary the gain and phase controls for the two paths until the image drops to a minimum value as done for the LO leak case. This technique is straight forward, does not need

vector down-conversion and just needs measurement of amplitudes at the wanted sideband and the image frequencies.

This technique gets cumbersome in the presence of bandwidth dependent IQ gain and phase offsets. The procedure for iterative tuning of gain and phase offsets would need to be repeated at multiple frequencies and the effectiveness of the calibration would depend on the fineness of the frequency spacing. Moreover, the problem does not end with just calibrating the gain and phase offsets at multiple frequencies. It also needs to be accompanied with compensation for ripples and tilt in the pass band gain and phase responses of the entire RF chain that follows the modulator such as bandpass filters, amplifiers, etc. Quick calibration with inexpensive apparatus has been a topic of research. . A brief review of prior art techniques and a detailed discussion of the published techniques proposed by the author of this thesis are presented below.

### 3.2.3. Review of prior arts

The task of achieving wideband amplitude and phase balance between two paths over wide bandwidths with single, multi-tone and chirp stimuli have previously been accomplished [22, 23, 24].

However, this is done using iterative procedures which can prove time consuming. In prior art [25], the authors use a modulated signal as stimulus and two envelope detectors tuned at the intended IF and at the image frequency and iteratively identify the correction values for IQ imbalance in a millimeter wave transmitter with a GHz of bandwidth. The timing offsets are modelled mathematically as deviations from ideal constellation points. The apparatus is low cost but the procedure is iterative, requires measurement at the wanted and the image sideband and hence time-consuming.

Prior art [23] provides a novel method of using a scalar measurements taken from a spectrum analyser and obtaining the correction factors in an iterative manner through automation. The technique is simple but iterative and requires multiple measurement cycles.

Prior art [26] describes an iterative method to calibrate the IQ imbalance in a LINC (Linear amplification with Nonlinear Components). LINC transmitters operate on the principle of outphasing where a complex envelope modulated signal is decomposed into two constant envelope phase modulated signals which are amplified in fixed envelope high efficiency power amplifiers such as Class E amplifiers and combined at the appropriate phase to restore the envelope. The constant envelope phase modulated signals occupy bandwidths as wide as twelve times the channel bandwidth whose frequency components can be dispersed when propagating through bandwidth selective media. Hence the transmitter's apparatus requires wideband calibration to balance the amplitudes and maintain the integrity of the phases of the constant envelope signals. The authors propose to perform an iterative calibration as a part

of pre-distortion. This would be time consuming when applied to wider channel bandwidths in the order of tens to hundreds of MHz.

In prior arts [24, 27], a method to calibrate multiple paths of a MIMO receiver using a wideband calibrated source is described. The test signal is applied to 8 receivers in a MIMO system through a calibrated 8-way splitter. The signal is subject to vector demodulation in each path and the gains and phases relative to one another are identified through a licensed proprietary software utility and the correction factors for the respective paths are evaluated. A similar technique is followed to calibrate a reference receiver described later in this chapter and further extended to calibrate I and Q paths in the same receiver.

In prior art [22], a wideband digital beam former is analysed for wideband IQ gain imbalance and quadrature phase errors using a chirp stimulus. The frequency response of each channel is analysed as a function of the azimuth angle. Each channel's frequency response is equalized by means of a time reversal derived from the measured data. In this technique, an input signal  $x(t)$  is transmitted to a receiver through a medium whose transfer function is  $h(t)$ . The received signal  $r(t)$  at the receiver is the convolution of  $x(t)$  and  $h(t)$ . In frequency domain, the Fourier Transform of  $r(t)$ , designated as  $R(f)$  may be viewed as multiplication of  $X(f)$  and  $H(f)$ , the Fourier Transforms of  $x(t)$  and  $h(t)$  respectively. Now if the signal  $r(t)$  is reversed in time domain to yield  $r(-t)$ , its corresponding Fourier Transform yields  $R^*(f)$  which is the complex conjugate of  $R(f)$ . If  $r(-t)$  transmitted over the same medium to the transmitter, the resulting signal  $y(t)$  corresponds to the convolution of  $r(-t)$  with  $h(t)$ . In frequency domain,  $Y(f)$  corresponds to multiplication of  $R^*(f)$  and  $H(f)$ . This is equal to  $X^*(f)H^*(f)H(f)$  which yields  $Y(f) = AX^*(f)$  where  $A$  is the result of multiplying  $H^*(f)$  and  $H(f)$  which is the square of the magnitude of  $H(f)$ . Therefore, the transmitter can deduce the magnitude of the medium's frequency response by computing the complex conjugate of  $Y(f)$ . This stimulus used in this novel technique is modified to include time interleaving for calibration of spatially combined transmitters in chapter 6.

Prior art [28] describes a novel self-contained technique to calibrate the quadrature gain and phase offsets in an ultra-wideband CMOS up-converter where the offsets are identified using an error amplifier consisting of a comparator, counter and two Digital to Analogue Converters (DACs) to generate the correction voltages. This is however more suitable for application in Radio Frequency Integrated Circuit (RFIC) designs and is less applicable in situations where a system designer such as a base station or a VSAT terminal designer has little insight on the implementation of the up-converter modules used which are generally purchased from third party vendors. A similar scheme is described in [29].

Prior art [30] obtains the correction co-efficient for each path using a wide bandwidth Pseudo Random Binary Sequence stimulus to the hardware under test. This technique is novel but requires complex signal processing operations to be performed.

Prior art [31] evaluates the RF path mismatches using a set of secondary mixers in

a CMOS RFIC based up-converter but this technique is however more suitable for application in RFICs designs as is the case with prior art .

Prior Art [32] accomplishes the task of calibration using an OFDM signal and performs a frequency domain estimation of the parameters on the basis of the signal received in each path. This is a novel technique that exploits the properties of an OFDM signal's spectral characteristics but could be computationally intensive depending on the amplitude and phase profile of the OFDM signal.

Prior art [33] employs multi-tone test signals to characterize the frequency dependent mismatches across the band of interest and use a digital filter for compensation of the defects. While the technique is novel, fineness of spacing of the multiple frequency tones in the frequency domain of the stimulus has a direct impact on the estimation of ripples in the gain and phase responses over the wide bandwidth of interest.

Prior Art [34] accomplishes the IQ imbalance calibration in a quadrature receiver using a received signal as a test signal and switching it between the 'I' and 'Q' paths along with LO switching to analyse the amplitude and phase variations across the two paths and compute the correction factors. This approach is however limited to a receiver.

Prior Art [35] employs bandpass test signals which are up-converted to the desired IF frequency and calibrates the IQ offset depending on the rejection of the up-conversion sideband. While this is a well proven approach, it is iterative and the number of iterations depends on the initial state of the DUT and step size of the amplitude and phase tuning algorithm.

Prior Art [36] employs bandpass test signals which are up-converted to the desired IF frequency and calibrates the IQ offset depending on the response of the transmitter and receiver sections to a bandpass input signal and further responses to two phase shifted versions of the input signal. This is also an iterative approach.

Prior Art [37] employs square law detectors at the output of the transmitter at the intended and image bands. Adaptive calibration is applied to mitigate the mismatches. This method is also iterative and is similar to [25].

### **3.3. Novel Non-Iterative Procedures to Perform Wideband Calibration**

In this section, novel non-iterative techniques published by the author are presented which require only one measurement cycle of signal parameters and only at the intended up-conversion band with a reference receiver to calibrate the entire band or sub-band. A stimulus similar to that used in [22] is applied in one of the techniques but the calibration procedures are simplified and are applicable to both in-circuit and spatially combined RF signal paths. The RF emissions in the image band are

automatically mitigated by application of calibration in the wanted band. The techniques are scalable to include any number of paths in the transmitting apparatus with ease and all the paths can be calibrated with just one measurement cycle per band/sub-band taken with a reference receiver.

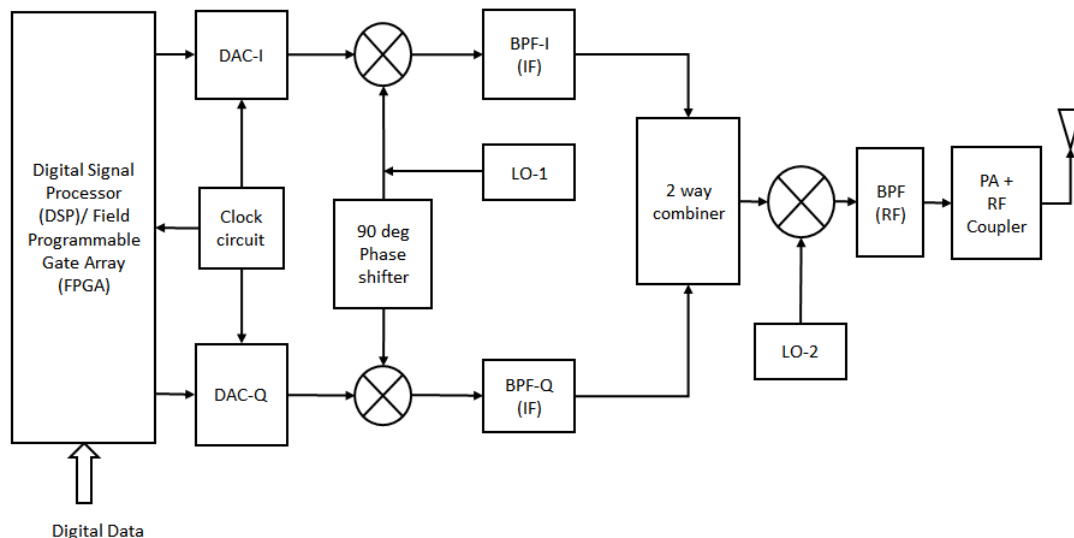


**Fig. 3.3.:** Modulator and up-converter of a super heterodyne satellite uplink transmitter.

### 3.3.1. Time Interleaved stimuli to signal paths

The technique involves a combination of time domain and frequency domain analysis of the impairments and imbalances that a wideband signal experiences along a chosen path and generation of correction coefficient matrix which could be applied to the input signal such that the desired output signal is obtained after the altered input signal undergoes the amplitude and phase distortions at each stage in the transmit chain.

#### 3.3.1.1. Synthesizing the stimulus waveform:

The choice of test signal (stimulus) depends upon several factors such as bandwidth, type of hardware under test, signal to noise ratio in the receiver, etc. Two special signals namely Truncated Sinc and Frequency Modulated Chirp are synthesized digitally to excite the hardware under test depending upon the type of hardware and the bandwidth of interest. These stimuli are described below.

a) Truncated Sinc Stimulus: In [38], the authors proposed to use multi-tone and OFDM signals respectively to provide the stimulus to the hardware under test. The extent of analysis of pass band characteristics in the hardware under test depends

on the fineness of the tones set in these two stimuli. A desirable test signal would be one which excites a whole band of the desired frequencies with the same amplitude, has no frequency component outside the band of interest and maintains a pre-determined phase across the band of interest. Such a signal would have a rectangular profile in the frequency domain. This is impractical since a rectangular response in frequency domain would imply an infinitely long signal in time domain in the form of a Sinc signal. The Sinc signal is obtained by dividing a Sinusoidal function with its parametric variable eg.  $\sin(x)/x$ . An ideal sinc signal is infinite in length and is not practical to generate in a finite time interval. Truncated Sinc functions have been in usage for over three decades to implement digital filters. Sinc pulses of finite length i.e. truncated sinc pulses could be used whose response in the frequency domain would be near trapezoidal instead of being rectangular. This can be used as the stimulus for calibration of RF hardware with linear and weakly non-linear modules but not with strongly non-linear modules. Yet, it provides a very convenient stimulus to calibrate the signal paths preceding RF power amplifiers in a transmitter. One of the popular truncated variants of Sinc functions is the Hamming window characterized by the polynomial which is commonly used to filter signals. This function has been exploited to generate a test signal instead of filtering and come up with a wide band stimulus that can excite a wide band frequencies in the bandwidth of interest and reduce the efforts involved in characterization of wideband performance indices of the modules of interest.

$$h(m) = \text{Sin} \frac{2\pi f_c (n - \frac{M}{2})}{(n - \frac{M}{2})} (0.54 - 0.46 * \cos(2\pi n/M)) \quad (3.8)$$

where  $M$  is the length of the Sinc pulse,  $n$  is the sample number ranging from 0 to  $M$ . This signal in time domain looks as in:

The signal in frequency domain looks like a wide bandwidth trapezoid with curved edges.

A key aspect to note is that the proposed test signal exhibits a linear phase characteristic in the frequency domain which is a desirable attribute to test frequency dependent phase distortion of an RF hardware module. Important to note: The test signal generated above exhibits a PAPR of around 23 dB and it's therefore important to ensure that the hardware under test is operated within dynamic range (range of signal powers over which the hardware under test could be called operational). The PAPR could be varied depending upon the truncation length of the Sinc pulse or depending upon the slope of the transition region of the frequency response from the desired frequency region to the undesired frequency region.

b) Frequency Modulated Chirp Stimulus: Presence of strongly non-linear modules such as RF power amplifiers (PA) in the signal path makes a less suitable case for characterization with truncated sinc Stimulus. This is due to the high PAPR in the Sinc stimulus which would drive the strongly non-linear elements to saturation

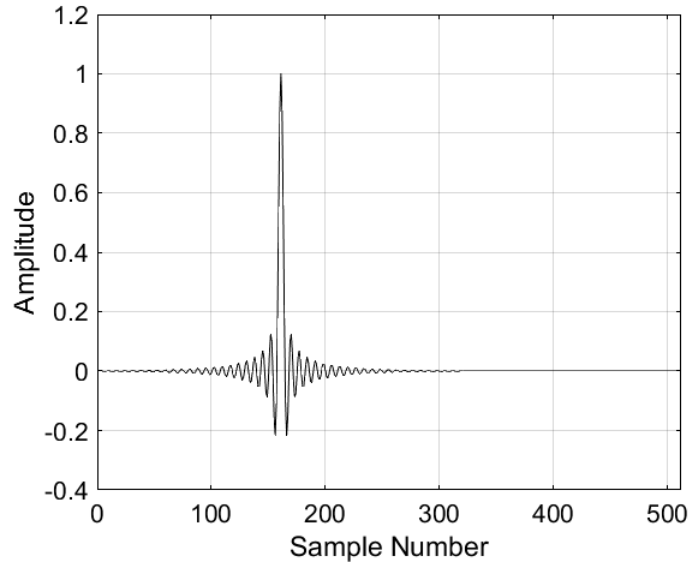


**Fig. 3.4.:** Truncated Sinc pulse generated using Hamming window kernel

with significant AM-PM distortion in its response along with spectral growth in the adjacent channels. These parameters of PAs will be discussed in detail in the next chapter. An alternate choice for the stimulus applicable to RF signal paths in hardware with strongly non-linear elements is a chirp signal. This is similar to the stimulus used in [22] but the method of application to calibrate multiple paths is new. This stimulus exhibits a constant envelope unlike the truncated sinc stimulus. A digitally generated chirp signal is described by the following equations

$$y(n) = \sin\left\{2\pi\left(\frac{nkT_s}{2} + f_{min}\right)nT_s\right\} \quad (3.9)$$

$$k = \left(\frac{f_{max} - f_{min}}{M}\right) \quad (3.10)$$

where  $y(n)$  is the value of the  $n$ th sample is,  $T_s$  is the sampling interval,  $M$  is the total number of samples,  $k$  is the frequency variation parameter,  $f_{max}$  and  $f_{min}$  are the maximum and the minimum frequencies respectively. Since a chirp signal is in essence a frequency modulated signal, it is essential to keep its modulation index to a minimum to limit the bandwidth expansion beyond the channel of interest. This implies that the factor ‘ $k$ ’ in eq.3.9 should be minimized implying that the factor ‘ $M$ ’ should be maximized. This factor can be chosen such that the bandwidth expansion is limited to 1% of  $(f_{max} - f_{min})$ . For example, consider operating the DACs in the hardware under test at 320 mega samples per second (MSPS). This implies that sampling time or duration of each sampling pulse is 3.125 nsec. Let  $f_{max}$  be set at 90 MHz and  $f_{min}$  be set at 0. The maximum frequency deviation in the FM chirp

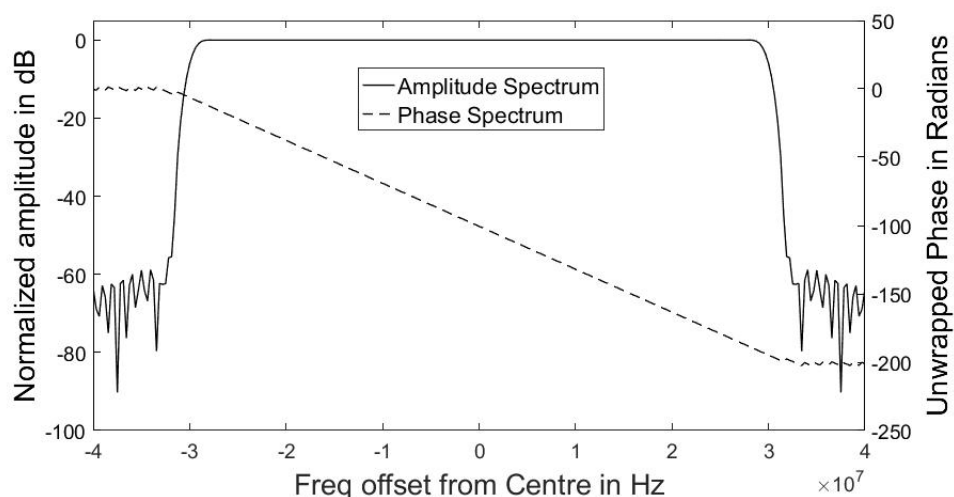


**Fig. 3.5.:** Frequency domain characteristics of the proposed truncated Sinc pulse test signal

signal is equal to  $f_{max}$ . Setting the extra bandwidth to 1% of  $f_{max}$  i.e. 0.9 MHz, the sweep rate  $k$  should be chosen such that the number of samples required to sweep from 0 to 90 MHz should be equal to  $(1/0.9 \text{ MHz})/ T_s$ . This yields a value of 356 samples for  $M$ . This can be visualized as an FM signal modulated by a tone of 0.9 MHz with a frequency deviation of 90 MHz having a total bandwidth of  $2(90 \text{ MHz} + 0.9 \text{ MHz}) = 181.8 \text{ MHz}$ . The bandwidth expansion can be reduced further by increasing  $M$  in eq. 3.10. The time domain waveform and the spectrum of a chirp signal with  $M$  set at 4000 samples and  $f_{max}$  set at 45 MHz are shown in Fig. 3.6 and Fig. 3.7 respectively.

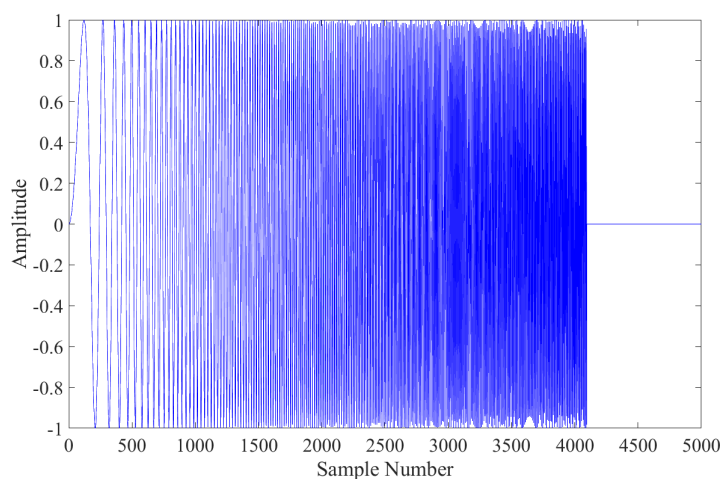


**Fig. 3.6.:** Chirp Waveform

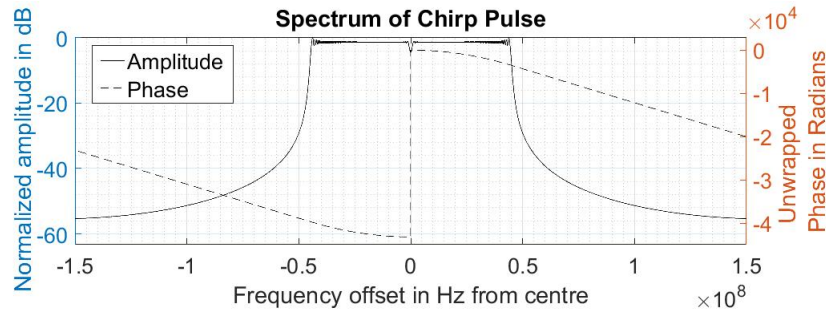


**Fig. 3.7.:** Chirp Spectrum

### 3.3.1.2. The Novel Non-Iterative Test Methodology

The test methodology may be classified into two steps and is similar for both chirp and truncated sinc stimuli with a few extra computations needed for the chirp case. The methodology is first described for the truncated sinc case and the extra computation steps needed for the chirp case are discussed in the end of this subsection. The first step is to characterize the amplitude and phase variation across the frequency band of interest in a single RF signal processing path. The second step is to characterize the amplitude and phase variation across the frequency band of interest in other single RF signal processing paths relative to the first path. The relative amplitude and phase responses across the frequency band of interest is of higher interest since they directly provide insight into the amplitude and phase imbalances across the frequency band of interest.

### 3.3.1.3. Wideband Amplitude and Phase characterization of a single RF path

The task involves application of the above test signal to the hardware under test at the desired centre frequency of operation. This could have two options.

- i) Apply the digitally generated Sinc pulse to the DAC at the baseband frequency to the up-converter so that the up-converted test signal is centred on the carrier frequency ' $f_c$ ' generated by the LO and occupies the bandwidth of interest. This is a straightforward option usually adopted in most direct-conversion transmitter architectures. A limitation with this option is that the leakage of the carrier signal generated by the LO caused by finite isolation between the ports of the mixer won't be distinguishable from the carrier leakage caused by the dc offset (output dc voltage at zero input) of the DAC.
- ii) Up-convert the test signal digitally to an intermediate frequency (IF) and then apply it to the DAC which would generate bandpass signals centred at frequencies ' $f_c + IF$ ' and ' $f_c - IF$ '. The response to the bandpass signal centred on the frequency ' $f_c + IF$ ' would be desirable to carry out the analysis due to the absence of phase inversion.

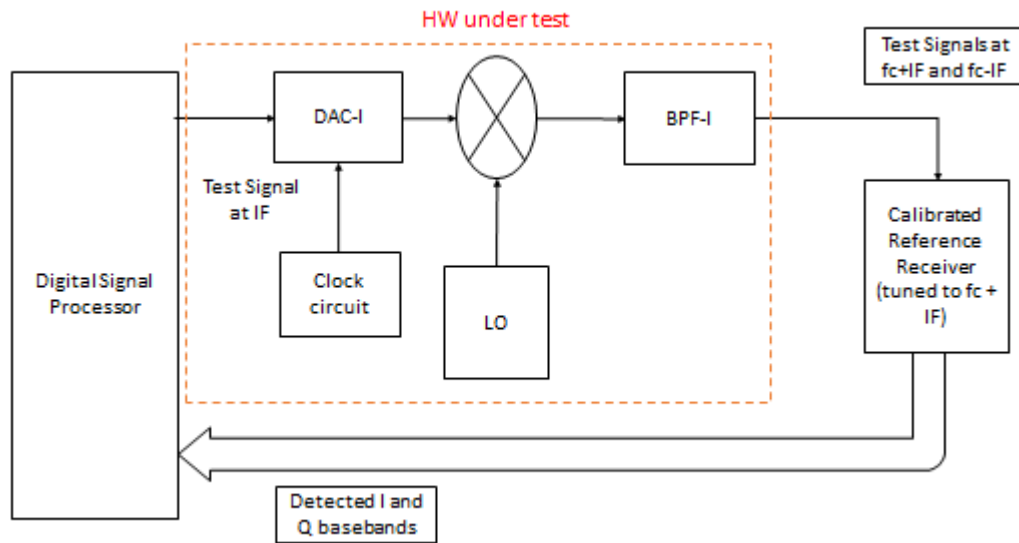


**Fig. 3.8.:** Single Path Test Setup

The proposed test apparatus for characterizing the wide bandwidth characteristics of a single RF path is shown in Fig. 3.8. The band pass filter is optional depending on the transmitter architecture. The bandpass filter here is considered a part of the transmit chain which also needs to be characterized and compensated for. A reference receiver is used to detect the amplitude and phase content across the frequency band of interest. This can either be a vector signal analyser, or combination of a down-converter and a high speed Analogue to Digital Converter (ADC). The down-converted IF is digitized by the ADC and the samples are subject to digital vector down-conversion to yield the in-phase (I) and quadrature (Q) components of the received. The reference receiver using a down-converter and a high-speed ADC has only one signal path to calibrate and may be done using prior art techniques.

Consider applying the truncated sinc stimulus described above to the DAC at a digital IF of 90 MHz. Let the sampling clock of the DAC be set at 320 MHz. Let the output of the DAC be subjected to up-conversion using an LO running at 2.24 GHz. This frequency is chosen for convenience to demonstrate novelty of the technique using available RF apparatus and its application at mm wave band will be shown in the upcoming chapters. The up-conversion would yield a wanted signal at  $2.24 \text{ GHz} + 90 \text{ MHz} = 2.33 \text{ GHz}$  and an image at 2.15 GHz. The spectrum of the up-converted response of the I path of the modulator in to the truncated sinc stimulus at a digital IF of 90 MHz is shown in Fig. 3.9. The in-band amplitude ripple tilt is visible in the output at the wanted frequency and this is the combined outcome of sinc roll off of the DAC and bandwidth dependent gain characteristics of the components in the RF stages after the DAC. The response at the wanted frequency alone is captured by the reference receiver where the response is subject to vector down-conversion.

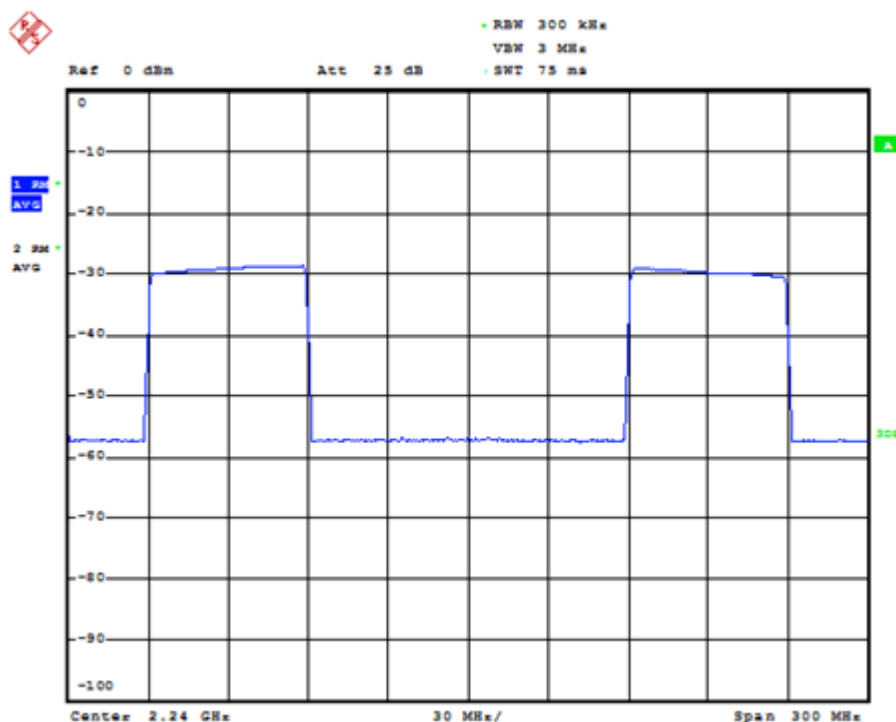
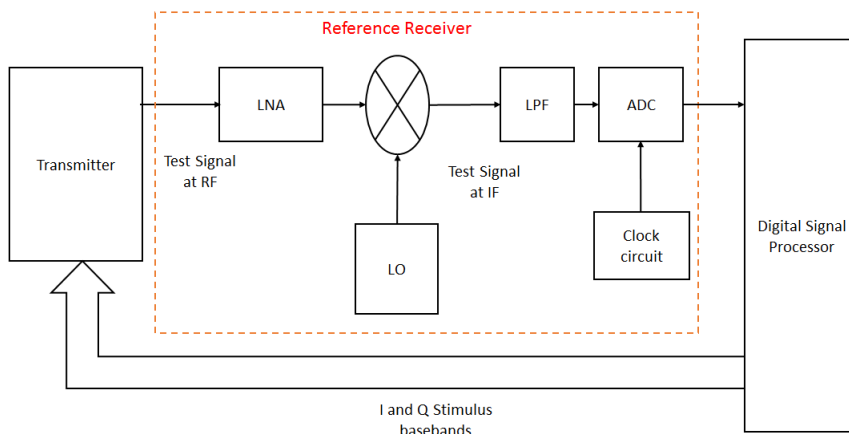


Fig. 3.9.: Spectrum of response to Sinc stimulus

Why is vector down conversion needed? The evaluation of phase variation across a band of frequencies requires that the relative phases of the frequency components of the signal obtained from the hardware under test in response to the test signal be identified. This is facilitated by vector down-conversion. The reference receiver can be a standard test equipment such as a vector signal analyser (VSA) or any calibrated receiver with vector down-conversion. If the reference receiver is of zero IF type, then vector down-conversion needs to be performed at RF. Else, a scalar down-conversion can be performed at RF and the IF output of the scalar down-converter can be digitized and subject to vector digital down-conversion.

The inverse tangent of the ratio of the magnitudes of the down-converted ‘Q’ components to the ‘I’ components provides a measure of the received phase. The phase of the LO signal in the reference receiver is unknown but a calibrated reference receiver is expected to have a phase relation of 90 degrees between the ‘I’ and ‘Q’ down-conversion paths. The down-converted ‘I’ and ‘Q’ components streamed by the reference receiver back to the digital signal processor form the basis for the amplitude and phase calibration across the signal path.

Reference receiver with scalar RF down-conversion and high speed ADC. The Discrete Fourier transform (DFT) of the response of the signal path under test is computed using Fast Fourier Transform (FFT) technique to obtain the amplitude and phase response at each excited frequency. The number of FFT points can be chosen depending upon the resolution needed. For the convenience of subtraction, the



**Fig. 3.10.:** Single Path Reference Receiver

amplitude spectrum of the FFT is plotted on dB scale. The amplitude spectrum computed directly indicates the in-band amplitude ripple and offset across frequency. The amplitudes are normalized to the maximum amplitude and directly subtracted from the normalized amplitude spectrum of the stimulus to yield the amplitude correction factors over the band of interest. A plot of the normalized amplitude response across the band of interest computed by taking the FFT of the response is shown in Fig. 3.11.

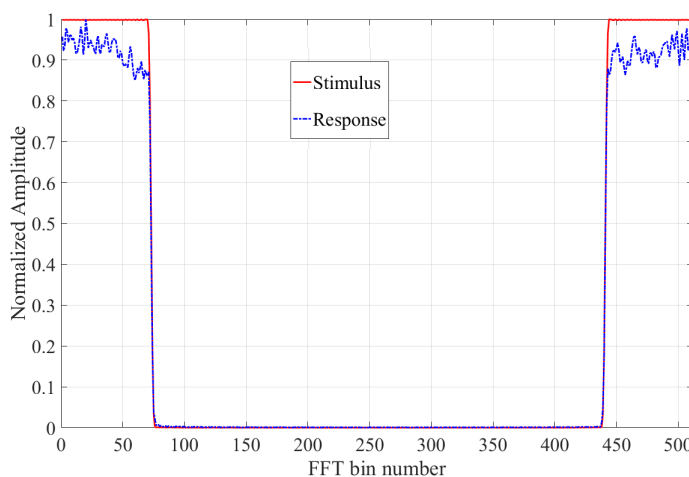


**Fig. 3.11.:** Amplitude plot of FFT of the single path response

The amplitude response of the signal path shown after calibration is shown in Fig 3.12 .

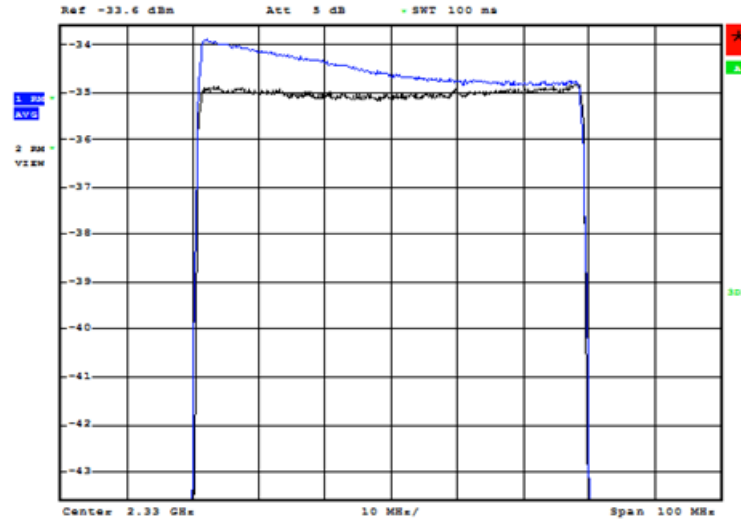


**Fig. 3.12.:** Amplitude response of the single path post calibration. Trace1 (Blue):Before Calibration. Trace 2 (Black): After Calibration.

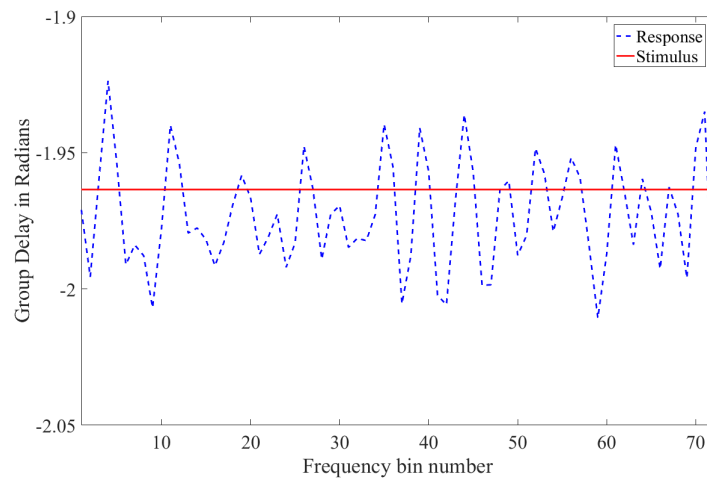


**Fig. 3.13.:** In-band group delay of single path

The first derivative of the phase spectrum in the band of interest is computed numerically to yield the in-band group delay variation or phase distortion over the bandwidth.

$$(Tg = (d\theta/d\omega)) \quad (3.11)$$

Where  $Tg$  is the group delay in seconds,  $\theta$  is the phase in radians and  $\omega$  is the angular frequency in radians/second. The first numerical derivative of the phase

spectrum of the response is subtracted from that of the stimulus to yield the phase correction factors over the band of interest. A plot of the in-band delay variation computed by taking the first differences of phases of the response’s FFT is shown in Fig. 3.13

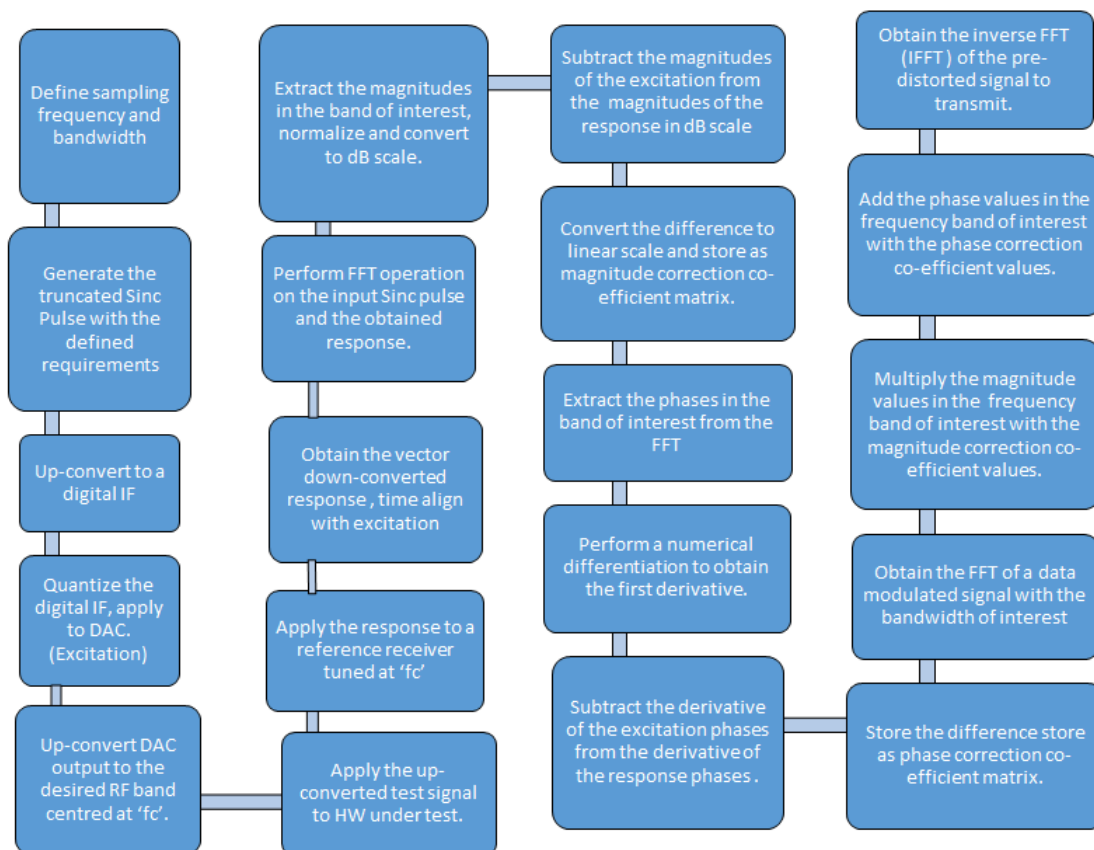
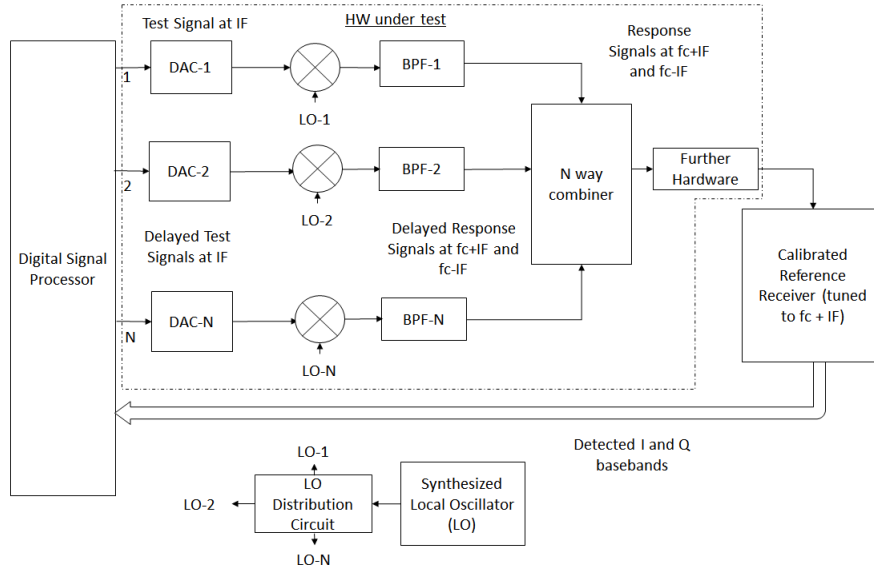


Fig. 3.14.: Single path calibration process

### 3.3.1.4. Wideband Amplitude and Phase characterization of a multiple RF paths:

The task of calibrating the signal paths in a transmitter like that shown in Fig. 3.8 involves application of the above test signal to the multiple parallel RF signal processing paths of the hardware under test at the desired centre frequency of operation at pre-determined time intervals and evaluating the response to yield the correction factors. The uniqueness of time intervals between the stimuli applied to each path enables identification of responses from each path uniquely. The system under test needs to warm up for thermal stability as a pre-requisite as is the case with most test equipment.



**Fig. 3.15.:** RF Transmitter with multiple signal paths

For simplicity, consider a case of parallel characterization of two RF paths where paths one and two are expected to be in phase quadrature and with equal amplitude responses across the intended frequency band of operation. Also it is desired that the variation of phase of the individual frequency components in the band of interest is identical in both the parts so that perfect quadrature relation is maintained between the two paths over the entire intended frequency band.

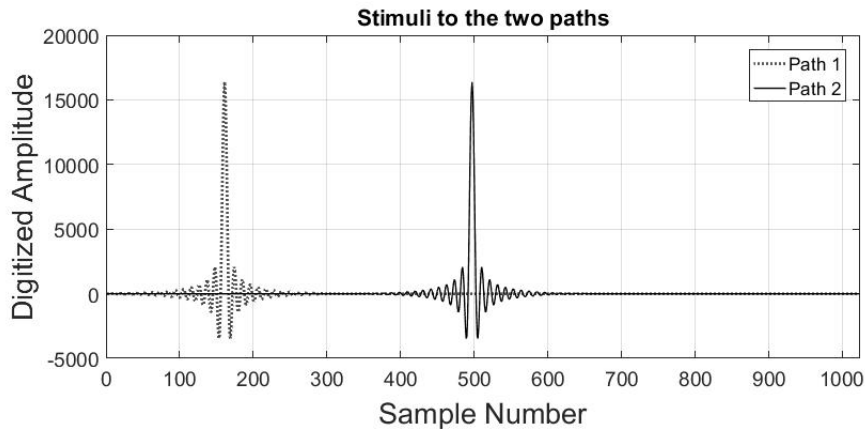


**Fig. 3.16.:** Stimulus for calibration of two paths in a transmitter

A digital signal processor generates the digital baseband signal at the intended IF and is applied to the DAC in each path whose outputs are further mixed with quadrature phases of the signal generated by local oscillator LO at frequency  $f_c$  and combined to yield a vector modulated RF output. Consider a digitally generated

test signal i.e. a truncated sinc pulse of 320 samples. This signal is zero-padded to extend the number of samples to the next power of 2 i.e. 1024 samples to yield the stimulus to the first path. A power of 2 is selected as the total length of the signal for the ease of computation of FFT. The stimulus to the second path is obtained by circularly delaying the stimulus of the first path such that it remains zero-valued in the duration when the stimulus to the first path takes the values of the truncated sinc pulse plus some guard interval. Two such signals are plotted on the same axis in Fig. 3.16. The response captured by the reference receiver at the center frequency  $f_c$  is the sum of the responses of the individual paths which are complex values representing the amplitude and phase at each sampling interval as shown in Fig. 3.17.

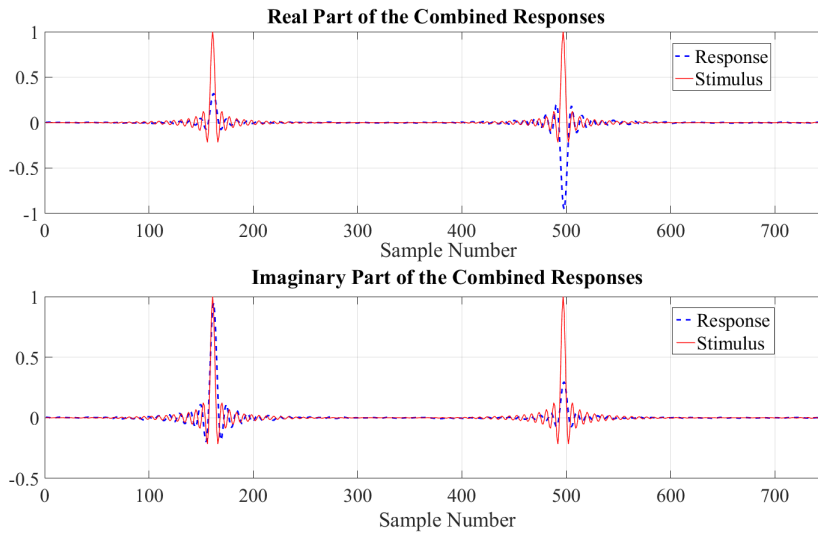


**Fig. 3.17.:** Correlated stimuli and responses

Considering the response signal captured in this example, samples from 1 to 336 represent the response of RF path 1 and samples from 337 to 583 represent the second RF path, path 2. The amplitudes of the extracted individual responses can then be cross-correlated to determine the relative timing offset between the two paths in terms of number of sampling intervals and the relative delay. A comparison of the amplitudes of the responses in time domain is shown in Fig. 3.18. It is for this reason that it is possible using this proposed method to derive the calibration co-efficients for all parallel signal paths in a single iteration. The amplitudes of the FFT of the responses of two paths is shown in Fig. 3.19.

The spectrum of the response of the I and Q paths of a vector modulator to a truncated Sinc stimulus post calibration is shown in Fig. 3.20. The roll off in pass band amplitude and the image have been mitigated by calibration.

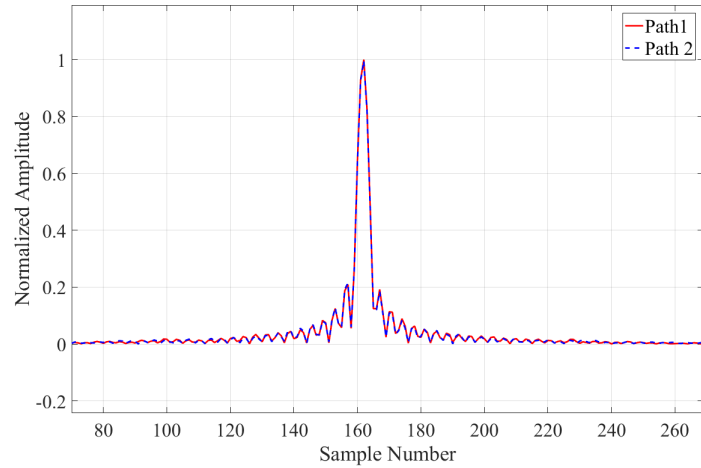


Fig. 3.18.: Time aligned magnitudes of paths 1 and 2.

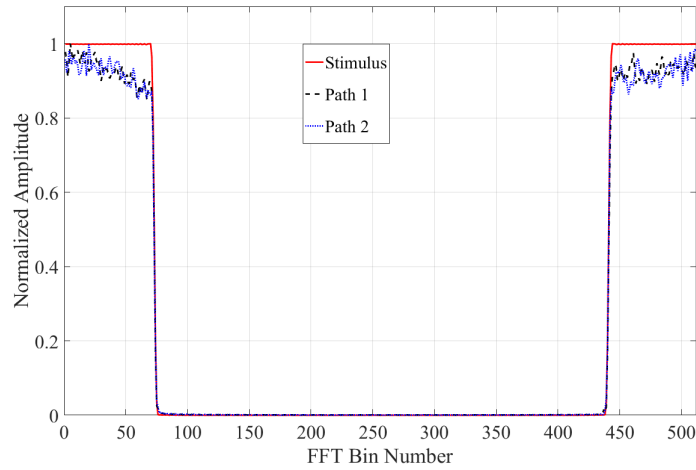


Fig. 3.19.: FFT plots of wideband amplitude responses of two paths

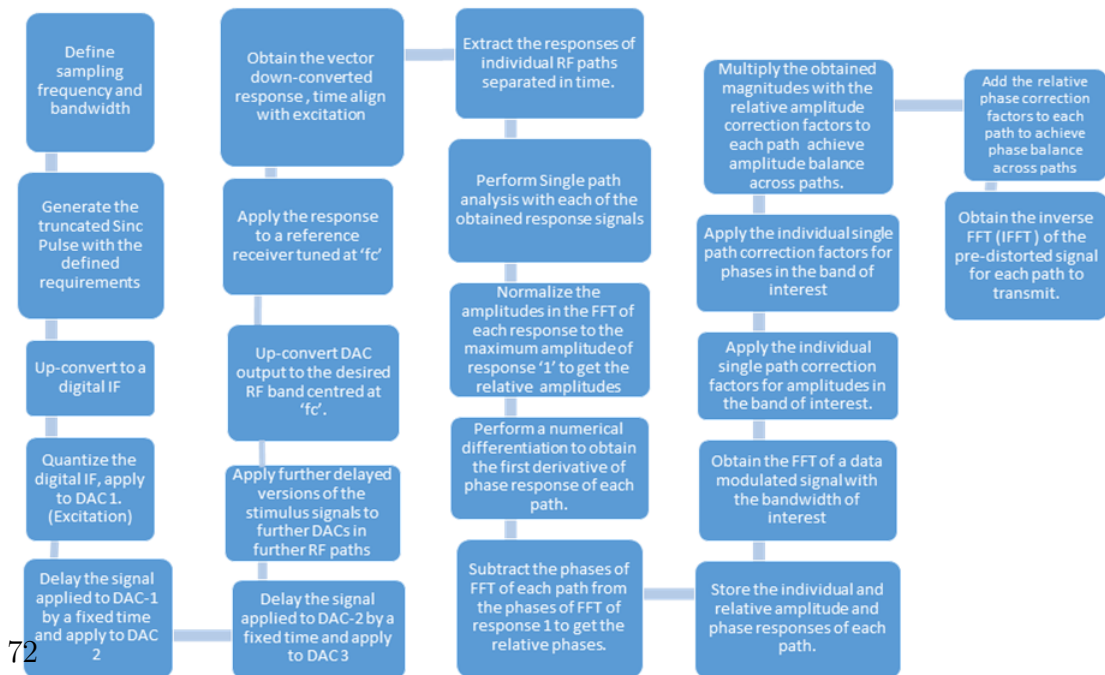
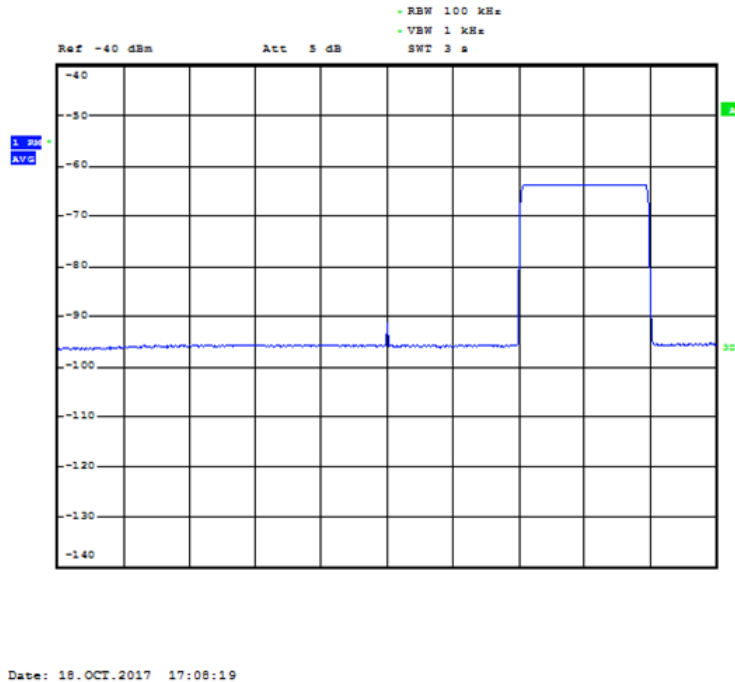


Fig. 3.21.: Calibration of multiple RF signal paths.



**Fig. 3.20.:** Response of IQ paths to Sinc stimulus post calibration

As seen above, the advantage of the proposed technique is that it needs just one iteration and just one measurement operation with the reference receiver to accomplish the required calibration of a set of parallel signal paths. The technique is scalable to a larger number of parallel transmitter paths with ease which only requires applying further delayed versions of the stimulus to each path and calibrating them as detailed above. The process is summarized in Fig. 3.21. Inherent by design, the technique can be scaled up to any number of signal paths.

The calibration procedure for the chirp case is the same as that described for the sinc case except that the correction co-efficient matrix extracted in the frequency domain needs to be filtered by a windowing function such as a Hamming Window to avoid out-of-band spectral growth, owing to the relatively wide transition region between the pass and stop bands in the stimulus and response signals. Relative to the sinc pulse characterization and compensation technique the chirp pulse technique is marginally more computationally demanding but its advantages outweigh the burden of extra computations. Chirp based calibration has been extensively used in the work described in this thesis and the applications are explained in next three chapters.

As in any electronic hardware, the performance of the transmitter post calibration depends is influenced by operating conditions and thermal characteristics of the components involved. As a rule of thumb, the system under test needs to be allowed to warm up so that the electrical parameters reach their steady state values prior

the calibration process. The EVM of the signal generated by the transmitter in operation may be used as the deciding factor to determine how often the system needs to be re-calibrated. This would be applicable irrespective of the calibration process followed. The experimental validation cases in this chapter are limited to in-circuit applications. The application of the described techniques to over the air channel characterization and spatially combined transmitters are presented in chapters 5 and 6.

### 3.3.1.5. Experimental Validation

A test bench was set up consisting of a computer (PC) running the tool MATLAB was used as a DSP, an evaluation board TSW30SH84 from Texas Instruments consisting of a quad DAC module DAC34SH84 with LVDS interface to connect to a digital interface board TSW1400EVM. A vector signal analyzer (VSA) FSQ-40 from Rohde and Schwarz was used as a reference receiver. The VSA was capable of demodulating an input modulated signal up to a bandwidth of 100 MHz. The outputs of DAC1 and DAC2 were treated as an IQ pair and connected to I and Q inputs of a vector up-converter module TRF3705 designated as UC1\_IF. The outputs of DAC3 and DAC4 were treated as the second IQ pair and connected to I and Q inputs of another vector up-converter module TRF3705 designated as UC2\_IF. The outputs from the DACs were up-converted to 2.24 GHz and the output. The reference oscillators of the onboard clock source module LMK02808 were synchronized with the reference output of the VSA after sufficient warm up time. A picture of the workbench is shown in Fig. 3.22.

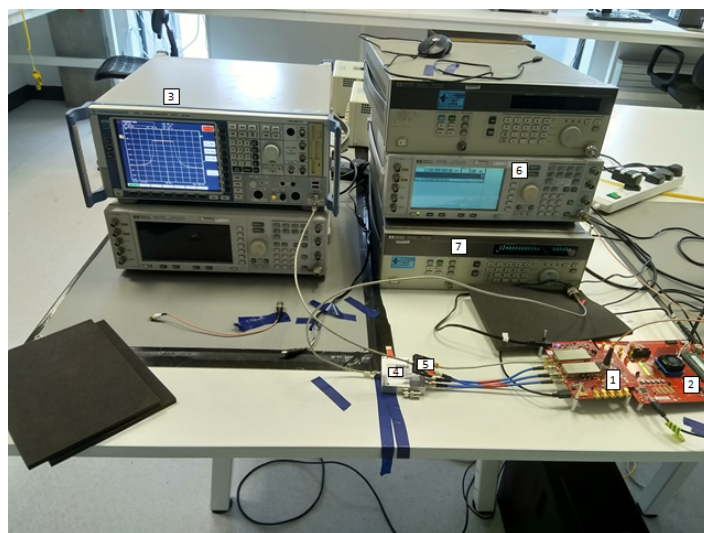


**Fig. 3.22.:** Work Bench with DAC, IF up-converter and RF test instruments

**Case 1: Zero IF with 4 paths at S Band** An outphasing/LINC transmitter consists of four RF signal paths. The operation of an outphasing transmitter is explained in chapter 4. In brief, it consists of two amplification branches where two constant envelope phase modulated signals are amplified and their outputs are combined to yield an amplified complex envelope modulated signal. The constant envelope phase modulated signals exhibit bandwidths as large as 10 times the bandwidth of the intended complex envelope modulated signal and hence it is essential to maintain the appropriate gain and phase relations between four RF signal paths over this extended bandwidth. This case was selected since it provided the opportunity to test a real world scenario where the outputs of an outphasing/LINC transmitter had to be combined at the appropriate phases. Mismatches in gain or phase responses of the outphasing branches over a bandwidth of 100 MHz had an adverse impact on the spectrum of the combined signal. The 4 paths of the LINC transmitter's modulator built with the quadrature modulator pairs described above were calibrated at zero IF over a bandwidth of 100 MHz. LINC baseband signals were generated for a 5 MHz WCDMA baseband signal with a power crest factor of 7dB. The LINC signals occupied a bandwidth over 100 MHz due to bandwidth expansion in the resulting phase modulated signals with high modulation index. Phase errors were deliberately introduced using LO feed cables of non-uniform lengths between the paths to replicate a more challenging use case. The calibration was performed using chirp stimulus in two different trials at a sample rate of 307.2 MSPS, center frequency of 2.24 GHz at a bandwidth of 100 MHz.. The sample rate of the ADC in the VSA was set equal to that of the DACs.

The block diagram of the test apparatus is shown in Fig. 3.23.

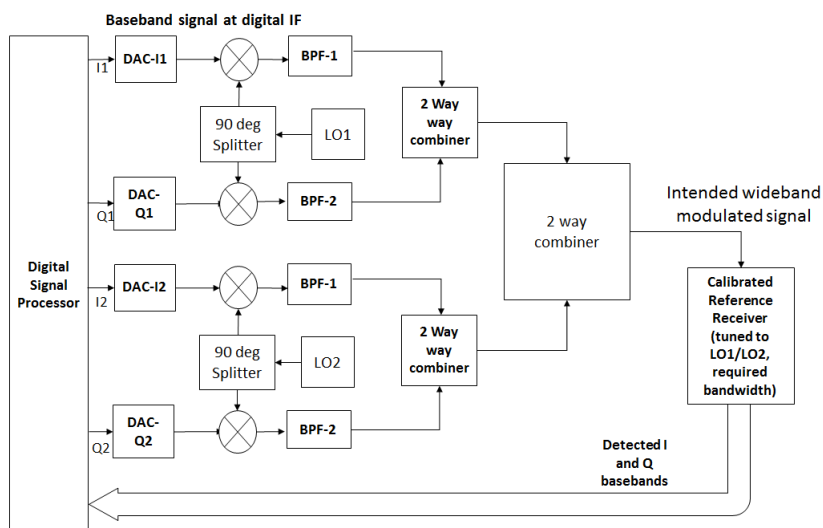


**Fig. 3.23.:** Four Signal Paths Test Apparatus

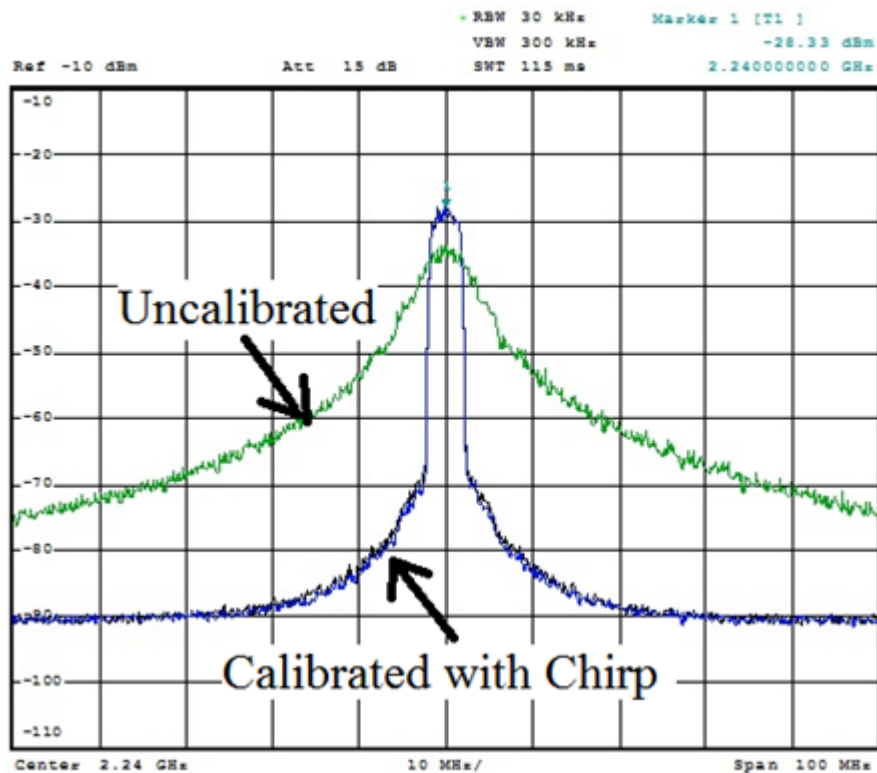


**Fig. 3.24.:** Four paths of LINC Transmitter calibrated with chirp stimulus

#### Observation:

An overall improvement of 36 dB was observed in the adjacent channel power rejection as shown in Fig. 3.24 after calibration with Chirp stimulus.

This case is revisited in Chapter 4 under the section on outphasing amplifiers and the results are analyzed in detail.

**90 MHz Digital IF with 2 paths, Single Heterodyne Modulator at S Band** This involved validation of the first IQ pair in the apparatus described for the previous case but at an IF of 90 MHz using truncated sinc stimulus with a channel bandwidth of 80 MHz. A pre-compensation FIR filter was synthesized with the computed calibration co-efficients and convolved with a QAM64 test signal modulated at a symbol rate of 80 MSPS and subject to root raised cosine filtering with a roll off factor of 0.1 and an oversampling ratio of 4.

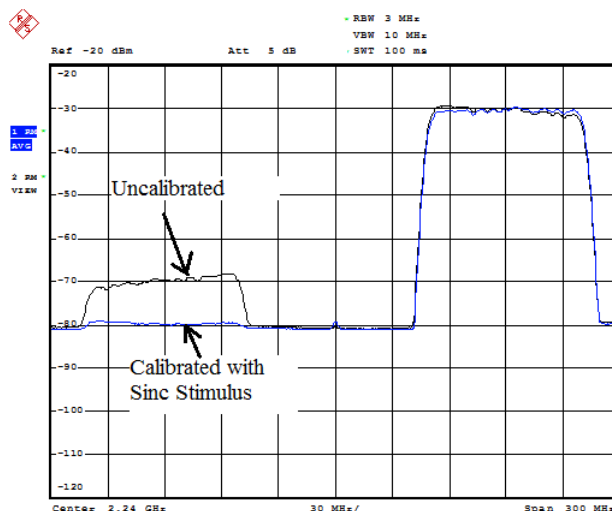


Fig. 3.25.: Comparison of spectrum of a 64-QAM modulated signal

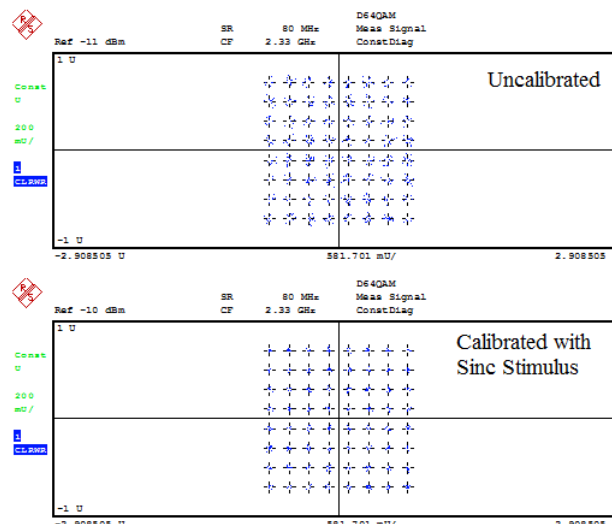


Fig. 3.26.: Comparison of constellations of 64-QAM signal post calibration

**Observation:** An overall improvement in image rejection by a factor of 10 dB could be observed as shown in Fig. 3.25. along with an overall improvement in EVM by 2% could be observed after calibration.

**90 MHz Digital IF with 2 paths, Double Heterodyne Modulator at Ku Band**

The third case chosen was a modulator for DVB-S2 transmitter in the Ku Band. The bench consisted of a Ku Band up-converter in addition to the apparatus shown in Fig. 3.22. The Ku Band apparatus is shown in Fig. 3.27.

For this case, test an 8PSK modulator at S-Band built with the first IQ modulator

described above, up-converted to Ku Band was used with the following settings: Symbol rate of 40MSPS, Root Raised Cosine Filter roll off factor of 0.2, digital IF generated at 90 MHz. The LO at S-Band was set at 2.24 GHz yielding up-converted signals at 2.33 GHz (desired) and 2.15 GHz (image). These were up-converted to frequencies of 14.23 GHz (wanted) and 14.05 GHz (image) respectively by a Ku band up-converter fed with an LO at frequency 11.9 GHz. A cavity tuned filter with a pass band of 14 to 14.5 GHz was used at the output of the Ku Band mixer. In this case two path calibration was performed on the entire cascaded system at 14.23 GHz by applying a truncated sinc stimulus of bandwidth 60 MHz and 512 points FFT for analysis.

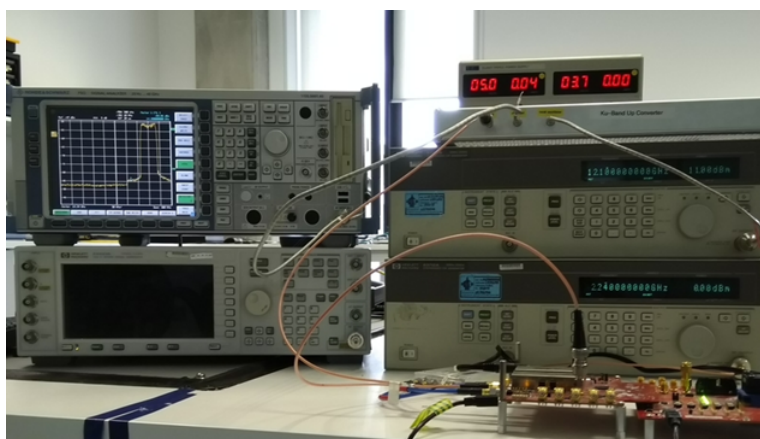


Fig. 3.27.: Ku-Band test bench

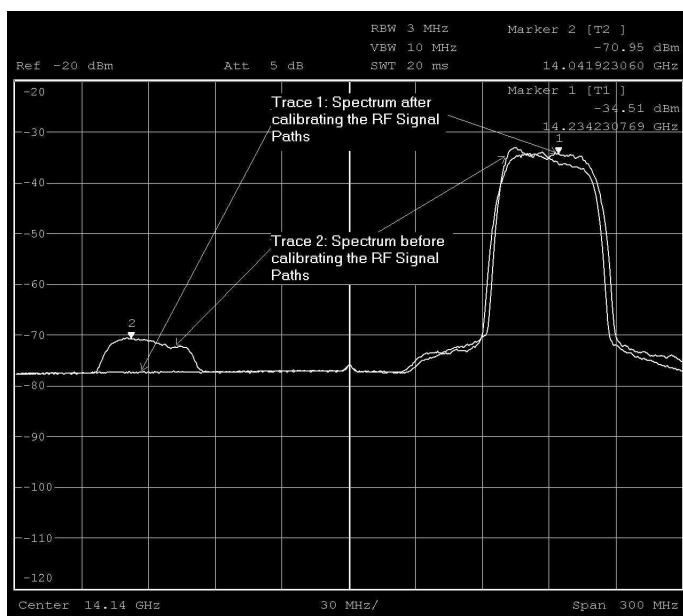
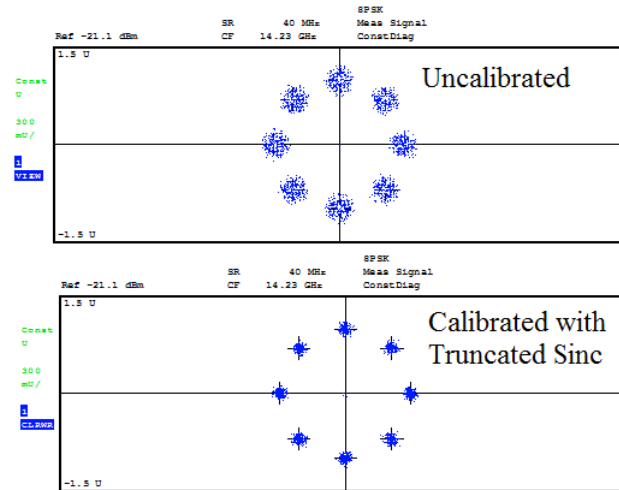


Fig. 3.28.: Comparison of spectrum of a DVB-S2 8PSK modulated signal at Ku Band before and after calibration



**Fig. 3.29.:** Comparison of 8PSK constellation before and after calibration of the double heterodyne Ku Band modulator

	CF 14.23GHz	Ref Lev -15dBm	SR 40MHz	Const: 8PSK			
	<b>Modulation Accuracy (Average)</b>						
	Before Calibration			After Calibration			Unit
	RMS	Avg	StdDev	RMS	Avg	StdDev	
<b>EVM</b>	14.205	12.995	5.737	6.898	5.606	4.020	%
<b>Magnitude Err</b>	10.341	8.417	6.008	5.208	3.511	3.920	%
<b>Phase Err</b>	5.680	0.010	5.680	2.590	0.010	2.590	deg
<b>Ampt Droop</b>	0.040	0.040	-65.470	0.000	0.000	-68.600	dB
<b>Origin Offset</b>	-52.090	-52.130	-72.720	-54.230	-54.280	-74.110	dB
<b>SNR (MER)</b>	16.950	16.950	-32.180	23.230	23.230	-12.790	dB

**Fig. 3.30.:** Modulation parameters reported by Vector Signal Analyser 'FSQ-40' of R&S at 14.23GHz

**Observations:** An improvement in image rejection i.e. frequency components around 14.05 GHz by a factor of 17 dB as shown in Fig. 3.28 and an overall improvement of Modulation Error Ratio (MER) of around 6dB could be observed as shown in and Fig. 3.30 respectively. An improvement in EVM by 7% along with an improvement in Modulation Error Rate (MER) by approximately 7 dB i.e. from 16.9 dB to 23.8 dB was observed. These figures can be improved further with DPD. A spectral growth in the adjacent channels could be observed due to the saturation of the driver amplifier at Ku Band. This would need digital pre-distortion (DPD) to mitigate. A test case with DVB-S2 signal has not been reported in the cited prior arts but the overall image rejection is comparable to that obtained using prior art methods.

The case of calibrating the signal paths in a spatially combined transmitter is deferred until chapter 6.

### 3.3.1.6. Calibrating Receivers:

A calibrated wideband reference receiver is essential for successful capture and analysis of responses from transmitters. However, the receiver itself is made of down-converters and ADCs whose responses depend upon frequencies of operation and hence needs calibration. One of the ways to perform calibration of the receiver is to use a calibrated transmitter, compare the stimulus and response and calculate the gain and phase correction factors for the response relative to the stimulus as explained for transmitters. The correction is applied in the form of FIR filters to the received signal prior to demodulation. The general block diagram of the apparatus for calibration of receivers with scalar RF down-conversion is shown in Fig. 3.31. The task requires more work for receivers with RF vector down-converters. The general block diagram of the apparatus for calibration of receivers is shown in Fig. 3.32. The calibration of dc offset in the ADC of receivers is relatively straight forward. A sinusoidal excitation with sufficient number of samples to yield at-least 5 cycles at the given sample rate is applied to the receivers RF input ports. The down-converted IF signal is digitized. The ideal average value of a sinewave is zero. The presence of any dc offset would manifest in the form of a sinewave varying about a fixed voltage other than zero volts. The average value of the signal computed over the number of sinusoidal cycles is subtracted from the digitized signal in the respective path. The calibration of IQ gain and phase imbalances can be performed using the same procedure as that of the transmitter but with a slight modification since each path in the receiver gets the same input signal. The number of interleaved signals is limited to two where the phase of the second signal is in quadrature to that of the first signal.

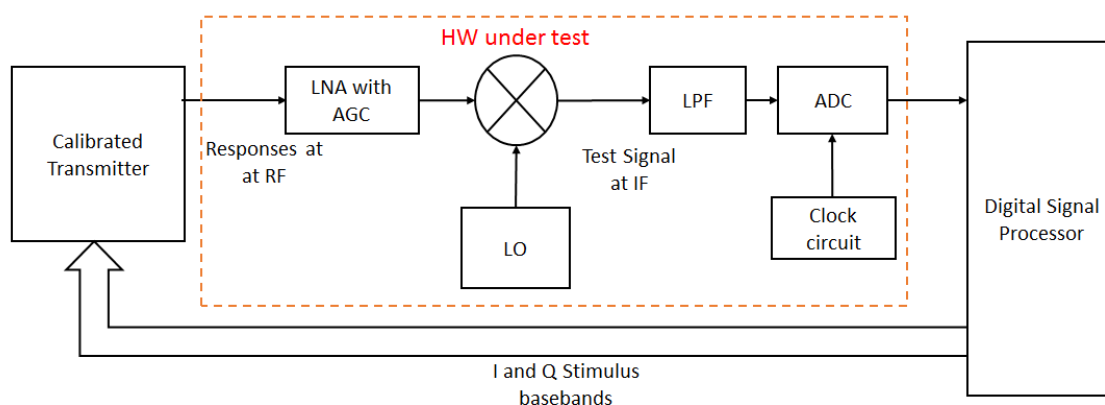


**Fig. 3.31.:** Calibration of a wideband receiver with scalar RF down-converter

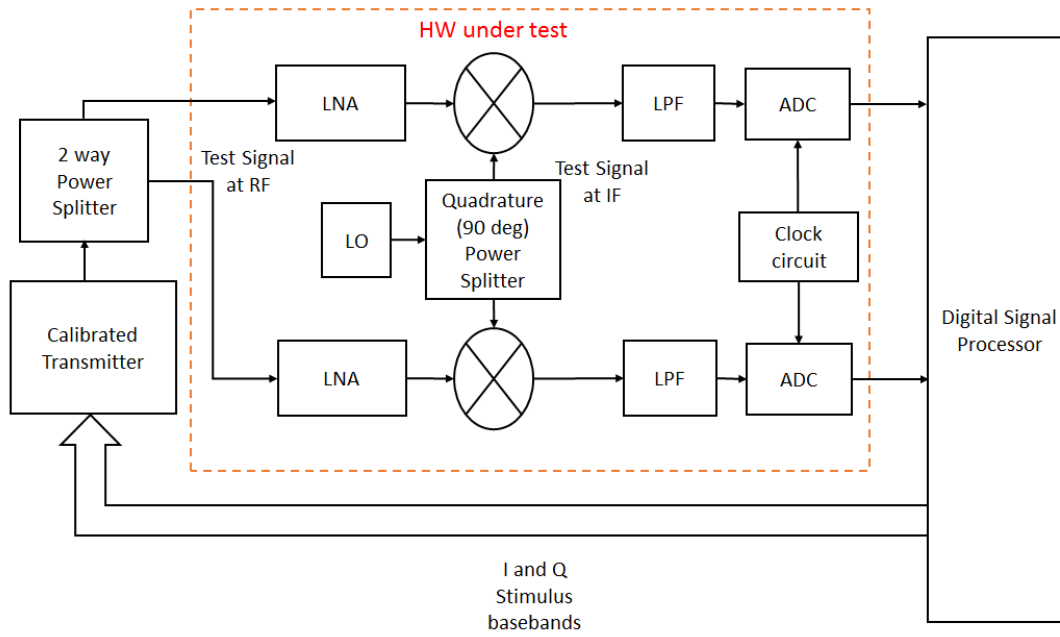


Fig. 3.32.: Calibration of a wideband receiver with vector RF down-converter

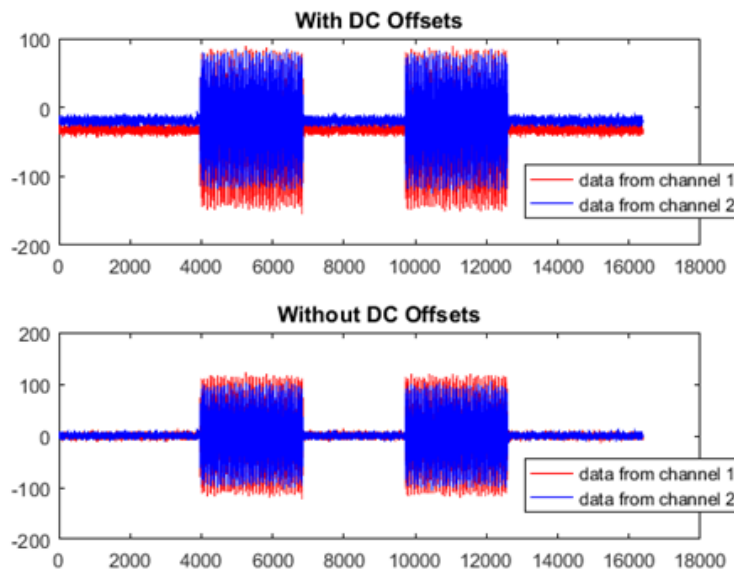


Fig. 3.33.: DC offset in ADCs of a receiver observed in response to chirp stimuli

This arrangement enables easy identification of quadrature gain and phase offsets in receivers with vector RF down-conversion. In case of I and Q paths of a single receiver, the common input signal (Sinc or Chirp at the intended RF) is fed to the

I and Q paths by means of an in-phase two way splitter.

The two time interleaved stimuli are designated as  $S_1(t)$  and  $S_2(t)$  respectively. A reference signal  $S(t)$  for wideband calibration is constructed by taking the complex sum of the two stimuli i.e.

$$S(t) = S_1(t) + jS_2(t) \quad (3.12)$$

Let the complex sum of responses to the stimuli in the I path be designated as  $R_I(t)$  and that of the Q path be designated as  $R_Q(t)$ .

$$R_I(t) = R_{I1}(t) + jR_{I2}(t) \quad (3.13)$$

$$R_Q(t) = R_{Q1}(t) + jR_{Q2}(t) \quad (3.14)$$

The IF in each path is digitized and acquired by the DSP. As in the transmitter's case, the I path is chosen as reference and the magnitudes of the signals received in the two paths are cross-correlated to determine the timing offset and the timing is aligned by delaying the path with a time lead. The RMS values of the magnitudes of the responses in the two paths are computed to determine the gain offset. The FFTs of the received signals are computed and subject to wideband correction of gain and group delay calibration in the band of interest. The phase difference between each frequency bin of the FFTs of the received responses are computed. This should be 90 degrees ideally. It needs to be noted that the FFTs to be considered for calibration are those computed on the signals presented in equations eq. 3.12eq. 3.13 and eq. 3.14. The inverse of the deviation from 90 degrees is saved as a correction factor for the respective frequency component. Similarly the ratios of the amplitudes of each frequency component in the FFTs are computed and the reciprocal of the ratios are saved as amplitude correction factors. The amplitude and phase correction factors are then integrated in the form of an FIR filter for the respective path. Any signal of interest is further subject to correction filtering by the saved FIR filters in each path and then subject to demodulation.

Limitations: Both truncated sinc and chirp stimuli are not standard modulation signals used in wireless communications. While they provide an insight of gain and phase distortions, it is relatively complicated to identify the cause of the impairments from the responses. For example, the presence of AM-AM and AM-PM distortions in the responses will manifest in the form of amplitude ripples and non-linear phase responses but it is complicated to identify whether these were caused by gain and phase responses of linear components or due to non-linear characteristics of active components. The ease of application, scalability in bandwidth and number of paths outweigh the limitations.

### 3.3.2. Calibration by Constellation Mapping

This is a non-iterative scheme that uses a complex envelope modulated signal as the stimulus to accomplish calibration. The stimulus designed is similar to that used in [25] but different in attributes and application procedure. A specially designed 64-QAM modulated stimulus of scalable bandwidth to characterize the wideband impairments in a vector modulated transmitter. This modulation format is close to that of a standard modulation scheme. Its response in the band of interest is used to mitigate the impairments in the form of a correction filter.

A 64-QAM modulated signal of bandwidth equal to the bandwidth of interest consists of multiple amplitudes and phases in the modulation constellation. This signal when applied as stimulus to the system under test (SUT) excites both frequency dependent and frequency independent transfer characteristics. It also excites power dependent transfer characteristics such as the AM-AM and AM-PM distortion factors in a nonlinear system. Each transition between different symbols of a 64-QAM constellation generates a different frequency component in the frequency domain. Accordingly, the calibration signal or stimulus  $S(t)$  is designed to contain all possible permutations [39] of unique transitions of a 64-QAM constellation as described in eq. 3.15.

$${}^n P_r = \frac{n!}{(n-r)!} \rightarrow {}^{64} P_2 = \frac{64!}{(64-2)!} = 4032 \quad (3.15)$$

where  ${}^n P_r$  is the number of permutations of selecting  $r$  variables from a set of  $n$  variables.

These values are close to those encountered in real-world communications. The number of vector transitions in the stimulus could be considered over constant envelope stimuli which be capable of capturing the amplitude dependent impairments. The signal to noise ratio (SNR) required to demodulate an uncoded 64 QAM signal at a BER of  $10^{-4}$  is around 26 dB which is expected from a typical transmitter. This makes it a viable choice over higher order constellations due to the relative ease of demodulation in terms of SNR.

Amplitude and phase variations can be captured and corrected. A 64-QAM modulated stimulus offers a higher level of amplitudes and phases in comparison to 16-QAM in time domain. The spectrum of a proposed stimulus example with 64-QAM modulation of symbol rate 80 Mega Symbols per second (MSPS) shaped with raised cosine filtering of roll off factor  $\alpha = 0.2$  with a resultant bandwidth of 100 MHz ( $80\text{MSPS} \times (1+\alpha)$ ) is shown in Fig. 3.34. The stimulus is transmitted through the nonlinear system under test and the response  $R(t)$  is captured using a reference receiver such as a VSA or a combination of a vector down-converter and an ADC.

The response provides to capture both frequency and power dependent transfer characteristics of the system under test simultaneously which is especially applicable

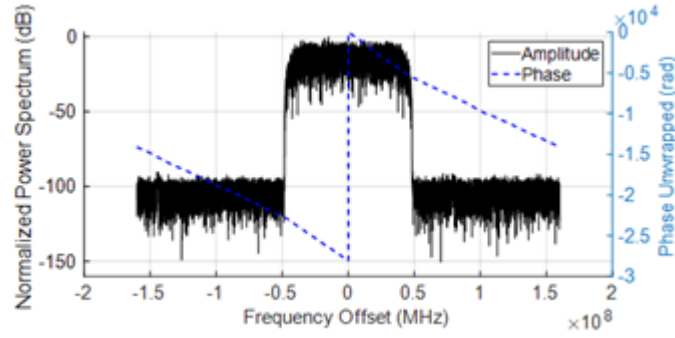


**Fig. 3.34.:** Frequency domain spectra of magnitude and phase of stimulus

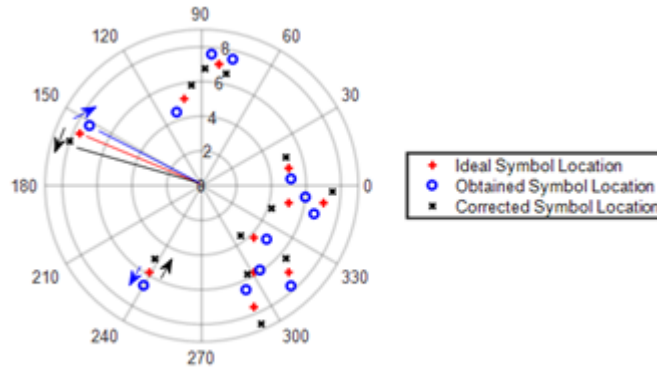


**Fig. 3.35.:** Constellation is mapped on a polar plot with 64-QAM modulation symbols.

to nonlinear systems such as power amplifiers (PA) operating in the saturation region. The response is demodulated and subject to digital evaluation of the vector constellation symbols. This involves vector subtraction of each constellation point in the response from the ideal values to yield the error vector  $e(k)$  at each point whose inverse  $c(k)$  yields the respective correction factors where  $k$  ranges from 1 to the number of constellation points in the stimulus. Adding the vector correction factors to each constellation point in the original stimulus pre-compensates it to mitigate the encountered impairments as shown in Fig. 3.35. The pre-compensated  $P(k)$  signal may be mathematically viewed as an outcome of convolution of the stimulus with a pre-compensating FIR compensation filter kernel  $f(k)$ .

$$e(k) = s(k) - r(k) \quad (3.16)$$

$$c(k) = -e(k) \quad (3.17)$$

$$P(k) = s(k) + c(k) \tag{3.18}$$

$$P(k) = f(k) * s(k) \tag{3.19}$$

Deconvolution of the pre-compensated signal and the stimulus would yield the coefficients for the pre-compensation filter. The filter can be convolved with an actual baseband signal to pre-compensate it against the impairments in the SUT.

$$f(k) = \text{deconvolution}P(k), S(k) \tag{3.20}$$

AMAM distortion identification – Constellation symbols are observed to have a shorter vector radii than their ideal locations as in Fig. 3.36plot (a).

AMPM distortion identification – Results in the symbol point to have the same vector radius, but to have an angular movement along the vicinity of the ideal location. This can be observed in Fig. 3.36 plot (b). Additionally, Inter-Symbol-Interference (ISI), random noise interference and phase noise can also be identified by observing the response of the stimulus [40, 41].

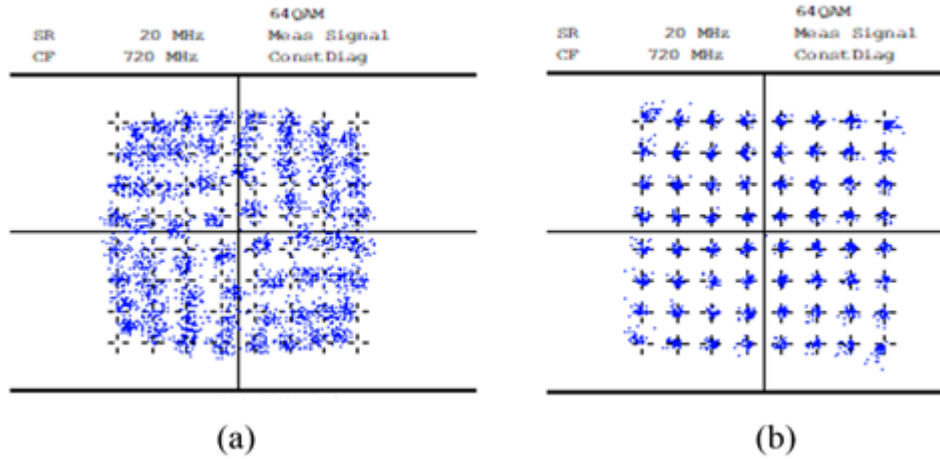


**Fig. 3.36.:** Identification of AM-AM and AM-PM distortions

Limitations: The applicability of this scheme is limited to sets of two signal paths at a time. But can be applied with ease if the total number of paths involved is even by time interleaving the stimuli to pairs of paths. This technique requires nearly four times the number of computations than the time interleaved sinc and chirp stimuli. However, the ability to detect AM-AM and AM-PM distortions makes this an attractive choice to calibrate RF hardware consisting of moderately and strongly non-linear modules such as Doherty amplifiers. Further experimental results on Doherty amplifiers are discussed in chapter 4.

### 3.3.2.1. Experimental validation of calibration by constellation mapping

A specially designed 64-QAM signal that covered all permutations of transitions between constellation points was used as stimulus and calibration was performed as explained in Chapter 3. A pre-compensating FIR filter was synthesized for each path to mitigate the signal path impairments. The pre-compensating FIR filter was then convolved with signals of interest to pre-compensate them against hardware impairments in the signal paths.

**Zero IF with 2 paths, Homodyne Modulator at S Band** This involved validation of the first IQ pair in the apparatus described for the previous case but at an IF of 90 MHz using truncated sinc stimulus with a channel bandwidth of 80 MHz. A pre-compensation FIR filter was synthesized with the computed calibration coefficients and convolved with a 256-QAM test signal modulated at a symbol rate of 80 MSPS and subject to RRC filtering with a roll off factor of 0.2 and an oversampling ratio of 4.

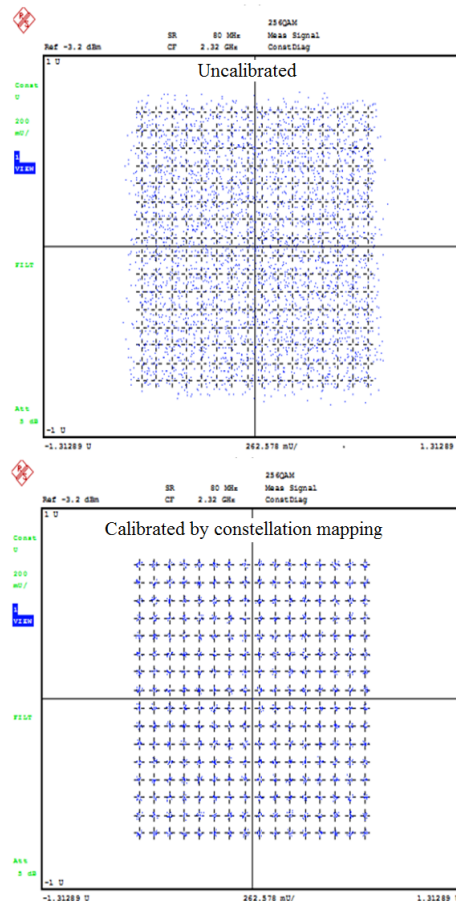


**Fig. 3.37.:** Comparison of constellations of a 256-QAM modulated signal before and after calibration by constellation mapping technique.

The validation was repeated with a DVB-S2 8PSK modulated signal of the same bandwidth and RRC filtering. The test apparatus for experimental validation of this scheme is the same as that shown in Fig. 3.22.

**Observation:** An improvement of 10.9 dB in Modulation Error Rate (MER) over the un-compensated case resulting in a value of 34.39 dB and an Error Vector Magnitude (EVM) of 1.907% were observed. A comparison of the demodulated constellations is shown in Fig. 3.37.

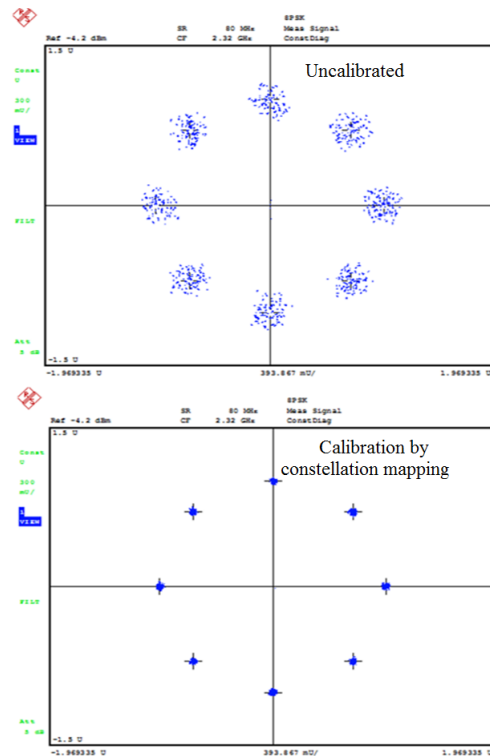


**Fig. 3.38.:** Comparison of constellations of an 8PSK modulated signal before and after calibration by constellation mapping technique.

**Observation:** An improvement of 15.7 dB in Modulation Error Rate (MER) over the un-compensated case resulting in a value of 34.51 dB and an Error Vector Magnitude (EVM) of 1.88% were observed. A comparison of the demodulated constellations is shown in Fig. 3.38.

**Single Heterodyne Modulator at Ku Band** A 64-QAM baseband of symbol rate 80 MSPS generated in MATLAB was applied to the first IQ pair in the apparatus described above to yield a modulated carrier at 2.32 GHz. This signal was then up-converted to Ku Band at 14.32 GHz using the test bench shown in Fig. 3.27. A comparison of the demodulated constellations with and without pre-compensation of the baseband by convolution with the pre-compensating filter are shown in

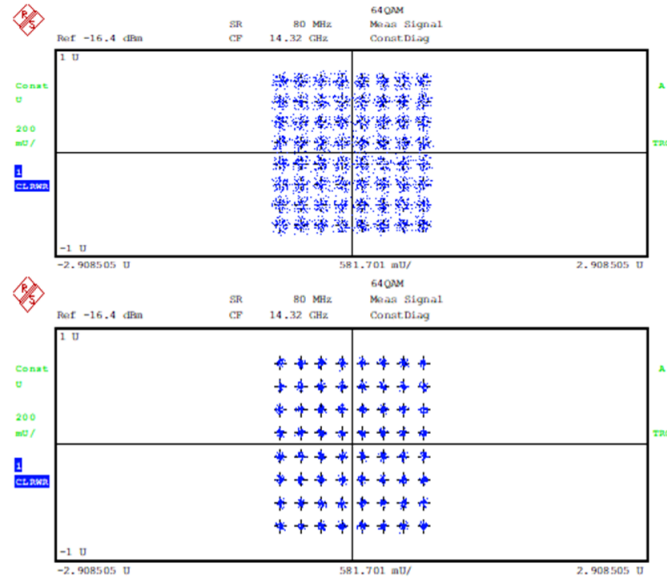


**Fig. 3.39.:** Comparison of QAM64 constellation before and after calibration of the single heterodyne Ku Band modulator

**Observation:** An improvement of 8.02 dB was observed in MER for a 100 MHz wide QAM 64 modulated signal along with a 5.5% improvement in EVM resulting figures of 34.2dB and 3.52% for MER and EVM respectively. This test case represented a weakly non-linear case.

**Zero IF 780 MHz transmitter with Doherty Amplifier** A strongly nonlinear system is in operation when a Doherty Power Amplifier (DPA) is driven with sufficient input power to operate beyond P1dB compression point. Both power and frequency dependent nonlinearities are in effect due to the strong nonlinearity. Power dependent impairments functioning as AM-AM and AM-PM conversion effects that are nonexistent/not-apparent in weakly nonlinear systems show up in a strongly nonlinear system and pose a greater challenge for RF path calibration. The knowledge of these impairments is essential to perform digital pre-distortion (DPD) of PAs.

The challenge is significant in a DPA as the RF signal must propagate through two amplifiers biased at different classes (Class AB, Class C) and then be constructively recombined. The demodulated responses of indicate Fig. 3.40 significant AM-AM, AM-PM distortions with ISI.

**Observations:** Both frequency dependent and power dependent impairments were compensated after calibration as observed in Fig. 3.40. Significant reduction in ISI was observed post-calibration with improvements in EVM by 6.64 % and in MER by 6.87 dB. The indicated linear performance after the proposed calibration is as

### 3.4 Conclusions:

---

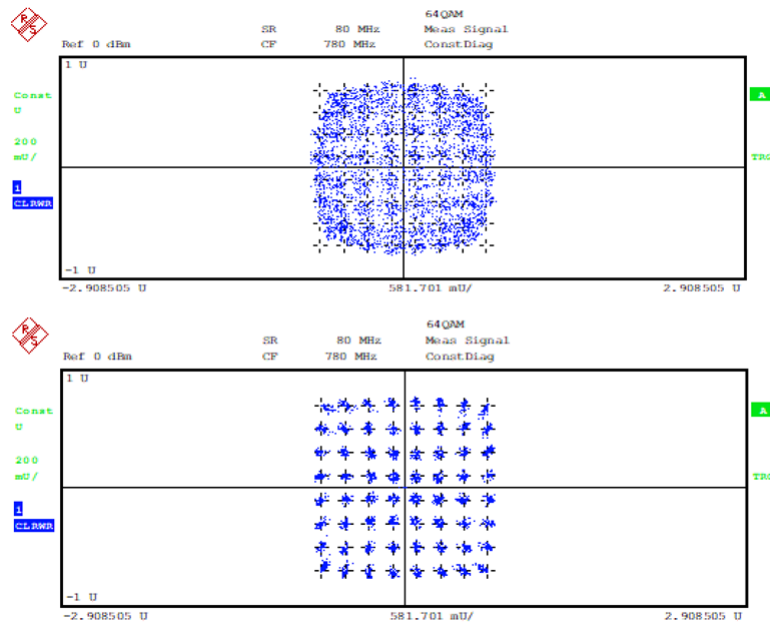


**Fig. 3.40.:** Comparison of QAM64 constellation before and after calibration of the transmitter with a Doherty Amplifier

if the system is driven at a lower input power level, delivering higher output power and reduced MER without heavy distortion in the RF signal constellation.

### 3.4. Conclusions:

In this chapter, system level manifestation of impairments in the building blocks of RF transceivers were examined and prior art methods to mitigate these impairments through digitally assisted calibration were discussed. The prior art techniques discussed though novel are iterative. The effort and needed to mitigate the impairments in RF systems that involve multiple signal paths such as outphasing transmitters and massive MIMO would increase proportional to the number of paths. The prior arts discussed were either designed for calibration of in-circuit combined RF signal paths or for calibration of beam forming i.e. spatially combined RF signal paths but not for both together. Two novel non-iterative schemes were presented to calibrate multiple RF signal paths in a single iteration.

**a) Calibration using time interleaved truncated sinc and chirp stimuli:** A novel low complexity and non-iterative scheme has been presented to calibrate the timing, amplitude and phase offsets and distortions across multiple RF signal paths over a wide frequency band of interest in a single measurement cycle. The scheme is applicable to both in-circuit and spatially combined RF signal paths where the phase

and gain relations between them can be of any arbitrary value. This scheme however requires a calibrated reference receiver operational over the band of interest but it is sufficient to have a receiver with just one signal path and the method to calibrate the reference receiver has also been presented. The technique is scalable with number of paths. This is particularly advantageous in applications involving beam forming and physical layer security. This scheme is however not convenient to identify non-linear distortions like AM-AM and AM-PM conversion in the hardware being tested and calibrated. However, this scheme is applicable to calibrate the paths over a wider bandwidth needed to mitigate the non-linear through digital pre-distortion which is introduced in the next chapter. The experiments carried out on the two paths of a Ku Band super heterodyne DVB-S2 modulator and a zero IF outphasing modulator with four paths where all the signal paths were calibrated with just one measurement with a reference receiver validate the presented technique. The advantages of non-iterative calibration of multiple RF signal paths where the gain and phase relations can be set arbitrarily and ability to scale up the technique with increasing number of signal paths outweigh the limitations. These advantages are exploited in the work presented in the upcoming chapters.

#### **b) Calibration by Constellation Mapping:**

A novel non-iterative method based on vector positioning of constellation symbols of a specially designed 64-QAM modulated signal that can calibrate RF path impairments has been presented. A primary advantage of the technique in comparison with the work reported in literature is that it is non-iterative. It uses a modulated waveform that closely resembles a current standard communication signal format and is able to alleviate both frequency and power dependent impairments such as amplitude ripple-tilt, group-delay, AM-AM and AM-PM conversion in linear, weakly non-linear and strongly non-linear systems. These advantages were proven by a variety of experimental test cases at different frequency bands and at power levels using three different test benches. A limitation of the scheme is that it can calibrate only two paths at a time. This limitation can be alleviated by combining this technique with time interleaving where the stimulus to a pair of paths can be time interleaved. The advantages of being non-iterative, using a waveform similar in attributes to that used in real wireless communications, applicability to both weakly and strongly non-linear systems with abilities to identify AM-AM and AM-PM distortions outweigh the limitations.

# 4. RF Power Amplifiers: Key Parameters, Classes, Topologies and Behavioral Modelling

This chapter is designed to provide a brief overview of RF power amplifiers in general, their classes, topologies and behavioral models. Some of the inferences from the experimental validation of the novelties presented in this chapter were considered in the next two chapters to mitigate problems of wide bandwidths and high PAPR. The primary novel contribution of the author of this thesis presented in this chapter corresponds to item 2 in the list of publications. This is in the wideband calibration of RF hardware applying the novel scheme presented in chapter 3. The secondary contributions of the author of this thesis correspond to items 5, 6, 12 and 13 with the role limited design review and verification along with editing the drafted papers as a co-author since RFPA design was not the principal objective of the research activity undertaken.

## 4.1. Introduction

An RF Power Amplifier is a device meant for boosting the power of the signal prior to transmission by an extent that the signal reaches the intended receivers at the intended distance 'd' with enough strength for demodulation. The extent of power to be transmitted depends on the link budget for the desired distance, bandwidth, type of modulation and fading environment. Consider for example a cellular base station operating at 30 GHz needed to transmit a modulated signal of bandwidth 200 MHz over a distance of 500 meters such that the receiver receives it with a signal to noise ratio of at least 10 dB, with transmitting and receiving antennas having directive gains of 5 dB respectively. The free space path loss experienced by this signal between the transmitter and the receiver as calculated by Friis formula i.e. eq. 4.1 is 106 dB. Considering receiver noise figure of another 5 dB along with the given bandwidth of 200 MHz and minimum SNR requirement of 10dB, the sensitivity of the receiver would be -76dBm. Considering a design margin of 7dB, the power of the signal at the transmitter's output should at least be +36dBm or 4 Watts. The task of delivering this power to the signal rests with the RFPA.

$$FSPL_{dB} = 10 \text{Log}_{10} \left( \frac{\lambda}{(4\pi d)} \right)^2 + G_T + G_R \quad (4.1)$$

where  $FSPL_{dB}$  is the free space path loss in dB,  $\lambda$  is the wave length of the signal,  $d$  is the distance in metres,  $G_T$  and  $G_R$  are the gains of the transmitting and the receiving antennas respectively in dB.

Like all active components, an RF power amplifier requires a specific value of DC bias power to operate. Unlike small signal amplifiers like the low noise amplifiers (LNAs) in receivers, the PA is a power hungry device and hence the challenge is in getting the signal of interest boosted to the maximum power possible for the extent of DC power consumed. Some of the typical operating classes and modes of RFPAs are discussed in the next sections.

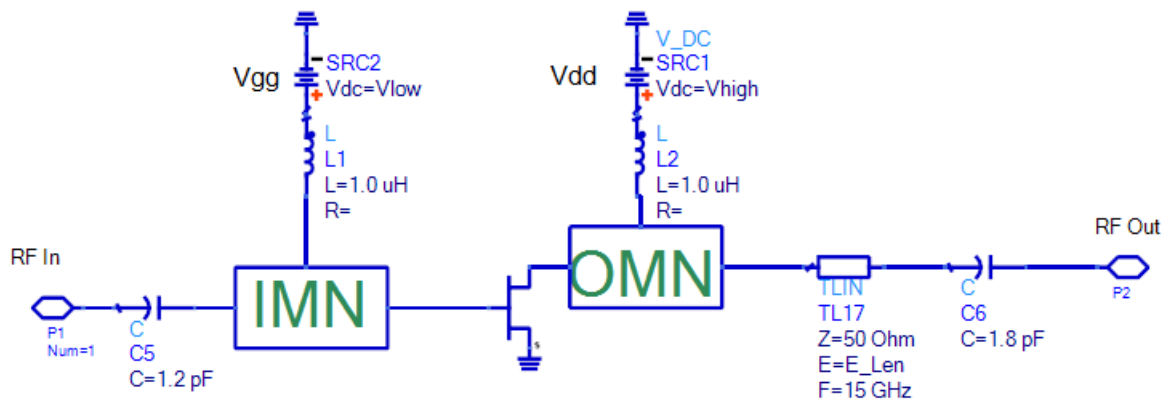


**Fig. 4.1.:** Typical Single Transistor RF Power Amplifier Circuit

A typical circuit schematic diagram of an RFPA is shown in Fig. 4.1 where IMN and OMN are the input and output impedance matching networks respectively, Vdd and Vgg are the DC power supplies for the drain and gate terminals of the PA.

## 4.2. Key Parameters of an RF Power Amplifier

**Gain 'G':** This is the ratio of output power to input power, a factor by which the power of the input signal is amplified. The gain should remain constant up to the maximum output power in an ideal amplifier. This is not practical since amplifiers generally reach a compression point, commonly called 1 dB compression point as explained in subsec. 2.3.1. At this point an increase of input power no longer relates to the same increase in output power.

**Saturated Power Output ' $P_{sat}$ '**: This refers to the maximum RF power that can be delivered to the load by the PA. This power is higher than the power available at the 1dB compression point.

**Linearity** : The term linearity was introduced in chapter2 which implies a constant gain relation between input and output powers such that the output  $y$  is equal to  $ax$  where the term  $a$  is a constant. However, all active components exhibit nonlinear behaviour and have a transfer function of the form shown in Fig.2.8, have saturation points and hence can be considered linear only over a limited range of input and output powers. The typical relation between the output power  $y$  and input power  $x$  in a PA is as shown in eq.4.2.

$$y = ax + bx^2 + cx^3 + dx^4 + ex^5 \quad (4.2)$$

An RFPA is a strongly non-linear module where co-efficients of all the powers of  $x$  in eq.4.2 are significant and hence lead to parasitic behaviours such as AM-AM output voltage conversion, AM-PM conversion and intermodulation. Another parasitic effect of non-linear response is the spectral emissions outside the allocated bandwidth causing interference with neighbouring channels. This has both performance and legal implications since it can deny the quality of service to a neighbouring wireless client. The amount of emission allowed in the neighbouring channels is enforced by the respective wireless standard and regulatory authority in the form of a spectrum mask. This was introduced in chapter 2. The primary cause of emissions in the neighbouring channels can be inferred by expanding the non-linear transfer on (eq.4.2) and substituting  $x(t) = M_1(t)\text{Sin}(\omega t + \phi(t))$  in. This may be described mathematically as shown in the equations below.

**AM-AM Conversion**: This is a parasitic behaviour where the amplitude of the RF input signal to an RFPA influences the gain of the PA such that an amplitude modulated input signal with modulation index  $M_1$  would result in an output signal with a different modulation index  $M_2$  after amplification. Let the input RF signal  $x(t)$  be described by a sinusoidal function

$$x(t) = M_1(t)\text{Sin}(\omega t + \phi(t)) \quad (4.3)$$

This when applied to an RF PA whose transfer function is described by eq.4.2 (considering only the first 3 terms on the right hand side (RHS) )would yield

$$y(t) = a(M_1(t)\text{Sin}(\omega(t) + \phi(t))) + b[M_1(t)\text{Sin}(\omega(t) + \phi(t))]^2 + c[M_1(t)\text{Sin}(\omega(t) + \phi(t))]^3$$

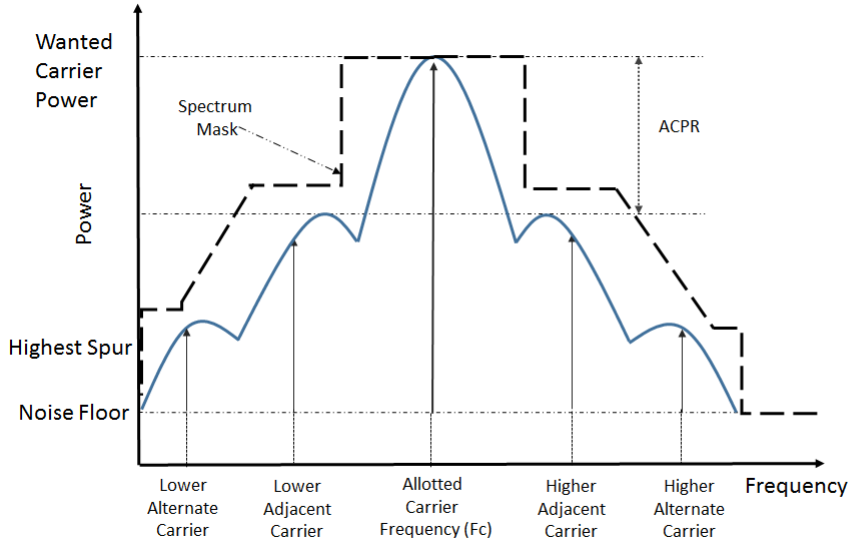


**Fig. 4.2.:** Power Amplifier's RF Output Spectrum

(4.4)

On expanding the third order terms on the RHS of eq. 4.4 and retaining only the products falling in the fundamental frequency  $\omega$ , the output  $y(t)$  would yield

$$y(t) = \left[ aM_1(t) + \frac{3c \{M_1(t)\}^3}{4} \right] [\text{Sin}(\omega t + \phi(t))] = M_2(t)\text{Sin}(\omega t + \phi(t)) \quad (4.5)$$

where the new amplitude function  $M_2(t)$  is not just a linearly scaled version of  $M_1(t)$ . AM-AM effects are significant when the output power from the PA is at peak due to gain compression in the transistor caused by saturation of charge carriers. The impact of AM-AM conversion on a 64 QAM modulated OFDM signal after amplification by a non-linear amplifier is shown in Fig. 4.3. It may be inferred that peaks of the OFDM signal are clipped in the output plot. The impact increases with increase in PAPR for a fixed bias condition. AM-AM conversion can also be identified from the demodulated constellation where the radii of the outermost symbols are shortened.

**AM-PM Conversion:** This is a parasitic behaviour where the amplitude of the RF input signal to an RFPA influences the conducting phase of the PA. The PA is built using RF power transistors with finite lengths of the conducting channels, gate and a finite gate width. The conductivity of the channel is accomplished by controlling the density of charge carriers in the channel by controlling the voltage applied to the gate. This is also accompanied by voltage controlled capacitance between the gate

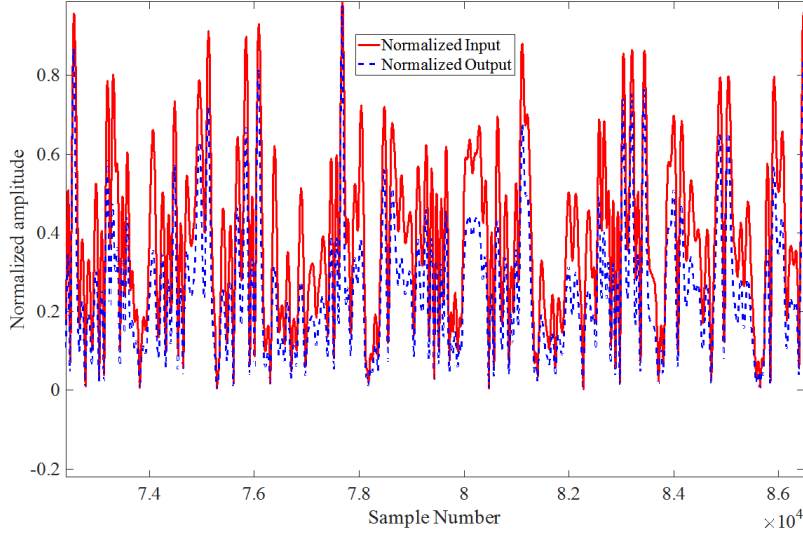


**Fig. 4.3.:** Impact of AM conversion on the amplitude of an OFDM signal subject to amplification by a non-linear amplifier

and the channel thereby resulting in a capacitive reactance between them whose reactance varies as a function of the applied voltage at the gate. Since the reactance influences the phase of the output signal, its variation with the voltage applied at the gate modulates the output phase of a PA thereby causing AM-PM distortion. This distortion is significant under large signal conditions that drive the transistor close to saturation. Elaborate information on the gate and channel characteristics of transistors may be found in references [42, 43, 44, 45]. A mathematical insight of this distortion may be obtained by considering the coefficient values in eq. 4.2 as complex numbers. From eq. 4.5, it may be inferred that if the terms  $a$  and  $c$  are represented as complex numbers with phases  $\theta_1$  and  $\theta_2$  respectively to account for the transfer reactance between the input and output ports, the output signal  $y(t)$  would also undergo phase modulation along with amplitude modulation.

The resulting equation for  $y(t)$  would be

$$\begin{aligned}
 y(t) &= \left[ a \angle \theta_1 M_1(t) + \frac{3c \angle \theta_2 \{M_1(t)\}^3}{4} \right] [\text{Sin}(\omega t + \phi(t))] \\
 &= M_2(t) \text{Sin}(\omega t + \phi(t) + \psi(M_1(t)))
 \end{aligned} \tag{4.6}$$

The impact of AM-PM conversion on a 64 QAM modulated OFDM signal after amplification by a non-linear amplifier is shown in Fig. 4.4. AM-PM conversion can also be identified in the demodulated constellation where the symbols have the appropriate vector radius, have angular displacements along the vicinity of the ideal location.

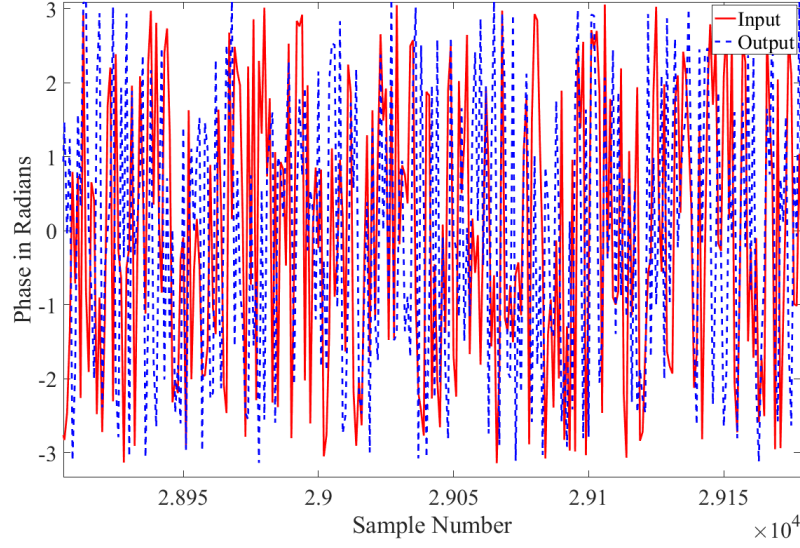


**Fig. 4.4.:** Impact of AM AM conversion on the amplitude of an OFDM signal subject to amplification by a non-linear amplifier.

**Efficiency:** This parameter is a measure of the extent of dc power consumed to produce the intended RF power at the load of a PA and is described in different way. Power Amplifier Drain Efficiency ' $\eta_d$ ' was introduced in chapter 2. It is the extent of DC power consumed to produce the measured output RF power.

$$\eta_d = \frac{P_{RF_{load}}}{P_{DC}} \quad (4.7)$$

The drain efficiency may be computed by integrating the DC power consumed over one complete cycle of the RF waveform as given by eq. 4.8.

$$P_{dc} = \frac{1}{T} \int_0^{T_c} V_{ds} I_d dt \quad (4.8)$$

where  $T_c$  is the period over which the DC power is consumed  $v_{ds}i_d$  is the product of drain to source voltage and drain current.

The overall efficiency ' $\eta$ ' refers to the ratio of the RF power delivered to the load of the PA to the sum of RF and DC input powers applied.

$$\eta = \frac{P_{RF_{load}}}{P_{DC} + P_{RF_{in}}} \quad (4.9)$$

Another figure of merit for PAs is the power added efficiency  $PAE$ . This is mathematically defined as the difference between the output and input RF powers to the DC power consumed. This figure provides an insight of the extent of RF input power needed to achieve a target efficiency at the target output power.

$$PAE = \frac{P_{RF_{load}} - P_{RF_{in}}}{P_{DC}} \quad (4.10)$$

The typical envelope of an OFDM signal with 762 QPSK modulated sub-carriers is shown in Fig. 4.5. The computed PAPR of this signal is 9.3dB i.e the peak power of this signal exceeds the average power by a factor of 8.5 times. The operating point of the RF power transistor would need to be chosen such that the amplifier's drain voltage and current have enough dynamic range to accommodate the amplitude swing i.e. the peak output power needs to be lower than the  $P_{1dB}$  compression point for linear operation. In order to accomplish this, the bias point should be chosen such that the average output power of the PA is backed off from  $P_{1dB}$  compression point by a value equal to or greater than PAPR. The available efficiency of the RFPA in the presence of back off is termed as back-off efficiency.

$$PAPR = \frac{P_{peak}}{P_{average}} \quad PAPR = \frac{V_{peak}^2}{V_{rms}^2} \quad (4.11)$$

$$PAPR_{dB} = 10 \log_{10}(PAPR) \quad (4.12)$$

**Harmonic Distortion:** This is the extent of distortion caused by the presence of harmonics of the input signal at the output due to the non linear transfer function msuch as that in eq.4.2. This is quantified by the factor Total Harmonic Distortion (THD).

$$THD = \frac{\sum_2^N P_{out_{nf}}}{P_{out_f}} \quad (4.13)$$

where  $f$  is the fundamental frequency and  $nf$  is the nth harmonic of the fundamental frequency.

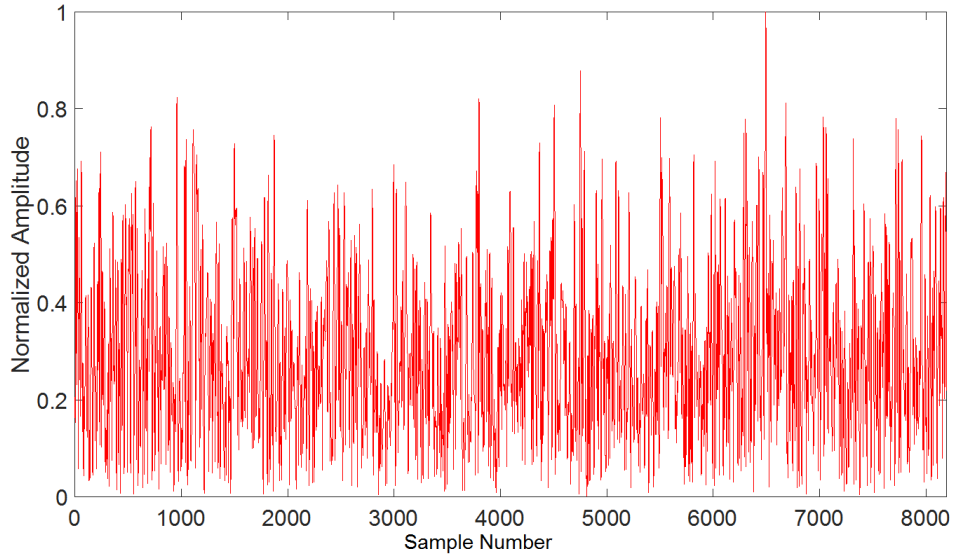


**Fig. 4.5.:** OFDM Envelope

**Intermodulation distortion:** This was discussed in chapter 2 and is repeated here for convenience. Intermodulation refers to the process of two or more signals with frequencies in the band of interest mixing (multiplying) with one another to yield parasitic signals. The parasitic signals thus generated are termed as intermodulation products. This is caused by non-linear characteristics of the gain blocks in the receiver. The frequencies of the parasitic elements. This is explained mathematically in the equations below. Let the output signal from the RF sub-system of the receiver be designated as ‘y’ and let the input signal be designated as ‘x’.

Let

$$x = A_1 \sin(\omega_1 t) + A_2 \sin(\omega_2 t) \tag{4.14}$$

$$x^2 = A_1^2 \sin^2(\omega_1 t) + A_2^2 \sin^2(\omega_2 t) + 2A_1 A_2 \sin(\omega_1 t) \sin(\omega_2 t) \tag{4.15}$$

$$x^3 = A_1^3 \sin^3(\omega_1 t) + A_2^3 \sin^3(\omega_2 t) + 3A_1 A_2 \sin(\omega_1 t) \sin(\omega_2 t) [A_1 \sin(\omega_1 t) + A_2 \sin(\omega_2 t)] \tag{4.16}$$

If the input is a linear combination of two sinusoidal signals and if the transfer function is non-linear as in eq. 4.2, the second order or square term yields parasitic components at frequencies equal to double the input frequencies, sum and difference

of the input frequencies along with a dc offset (zero frequency component) as can be inferred from trigonometric identities applied to the terms in eq. 4.16. The parasitic signal components would interfere with actual modulated RF signals intended to be received at those frequencies for demodulation in a wideband receiver. The second order term results in spurs at frequencies  $\omega_2 + \omega_1$  and  $\omega_2 - \omega_1$  is a matter of concern in systems that operate over an octave of bandwidth such as video broadcast transmitters. This can be mitigated using appropriate RF filters. The third order or cubic term would yield parasitic components at triple the fundamental frequencies and at frequencies  $2\omega_1 - \omega_2$  and  $2\omega_2 - \omega_1$ . These components fall within the operating frequency band of the transmitter in most cases and cannot be mitigated by just using an RF filter.

**Cross Modulation:** This is a parasitic behaviour where the modulation on an input signal is transferred to another signal at the the output caused primarily by third order non-linearity. This distortion however occurs between two carriers that are in different signal bands and is a matter to be considered while operating the PA in multiple bands.

**Memory Effects:** It was discussed that RF power transistors have capacitive reactances which cause AM-PM effects. All practical transistors have a finite transit time for the signals they conduct during which thermal and structural factors such as charge trapping become apparent which make the output signal dependent on the present and earlier input signals. This phenomenon is termed as memory effect. Looking at the RF power amplifier as a system, the memory effects are also contributed by bias circuits and resonant circuits in filters in addition to those arising from the operation of the RF power transistor itself. Memory effects may be classified into short term memory effects and long term memory effects. Short term memory effects last for time durations comparable to the time period of the RF signal being amplified. Long term memory effects last for time duration on the scale of the baseband. These effects can cause degradation in EVM due to dispersion of envelope components and is particularly significant with wide modulation bandwidths [46, 47].

The primary factors of short-term memory are charge storage in the transistors, non-zero transit times in transistors and impedance mismatches at the fundamental RF frequencies. The primary causes of long term memory are dynamic self-heating in power transistors, hysteresis in bias components and charge trapping in field effect transistors particularly in GaN based high electron mobility transistors (HEMTs).

The RF output of an RF power amplifier with memory can be mathematically expressed as a function of present and past inputs as shown in eq. 4.17/

$$y(t) = Ax(t) + A_1x(t - \tau_1) + A_2x(t - \tau_2) + \dots + A_nx(t - \tau_n) \quad (4.17)$$

## 4.3. Behavioural Modelling and Digital Pre Distortion

### 4.3.1. Behavioural Modelling

The internal structure of an RF power amplifier is transparent to a system designer and is usually a protected design of the vendor. It is a black box from a system perspective whose performance characteristics are critical to the design of the entire wireless transmission system. One of the ways to assess performance and to attempt to mitigate the impairments at a system level by pre-compensating the input signals is to describe the performance of the PA in the form of mathematical equations or transfer functions called behavioural models. They have proven to be very useful for modelling of non-linear radio frequency components, particularly when applying modulated signals. Carrying out wide band system characterisation using traditional circuit simulators is computationally expensive and not practical once the product is deployed in the field. Behavioural models provide a sufficiently accurate system model while greatly reducing the computational overhead. The accuracy of the model is dependant on both model parameters and available system information. To achieve an accurate system model all inputs which affect the system operation must be accounted for. There have been several modelling polynomials developed over the past five decades. In this section two popularly used polynomials namely Volterra series and Memory Polynomial are discussed in brief.

**1) Volterra Series:** Volterra series behavioural modelling is a powerful time series estimator for non-linear systems. The model uses every possible combination of terms up to a given order and for a given memory depth. It has been extensively used in both biological and financial modelling in both its continuous time and discrete form. To model RF power amplifier, we use the discrete time, base-band from the the series [73]. To date it has been successfully used to model various RF power amplification systems. The Volterra series is outlined in equations eq. 4.18

$$Y(n) = \sum_k \sum_{l_1} \dots \sum H_{(2k+1)}(l_1, l_2, \dots, l_{2k+1}) \prod_{i=1}^{k+1} X(n-l_i) \prod_{i=k+2}^{2k+1} X^*(n-l_i) \quad (4.18)$$

Where  $Y$  is the output,  $X$  is the input,  $H$  represents the Volterra coefficients,  $k$  is the order of non-linearity and  $l$  is the memory depth. The Volterra series is composed of all possible combinations of non-linear order and memory terms and as the terms  $P$  and  $M$  increase the number of weights increases rapidly. The memory depths particularly increase rapidly with increasing bandwidths of the envelope. It may be noted that (eq. 4.18) is a square matrix whose rank will increase with memory depths. This is undesirable since it defeats the objective of a behavioural model of reducing the computational complexity therefore several reduced forms of the full Volterra kernel have been presented for power amplifier modelling. It is of primary

importance to model the RFPA in order to estimate and mitigate the RF emissions in the neighbouring channels as shown in Fig. 4.2. From sec. 4.2 we know that intermodulation distortion generally results from odd order non-linear harmonics. Therefore it would just be sufficient to consider only the odd order non-linear terms on the RHS of eq. 4.18.

## 2) Memory Polynomial

$$\mathbf{y}(n) = \sum_{k=1}^K \sum_{m=0}^M \mathbf{a}_{km} \mathbf{x}(n-m) |\mathbf{x}(n-m)|^{k-1} \quad (4.19)$$

eq. 4.19 represents a simplified polynomial that can be used for behavioral modelling. This is obtained by considering only the diagonal elements of the Volterra matrix described in eq. 4.18. This polynomial is popularly used for digital pre-distortion (DPD) of RF transmitters due to reduced computational complexity and acceptable performance.

There are several other behavioral modelling kernels namely Weiner, Hammerstein, Saleh models whose details can be found in literatures [48, 49].

### 4.3.2. Digital Pre-distortion

It was found in section sec. 4.2 that the non-linear transfer functions cause distortions. This is a process of learning the mathematical model of the distortion caused and convolving the baseband input signal with the inverse of the distortion model is abbreviated as DPD. It may be inferred from section sec. 4.2 that the bandwidth of the RF output signal of a non-linear power amplifier expands into neighbouring channels. This may be viewed as the intended RF carrier being modulated by an envelope that is as wide as the overall expanded bandwidth. This implies that it is essential to have baseband components capable of generating signals with the expanded bandwidth to accomplish DPD. This will be a limiting factor in wideband radios. In order to learn the transfer non-linear function, it is essential to couple a minor sample of the RFPA's output through a receiver as shown in Fig. 4.6 and feed the signal back to the DSP after digitizing it. This implies that the receiver in the feedback path ideally requires an operating bandwidth equal to or wider than that occupied by the distorted output of the RFPA. Considering five orders of non-linearity, the bandwidth of the data converters would ideally require a bandwidth of five times the intended channel bandwidth to accomplish DPD.

**Adaptive learning** The success of DPD lies in the ability to model the non-linear transfer function as close as possible to reality. However, the non-linearity is a function of the envelope of the input signal and hence it is not feasible to estimate

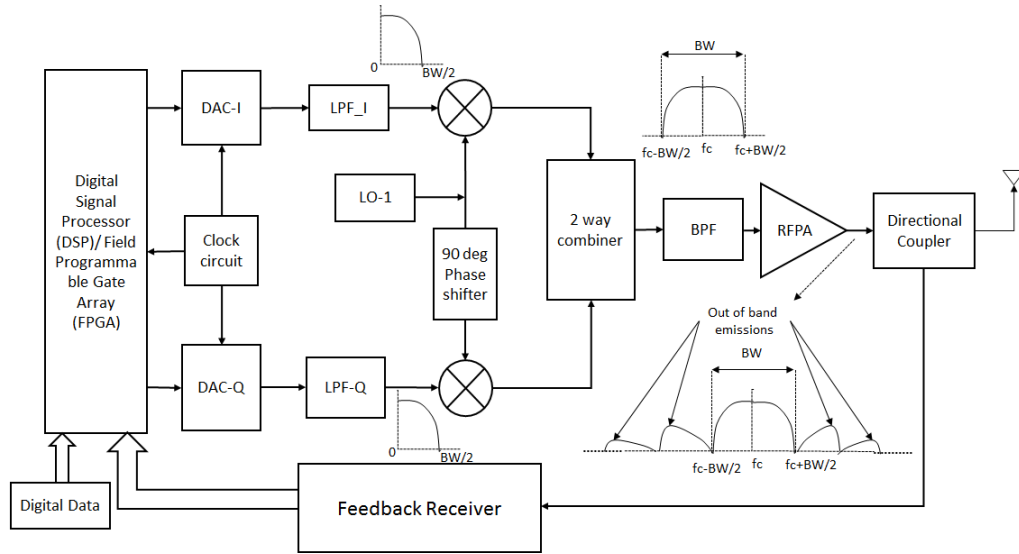


**Fig. 4.6.:** RF Transmitter with Power Amplifier and Receiver for DPD

the transfer function with a single excitation. Adaptive learning is therefore applied using adaptive filtering algorithms such as Method of Least Squares whose filter taps are coefficient values of the non-linear terms in Memory Polynomial or Volterra Series or similar mathematical kernels. These taps are tuned in an adaptive fashion using updated samples of the RFPA's responses to excitations and converge when the response meets the criteria for reduction of distortion. The typical block diagram of adaptive learning set up is shown in Fig. 4.7.

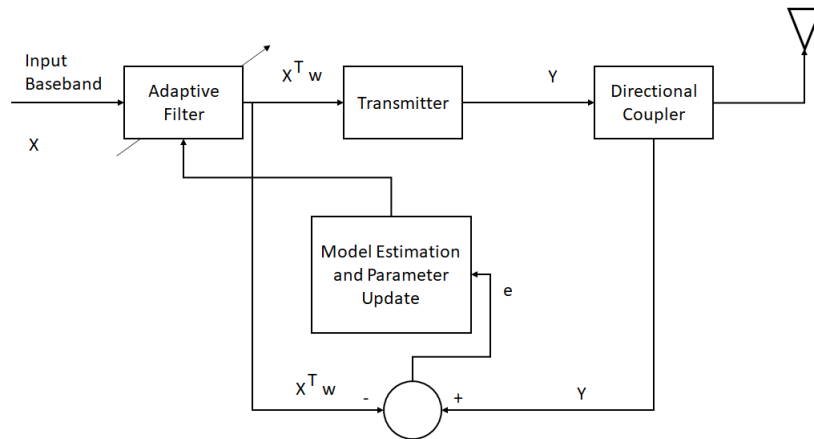


**Fig. 4.7.:** Adaptive Learning

**Method Of Least Squares** Method of Least Squares is an estimation process where the input and output signals are analysed in vector form and an optimal

solution is derived from direct matrix inversion. The least squares algorithm chooses the weights to minimise the function in eq. 4.21 which is the RMS value of the error between the actual and estimated output signals represented by eq. 4.20. The optimal weight solution is given by eq. 4.22. The process involves computation auto-correlation of the input signal and cross correlation of the input and output signals as shown in eq. 4.23 and eq. 4.24 respectively.

$$e(t) = (Y(t) - X^T(t)\vec{w}) \quad (4.20)$$

$$J(m) = \frac{1}{M} \sum_{t=1}^M (Y(t) - X^T(t)\vec{w})^2 \quad (4.21)$$

$$w_{opt} = R_{xx}^{-1} P_{dx'} \quad (4.22)$$

$$R_{xx} = \frac{1}{M} \sum_{t=1}^M (X(t)X^T(t)) \quad (4.23)$$

$$P_{dx'} = \frac{1}{M} \sum_{t=1}^M (y(t)X(t)) \quad (4.24)$$

The optimum co-efficient set is guaranteed to be extracted as long as the dataset is representative of the device under test (DUT). This depends on the accuracy of the feedback path whose frequency response needs to be equalized through calibration as detailed in chapter 3 failing which the weights will not converge. The main drawback with the least squares approach is the computational complexity in the parameter extraction operation. The size of the matrix X is determined by the number of samples in the input - output data set as well as the number of coefficients in the behavioural model.

## 4.4. Power Amplifier Classes

A brief introduction to some typically used classes and modes of operation for power amplifiers are described in this section. It is not in the scope of this thesis to provide elaborate theories for design of RFPAs. Interested readers are referred to [50] and [51] for detailed theories and guidelines on RFPAs.

An RFPA's class of operation may be described by the duty cycle over which it conducts the signal. An RF carrier signal is a sinusoidal function whose duty cycle 360 degrees. This in turn depends on the bias of the RF power transistor. Typical DC characteristics of an RF transistor is shown in Fig. 4.8. The class of operation is depends on when the transistor actually starts drawing current from the drain supply when an RF input is applied. Typical parameters affected by the class of operation of a PA are Linearity, Efficiency, Bandwidth and Gain. These parameters were defined in chapter 2.

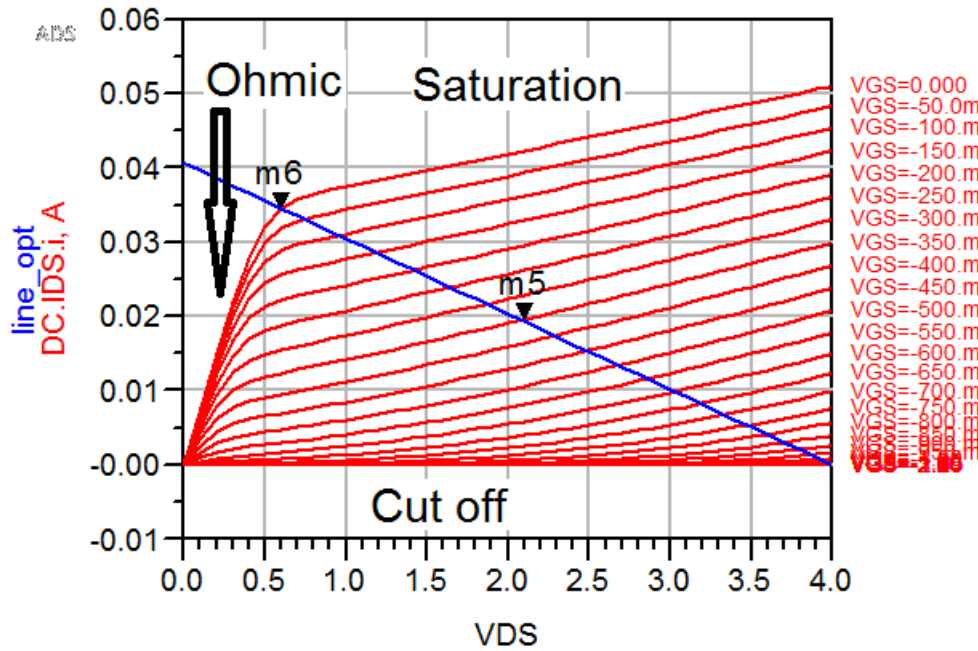
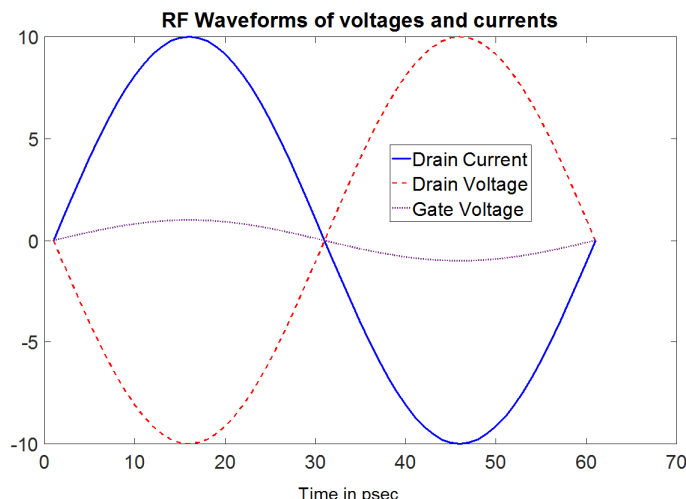


Fig. 4.8.: Typical DC bias characteristics of RF power transistor

**Class A operation:** The PA conducts the signal for the entire 360 degrees of the input signal. Typically, the bias current is set at half of the maximum current value so as to accommodate a complete sinusoidal variation of the output signal throughout its 360 degrees of conduction phase. This class is the most linear of all PA configurations since it conducts the entire envelope of the signal without saturation. The typical waveform relations between RF voltages and currents in a class A amplifier is shown in Fig. 4.9.

This mode of operation will draw a DC current equal to half of the maximum value even in the absence of an RF input signal and therefore the theoretical maximum efficiency of a Class A amplifier is only 50% as can be evaluated from integral in



**Fig. 4.9.:** Waveforms of RF voltage and current in a Class A Amplifier

eq. 4.8. This operating point would be in the vicinity of the point m5 on the DC loadline shown in Fig. 4.8. The theoretical efficiency is only achievable for a constant envelope signal. Practically an envelope modulated signal would exhibit peaking in its amplitude and hence a Class A amplifier’s efficiency would be reduced further due to back off from the saturated power output.

**Class B and AB operation:** In Class B , the PA conducts the applied RF signal for only half of the duty cycle i.e. for only 180 degrees. The bias point is chosen to be in the cut-off state so that the transistor does not conduct or draw current when the input signal amplitude is below 0V i.e in the negative half cycle.

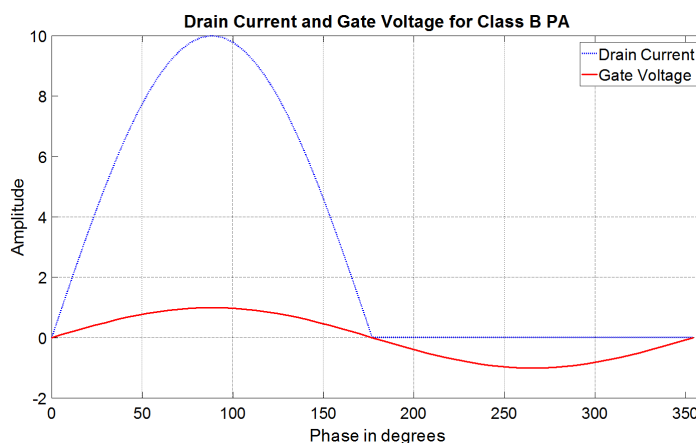


**Fig. 4.10.:** Waveforms of RF gate voltage and drain current in a Class B Amplifier

In this class, the theoretical maximum efficiency of the PA as calculated from eq. 4.8 is 78.4%. This is an improvement over Class A in efficiency but at the cost of non-

linearity. As the output waveform is clipped, it is rich in harmonics which need to be terminated. The filtering circuit needed to suppress the harmonics implies reduction in operational bandwidth relative to Class A.

A hybrid between Class A and Class B modes is the Class AB where the transistor is allowed to conduct the signal for more than 180 degrees of duty cycle. This mode provides an improvement in efficiency over Class A and an improvement in linearity over Class B. This is the most popular class of operation for medium power applications. The theoretical efficiency is below 78.4%

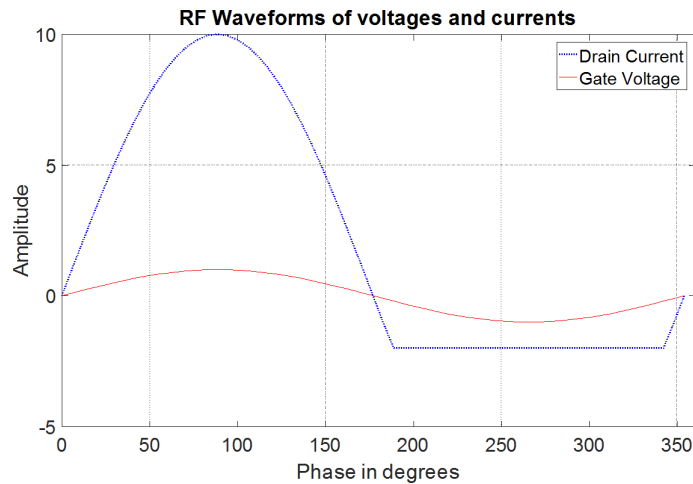


**Fig. 4.11.:** Waveforms of RF gate voltage and drain current in a Class AB Amplifier

**Class C** In this class, the transistor in the PA conducts the signal for less than 180 degrees. The transistor is biased in the cutoff region of its transfer characteristics. A finite portion of the input signal is involved in actually turning on the device. The reduction in conduction angle implies a further reduction in DC power consumed for a target RF output power and hence higher power added efficiency compared to Class A and Class B. But the class is less linear making it suitable only for constant envelope modulated signals such as QPSK, 8PSK, FSK, FM and constant envelope PM. Since a finite portion of then input signal is involved in actually turning on the transistor, the power gain is reduced compared to Class A and Class B. Typical gain of a single stage Class C power amplifier is below 10 dB.

All the classes discussed until now are continuous conduction modes i.e. the voltages and currents vary smoothly following the input sinusoidal curve over a limited range. It may be inferred from the integral in eq. 4.8 that the efficiency can be maximized if the value of this integral is minimized or made zero. This is theoretically achieved by operating the RF power amplifiers in swithing modes such as Class D, Class E, Class F and Class S. The input is hard switched such that the amplifier minimizes operation linear region for as little time as possible. The involves operating the

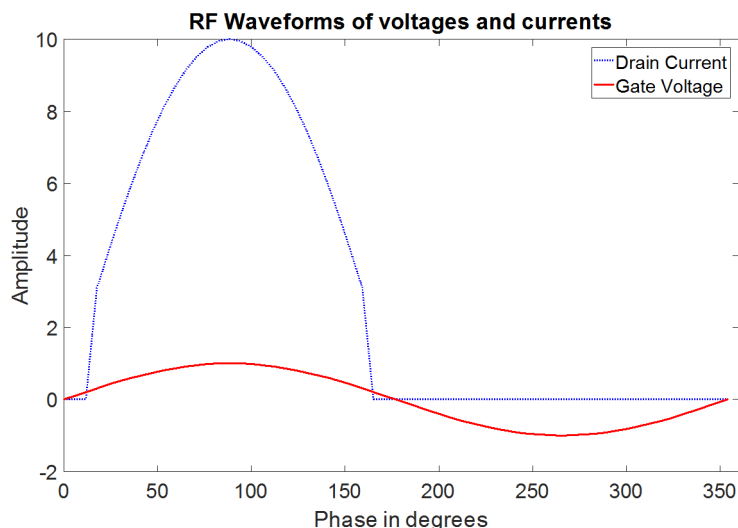


**Fig. 4.12.:** Waveforms of RF gate voltage and drain current in a Class C Amplifier

transistor in switch mode where it either conducts fully allowing maximum current to flow from the drain to source terminal or does not conduct at all presenting the full dc voltage across the drain and source terminals with zero current flowing between them. This makes the voltage and current waveforms mutually exclusive i.e. they have no overlap and hence no power is dissipated. This implies a theoretical efficiency of 100%. Discussion in this section is limited to Class E and interested readers are referred to literature [50].

**Class E** A typical circuit schematic of a Class E amplifier is shown in Fig. 4.13. It is a single transistor switching amplifier which conducts current for 180 degrees of the input switching waveform. The parallel capacitor  $C_p$  connected between the drain and source terminals is initially charged to the DC bias voltage applied to the drain terminal. When the input signal is applied to the gate, the transistor acts like a switch and draws maximum drain current during the positive half cycle or first 180 degrees of the input waveform forcing the voltage between the drain and source terminals of the transistor to zero volts. This ideally makes the current flowing into the load zero. The capacitor that was charged before the application of the signal now discharges through the channel of the transistor. During the second half cycle of the input waveform, the transistor is cut off and the capacitor gets charged again. This operation of charging and discharging ideally results in a switching waveform at the drain terminal at the operating RF frequency as shown in and causes an alternating current (AC) to flow to the load at the fundamental RF frequency. The RF choke presents a large impedance at the RF frequency. The switching signal is rich in harmonics. The resonator tuned to the fundamental RF frequency presents low impedance at the fundamental frequency and high impedances at the harmonic frequencies thereby passing the fundamental component of the waveform. Since the

resonator has a high quality factor, it rejects the higher harmonics present in the switching waveform thereby yielding a sinusoidal waveform at the load.

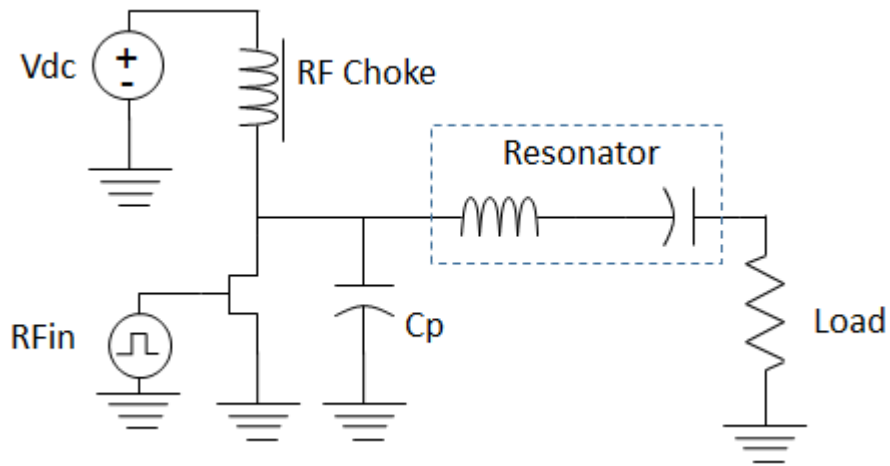


Fig. 4.13.: Class E Amplifier Schematic

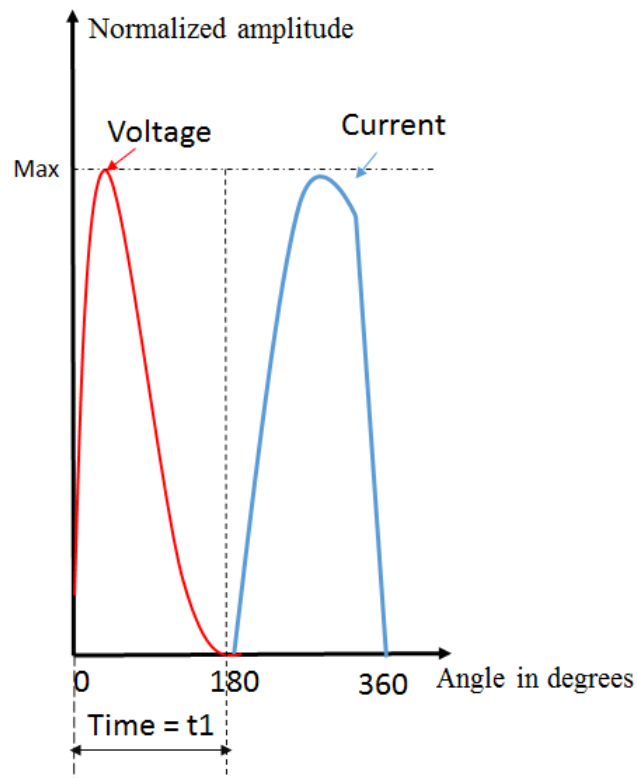


Fig. 4.14.: Typical Class E Drain-Source Voltage and Current Waveforms

$$\begin{cases} V_{sw}(t_1) = 0 \\ \frac{dV_{sw}}{dt} = 0|_{t=t_1} \end{cases} \quad (4.25)$$

Typical voltage and current waveforms between the drain and source terminals are shown in Fig. 4.14. To ensure that there are no switching losses the amplifier must satisfy the switching conditions in eq. 4.25 that state that the voltage and the derivative of the voltage must be zero when the switch closes.

It may be inferred that the Class E amplifier works on the principle of hard switching between open and close states where the current and voltage never overlap and can theoretically provide a drain efficiency of 100%. But practically, this figure drops to around 81% due to power in the harmonics which are grounded. This class is ideally suited for constant envelope operation. It will be shown that this class can be used for operation in a specific topology called Outphasing to accomplish power amplification of envelope modulated signals. In order to eliminate the switching losses, the amplifier must satisfy the switching conditions in eq. 4.25 that state that the voltage and the and its derivative must be zero when the switch closes.

## 4.5. Power Amplifier Topologies

A selection of operating classes of RF power amplifiers were discussed briefly in the previous section. The amplifiers in those classes may be operated as individual modules or may be operated together with two or more modules to accomplish specific tasks. It is observed that a Class AB amplifier is more linear than a Class C amplifier but a Class C amplifier is more efficient. It may be inferred from the previous subsection that non-linear power amplifiers which operate at their saturated power levels are the most efficient due to the reason that the amount of power dissipated in lossy components is minimized. It was also seen that the Class E amplifier is the most efficient of all the classes discussed. A number of topologies have been developed to achieve both linear and efficient amplification using multiple amplifier stages operating in branches of a larger amplification system namely Doherty, Outphasing, Envelope Tracking and Envelope Elimination and Restoration. Outphasing and Doherty are discussed in brief in the next subsections. Interested readers are referred to literatures in [50] for elaborate information on the other topologies.

### 4.5.1. Introduction to Outphasing Amplifiers

This configuration is popularly termed as Linear amplification using Nonlinear Components (LINC) where two amplifiers are fed with constant envelope phase modulated signals and their outputs are combined in the appropriate phase relation to

produce an envelope modulated amplified signal. This task is accomplished by converting a complex envelope modulated signal into two constant envelope phase modulated signal which when summed together would restore the envelope. This topology has the unique advantage of constant envelope in the RF signal to be amplified by the RF power amplifier and hence high efficiency classes such as Class C and Class E may be used.

The mathematical description of the outphasing action is described in the paragraph below.

Let the complex envelope of a modulated signal  $S_{in}(t)$  in each model be written in vector form

$$S_{in}(t) = A(t)e^{j\theta(t)} \tag{4.26}$$

where  $A(t)$  is the time varying instantaneous amplitude and  $\theta(t)$  is the time varying instantaneous phase. Let the required power gain be designated ' $Gt$ '. Let us define a variable  $\psi(t)$  such that

$$\psi(t) = \cos^{-1} \left( \frac{A(t)}{\max(A(t))} \right) \tag{4.27}$$

using the value of  $\psi(t)$  from eq. 4.27

Now if two constant envelope phase modulated signals  $S_1(t)$  and  $S_2(t)$  are generated with unity amplitude i.e. fixed amplitude of '1' as in equations below

$$S_1(t) = e^{j\{\theta(t)+\psi(t)\}} \tag{4.28}$$

$$S_2(t) = e^{j\{\theta(t)-\psi(t)\}} \tag{4.29}$$

If both  $S_1(t)$  and  $S_2(t)$  are amplified by a constant factor of  $\frac{G}{2}$  and summed, the operation yields

$$\frac{G}{2}S_1(t) + \frac{G}{2}S_2(t) = \frac{G}{2}[2\cos\{\psi(t)\}]e^{j\theta(t)} = G.A(t)e^{j\theta(t)} \tag{4.30}$$

The description in eq. 4.30 implies that two constant envelope phase modulated signals termed as outphasing signals if combined in the appropriate phase can yield

the required constant envelope modulated signal. This enables the use of high efficiency amplifier classes such as Class E.

The typical block diagram of an outphasing amplifier is shown in Fig.4.15. The input signal is fed to a signal component separator (SCS) where the two constant envelope phase modulated signals i.e. outphasing signals are generated and applied to high efficiency amplifiers whose outputs are summed together to produce an amplified version of the original complex envelope modulated signals.

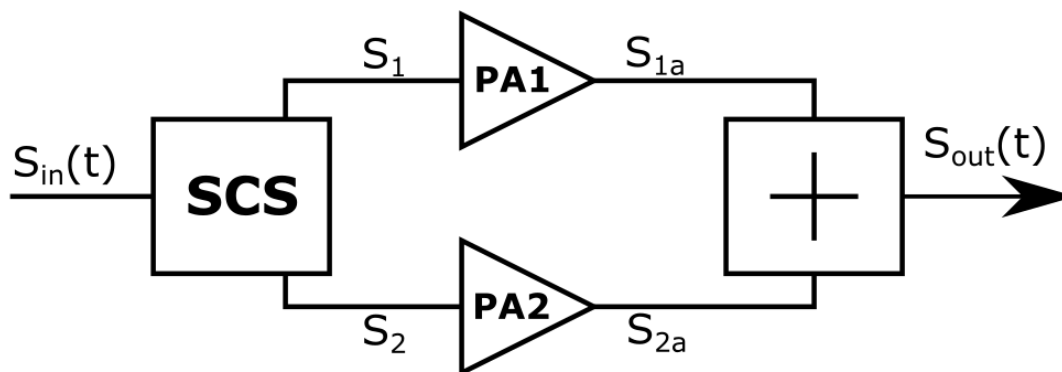


**Fig. 4.15.:** Block Diagram of Outphasing Amplifier

The two amplified outputs are combined to produce the amplified signal with the original modulation envelope. The integrity of gain and phase of the amplified constant envelope phase modulated signals across the bandwidth occupied by the phase modulated signals are critical to quality of the output of the combiner. Since it is not feasible to generate the inverse cosine of amplitudes in the analogue domain, practically most outphasing amplifiers operate with digitally generated outphasing signals which are up-converted to the carrier frequency and applied to the high efficiency amplifiers. Since each branch literally consists of a complete transmit chain from baseband to the RF power amplifier, the whole system may be designated as an Outphasing Transmitter.

The combiner at the output of the amplifiers may be of two types i.e. an isolating combiner such as a Wilkinson combiner or a non-isolating combiner i.e. Chireix combiner. This will be explained in the next sub-section. Since the outphasing signals are constant envelope phase modulated signals, they occupy a bandwidth as wide as ten times the bandwidth of the original complex envelope modulated signal. This limits the application to channel bandwidths that are a tenth or lower than that supported by the fastest available data-converters. Nevertheless, the advantages in efficiency are hard to ignore.

The magnitude plots of FFT of a 5 MHz wide WCDMA signal sampled at 307.2 MSPS and the outphasing signals generated from it are shown in Fig. 4.16 Fig. 4.17

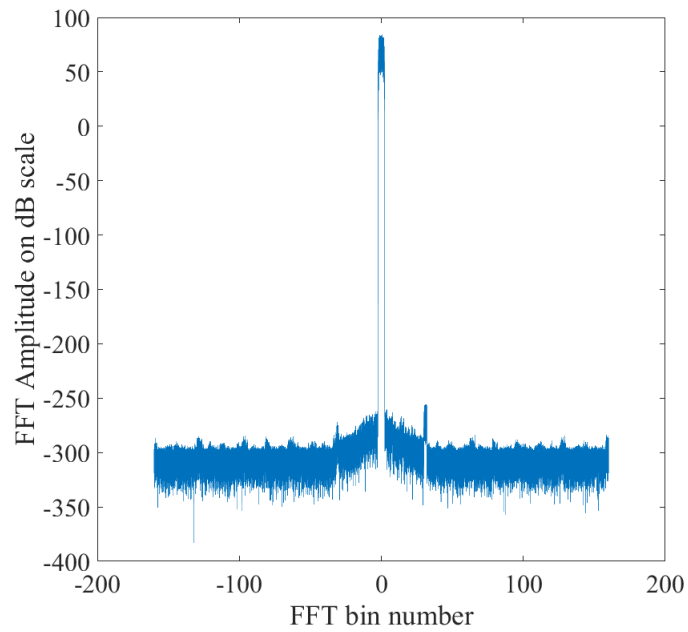


**Fig. 4.16.:** Spectrum of Original WCDMA signal

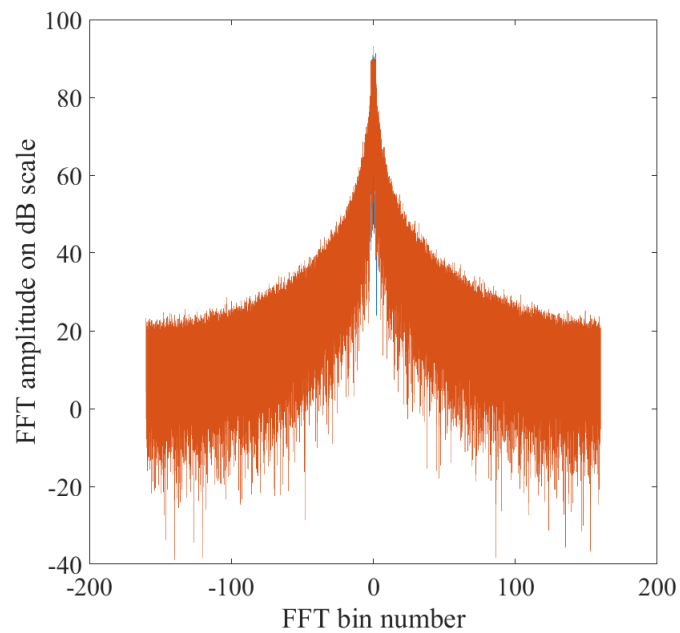


**Fig. 4.17.:** Spectrum of outphasing signals generated for the WCDMA signal

The time domain constellation plot of an ideal outphasing signal would represent a circle due to constant envelope and phase variations from 0 to 360 degrees as shown

in Fig. 4.18.

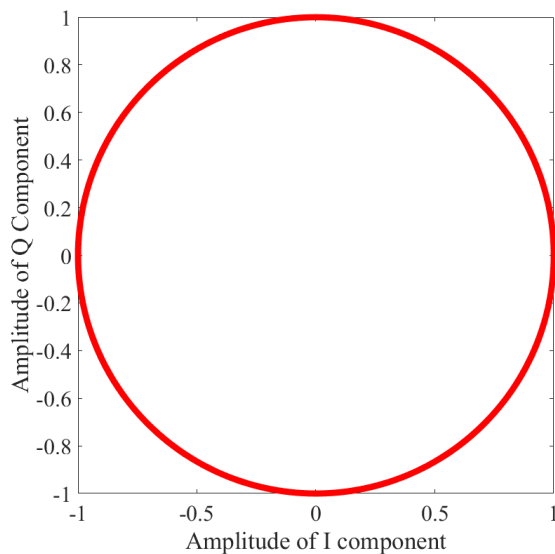


**Fig. 4.18.:** Outphasing Constellation

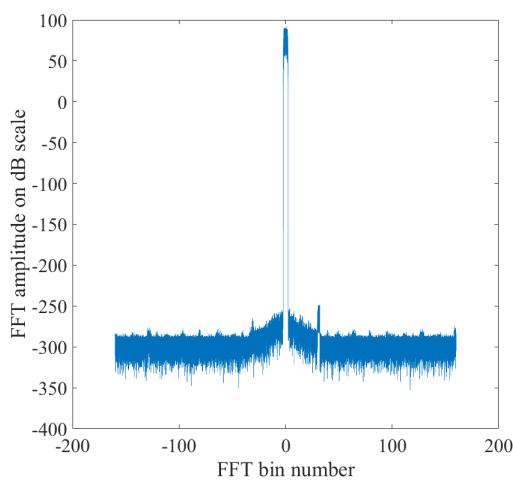


**Fig. 4.19.:** Spectrum of the ideally re-combined outphasing signals

In order to recombine the signal after amplification stage isolated and nonisolated combiners are widely used. Isolated combiners provide very high linearity of the output signal. However, since a lot of power is dissipated in the resistor these combiners have very low efficiency. Nonisolated combiners, such as Chireix combiners, were initially introduced in [52]. It has been shown that these combiners can significantly improve efficiency of LINC systems at the cost of linearity [53].

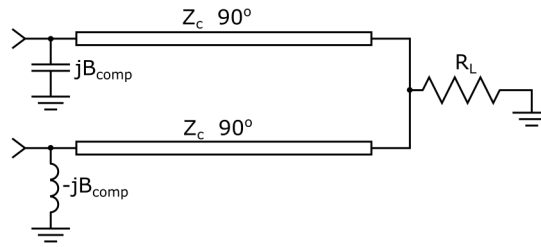


**Fig. 4.20.:** Structure of nonisolated Chireix combiner.

Outphasing amplifiers with isolated, non-isolated and partially isolated combiners have been presented in the literature. However, since the use of an isolating resistor degrades the power efficiency [53], non-isolated combiners with compensating reactive elements have more recently found a wider application in outphasing transmitters. Outphasing PAs with non-isolated combiners show significant nonlinear behaviour and phase distortion due to amplitude imbalance between branches [54]. It has been shown that the primary source of this distortive behaviour is the load modulation effect in the outphasing PA branches.

#### 4.5.2. Introduction to Doherty Power Amplifier

A Doherty power amplifier consists of a Class AB carrier amplifier module and a Class B or Class C peaking amplifier module in two parallel branches with their outputs combined using a non-isolated RF combiner [50]. The block diagram of a typical Doherty Amplifier is shown in Fig. 4.14. The amplifier was invented in 1936 and is named after the inventor William H. Doherty [55].

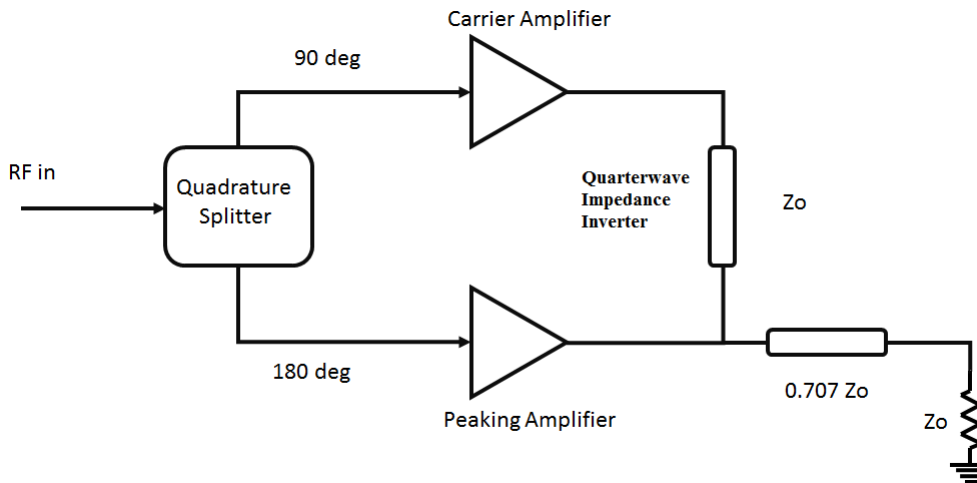


**Fig. 4.21.:** Doherty Amplifier Block Diagram

When an envelope modulated input signal is applied, the carrier amplifier begins to conduct depending on the amplitude of the envelope, injects current  $I_1$  into the

load and its output power rises in a linear fashion until the  $P_{1dB}$  compression point is reached where it enters saturation. At this stage, the carrier amplifier is most efficient. The peaking amplifier now turns on and begins to inject current  $I_2$  into the load. The turning on of the peaking amplifier now modulates the load impedance seen by the carrier amplifier. Let the output impedance seen by the carrier amplifier be  $Z_1$  and that seen by the peaking amplifier be  $Z_2$  and let the load impedance be  $Z_L$  which is matched to the system impedance  $Z_0$ .

In the absence of impedance inverter, the output impedance seen by the carrier and peaking amplifiers would be as in eq. 4.31 and eq. 4.32 respectively.

$$Z_1 = Z_L \left( 1 + \frac{I_2}{I_1} \right) \quad (4.31)$$

$$Z_2 = Z_L \left( 1 + \frac{I_1}{I_2} \right) \quad (4.32)$$

If  $I_1$  and  $I_2$  are in phase, it causes the effective output impedance  $Z_1$  to increase and the voltage across the load also increases. Now, the efficiency of the carrier amplifier can be increased if the voltage swing across its output impedance is maintained constant while the peaking amplifier conducts. This task is accomplished by the quarter-wave impedance inverter which would reduce  $Z_1$  if  $I_1$  and  $I_2$  are in phase and vice versa. The load impedance of the carrier amplifier is hence modulated by the output current of the peaking amplifier. The topology yields two efficiency peaks i.e. first one when the carrier amplifier enters saturation and peaking amplifier is still on conducting and again while both the amplifiers are in saturation. In a symmetric Doherty amplifier, the maximum output power is due to equal contributions from both peaking and carrier stages. A plot of the efficiency curve of a Doherty amplifier as a function of output power is shown in Fig. 4.22.

Elaborate set of design guidelines and accompanying mathematical relations have been provided in literatures [56, 57, 58, 59]. In [59], an extensive research on a variety of Doherty power amplifier (DPA) architectures that were introduced since the original idea of a Doherty amplifier was invented by William H Doherty in 1936 [55] is presented. This analysis includes Multistage, N-way and dual Doherty power amplifiers digitally driven dual input Doherty architecture, etc. In [49], 3-way digitally driven amplifiers and its advantage in achieving greater performance over a wide fractional bandwidth of over 50% is presented. In [60], a 3-way Doherty power amplifier is designed as an integrated structure in a die assembly. Further state of the art designs are presented in literatures [61, 58, 62, 63, 64, 65, 66, 67].

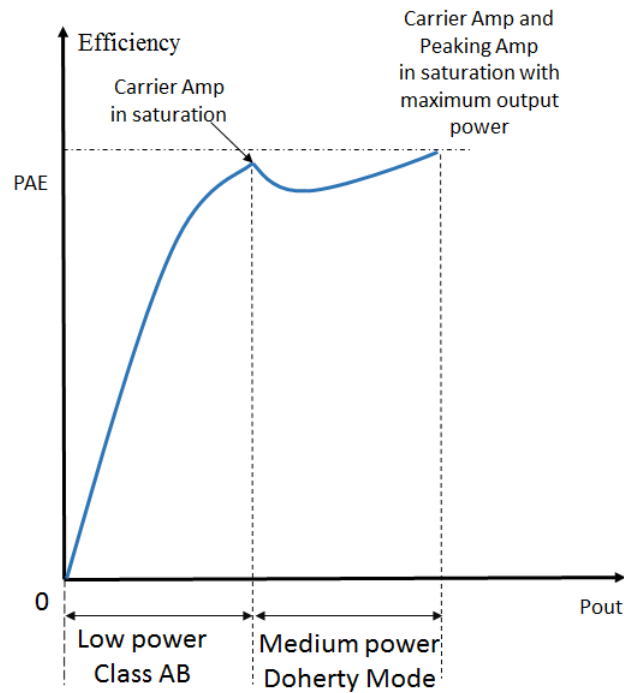


Fig. 4.22.: Doherty Amplifier Efficiency curve

## 4.6. Novel Contributions in the area of RF Power Amplifiers

### 4.6.1. Primary Contribution: Calibration Of RF Signal Paths In Outphasing Amplifiers

This corresponds to item number 2 in the list of publications. The equations for the outphasing operation were described in the previous section. It may be inferred that balance of gain and phase responses over the two outphasing branches is critical to performance. A digital outphasing transmitter would effectively need two inphase (I) and two quadrature (Q) paths i.e. one I-Q pair per each outphasing branch. This implies a total of four DACs, four low pass filters and four mixers. The constituent frequency components of outphasing signals are susceptible to parasitic effects in practical RF hardware such as amplitude ripple and tilt, group delay along with frequency dependent gain and phase offsets between the paths. A novel wideband calibration technique using truncated chirp pulses was described in chapter 3. The same technique was used to calibrate the four RF signal paths of an outphasing transmitter prior to the connection of the RF power amplifiers using a vector signal analyzer as the reference receiver.

The spectrum screenshots of the output of the outphasing modulator before and

after calibration are shown in Fig. 4.25. A isolated combiner is used during the calibration process.

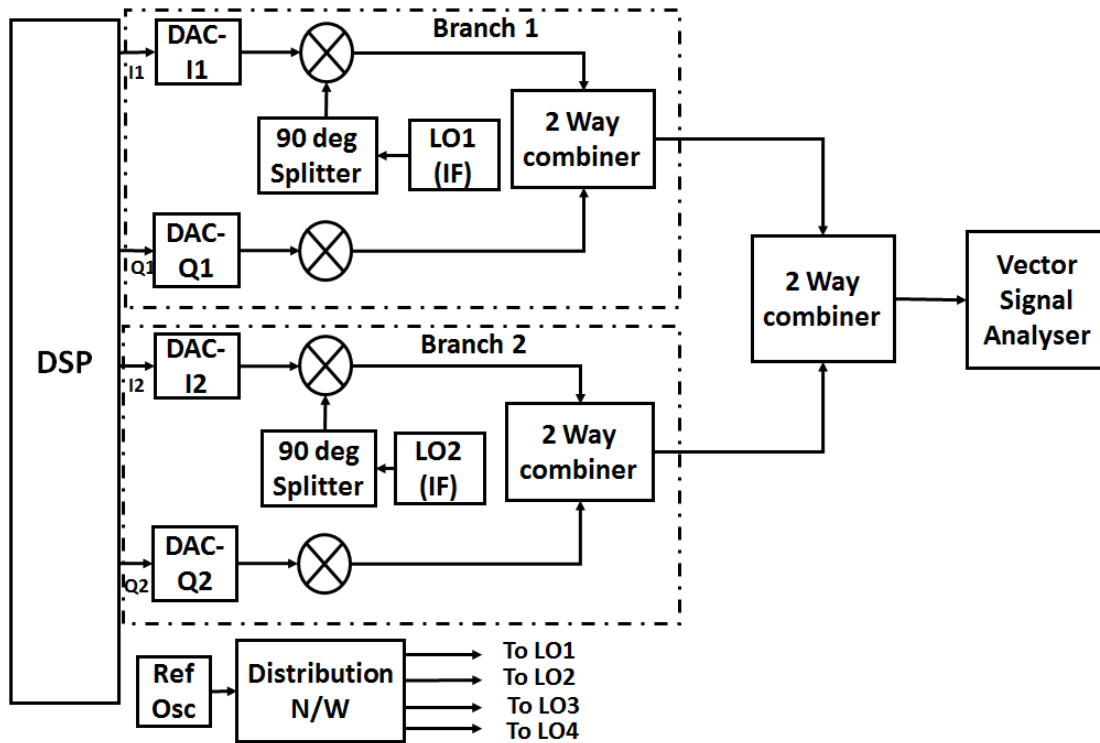
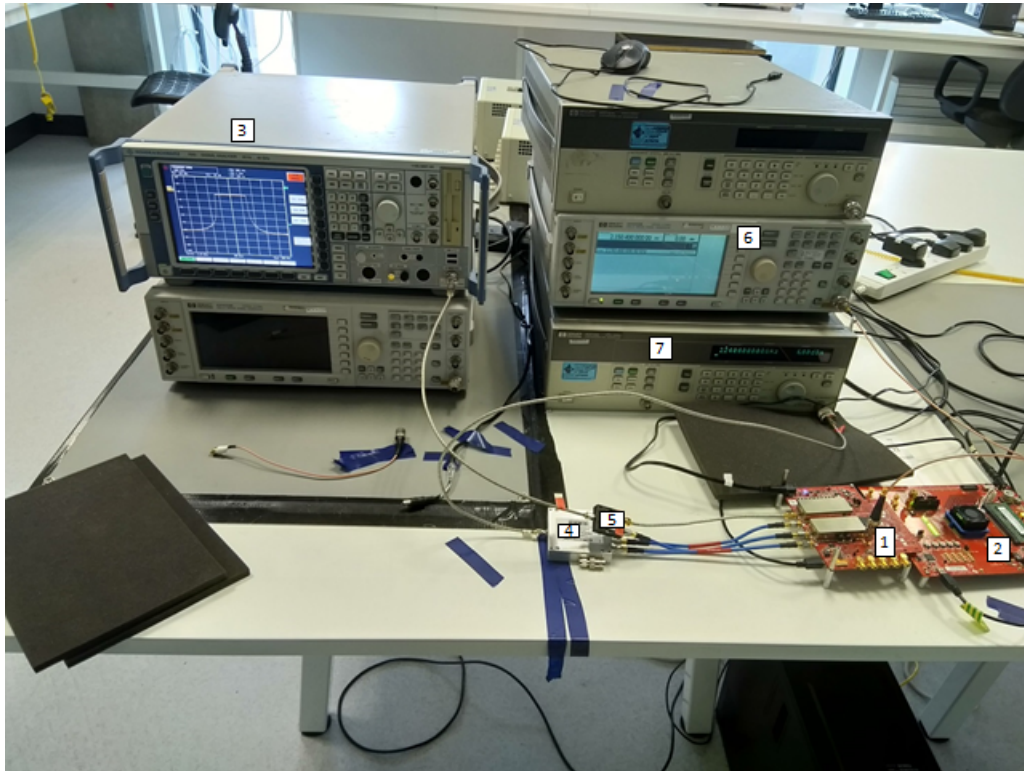


Fig. 4.23.: Outphasing Modulator Calibration Setup

A test bench was set up consisting of a computer (PC) running the tool MATLAB, an evaluation board TSW30SH84 from Texas Instruments consisting of a quad DAC module DAC34SH84 with LVDS interface to connect to a digital interface board TSW1400EVM. A vector signal analyzer (VSA) FSQ-40 from Rohde and Schwarz was used as a reference receiver. The VSA was capable of demodulating an input modulated signal up to a bandwidth of 100 MHz. The outputs of DAC1 and DAC2 were treated as an IQ pair and connected to I and Q inputs of a vector up-converter module TRF3705 designated as UC1\_IF. The outputs of DAC3 and DAC4 were treated as the second IQ pair and connected to I and Q inputs of another vector up-converter module TRF3705 designated as UC2\_IF. The outputs from the DACs were up-converted to 2.24 GHz and the output. The reference oscillators of the onboard clock source module LMK02808 were synchronized with the reference output of the VSA after sufficient warm up time. A picture of the workbench is shown in Fig. 4.24.



**Fig. 4.24.:** Work Bench with DAC, IF up-converter and RF test instruments

Mismatches in gain or phase responses of the outphasing branches over a bandwidth of 100 MHz had an adverse impact on the spectrum of the combined signal. The 4 paths of the LINC transmitter's modulator built with the quadrature modulator pairs described above were calibrated at zero IF over a bandwidth of 100 MHz. LINC baseband signals were generated for a 5 MHz WCDMA baseband signal with a power crest factor of 7dB. The LINC signals occupied a bandwidth over 100 MHz due to bandwidth expansion in the resulting phase modulated signals with high modulation index. Phase errors were deliberately introduced using LO feed cables of non-uniform lengths between the paths to replicate a more challenging use case. The calibration was performed using both chirpstimuli in two different trials at a sample rate of 307.2 MSPS, center frequency of 2.24 GHz at a bandwidth of 100 MHz. An overall improvement of 36 dB was observed in the adjacent channel power rejection as shown in Fig. 4.25 after calibration with Chirp stimulus. The sample rate of the ADC in the VSA was set equal to that of the DACs.

An overall improvement of 27 dB was observed in the adjacent channel power rejection as shown in Fig. 4.25 after calibration with truncated sinc stimulus. In a real field case scenario, the truncated sinc stimulus cannot be applied to an outphasing transmitter due to extremely high PAPR in the order of 16 dB and the amplifiers in the outphasing branches are supposed to be Class E amplifiers. This case was just to study the difference in the quality of calibration that could be obtained from

Chirp and truncated Sinc stimuli.

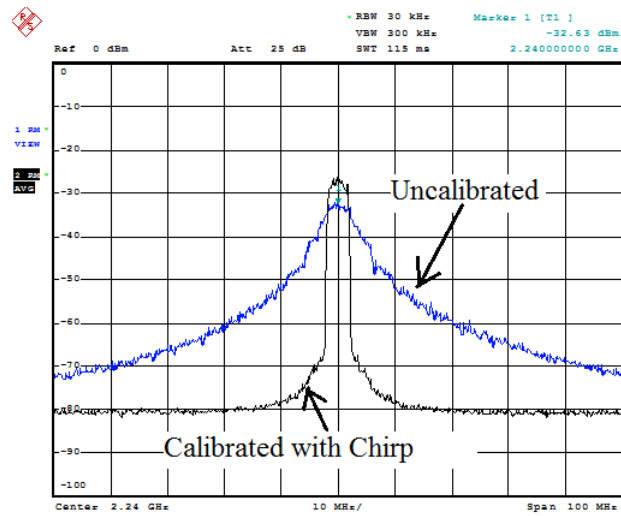


**Fig. 4.25.:** Outphasing transmitter Spectrum before and after calibration with Chirp stimulus

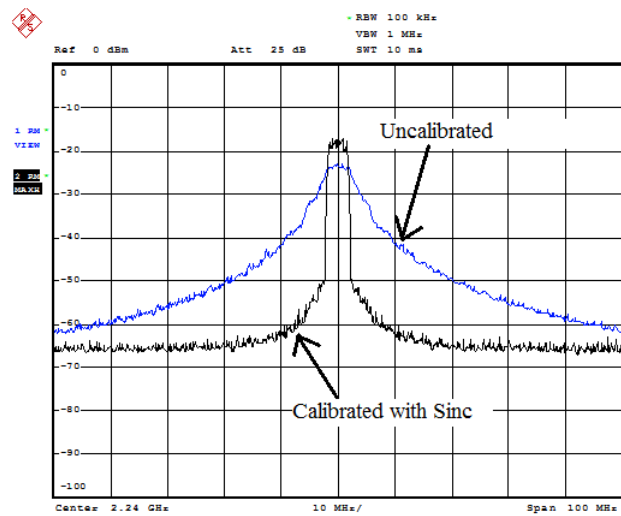


**Fig. 4.26.:** Outphasing transmitter Spectrum before and after calibration with Sinc stimulus

It can be inferred that the response to the chirp stimulus provides information on the bandwidth dependent impairments for digital calibration. The reason for this is that the SNR requirement for sensing the response to a truncated Sinc stimulus is higher than that needed for a Chirp stimulus due to high peak to average ratio as described in Chapter 2 and Appendix B.

## 4.6.2. Secondary Contributions:

RF Power Amplifier design was not the primary objective of the research work undertaken. Secondary contributions were made in the area of RF Power Amplifiers in collaboration with co-researchers where the role involved calibration of the RF signal paths for Outphasing and Doherty amplifiers using the techniques described in chapter 2 along with contributing towards design review, experimental validation, and editing the literature drafted for publication of items 5, 6, 12 and 13 in the list of publications. The description of these contributions in this thesis are limited to abstracts and inferences in order to avoid duplication of data presented in the theses of the respective primary contributors. Interested readers are redirected to the respective publications for detailed information.

### 4.6.2.1. Design of N-way Doherty Amplifiers

This work corresponds to item 5 in the list of publications.

**Abstract:** With an increasing interest in backwards compatibility for existing satellites and the emerging satellite markets, wireless transceivers at Ku band are increasing in popularity. This work presents the design of a four-way digitally driven Doherty amplifier, aimed at applications in Ku-band. Single tone measurements indicate a maximum drain efficiency of 53.4% at a maximum of 19.2 dBm output power. The final output power can readily be adjusted by changing the biasing in each stage accordingly. The N-way Doherty power amplifier was tested with an 800 MHz bandwidth, 64 QAM test signal aimed for future communication signal standards. An analysis of this configuration has also been performed for 2-way, 3-way and 4-way architectures.

**Inference:** A design to implement an N-way Doherty power amplifier for Ku band applications has been presented in this work. The performance of the N-way design was extensively tested using unmodulated single-tone and a 64 QAM signal with 800 MHz bandwidth. With the emergence of low-earth orbit satellite constellations where a large power output is not a requirement, the presented design provides a viable option for ground station transmission as shown by its performance within spectral mask limits for satellites communications.

### 4.6.3. Behavioral Modelling of Asymmetric Doherty PAs

This work corresponds to item 6 in the list of publications.

**Abstract:** Behavioral models are intended as high level mathematical descriptions which require less computational effort to simulate behavior compared to physical or circuit level equivalent models. When designed and dimensioned properly they are well suited to concise characterization of power amplifiers under different operating conditions. In this work a comparison of the relative performance of several behavioral models for modelling an asymmetric Doherty power amplifier was performed for their use in distributed arrays.

**Inference:** In summary a tuned asymmetric Doherty PA was fabricated and tested using an LTE test signal, which was then characterized using four different behavioral modelling techniques namely AM/AM & AM/PM, classic Volterra series and piecewise Volterra series. The piecewise Volterra series provides a more accurate representation of PA behavior compared to the other approaches. This level of precision and fast modelling proves their value in using behavioral models in testing a several advanced DPA structures in a more complex integrated structure such as a distributed array.

Though this validation was not carried out on a millimetre-wave device, it gave an insight of the extent of the extent to which the proposed behavioral models tallied with the actual performance. The validation was carried out at a carrier frequency of 930 MHz with a modulation bandwidth of 20 MHz. This corresponds to a fractional bandwidth of 602 MHz at 28 GHz. The validation could not be carried out at millimetre wave frequencies due to non-availability of devices at the time of conducting the validation but a similar fractional bandwidth was tested.

### 4.6.4. Nonlinearity Modeling of Chireix Outphasing PowerCombiner Under Amplitude Imbalance

This corresponds to item 13 in the list of publications.

**Abstract:** This work proposes a concise standalone model for Chireix power combiner. The model is based on the analysis of the nonlinear behaviour of a Chireix power combiner under amplitude imbalance. The generalised equations for input impedance of Chireix combiner branches excited by signals with different amplitudes are derived. The results predicted by the model were validated using both commercial high frequency circuit simulations and experimentally measured results. As a result the proposed model serves two purposes. For one it can be used directly in a larger circuit simulation to predict the performance of an outphasing power amplifier. It can also be used as the basis for a linearization strategy for outphasing power amplifiers.

**Inference:** A new analysis of Chireix power combiner has been presented that is used to derive a model which can describe the effect of amplitude imbalance between two branches. Explicit analytical expressions for output voltage are derived. The derived model was validated using simulations in commercial high frequency simulator and experimental measurements. Plots and figures of merit for goodness of fit have been provided for a range of amplitude imbalance levels and show good agreement with the experimentally measured performance.

#### 4.6.5. Phase only Pre Distortion of Outphasing Amplifiers

This corresponds item 12 in the list of publications.

**Abstract:** Efficient and linear power amplifiers (PA) are an essential part of forthcoming 5G wireless systems. Outphasing class-E PAs offer high power efficiency and an option for higher efficiency cellular networks. However, they employ signal component separators, which split the signal into two paths. In order to efficiently recombine the signal, nonlinear power combiners are used. This work proposes a novel phase-only predistortion technique for outphasing class-E PAs. The predistortion coefficients can be extracted based on AMAM characteristics of the output signal and an analytical model of an outphasing Class E PA. The proposed technique has been validated by simulation of an outphasing power amplifier in ADS Ptolemy software. It is shown that applying this technique to a 16QAM OFDM modulated signal with 20 MHz bandwidth improves error vector magnitude (EVM) from 10.39% to 2.43% compared to the signal without predistortion.

**Inference:** High efficiency outphasing PAs require predistortion in order to ensure linear operation. A phase-only predistortion technique for class-E outphasing power amplifiers has been presented. The technique is based on the analytical relationship between the amplitude of the output signal and the outphasing angle at the input of the Chireix combiner. The proposed technique has been validated by extensive simulation in ADS. It has been shown that the proposed phase-only predistortion applied to an outphasing PA, improves the EVM performance from 10.39% to 2.43% for a 20 MHz 16QAM OFDM modulated signal. The case chosen for simulation was not in the millimetre wave band but at 3.5GHz due to non-availability of device models for simulation at millimetre wave bands. The fractional bandwidth of the chosen case was 5.7%. This will be comparable to having a channel bandwidth of 160 MHz at a carrier frequency of 28 GHz.

## 4.7. Conclusions

An overall insight of key parameters, operating classes and configurations, behavioral modelling and key challenges involved with RF power amplifiers for present and next generation wireless communications was presented in this chapter along with research contributions in the area of Doherty and Outphasing amplifiers. It is inferred in general that greater back-off in the operating point of an RF Power amplifier is needed to maintain the integrity of signals with high PAPR which consequently reduces the efficiency. It is also inferred in general that impact of long term memory effects increases with bandwidth and consequently increases the computation complexity involved in behavioural modelling and digital pre-distortion. The abstracts and inferences of secondary research contributions undertaken in collaboration with co-researchers were presented where techniques to design N-way Doherty Amplifiers, model the behaviour of asymmetric Doherty Amplifiers, model the non-linearity caused by Chireix combiners under amplitude imbalance condition in outphasing amplifiers and phase only predistortion of outphasing power amplifiers are illustrated.

-



# 5. Combined Physical Layer Security and PAPR Reduction in Wideband Transmitters

In this chapter, a novel scheme is presented aimed at jointly providing security in wireless communications in the physical layer and reducing PAPR in OFDM signals before transmission. It was seen in chapters 2 and 3 that non-linear phase response across the signal's occupied bandwidth has an adverse impact on the EVM due to dispersion of the modulated phases. Transmitter circuit characterisation for the wide-band frequency response is needed to pre-compensate the signal to be transmitted. It was seen in chapters 2 and 4 that PAPR of signal being transmitted has an adverse effect on the efficiency of the transmitter. In this chapter a novel scheme is presented where a non-linear phase variation is deliberately introduced in the occupied bandwidth of a signal to provide security of communications in the physical layer and also reduce the PAPR of the signal being transmitted by a figure of 3 dB for QPSK modulated OFDM signals and by 5 dB for 64-QAM modulated signals. The scheme exploits the hardware impairments in the transmitter section of a wireless transceiver and the reciprocal channel response between any two nodes in a wireless network to generate unique encryption keys which are used to encode the bit-stream and disperse the phases of the modulated constellation. While the channel response is reciprocal, the hardware responses are unique. The combined effect of channel and hardware impairments on a probing signal observed by each node is different. A scheme is presented where the asymmetric channel probing data by each node is used to generate symmetric encryption keys with its peer while obfuscating the eavesdropper. The keys are used to disperse the modulated phases of the signal being transmitted thereby concealing its modulation scheme and reducing its PAPR together. The contributions of the author in the novelties presented in this chapter are end to end system design, experimental validation including design of the test apparatus, publication and application for patent. The novelties presented in this chapter correspond to items 8, 10 and 11 in the list of publications.

## 5.1. Introduction:

Modern wireless communications involve transmission of digital data over vector modulated radio frequency (RF) carriers. Unlike, wired communication schemes,

wireless data transmission is broadcast where the occurrence of transmission is sensed and can be received by multiple receivers including the legitimate nodes and eavesdroppers. The security of the data transmitted depends on the ability to encrypt the data such that only the legitimate receivers are able to interpret the message. This task is conventionally handled in the higher layers of the network protocol stack with techniques such as scrambling, bit and packet encryption. These techniques however do not encrypt the air interface of the wireless network and therefore leave the nodes open for traffic analysis and interception by eavesdroppers and man-in-the-middle platforms [11, 12]. One of the ways to reduce the probability of interception by an unauthorized node is to provide a degree of security in the physical layer (PHY) independent of the network protocols and infrastructure. Physical layer security has been gaining interest among researchers in recent years. A number of PHY security schemes such as data encryption in physical layer [68, 12, 69, 70, 71, 72, 73, 74] directional modulation [75, 76, 77, 78], RF fingerprinting, and discrete Fourier transform spread orthogonal frequency division multiplexing (DFT-SOFDM) have been proposed [79].

OFDM was introduced in Chapter 1. PAPR is a critical factor that determines the trade-off between linearity and efficiency of the RF power amplifier in a wireless transmitter. The higher the PAPR, the greater is the linearity requirement and hence greater is the back-off in the operating point needed for the PA from the P1dB compression which implies lower efficiency. PAPR reduction techniques have been hot topics of research in the area of signal processing and consequently several techniques namely Clipping and Peak Windowing [80, 81] Tone Injection [82], Tone Reservation [83, 84], Selective Mapping (SLM) [85, 86, 87] and Partial Transmit Sequence (PTS) [88, 89] have been published. Each of these schemes present their own advantages and limitations which affect the bit error rate (BER), spectral efficiency and computational complexity.

In this chapter, a novel scheme that provides a degree of security in the physical layer along with reducing the PAPR of OFDM modulated signals is presented.

## 5.2. Physical Layer Security Techniques

Data encryption in the physical layer involves scrambling the bit stream with a secret code that is mutually agreed by the legitimate nodes and unknown to eavesdroppers. A generic block level representation of an ideal channel probing model to probe the signal propagation between the wireless nodes in a wireless network is shown in Fig. 5.1 where Node 1 and Node 2 are legitimate nodes probing the wireless channel between. The channel response is computed by evaluating a known signal received by a legitimate node that was transmitted by its peer. The receiving node evaluates the signal transmitted by its peer. The impacts of the propagation characteristics on the known probing signal are used to compute the channel transfer function and the probing is repeated in the reverse direction. If  $H_{21}$  is the channel response computed

evaluated by Node 2 by evaluating the probing signal from Node 1 and  $H_{12}$  is the channel response computed evaluated by Node 2 by evaluating the probing signal from Node 2,  $H_{12} = H_{21}$  under ideal conditions of reciprocity.

In [12], the genuine nodes operate in a timed manner. The two nodes exchange packets of data sequentially at 2.4 GHz (802.11 standard) where the receivers run a level crossing algorithm to parse the received bits. The time indices where valid bits were found are recorded at both nodes and exchanged after a sufficient number of probes. The parsed bits are windowed and a bit is considered to be present at both nodes if there's a run of N bits in a row. The time indices where valid bits were found are recorded at both nodes and exchanged after a sufficient number of probes. While an eavesdropper would get information on the time indices where valid bits were present, it won't have the parsed values thereby maintaining secrecy between the genuine nodes. This scheme was experimentally validated on an indoor 2.4 GHz system in accordance with 802.11 standards.

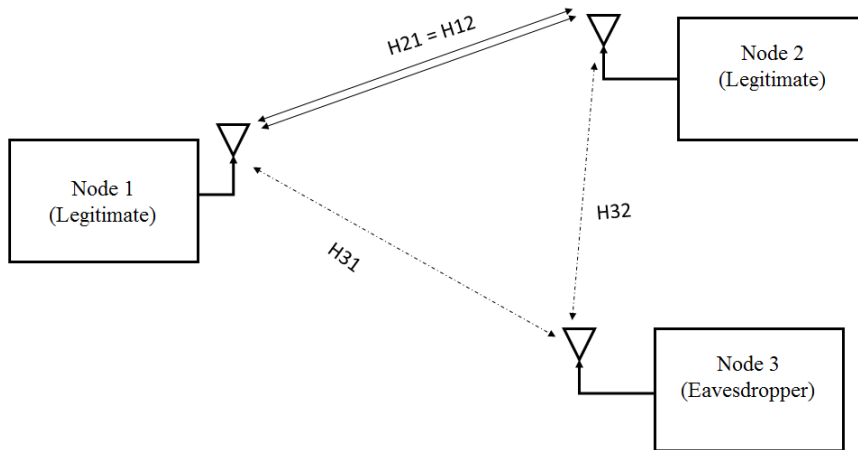


**Fig. 5.1.:** Channel probing model between legitimate wireless nodes in the presence of an eavesdropper.

In [68, 69], the key is generated from the channel variation statistics instead of using the current channel state information to generate the encryption keys. In [68], the proposed scheme is experimentally validated using software defined radio (SDR) modules configured for operation in accordance with the WiFi standard.

In [72], the authors exploit the channel reciprocity between two legitimate nodes in a given time-slot to probe the channel with preamble of the 802.11i standard to generate symmetrical encryption keys at the two nodes which are used to scramble the data before transmission.

A similar scheme employing discrete Fourier transform spread orthogonal frequency division multiplexing (DFT-S-OFDM) has been proposed in [75].

In all these schemes, the probing signal chosen is OFDM modulated. This provides

a very convenient stimulus where the amplitudes and phases of sub-carriers are well defined but exhibits a high PAPR. PAPR of a complex envelope modulated signal  $s(t)$  may be expressed mathematically in the form

$$\text{PAPR}_{\text{dB}} = 10\text{Log}_{10}\left(\frac{\max[s(t)s^*(t)]}{E[s(t)s^*(t)]}\right) \quad (5.1)$$

$$\text{Prob}(\text{PAPR} > \text{PAPR}_T) = 1 - [(1 - e^{-\text{PAPR}_T})]^N \quad (5.2)$$

where  $E[.]$  represents the mean of the variable enclosed in the square brackets. Non-linearity of the RF power amplifier (RFPA) would cause amplitude modulation-amplitude modulation (AM-AM) distortion. This in turn requires techniques such as PAPR reduction followed by digital pre-distortion (DPD) for linear operation. The PAPR of a modulation scheme is specified by the statistical measure of Complex Cumulative Distribution Function (CCDF). The CCDF plot of a 2048 point OFDM signal with 1664 QPSK modulated sub-carriers exceeding given threshold of PAPR values is shown in Fig. 5.2. This can be expressed mathematically by means of a cumulative distribution function [90] of the form of eq. 5.2 where  $N$  is the number of sub-carriers and  $\text{PAPR}_T$  is the threshold PAPR value.

In [12], the authors mitigate the impact of time variant behaviour of the channel by using the application layer traffic information for key generation and have experimentally validated the scheme using SDR modules. This can serve to mitigate the impact of AM-AM distortion to a limited extent but its effectiveness when applied to probing signals received from transmitters subject to PAPR reduction schemes is currently not clear. In [70], the phase response of the channel between two authentic nodes is probed and is used for encryption key generation. This provides a greater degree of secrecy in comparison with schemes that involve RSSI (Received Signal Strength Indicator) figures due to greater sensitivity of phase to signal propagation path. The probing signal here is also OFDM modulated whose high PAPR would cause AM-PM (Amplitude Modulation-Phase Modulation) when passed through a non-linear PA. This would introduce an uncertainty in the phase perceived by the receiver. The authors propose to quantize the received phases to nearest fixed values to mitigate the effect of non-ideal channel which is not exactly reciprocal. This can help to mitigate the problem with AM-PM distortion to a limited extent but experimental validation with hardware has not been performed to test its effectiveness. In work presented in this chapter, the idea of generating physical layer encryption information published previously is expanded to include the practical non-ideal hardware and channel aspects that affect the key generation process and evolve a scheme to further strengthen the secrecy of the channel encryption data.

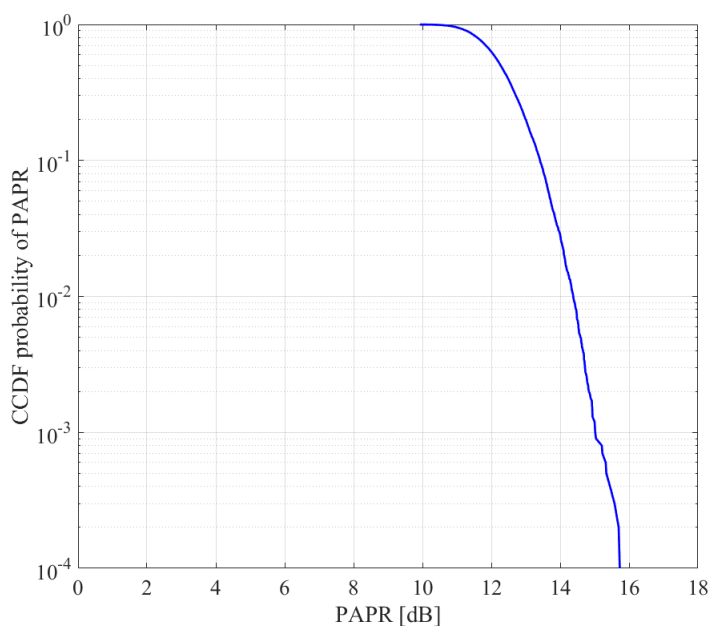


**Fig. 5.2.:** CCDF plot of a 2048 point OFDM signal with 1664 QPSK modulated sub-carriers exceeding threshold PAPR values

The above schemes focus on scrambling the data such that the data interpreted by the eavesdroppers from the received bitstreams is erroneous. Schemes such as directional modulation (DM) [75, 76, 77, 78] and fast polarization hopping [91] impair the ability of an eavesdropper to receive the transmitted modulation symbols. The scheme proposed in this work aims to complement the above schemes aimed at impairing the ability of eavesdroppers to receive the transmitted symbols to strengthen the security further.

### 5.3. PAPR Reduction Techniques

The problem of high PAPR mentioned above has been mitigated in multiple ways involving time and frequency domain techniques. A review of these techniques has been presented in [80]. Clipping with is a time domain technique where a signal's amplitude swing is limited to a preset value. The operation can be described by eq. 5.3 where  $C$  is the clipping magnitude,  $|A(t)|$  is the instantaneous amplitude of the clipped signal and  $x(t)$  is the instantaneous amplitude of the original signal at time instant  $t$ . A comparison of original and clipped OFDM time domain signals is shown in Fig. 5.3.

$$|A(t)| = \begin{cases} x(t) & x(t) \leq C \\ C & x(t) > C \end{cases} \quad (5.3)$$

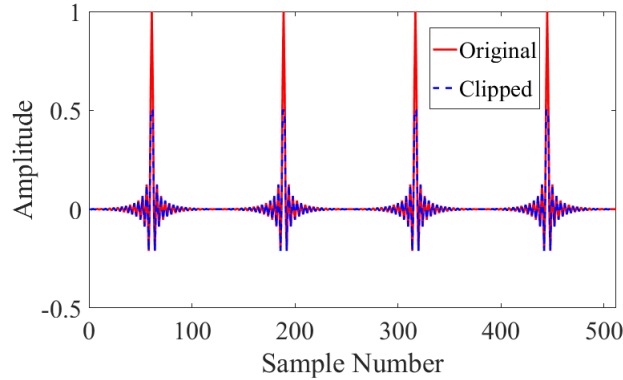


**Fig. 5.3.:** PAPR reduction by clipping.

This scheme is non-linear and results in both in-band and out-of-band distortions owing to the abrupt discontinuity in amplitude and would need over sampling and filtering to mitigate the impact. Since a significant portion of the signal's amplitude would be lost, it would lead to increased BER at the receiver which would need additional error correction schemes. Another time domain scheme to reduce PAPR in OFDM signals is peak windowing where the time domain signals are multiplied with windowing functions such that the peak of the OFDM signal falls in the valley of the windowing function.

$$W(t) = 0.5(1 - \cos(\frac{2\pi t}{(T-1)})), 0 < t < T \quad (5.4)$$

In [81], a hybrid scheme is presented where peak windowing is applied prior to clipping to reduce the impact on BER while reducing the PAPR. A Hanning window defined by eq. 5.4 is used. The optimization problem here with this technique is in choosing the window length where a small length is preferred to localize the application of the function to just the samples above a threshold level but using small window length implies more efforts needed to search and pin-point the peaking regions.

Tone injection is a technique where the modulation constellation of the signal of interest is expanded to higher orders and the amplitudes of the sub-carriers in the outer periphery of the original constellation are mapped on to distant points such that the distance between the constellation points of adjacent sub-carriers is maximized. This scheme is explained in [80] and experimentally validated in [82]. This

scheme would require the mapping information to be passed to the receiver to recover the original symbols.

Tone reservation is a technique where un-modulated sub-carriers are inserted along with the original modulated sub-carriers in the OFDM signal to cancel the peaks. An overview of the technique is provided in [80]. The technique requires multiple computations to decide the frequency bins and number of tones to be inserted and this problem complicates further when the number of data sub-carriers is in the order of thousands as is the case with 5G-NR schemes. A simplified scheme to implement tone reservation is published in [84].

A popular frequency domain technique for reduction of PAPR is SLM (Selective Mapping) where the sub-carriers in an OFDM signal are subject to elementwise multiplication with phase rotating sequences. A number of such phase rotation sequences are generated and the signal of interest is multiplied with each of them. The product that features the least PAPR is then selected for transmission. This process is described in Fig. 5.4.

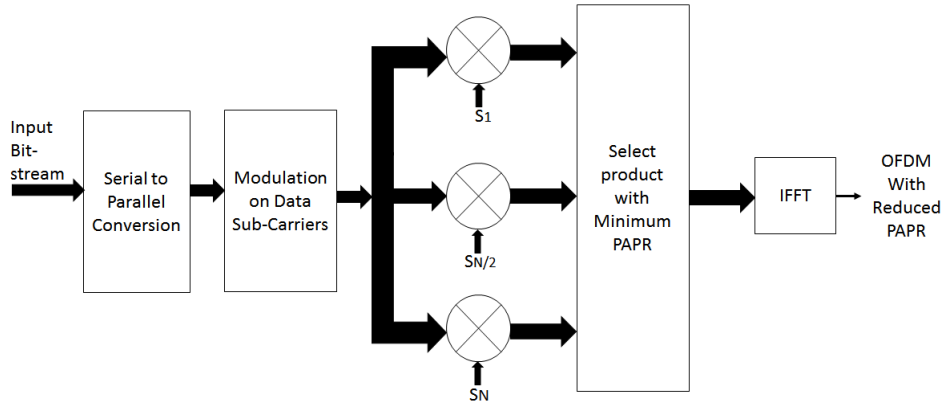


**Fig. 5.4.:** Selective Mapping

Each sequence  $S_n$  where  $n$  varies from 1 to  $N$  is a complex number of magnitude 1 and phase  $\theta_n$ . A number of research articles have been published on the criteria for selecting the values of  $\theta_n$ . In [85], the authors accomplish both physical layer security and PAPR reduction for optical communication through the use of chaotic sequences generated using a two dimensional logistic mapping. Each OFDM frame is encrypted  $U$  times with  $U$  encrypting chaotic sequences. The encrypted OFDM symbols are accompanied with pilot symbols which contain the labels of the encrypting sequence. In [92], the authors present a scheme of PAPR reduction in a sub-carrier index modulated OFDM (SIM-OFDM) scheme using SLM technique where Riemann binary sequences mapped on a Reimann matrix are used to generate phase shifts of 0 or 180 degrees. In [86], the authors propose a reduced complexity SLM scheme where half of the sub-carriers are first subject to IFFT operation and then subject to phase scrambling rotation by circular convolution with a complex sequence known as a perfect sequence and the other half of the sub-carriers are

subject to conventional SLM. This reduces the number of computations needed in comparison with a conventional SLM scheme. In [87], the authors evaluate the effect of SLM on oversampled signals. SLM requires side information or key to be transmitted to the receiver to restore the original phases of the sub-carriers prior to demodulation.

Another frequency domain technique where PAPR is reduced using phase rotations is PTS (Partial Transmit sequence) where the sub-carriers are divided into  $N$  subsets and each subset is first subject to IFFT and further subject to phase optimizations such that the overall PAPR of the OFDM signal is reduced. The basic block diagram of a PTS scheme is as shown in Fig. 5.5.

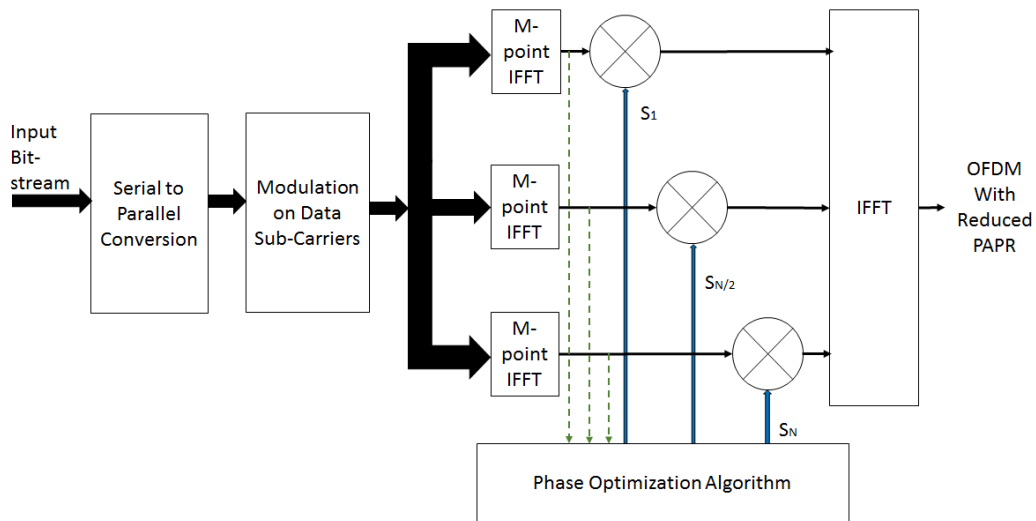


Fig. 5.5.: Scheme of Partial Transmit Sequence

In [88], the authors have evaluated the extent of PAPR reduction achievable by PTS for several modulation schemes. In [93], the authors propose an iterative scheme for selection of phase sequences to adaptively reduce PAPR. In [94] the authors propose a scheme for selecting the phase rotation symbols for the partial sequences based on particle swarm organization (PSO) where the number of computation for the selection of phases is decreased. In [89], the authors have published a hybrid scheme that applies both SLM and PTS for PAPR reduction. PTS also requires side information to aid the restoration of the original modulated constellation at the receiver prior to demodulation.

In summary, it may be inferred from the above that PAPR reduction is accomplished by modifying the signal being transmitted either in time or frequency domain. The modifications need to be undone at the receiver to retrieve the original modulated constellation of the sub-carriers for faithful demodulation. This needs additional information to be transmitted to the receiver to convey the modifications performed on the original signal. This aspect can be exploited to provide security in the

physical layer together with reduction of PAPR if the modifications to the original signal can be done with mutually known secret information. This is the the focus of the work presented in this chapter. In [89], the authors accomplish both physical layer security and PAPR reduction for optical communication through the use of chaotic sequences generated using a two dimensional logistic mapping. The maps are stored symmetrically at the two communicating nodes and the pilot sub-carriers in the OFDM signal carry the labels of the chaotic sequence used so that the receiving node can identify the right set of phases to undo the phase rotations. While the scheme is novel, it is essential to communicate the set of phase rotating sequences and their labels to the peer prior to transmitting the data. In this chapter of the thesis, a scheme to reduce PAPR similar to that employed in SLM together with providing security in the physical layer for generation of encryption information is accomplished using convolved channel and hardware responses at each node as keys. This does not require transmission of keys or side information. While the prior art schemes use channel response as the unique input to their key generation algorithms, the scheme presented here enhances the secrecy by using the convolved hardware and channel frequency responses as input to key generation algorithms as explained in the next section.

## 5.4. Physical Layer Authentication and PAPR Reduction

Communications in the millimeter wave band can involve wide bandwidths and multiple modulation schemes which are selected adaptively depending on the channel state and available resources. Advanced wideband communications employing OFDM schemes such as 5G-NR feature channel bandwidths up to 400 MHz in Ka-Band with FFT sizes up to 4096 as discussed in the earlier chapters. This indicates a high probability of PAPR increasing above 10 dB. It was also discussed in chapter 2 that bandwidth dependent impairments such as ripple and tilt in gain and group delay caused by non-ideal critical blocks in a transmitter such as digital to analogue converters (DACs), mixers, band pass filters (BPF) and amplifiers become significant with increasing signal bandwidths. It is imperative to analyze these impairments and pre-compensate the input signal to mitigate them by means of calibration and digital pre-distortion (DPD). These impairments when sensed and recorded can be used to uniquely identify a transmitter and can hence act as its signature. The communication channel between two nodes in a network is unique to the respective path between them and its transfer function is reciprocal within the channel coherence time. The combination of channel response and hardware responses over the band of interest can therefore be used to generate encryption information unique to the transmitter and receiver. In this section a novel scheme to encrypt the phases of a modulated signal to jointly accomplish physical layer authentication and reduce PAPR in wideband OFDM signals without the need to

transmit additional information is presented. The encryption keys are generated symmetrically at the two authentic communication nodes by exploiting the unique combination of the frequency responses involving their non-ideal hardware modules and the wireless channel.

The encrypted constellation is used to authenticate the generation of 512 bits strong bit level encryption keys as per Diffie Hellmann scheme [95] to increase the security further.

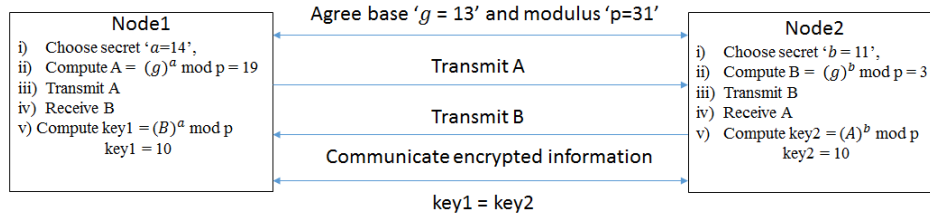


Fig. 5.6.: Diffie Hellman Key Agreement

1. The work presented in this chapter provides a novel scheme to accomplish encryption of modulated signals to provide security together with reduction of PAPR in OFDM schemes.
2. A scheme to generate encryption keys using the channel characteristics between two legitimate nodes in convolution with the circuit characteristics of the transmitting hardware at the two nodes.
3. A legitimate node transmits a constant envelope stimulus without pre-compensating the signal to mitigate its circuit impairments. The second legitimate node receives the transmitted signal and measures the impairments in it which is a convolution of the channel and circuit characteristics of the transmitter at the first node. The second node re-transmits the stimulus without pre-compensating the stimulus to mitigate its circuit impairments. This is received by the first node which measures the channel characteristics convolved with the circuit characteristics of the second node.
4. Each node then convolves its own circuit characteristics with characteristics evaluated from the received signal. This leads to symmetric information at both the legitimate nodes to generate the modulation encryption keys. The eavesdropper would find it difficult to distinguish the circuit characteristics from channel characteristics by evaluating the signals it received.
5. The modulation encryption key is used to generate frequency domain phase offsets which disperse the phases of the signal's constituent frequency components thereby encrypting it.
6. The two nodes agree values for base ' $g$ ', modulus ' $p$ ' and exchange  $A = (g^a) \bmod p$  and  $B = (g^b) \bmod p$  respectively over the wireless link through the

constellation encrypted signals. Each node then computes symmetric keys from the received values of A and B by computing  $(B^a) \bmod_p$  and  $(A^b) \bmod_p$  respectively to yield the bit encryption keys.

7. The proposed dispersion of phases in the frequency domain also reduces the PAPR of OFDM signals.
8. The entire scheme has been experimentally validated successfully with zero BER (Bit Error Rate) at the legitimate receiver.

### 5.4.1. System Design

The generalised block diagram of a wireless transceiver was discussed in chapter 2. As discussed in the earlier chapters, the digital signal processor (DSP) performs the task of vector modulation symbol generation, baseband filtering, digital up-conversion (optional), baseband filtering, quantization and yields the in-phase I and quadrature Q components of the intended digital baseband modulated signal. These signal components are then applied to digital to analogue converters (DACs) whose outputs are vector up-converted to an intermediate frequency (IF), further up-converted to the intended RF carrier frequency, amplified and subsequently transmitted. The non-ideal characteristics of these hardware blocks such as sinc roll-off in DACs, amplitude ripple, tilt and group delay in the amplifiers, mixers and filters respectively result in non-uniform gain and phase responses to wideband signals. These impairments would need to be compensated by means of a calibration process as described in chapters 2 and 3 to maintain the integrity of the modulated signal being transmitted in addition to AM-AM and AM-PM characteristics of the RFPA. In the receiver, the signal sensed by the antenna is subject to low noise amplification by the RF low noise amplifier (LNA), down-conversion to an intermediate frequency, further vector down-conversion to extract the I and Q baseband components which are digitized in the analogue to digital converter and applied to the DSP for digital demodulation and further processing. The wide band non-uniform gain and phase responses are also observed in the receiving blocks. This also requires calibration over the band of interest to maintain the integrity of the received wideband signal. The non-ideal frequency response of the transmitter's hardware and the channel between the legitimate nodes is evaluated and the information is used to generate keys to encrypt the phases of a modulated signal of interest in a reciprocal manner to provide a degree of security in the physical layer along with reducing the PAPR of the signal being transmitted. An example of Diffie Hellman key exchange is summarised in Fig. 5.6. While the scheme is novel, it is critical to ensure that the key exchange does not take place with an impersonating attacker. The phase encryption provided on the modulated constellation during the Diffie Hellman key agreement phase is only known to the authentic nodes and hence authenticates the genuineness of the key generation operation.

### 5.4.2. Key Generation scheme in TDD systems

A practical channel probing model with non-ideal channel and hardware characteristics is shown in Fig. 5.7. This case represents the potential application scenarios in small cells and short range wideband millimetre wave wireless communications. The key generation in this case exploits channel reciprocity between two legitimate nodes. Practically, a channel is never reciprocal but may be assumed reciprocal within the channel coherence time. This time interval is dependent on the frequency of operation, environmental fading and Doppler effect in the channel of operation. The first step is to let the two legitimate nodes probe the channel. The probing signals are required to be shorter than the channel coherence time  $T_c$  [70].

$$T_c = \frac{9}{16\pi f_d} \tag{5.5}$$

$$f_d = \frac{vf}{c} \tag{5.6}$$

where  $f_d$  is the Doppler shift in Hz,  $v$  is the relative radial velocity between the nodes and  $c$  is the velocity of propagation of an electromagnetic wave in free space i.e.  $3 \times 10^8$  m/sec.

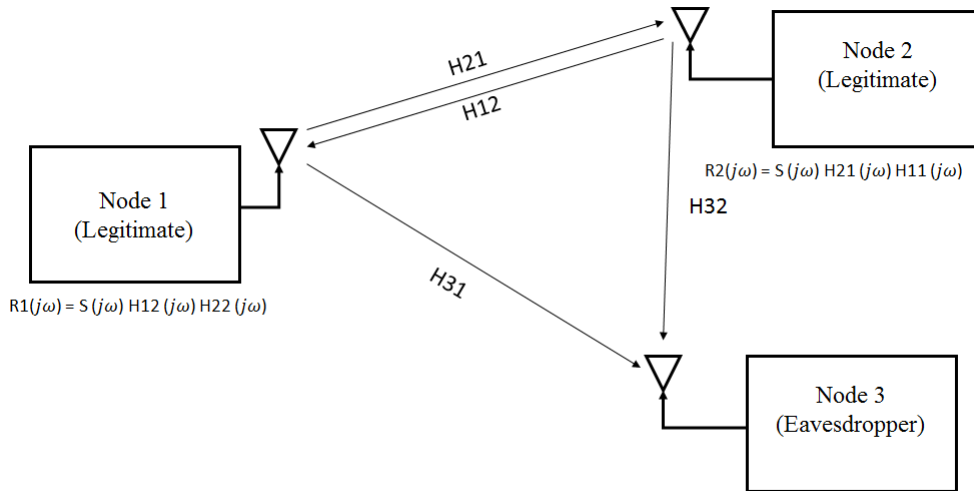


**Fig. 5.7.:** Fig. 5.7 Practical Channel Probing Model.

In a TDD system, the transmission is half duplex implying that only one node can transmit in a given time-slot. Therefore, the combined signal duration and propagation delays for channel probing by both nodes needs to be significantly

lower than the channel coherence time. Prior arts discussed in the previous section use OFDM signals to probe the channel. One of the problems encountered with OFDM signals for probing is their varying envelope with a high PAPR as explained in the previous section. This signal when amplified by non-linear power amplifiers in the transmit chain would result in distortion in the probing signal itself before the digital linearization blocks in the transmitter act to linearize the power amplifier. An alternate approach is to use a probing signal whose envelope is constant and has a bandwidth equal to or greater than the channel bandwidth of interest. An apt choice is the chirp signal described mathematically in Chapter 3 and repeated below for convenience

$$y(n) = \sin \left\{ 2\pi \left( \frac{knT_s}{2} + f_{min} \right) nT_s \right\} \quad (5.7)$$

$$k = \frac{f_{max} - f_{min}}{M} \quad (5.8)$$

where  $y(n)$  is the value of the  $n$ th sample,  $T_s$  is the sampling interval,  $M$  is the total number of samples,  $k$  is the frequency variation parameter,  $f_{max}$  and  $f_{min}$  are the maximum and the minimum frequencies respectively. An advantage of chirp stimulus is that the received signal at the legitimate nodes can be subject to piecewise analysis since the spectral content of each piece is distinct and does not overlap with spectral content of other pieces.

The duration of the probing signal is  $MT_s$ . This needs to be chosen such that the sampling interval is lower than the Nyquist rate for the intended bandwidth and the overall signal duration is significantly lower than half of the channel coherence time. The two nodes also need to be synchronised in time so that they transmit without collision at the appropriate time slots.

A generic wireless channel model with three communication nodes considered for probing is shown in Fig. 5.7. The procedure to probe the convolved channel and circuit characteristics of the transmitting node by assessing their impact on a known test signal can be derived assuming the following conditions.

1. Node 1 and Node 2 are the legitimate nodes and Node 3 is an eavesdropper.
2. The legitimate nodes have their clocks and timing circuits synchronized with a common reference source such as a GPS, an appliance running IEEE 1588 precision time protocol (PTP) or similar. A timed interrupt logic runs on each node to enable transmission.
3. The carrier phases of the local oscillators (LOs) are synchronized with GPS disciplined oscillators or similar reference sources.

4. The hardware signal paths in the receive section of each node are calibrated to mitigate hardware impairments such as IQ phase offset, IQ gain imbalance, etc using techniques described in chapter 3. The hardware signal paths in the transmit section of each node are not calibrated for wideband gain and phase variations.
5. The impact of RFPA non-linearities such as AM-AM and AM-PM distortion on the constant envelope probing signals is negligible.
6. The receiver at each node is calibrated over the bandwidth of interest for pass-band gain flatness and phase linearity.

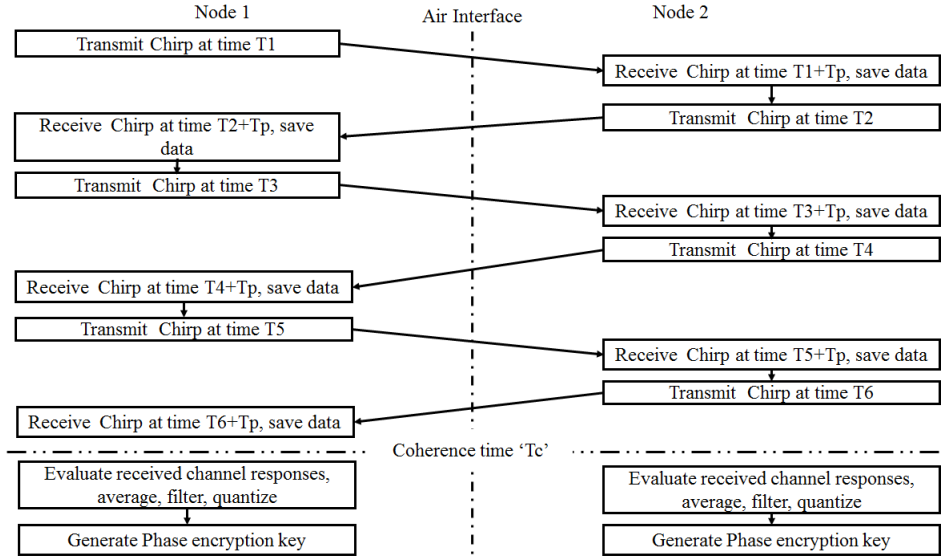


**Fig. 5.8.:** Channel Probing Procedure

The proposed procedure to probe the channel response is summarised in Fig. 5.8.

First we let Node 1 initiate the probing by transmitting a predefined chirp signal at time interval  $T_1$ . Node 1 switches to receive mode after transmission. Node 2 is maintained in receive mode till time interval  $T_2$ .

$$T_2 > T_1 + T_{sym} + T_p + T_g \quad (5.9)$$

where,  $T_{sym}$  is the probe signal duration,  $T_p$  is the propagation time,  $T_g$  is the guard interval and  $T_g \leq T_p$ . Node 2 receives the transmission from Node 1 until time  $T_2$  and transmits the pre-defined chirp pulse at time  $T_2$ . Node 1 receives the transmission from Node 2 during this period until time interval  $T_3$  where  $T_3 - T_2 = T_2 - T_1$ .

This is repeated at time slots  $T_3$ ,  $T_5$  and  $T_4$  and  $T_6$  respectively.  $T_6 - T_1 < T_c$  (channel coherence time). The received magnitude responses are normalised to the

peak amplitude values observed in each time slot and are averaged. Let  $r_2(n)$  and  $r_1(n)$  denote the time domain signals received at Node 2 and Node 1 respectively. The averaged response  $r_2$  received by Node 2 is an ideal chirp signal  $y(n)$  convolved with the impulse response  $h_{11}$  of Node 1's transmitting hardware and the impulse response of the channel  $h_{21}$ . Similarly, averaged response  $r_1$  received by Node 1 is an ideal chirp signal  $y(n)$  convolved with the impulse response  $h_{22}$  of Node 2's transmitting hardware and the impulse response of the channel  $h_{12}$ . The fast Fourier transform (FFT) of the averaged responses is computed at both nodes for ease of analysis. The FFTs may be expressed as in the equations below. Since the receivers in the nodes are calibrated, their hardware responses may be absorbed into  $H_{21}$  and  $H_{12}$ .

$$R_2(j\omega) = Y(j\omega)H_{11}(j\omega)H_{21}(j\omega) \quad (5.10)$$

$$R_1(j\omega) = Y(j\omega)H_{22}(j\omega)H_{12}(j\omega) \quad (5.11)$$

Node 2 then de-convolves  $y(n)$  from  $r_2$  and convolves the result with its own transmitting hardware's impulse response  $h_{22}$  to yield the convolved hardware and channel response  $e_2$  ( $E_2(j\omega)$  in frequency domain). Node 1 then de-convolves  $y(n)$  from  $r_1$  and convolves the result with its own transmitting hardware's frequency response  $h_{11}$  to yield the convolved channel and hardware response  $e_1(n)$  ( $E_1(j\omega)$  in frequency domain). If  $H_{12} = H_{21}$ , then  $E_1 = E_2$  as can be seen from the equations below.

$$E_2(j\omega) = \frac{R_2(j\omega)}{y(j\omega)}H_{22}(j\omega) \quad (5.12)$$

yielding

$$E_2(j\omega) = H_{11}(j\omega)H_{21}(j\omega)H_{22}(j\omega) \quad (5.13)$$

$$E_1(j\omega) = \frac{R_1(j\omega)}{y(j\omega)}H_{11}(j\omega) \quad (5.14)$$

yielding

$$E_1(j\omega) = H_{22}(j\omega)H_{12}(j\omega)H_{11}(j\omega) \quad (5.15)$$

The above scheme aims to generate symmetric encryption keys at both nodes with asymmetric transmitted information. The eavesdropper Node3 will be able to receive the transmitted chirp signals but will not be able to distinguish the impairments caused by the channel from that caused by un-calibrated transmitting hardware at each legitimate node. Since the transmission of the chirp signals is controlled by timed interrupts, response by the eavesdropper Node3 to the stimulus from Node 1 will accompany the response from Node 2. This can delay the agreement of symmetric keys between Node 1 and Node 2 but Node 3 will not be able to get the key data.

In a practical scenario,  $E_1(j\omega)$  will not be equal to  $E_2(j\omega)$  owing to noise, variations in performance of receiving hardware and measurement errors but will be highly correlated showing similar trends. A shifted Fast Fourier Transform (FFT) plot of convolved channel and circuit characteristics computed over a bandwidth of 100 MHz at a carrier frequency of 28.9 GHz is shown in Fig 5.9. The evaluated responses  $E_1$  and  $E_2$  are subject to moving median filtering of a predetermined window length to mitigate the effect of noise and receiving hardware introduced impairments. One of the ways to extract symmetric data for encryption is to perform nonlinear curve-fitting on sections of the computed responses and to use the evaluated coefficient values for key generation.

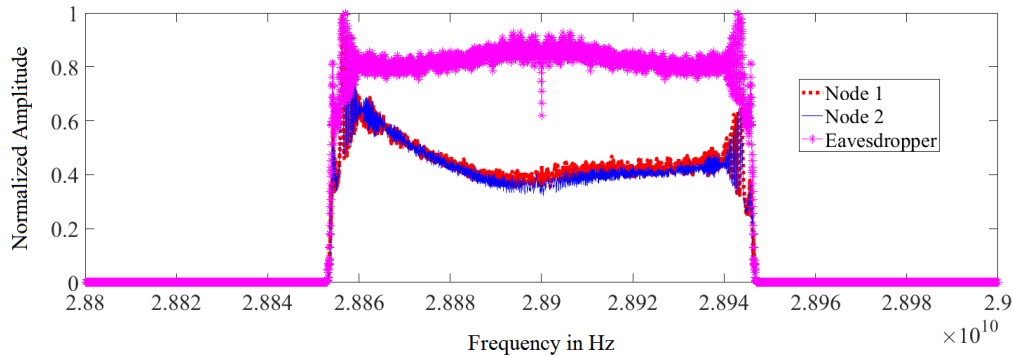


**Fig. 5.9.:** Normalised Convolved Channel and Hardware Frequency Responses

For example, the filtered responses may be classified into regions depending upon change of slope of the frequency response and each region is subject to piece-wise non-linear curve-fitting operations applying the method of least squares. In Fig. 5.9, the responses in the frequency band 28.85 GHz to 28.86 GHz show a rising slope. This may be classified as a region. Similarly, the responses in the bands 28.6 GHz to 28.9 GHz, 28.9 to 28.92 GHz, 28.92 GHz to 28.94 GHz and 28.94 to 28.95 GHz may be classified as four more regions after being subject to moving median filtering operation to mitigate the impact of noise. The responses in the above regions may be subject to curve-fitting operation applying the method of least squares in accordance

with equation

$$y(n) = ax^3 + bx^2 + cx + d \quad (5.16)$$

The ratio of the curve-fitting coefficient values are computed, rounded off to nearest integer values and quantized to the nearest prime numbers to yield a set of encryption keys which may be designated as key1.

The filtered responses are then divided into a convenient number of regions or sub-bands of equal lengths and classified on the basis of signal power distribution. This may be divided into 8 sub-bands of bandwidth 12.5 MHz each and may be numbered in descending order according to the measured power in each sub-band. The range of indices or frequency bin numbers denoting each region are extracted and the highest prime number in each region is extracted. For example, if the responses were sampled at a frequency of 200 MHz and the FFT was computed with 2048 frequency bins, a bandwidth of 100 MHz would occupy 1024 frequency bins with each bin representing a frequency resolution of 97.65625 kHz and each sub-band of 12.5 MHz bandwidth would occupy 128 points in the FFT space. Fig. 5.9 represents a shifted FFT plot where the band of interest lies between FFT bin numbers 513 to 1537. The sub-band of 12.5 MHz having the highest band power would occupy the frequency bins from 641 to 768. The highest prime number in this band 761. This will be the first element of second key set designated as key2. Similarly, the highest prime number in the band with the next highest band power is extracted and is stored as the second element of key2. This continues till all eight elements of key2 are extracted. The sequence in which the prime numbers are entered in the space of key2 is critical. The key sets key1 and key2 are expected to be the same at the legitimate nodes Node 1 and Node 2 due to highly correlated responses and different at Node 3. This can be inferred from Fig. 5.9 which shows plots of experimentally determined convolution of frequency responses of the channel the hardware at 28.9 GHz over a bandwidth of 100 MHz. The encryption data extraction procedures mentioned above are not exhaustive and there can be several other ways of extracting symmetric encryption keys depending upon the application. A subset of prime numbers is chosen from both the keys and applied as coefficient values to a non-linear function such as an elliptic function to derive a set of random phases. The derived set of phases are applied as offsets to the phase spectrum of the modulated signal to be transmitted thereby randomizing it. The encrypting symbols and the phases are updated with new values after convenient intervals using different non-linear functions and a different set of prime numbers from the two key sets to maintain security against brute force attacks and avoid letting the adaptive equalizers in the eavesdropping nodes learn the encrypting information.

The effectiveness of encryption is proportional to the number of secret bits that can be generated by channel probing. But this value is limited by the channel noise and dynamic range of the hardware modules in the transceivers at the communicating

nodes. But the encryption information generated so far would be suitable to authenticate a stronger key generation process. A Diffie-Hellman key exchange scheme is initiated to increase the security against brute force attacks. The values of modulus and base are either pre-determined or transmitted from Node 1 to Node 2 over through modulation encrypted signals. The encrypted modulation symbols authenticate the origin of the probing signals and increase immunity against impersonation attacks. Node 1 and Node 2 then exchange the preliminary keys A and B through modulation encrypted signals. Each node then computes the bit level encryption keys as illustrated in 2. The data to be communicated is first encrypted at bit level using the bit encryption keys, modulated in baseband, subject to encryption of the modulated constellation and transmitted. The process is reversed at the receiver to recover the transmitted data. The length of the bit encryption key is chosen to be at least 512 bits.

The encryption of phases when applied to an OFDM signal has an effect similar to the SLM scheme of reducing PAPR but does not need multiple iterations and transmission of side information since the encryption phases are known to both transmitting and receiving nodes. This is elaborated in the later sub-sections.

The process of physical layer authentication through encryption of modulated phases is applicable to both single carrier and OFDM modulated schemes. Both these cases are explained in the upcoming subsections. Though the PAPR reduction by the proposed method is not applicable to single carrier schemes, the security aspect is still applicable.

### 5.4.2.1. Encrypting OFDM Modulated Signals

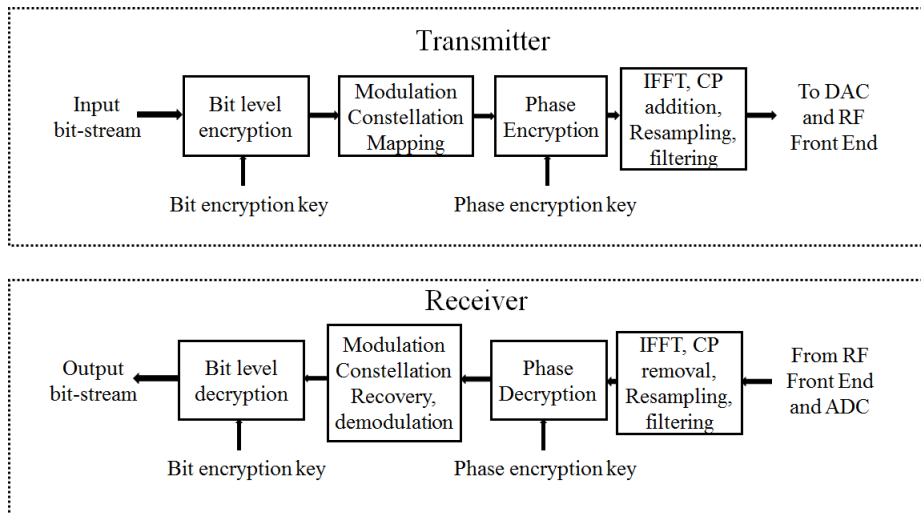


Fig. 5.10.: Encrypting OFDM Modulated Signals

A subset of prime numbers chosen by a symmetric algorithm from the two key sets are applied as coefficient values in a non-linear function such as an elliptic function shown in eq. 5.17 to generate encrypting phases.

$$y = p^2 = (x^3 + f_1x + f_2) \bmod_{f_3} \quad (5.17)$$

where  $f_1$ ,  $f_2$  and  $f_3$  are three prime numbers selected by a symmetric algorithm from the two key sets,  $x$  is the sub-carrier or frequency bin number,  $p_2$  is the outcome of the nonlinear mathematical operation for a given value of  $x$  that yields the encrypting phase value designated as  $y$ . The positions of the prime numbers in the non-linear function are interchanged and the non-linear function is executed again to obtain a convenient number of encrypting phase sequences. The sequence with maximum variance is chosen to encrypt the OFDM symbols to minimise PAPR. Unlike the single carrier schemes, each modulated symbol is transmitted on a subcarrier in OFDM modulated signals. The encrypting phases thus generated are added directly as offsets to the phase of each sub-carrier. Three phase sequences were generated in the experimental validation of this technique and their elementwise product was taken to maximise variance. Randomisation of phases of the sub-carriers in an OFDM modulated signal reduces its PAPR [85] along with providing security of information [90]. The eavesdropper is obfuscated since there is no means for it to generate the same encryption keys as the authentic nodes due to entirely different convolution of hardware and channel responses seen at its end. This is demonstrated in the section on experimental validation where a sophisticated vector signal analyser running an adaptive filter algorithm was used as an eavesdropper and it could not recover the transmitted constellation. This scheme is an enhancement over prior art where security of communications is enhanced along with reduction in PAPR and without the need to transmit side information for the receiver to restore the original constellation.

A reduction in PAPR by over 3 dB after encryption. The detailed plots are provided in the section on experimental validation in this chapter.

The generated keys are first tested for symmetry with random data where Node 1 generates a set of random bits and modulates them on to the data sub-carriers with intended constellation QPSK for example. The encrypting phases are added to the phases of the modulated sub-carriers and the IFFT operation is performed to yield the encrypted time domain baseband. The baseband is transmitted after the other necessary signal processing operations. Node 2 receives the signal transmitted by Node 1, digitizes it, applies noise filtering and subtracts the encrypting phases to recover the original modulation constellation. The recovered baseband is then subject to equalization to compensate for channel impairments. If the recovered modulation phases at this stage do not correspond to standard values within an agreed deviation limit, a failure message is sent to Node 1 and the entire key generation process restarts. Else, the recovered baseband modulation symbols are

demodulated to recover the transmitted symbols. Node 2 remodulates the recovered symbols on to another baseband with the same modulation scheme, encrypts the phases with its key and re-transmits it. Node 1 now receives, decrypts and demodulates the data to recover the bit-stream and compares it with that it transmitted. If a match is found, a success message is transmitted to Node 2. This completes the phase encryption key generation and agreement process along with the design of symmetric encryption and decryption filters. It may be noted that no confidential data is transmitted until this stage. The encrypting phases and symbols are updated to new values at both nodes by running a common algorithm that selects different non-linear functions and a different sub-set of key values symmetrically at both nodes after a definite interval of time has elapsed. This is done through timed interrupts. On successful verification of the symmetry of constellation encryption, Diffie Hellman key agreement is initiated. The preliminary keys A and B which are over 400 bits in length are exchanged by modulating them on the chosen constellation, subjecting the constellation to phase encryption and transmission over the channel. The transmission over phase encrypted modulated signals authenticates the genuineness of the initiating node thereby providing immunity against impersonation attacks. The data to be transmitted is then secured at both bit level and at the constellation by the respective encryption keys.

### 5.4.3. Encrypting Single Carrier Modulated Signals

A key parameter of the physical layer components that can have an adverse impact on the integrity of the modulated symbols transmitted is the group delay (GD) variation over the bandwidth of interest. Group delay is defined as the rate of change of phase with angular frequency.

$$GD = \frac{d\theta}{d\omega} \tag{5.18}$$

where GD the group delay is in seconds,  $\theta$  is the phase in radians and  $\omega$  is the angular frequency in radians/second. It's a parameter that refers to the dispersion of the individual frequency components that constitute the spectrum of the desired modulated signal. This is a key parameter to be considered in the selection of RF front end filters. The modulation symbol generation, wave shaping and baseband filtering operations are handled by a DSP chip in most modern wireless communication equipment. Finite Impulse Response (FIR) filters are preferred in the area of digital baseband filtering due to the flexibility available in shaping the spectral characteristics. FIR filter kernels are usually designed to exhibit a near flat amplitude response and a linear phase response over the bandwidth of interest. An example of an FIR filter that meets this criterion in a Hamming window based truncated

sinc filter whose impulse response is defined by the kernel in eq. 5.19. This was introduced in Chapter 3 and is repeated here for convenience.

$$h(n) = \frac{\text{Sin}\left(2\pi f_c\left(n - \frac{M}{2}\right)\right)}{\left(n - \frac{M}{2}\right)} (0.54 - 0.46 * \cos(2\pi n/M)) \quad (5.19)$$

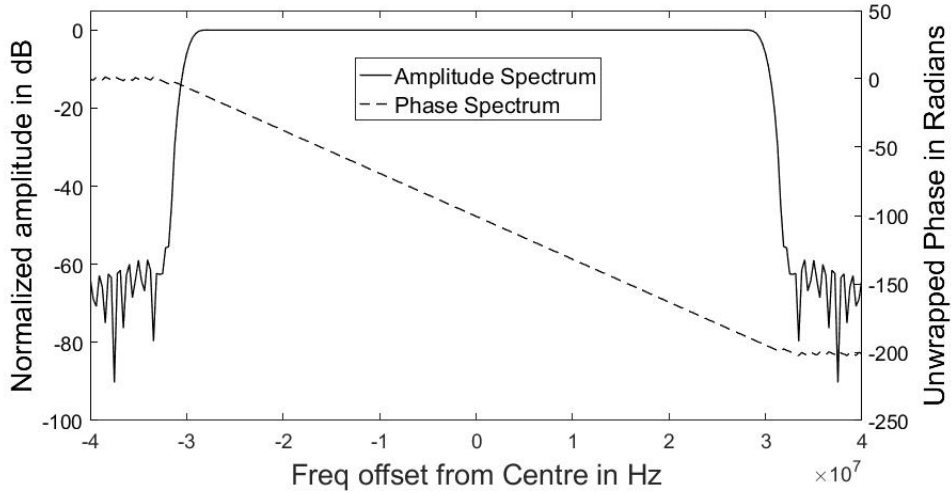


**Fig. 5.11.:** Frequency Response of Hamming Windowed FIR Filter

Linear phase response in the band of interest would imply a constant GD. This could be verified mathematically by taking the first derivative of a straight line which would yield a constant equal to its slope. This refers to a non-dispersive transfer characteristic of the filter. This filter may be made dispersive enough to cause constellation distortion if ripples of suitable amplitudes are introduced in the phase response of the filter thereby making GD and its variation non-linear. Experimental results in [96] indicate that a significant amount of constellation distortion is introduced in a QPSK modulated carrier if a parabolic group delay variation higher than 1.15 times the symbol duration  $T_s$  is introduced.

The spectral characteristics of single carrier modulated signals can be encrypted using dispersive filters to distort the modulation phases. A dispersive filter is one which exhibits a non-linear phase response or group delay in the frequency domain. Such a filter can be designed in the digital domain by manipulating the phase response of a finite impulse response (FIR) filter in the frequency domain to have the required nonlinear phase variation for encryption.

Obtain the symbol rate, occupied bandwidth (BW) and modulation constellation of the modulated carrier intended to be transmitted.

Calculate the minimum variation in GD over the bandwidth of interest needed to cause constellation distortion using the mathematical relation:

$$\frac{GD}{T_s} \geq 1.15 \tag{5.20}$$

Calculate the peak variation  $d_{\theta_{max}}$  required in the phase response by equating  $d\omega$  in equation ‘1’ to BW noted in step ‘i’ and using the value of GD obtained in step ‘ii’.

Obtain the Fast Fourier Transform (FFT) of the filter designed in step ‘iv’, extract the amplitude and phase values of the resulting spectrum.

Calculate the number of points occupied by the bandwidth of interest in the FFT plot. For example, if the bandwidth of the signal of interest is 160 MHz, generated digitally at a sample rate of 640 MHz and if the number of points chosen for the FFT is 1024, the number of FFT points occupied by the signal of interest would be 256. Since FFT is a two-sided spectrum, half of the frequency components would occupy the position from 1 to 128 and the other half would occupy the points 897 to 1024 in the example considered. The prime numbers chosen from the first and second key sets are used as coefficient values of parameter  $x$  to provide encryption phases  $y$  in a non-linear mathematical function such as an elliptic function in the form shown in equation (5.15). One of the challenges in designing the group delay variation curve for single carrier schemes is that the variation needs to be continuous to maintain the integrity of the signal’s envelope. This is accomplished by subjecting the values of  $y$  in eq. 5.17 to raised cosine filtering.

The encryption phase values are added to the phases of the FFT of a pre-determined FIR filter and its IFFT is derived to yield the encrypting filter. The phases of the encrypting filter in FFT domain are inverted and subject to IFFT operation to yield the decrypting filter. This completes the design of encryption and decrypting filters to conceal and recover the modulated constellation respectively. These filters are expected to be identical at the two legitimate nodes.

The encryption of the modulated constellation is accomplished by convolving the modulated baseband with the encryption filter at the transmitter in the digital domain prior to conversion to analogue domain and transmission. The recovery of the encrypted modulation symbols is accomplished by convolving the encrypted baseband signal with the decryption filter in digital domain at the receiver. The overall scheme is summarized in Fig. 5.12.

The generated keys are first tested for symmetry with random data case followed by Diffie-Hellman key exchange over phase encrypted signals as explained for the OFDM

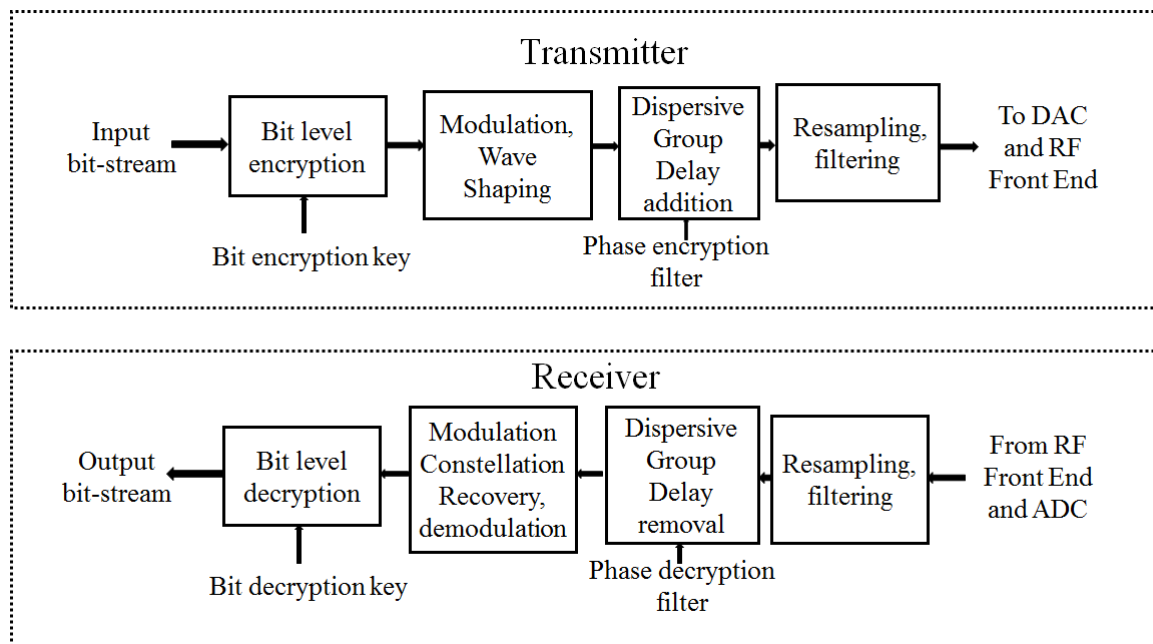


Fig. 5.12.: Proposed Physical Layer Encryption Scheme with Encryption Filter

## 5.5. Experimental Validation

### 5.5.1. Validation of the constellation encryption scheme:

As the first case, it was deemed necessary to validate the scheme of providing security in the physical layer by dispersing the phases and to verify that the original constellation can be restored at the receiver upon decryption. An 8PSK signal was generated in accordance with DVB-S2 standard at a symbol rate of 40 Msps, shaped with a Root Raised Cosine (RRC) filter of roll off factor ' $\alpha$ ' of 0.2 resulting in an occupied bandwidth of 48 MHz. A dispersive filter was designed in MATLAB as described in subsec. 5.4.3 with a peak phase deviation of 10 radians. This filter was convolved with the 8PSK signal to cause constellation distortion to conceal the modulation scheme. These analogue baseband signals were vector modulated through a pair of I and Q DACs, vector up-converted to Ku Band at a carrier frequency of 14.23 GHz. The experimental apparatus used was the same as that described in Chapter 3. A picture of the apparatus is shown in Fig. 5.13 for convenience. The constellation of the modulated Ku Band carrier was observed on a Vector Signal Analyzer (VSA) 'FSQ' of Rohde and Schwarz which was used as a reference receiver.

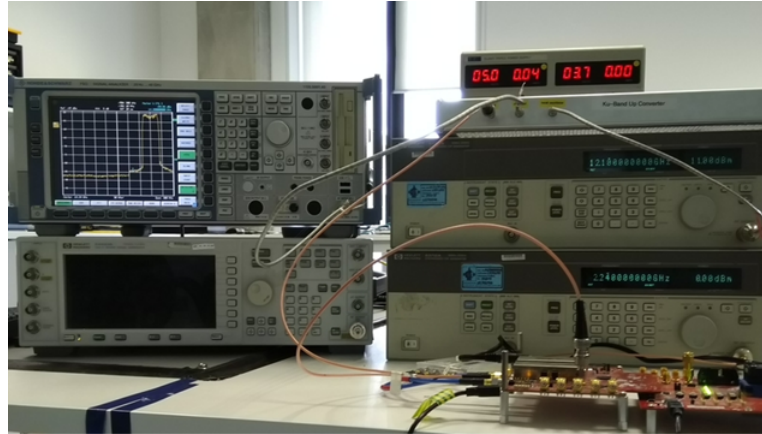


Fig. 5.13.: Ku-Band test bench

i) Undistorted condition: This was the modulated signal constellation before application of the proposed encryption scheme. The screenshot of the 8PSK constellation demodulated by the VSA is shown in Fig. 5.14. The Error Vector Magnitude (EVM) displayed by the instrument was 4.8%.

ii) Encrypted/Distorted condition: This was the condition after the proposed physical layer encryption scheme was applied. The constellation could not be identified as shown in Fig. 5.15

iii) Decrypted/Recovered Condition: This was the condition after applying the recovery filtering to the signal encrypted in 'ii'. The screenshot of the 8PSK constellation demodulated by the VSA is shown in Fig. 5.16. The Error Vector Magnitude (EVM) displayed by the instrument was 4.9%. This was done to verify that the encryption process could be reversed. No change was observed in the power spectrum or occupied bandwidth in all the above cases as shown in the spectrum comparison screenshot shown in Fig. 5.17. The spectrum plots are nearly indistinguishable

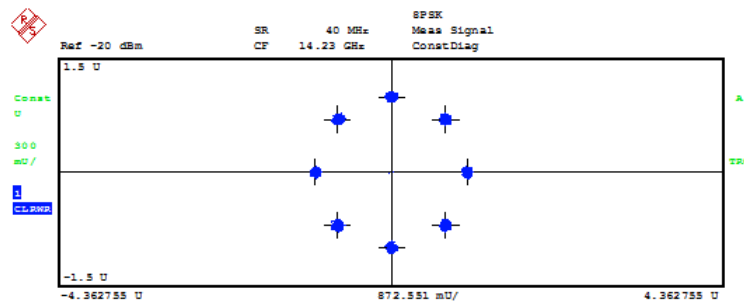


Fig. 5.14.: Original Constellation

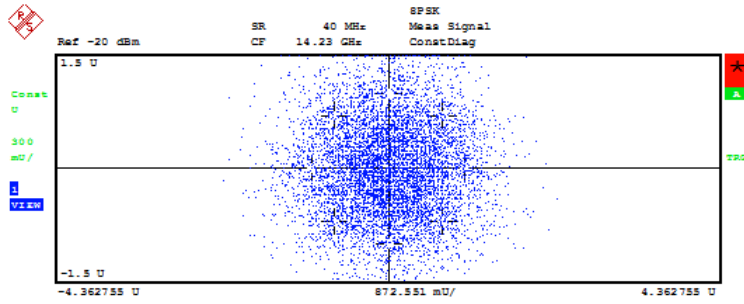


Fig. 5.15.: Encrypted Constellation

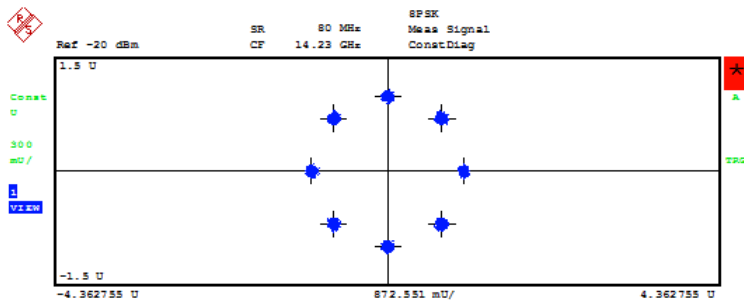


Fig. 5.16.: Recovered Constellation Re-modulated

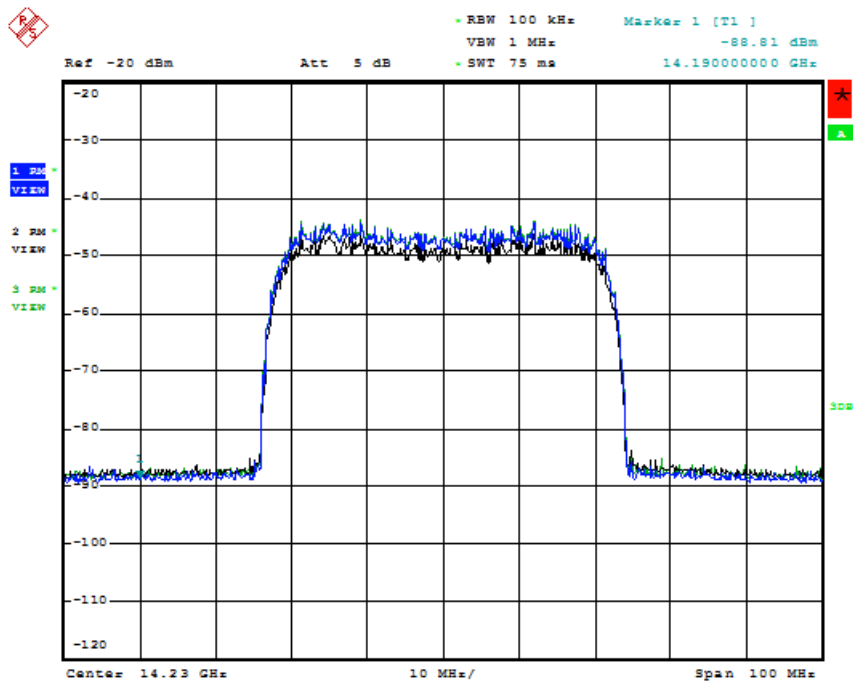
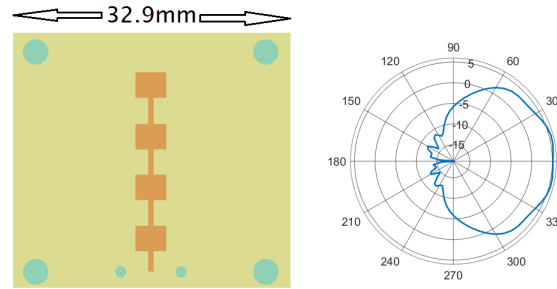


Fig. 5.17.: Spectrum Comparison



**Fig. 5.18.:** Gerber screenshot of the antenna designed and its simulated gain pattern (dBi) in azimuth plane.

### 5.5.2. Experimental Validation of symmetric key generation, encryption and PAPR reduction

The experimental validation was conducted for a QPSK-OFDM signal and for an 8PSK signal case of bandwidth 100 MHz of the same bandwidth. The transmitter and the receiver were built for transmission at carrier frequency 28.9 GHz. The transmitter followed a heterodyne architecture with the intermediate frequency (IF) selected at 600 MHz which was then up-converted to 28.9 GHz. The LO for RF up-conversion was a tuned to 14.15 GHz and was multiplied in frequency by a factor of 2 owing to better phase noise performance than using an oscillator directly at 28.3 GHz to mix with the IF at 600 MHz to yield the modulated carriers at 28.9 GHz at power +2 dBm. The receiver consisted of an RF front end with a noise figure around 3 dB and gain of 13 dB which down-converted the received signal to an IF at 600 MHz. This was followed by an ADC clocked at 4 Gsps that digitized the IF. Further down-conversion and demodulation were accomplished in the digital domain. The antennas were designed to have beam-widths of 120 degrees in the azimuth plane as shown in Fig. 6.23 and etched on RO3003 substrate from Rogers Corporation. An IF amplifier with a gain of 10dB was used in the receiver section of Node 1 and no IF amplifier was used in the receiver section of Node 2 to introduce hardware differences at the two nodes which would introduce differences in the noise figures at the two nodes. The LOs of the nodes were phase locked to a common reference oscillator in this laboratory based experimentation. The techniques to synchronize the oscillators of wireless nodes in the field are provided in [97].

### 5.5.3. Modulation Encryption Key Generation

A wooden test apparatus was designed with propagation path length of a meter between its ends. This distance corresponds to 96 wavelengths at 28.9 GHz. One of the ends of the apparatus was mounted with a patch antenna and termed Node 1. Two additional antennas were fabricated on a similar substrate for Node 2 and Node 3 at a spacing of eight wavelengths with a ground plane in between them.

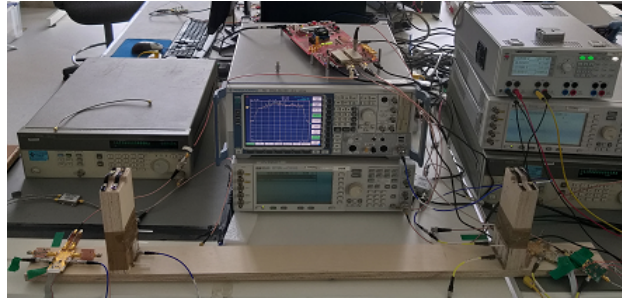


**Fig. 5.19.:** Test Bench used for validation. Node 1 is on the left. Node 2 and Node 3 are on the right. Node 3 is connected to a Vector Signal Analyzer.

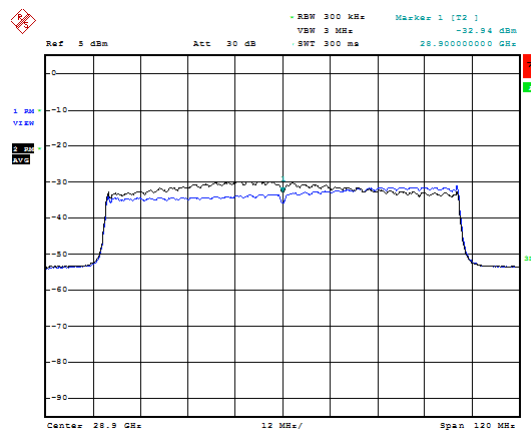


**Fig. 5.20.:** Frequency Responses of Node 1 and Node 2 at 28.9 GHz

Node 2 was termed the second legitimate node and Node 3 was designated to be the eavesdropper. An overall path loss of 51 dB was observed between the legitimate nodes. The evaluation was performed in a regular laboratory environment instead of an anechoic chamber to emulate a real use case scenario that would include multipath propagation effects. A picture of the test bench is shown in Fig. 5.19.

The first task was to calibrate the receiver sections of the two legitimate nodes for flatness of frequency response. This was done using a calibrated signal generator SMW200A of Rohde and Schwarz by sweeping the frequency of an input single tone sine wave from 28.8 GHz to 29 GHz in steps of 5 MHz and recording the variation whose values were used to build an FIR filter to calibrate the frequency response. The next task was to determine the hardware frequency responses of the two nodes over the band of interest. The RF output of each node was connected to a calibrated spectrum analyzer (FSQ40 Vector Signal Analyzer from Rohde and Schwarz). A screenshot of the un-calibrated hardware frequency responses of Node 1 and Node 2 to a chirp stimulus captured on the spectrum analyser is shown in Fig. 5.20.

The third task was to measure the extent of reciprocity of the channel response

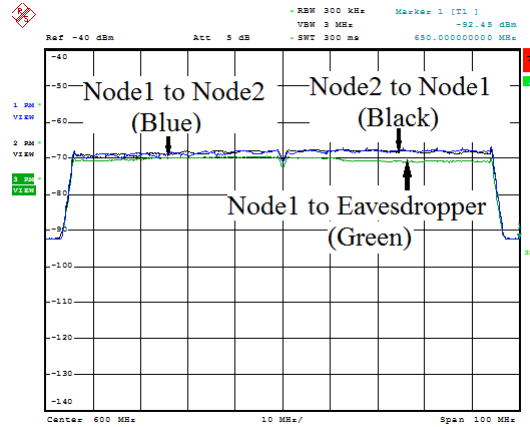


**Fig. 5.21.:** Screenshot of measured channel responses between legitimate nodes and the eavesdropper

between Node 1 and Node 2 (legitimate) and the channel response between Node 1 and Node 3 (eavesdropper). The frequency responses of the transmitting sections of the nodes were measured and recorded in the form of an FIR filter. This was done by taking the element-wise ratio of response to stimulus in frequency domain and multiplying the ratios with the frequency response of a hamming window defined in eq:(eq.5.19).The procedure for this task is detailed in Chapter 3. The inverse transfer function of this FIR filter was derived for each node in the form of another FIR filter to calibrate the transmitting hardware over the bandwidth of interest. Node 1 was configured to receive and Node 2 and Node3 were made to transmit a chirp pulse of duration  $3.125 \times 10^{-6}$  secs at alternate time intervals after the transmitter in each node was calibrated. The sample rate chosen was 640 MSPS. The down-converted IF output of Node 1 was connected to a spectrum analyser and the responses were observed with the traces saved. Node 1 was now configured to transmit and Node 2 was configured to receive and its down-converted IF output was connected to the spectrum analyzer. A screenshot of the recorded channel responses is shown in Fig. 5.21. The channel responses between Node 1 and Node 2 are nearly reciprocal and the channel response between the eavesdropping node Node 3 and Node 1 rolls off at the upper band edge by 2 dB.

Having established the difference in the legitimate and the eavesdropping channels, the next task was to generate symmetric keys between Node 1 and Node 2. The block diagram of the apparatus used is shown in Fig. 5.22. A PC running MATLAB was used as the DSP and timed interrupt generator. A pair of DACs followed by a Ka Band transmitter was connected to each of the legitimate nodes Node 1 and Node 2. The receivers and transmitters RF paths were duplexed with SPDT switches. The probe signal chosen was a chirp pulse of duration  $3.125 \times 10^{-6}$  secs with a bandwidth of 100 MHz generated at sample rate 640 MHz. The transmitters at Node 1 and Node 2 were made to transmit thrice at alternate time intervals of  $3.125 \times 10^{-6}$  sec. The first transmission was from Node 1 and the last was from Node 2.

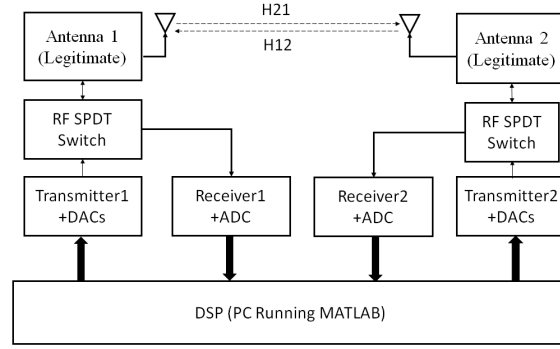


**Fig. 5.22.:** Apparatus used for symmetric key generation

The responses were extracted at the appropriate controlled time slots and saved in separate files for analysis. The responses over three time slots recorded at each node were averaged, filtered, down-converted digitally to zero IF and down-sampled to 400 MSPS. The received signal consisted of a chirp pulse subject to convolution with the impulse response of the channel and the hardware of the transmitting node. The received signal was transformed to frequency domain by an FFT operation to de-convolve the stimulus and the resulting amplitude and phase values were saved in the form of an FIR filter kernel. This was further convolved with the receiving node's own hardware impulse response in transmitting mode. This yielded similar data at both the legitimate nodes whose FFT could be used to derive encryption keys as detailed in Chapter 5.

A bandwidth of 112.5 MHz (100 MHz + additional bandwidth of 12.5 MHz) in a 512 point FFT space sampled at 400 MHz would occupy 144 points symmetrically on both sides. The first and last 72 points which contain the convolved responses were extracted, subjected to moving median filtering of span 3 to be used as the basis for encryption at each node. These basis curves were subject to curve fitting operation for key generation. Plots of the normalised basis curves extracted from the convolved circuit and channel responses individually at each authentic node is shown in Fig. 5.23. The plot of the characteristics measured at Node 2 indicates higher amount of noise. This was due to reduction in the gain at Node 2 which was introduced deliberately to assess the ability to produce symmetric encryption keys in the presence of noise. The effect of noise was mitigated by moving median filtering.

The plotted curve was divided into regions on the basis of change of slope after filtering. Each region was subject to piece-wise curve-fitting operation to a non-linear function of the form  $y = ax + bx^3 + cx^5 + d$  by applying the method of least squares on MATLAB. The values at the 14 frequency bins located at the centre of the curves pertaining to band edges in the received responses were ignored. The ratio  $(d/a)+b$  was computed in each case. In cases where the values obtained for any of the coefficients were less than 0.1, they were replaced by 0. The ratios  $k_{11}$  and  $k_{22}$  obtained at Node 1 and Node 2 when the curves were divided into five regions

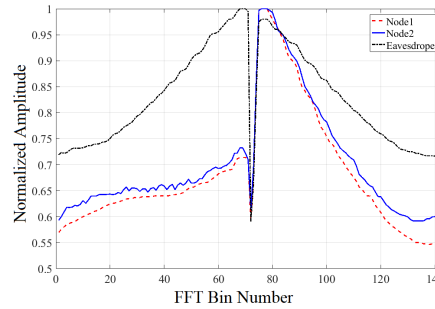


**Fig. 5.23.:** Key generation information consisting of convolved channel and hardware responses evaluated at each node.

are as copied below.

$$set_1 = 5.06257, -1.49450, 0.9875, 30.0487, -11.475$$

$$set_2 = 5.20483, -1.49222, 0.9723, 30.0430, -10.633$$

Each of the coefficient values were multiplied by a power of 10 such that there were atleast two digits before a decimal point and the magnitude was rounded off to the nearest prime number which yielded symmetric sets of the first key at the two nodes.

$$Node1Key1 = 51, 13, 97, 31, 11.$$

$$Node2Key1 = 51, 13, 97, 31, 11$$

The key sets Node1Key1 and Node2Key1 generated were identical at the two legitimate nodes.

This was followed by a second key generation task which involved division of the filtered responses into eight regions of equal lengths of 18 data points and evaluating the RMS (root mean squared) of the magnitudes of the normalised responses in each region. The largest prime number of the index in each region was extracted. The extracted prime numbers were arranged in descending order of the rms value of the region from which they were extracted. The rms values of each region evaluated at Node 1 and Node 2 are as copied below.

$$rmsNode1 = 0.6209, 0.6447, 0.6543, 0.6830, 0.8985, 0.7882, 0.6563, 0.5930;$$

$$rmsNode2 = 0.5719, 0.6072, 0.6217, 0.6504, 0.8871, 0.7815, 0.6351, 0.5551;$$

Referring to Fig. 5.23, one can observe by inspection that the region between data points 73 and 90 would have the maximum rms value. The highest prime number in this region is 89 and hence it would be the first entry in the second key set.

$$Node1Key2 = 89, 107, 71, 113, 53, 31, 17, 139$$

$$Node2Key1 = 89, 107, 71, 113, 53, 31, 17, 139$$

The key sets generated were identical at the two legitimate nodes. The entries in the second key set are just the highest prime numbers in each region but the sequence in which they are entered is critical to generation of the encryption phases. Higher

number of entries can be obtained for both the key sets from response curves with higher number of data points. Subsets of 3 prime numbers from the two key sets at the two nodes were selected by a symmetric algorithm to generate the phase offsets needed to encrypt the spectral characteristics of the modulated signal to be transmitted.

In order to assess the extent to which the encryption data could be generated by the eavesdropper, the RF front end section of Node 2 was connected to Node 3 but a different DAC was used in the base-band section. The convolved channel and hardware frequency responses evaluated at Node 3 with the Chirp stimulus eavesdropped from Node 1 is also shown in Fig. 5.23. This curve is significantly different from that computed at the legitimate nodes and hence would result in different key sets.

Values of base  $g$  and modulus  $p$  for the Diffie-Hellman scheme were chosen to be 51 and  $2^{512} - 51$  respectively. The exponent 'a' chosen at Node 1 was 61 and 'b' chosen at Node 2 was 71. These yielded values of A and B as below. An online tool was used for computation along with low level file read and write operations since a 512 bit number was beyond the ability of the version of MATLAB available.

A = 145137868916494326392263332766856464129464670643080753119747167566412  
174888653062050070925329124534578051;

B = 172775637049938565322123634515964475966237717006844096304361739492667  
84426333262575344791804129467839402142422442056841051

These values were converted to bits and transmitted by Node 1 and Node 2 on modulation encrypted carriers in each of the validation case explained below. The raw bit stream was transmitted in each case without forward error correction (FEC) since the distance was small. FEC may be added as needed in field.

#### **Inference from the test:**

It could be inferred that the presented scheme of exploiting channel reciprocity between two authentic communicating nodes in a wireless network and the uniqueness of their hardware frequency responses provided means to generate symmetric encryption/authentication information with asymmetrically sensed information. While an eavesdropper would be able to receive the transmitted chirp signals by the legitimate nodes, the signals would have traversed through channels whose frequency responses were different from that between the legitimate nodes. Since the impairments in the chirp signals received by the eavesdropper are essentially a convolution of the channel (eavesdropping) and hardware responses and both are unknown, the encryption information is obfuscated from the eavesdropper.

#### **5.5.4. Encryption of an OFDM signal**

The proposed security scheme was tested on an OFDM system as the second case. A 2048 point FFT based OFDM signal with 1664 active sub-carriers including 128

pilots was generated at sample rate 100 MHz. The modulation chosen for the sub-carriers was QPSK. The data to be transmitted was mapped on to QPSK constellation points on the 1536 active sub-carriers. The amplitudes of all the active sub-carriers were constant since the chosen modulation scheme was QPSK. A constant phase of 45 degrees was chosen for the pilots. The objective here was to encrypt the signal to jointly achieve PAPR reduction and security in the physical layer. The randomization of the phases of the sub-carrier is one of the ways to reduce PAPR for which the selection of the encryption phases at the transmitter and its knowledge at the receiver are critical. A random stream of 3072 bits was generated at Node 1 and modulated on the 1536 data subcarriers with QPSK modulation.

$$z_1 = ((f_1x^3 + f_2x) \bmod_{f_3}) \bmod_{2\pi} \quad (5.21)$$

$$z_2 = ((f_2x^3 + f_3x) \bmod_{f_1}) \bmod_{2\pi} \quad (5.22)$$

$$z_3 = ((f_3x^3 + f_1x) \bmod_{f_2}) \bmod_{2\pi} \quad (5.23)$$

$$z_4 = (z_1z_2z_3) \bmod_{2\pi} \quad (5.24)$$

The next task was to generate chaotic phase values to encrypt the spectrum of the OFDM signal. This was done by applying a subset of three prime numbers in the key sets Node1Key1 and Node1Key2. The values of  $f_1, f_2$  and  $f_3$  selected for this operation were 47, 89 and 17 respectively. Three sets of encryption phases each of length 1664 were generated applying the selected prime numbers in elliptic functions as per equations (eq. 5.21, eq. 5.22 and eq. 5.23) and a fourth set was generated by taking the element-wise products of the first three sets to modulo  $2\pi$  as described by (eq. 5.24). The ratio of variance to mean was computed for each set and the phases in the set that had the highest ratio was chosen for encryption. This was computed at both nodes for symmetric encryption and decryption. The set  $z_4$  was the best candidate hence the phase values in its set were added to the phases of the 1664 active sub-carriers (excluding null sub-carriers) at Node 1 for encryption. A plot of the constellation of the encrypted sub-carriers is shown in Fig. 5.24. The IFFT of the encrypted subcarriers was computed to yield the time domain signal. A cyclic prefix of 144 samples was appended and the signal was up-sampled by a factor of 2 and transmitted over the 28.9GHz air interface after the necessary signal processing operations. It was observed that the average PAPR of the encrypted signal was

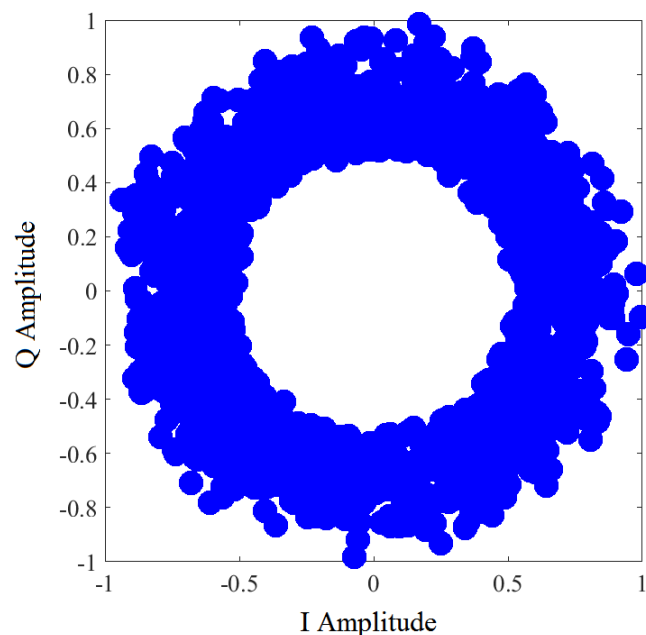


**Fig. 5.24.:** Phase encrypted OFDM sub-carriers received over the 28.9GHz wireless link.

reduced by 3 dB. This aspect is explored further in the next sub-section. The signal was received at Node 2, down-sampled to the original sample rate after the necessary signal processing operations and the added cyclic pre-fix was removed. The FFT of the received signal was computed and the sub-carriers and subject to decryption of phases. This led to the successful recovery the transmitted constellation. A plot of the constellation of the decrypted sub-carriers is shown in Fig.5.25. The amplitudes of the sub-carriers were equalized and were demodulated to recover the original bit stream without errors. As the next task, the preliminary Diffie-Hellman keys A and B were exchanged on the wireless link after appending zeros in the beginning to make the length equal to 3072 bits and encrypting the resulting bit-stream with the random bit-stream exchanged earlier. The process was reversed at the receivers to recover the values of A and B which were then used to compute the values of the final keys  $A_1$  and  $B_1$  as in the single carrier case.  $A_1$  and  $B_1$  were used as the encryption and decryption keys for further transmissions. The validation was repeated thrice successfully with different bit streams and encryption keys.

**Inference from the test:** Symmetric keys for encrypting the modulated constellations of an OFDM signal were generated. The encryption of the modulated constellations authenticated the generation of bit level encryption keys as per Diffie Hellman key exchange scheme. This authentication serves to mitigate impersonation attacks in a wireless network where an un-authorized node can attempt to initiate key exchange with an authentic node.

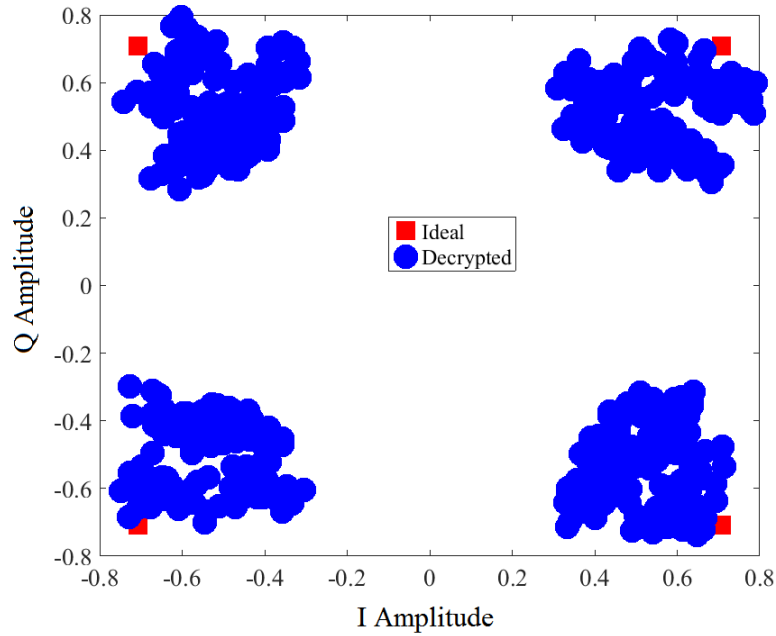


**Fig. 5.25.:** Recovered QPSK constellation of OFDM sub-carriers received over the 28.9 GHz wireless link.

### 5.5.5. PAPR Reduction

Simulations were carried out in MATLAB for 10000 cycles of randomly generated bit streams, modulation and encryption of the subcarriers with the same encrypting phases generated using the encryption key as that used for the validation of the security aspect in the previous subsection. From this it was possible to identify a scheme that would simultaneously reduce PAPR and provide physical layer security. The CCDF plots for the resulting reduced PAPR signal are shown in Fig. 5.26 as mentioned in Chapter 5. The proposed scheme reduced the PAPR by 3.5dB on average and by over 4.2 dB when there is a  $2 \times 10^{-4}$  probability of the original signal exceeding a threshold PAPR of 15.5 dB on the OFDM signal generated in the previous sub-section.

The above test was repeated with QAM 64 modulated sub-carriers and keeping the rest of the parameters same. The proposed scheme reduced the PAPR by 5.2dB on average and by over 5.5dB when there is a  $1 \times 10^{-4}$  probability of the original signal exceeding a threshold PAPR of 17.2dB

A comparative plot of the original and the reduced PAPR is shown in Fig. 5.28

A plot of the PAPR recorded over 10,000 simulation cycles is shown in Fig. 5.29. A limitation in this scheme is that the receiver would need a higher signal to noise ratio than time domain PAPR reduction schemes when this scheme is applied to OFDM signals with higher modulation constellations but the ability to recover the

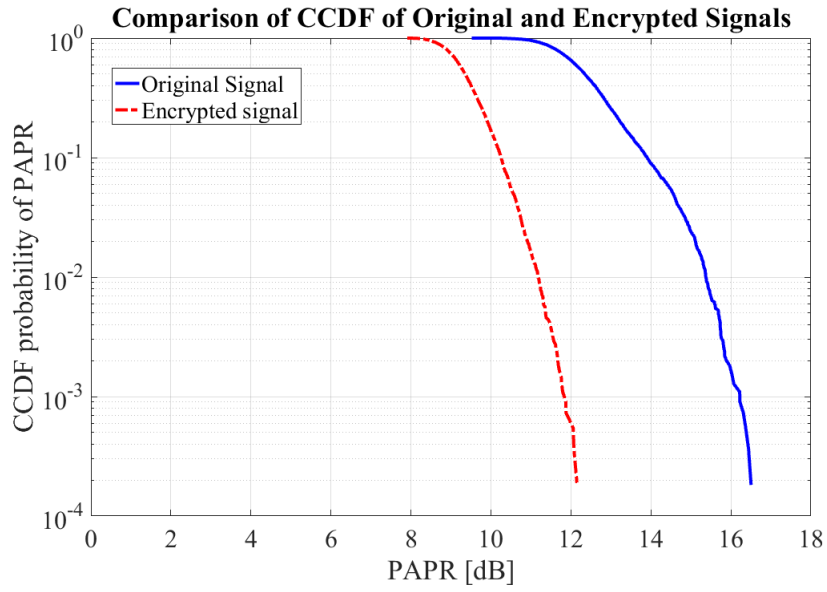


**Fig. 5.26.:** CCDF of PAPR of Original and Encrypted 2048 point QPSK-OFDM modulated signals with 1664 active sub-carriers

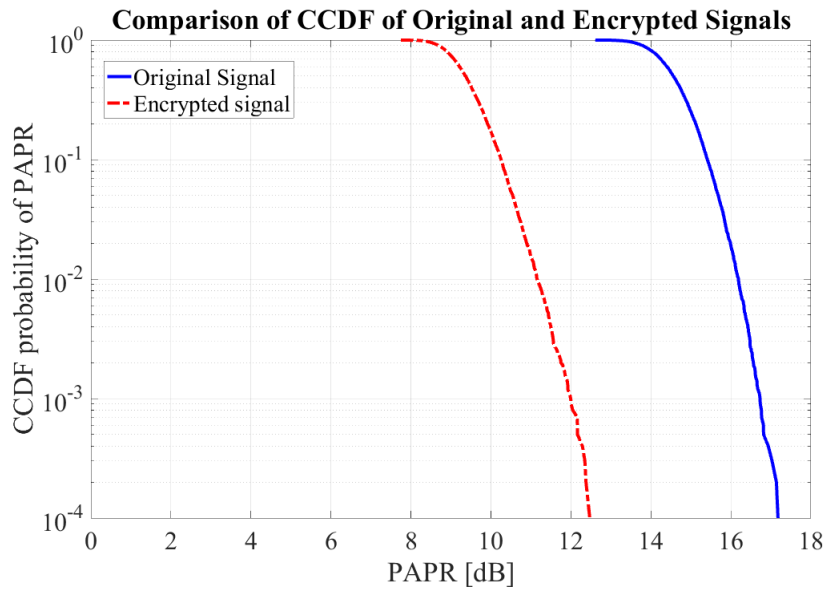


**Fig. 5.27.:** CCDF of PAPR of Original and Encrypted 2048 point QAM64-OFDM modulated signals with 1664 active sub-carriers

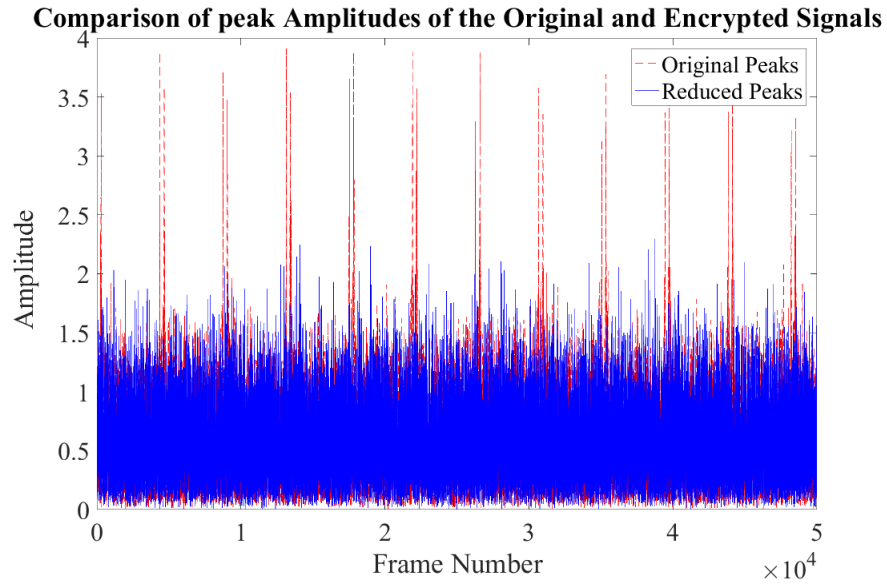


Fig. 5.28.: Comparison of amplitudes of the original and encrypted signals

bit-stream without the need for side information and the reduction in linearity requirements of the PA in the transmitter outweigh the limitation.

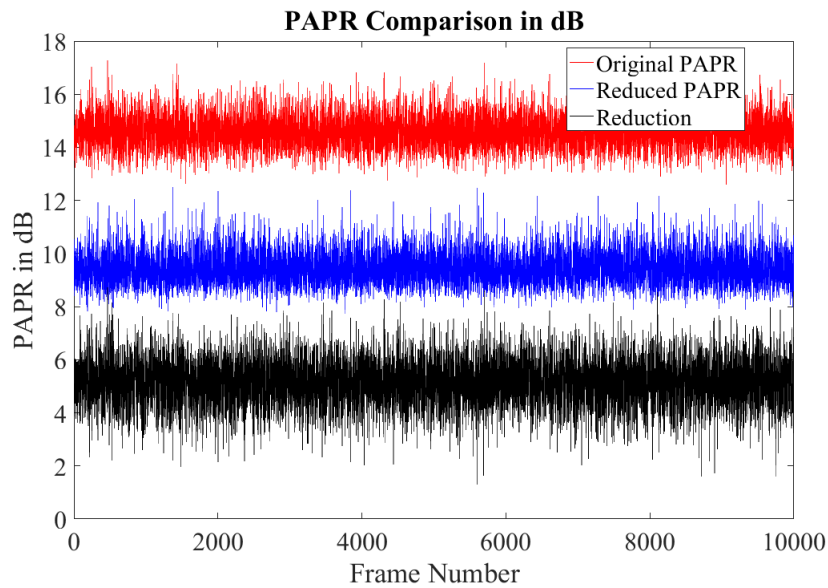


Fig. 5.29.: PAPR comparison over 10000 simulation cycles

**Inference from the test:** The proposed encryption of the modulated constellations of an OFDM modulated signal reduces PAPR by more than 3dB which would benefit in increasing the efficiency of RF power amplifiers in wideband transmitters for next

generation wireless communications.

### 5.5.6. Encryption of Single Carrier Modulated Signals

An 8PSK modulated signal of bandwidth 96 MHz was chosen for this case. The symbol rate was set at 80 Msps. The modulated digital baseband was subject to raised cosine filtering with roll off factor  $\alpha = 0.2$  at an oversampling ratio of 4. The resulting sample rate was 320 Msps and the occupied bandwidth was  $80 \times 10^6 (1 + \alpha) = 96$  MHz. The minimum in-band nonlinear peak phase variation needed to encrypt this signal calculated as explained in chapter 5 was 7.23 radians.

A random bitstream of 18000 bits was chosen to test the symmetry of the constellation encryption keys. The phases for the encrypting filter at Node 1 were derived by applying three of the thirteen entries in the key sets Node1Key2 and Node1Key2 as coefficient values in the elliptic function described by eq. 5.25.

$$y = p^2 = (x^3 + f_1x + f_2) \bmod_{f_3} \quad (5.25)$$

The values of  $f_1$ ,  $f_2$  and  $f_3$  selected for this operation were 47, 89 and 17 respectively to encrypt the first 6000 bits. The values of  $f_2$  and  $f_3$  were swapped to generate the encrypting symbols for the next 6000 8PSK modulated data symbols and so on to test for symmetry of the constellation encryption keys generated at both nodes.

The first 39 values of the designed phase response were extracted, subject to root-raised cosine filtering with an up-sampling factor of 4 and added to the phases of the FFT of a Hamming windowed FIR filter of length 320. The IFFT of the modified filter was computed to obtain the encrypting filter at Node 1. The phases of the encrypting filter in the frequency domain were inverted and the IFFT was computed to obtain the decrypting filter at Node 2. The 8PSK modulated data symbols of the random bitstream were subject to RRC filtering as per DVB-S2 standard, convolved with the encrypting filter at Node 1 to conceal its constellation. The encryption and decryption filters were switched after transmission of 6000 symbols to avoid detection of the encrypting phases by an adaptive equalizer in the eavesdroppers. The encrypted signal was transmitted over the air interface at 28.9 GHz, received by Node 2, subject to equalization and decryption filtering, down-sampling and recovery of symbols. The recovered symbols were decrypted and the transmitted bit-stream was demodulated without errors. A plot of the received constellation of an 8PSK signal prior to equalization and decryption is shown in Fig. 5.30. The 8PSK constellation after decryption and channel equalization is shown in Fig. 5.31. This task verified the symmetry of the constellation encryption keys.

A VSA (Vector Signal Analyzer) with an internal equalizer based on LMS (Least Mean Squares) was used as the eavesdropping receiver. The length of the equalizer was set at 10 and step size was set at 0.05. The sampling frequency of the VSA

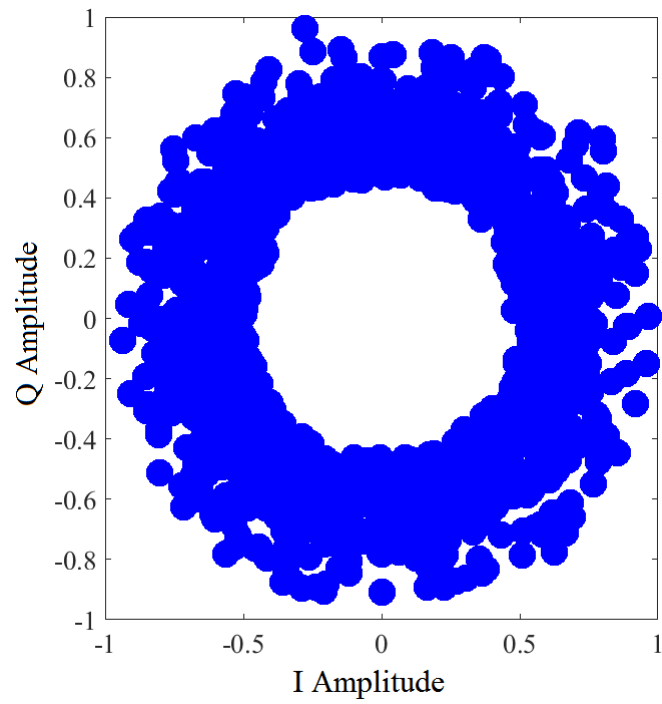


**Fig. 5.30.:** First 1000 symbols of the received encrypted 8PSK signal before decryption and equalization.

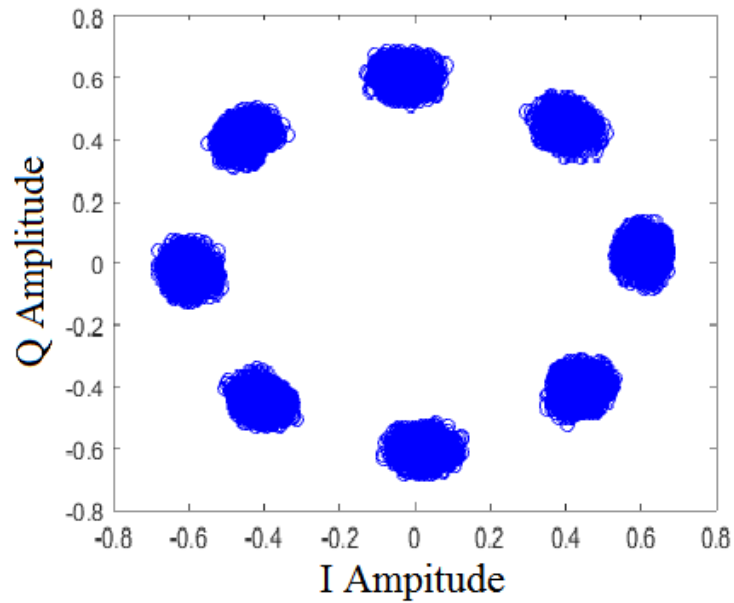


**Fig. 5.31.:** Recovered 8PSK constellation after decryption filtering and equalization.

was also set at 320 MHz. This implied 40 taps for the internal filter due to an over-sampling factor of 4. The transmission was repeated continuously for five minutes and a faithful recovery of the constellation could not be observed. The length of the equalizer in the VSA was varied from 5 to 20 in steps of 5 and step size was also switched between 0.01 and 0.05 in each case after running for 5 minutes. No faithful recovery of the constellation could be observed in any attempt. All the modulated symbols were then subject to encryption by only the first filter instead of switching between multiple filters. This led to partial identification of the symbols after a learning time of 8 minutes. It was inferred that switching the encryption filter provided tighter security against eavesdroppers. The observations demonstrate that it is essential to use the appropriate decryption filter to first recover the modulation symbols before attempting to demodulate the signal. As the next step, the bitstream for Diffie-Hellman preliminary keys A and B were generated at Node 1 and Node 2 respectively. Since A and B could be of different lengths, zeros were appended in the beginning of the respective bitstreams to make the length  $l$  equal to that of the modulus. The resulting bitstream was encrypted with the first  $l$  bits from the random bitstream transmitted earlier, modulated on 8PSK symbols and transmitted after encrypting the constellation. The process was reversed at the respective receivers and the transmitted values of A and B were recovered. These were subject to the computation of final keys:  $A_1 = (B^a) \bmod_p$ ;  $B_1 = (A^b) \bmod_p$ ;

The values of  $A_1$  and  $B_1$  were used to encrypt and decrypt data bits in further transmissions without errors.

**Inference from the test:**

Symmetric keys for encrypting the modulated constellations of a single carrier wide-band signal were generated. The encryption of the modulated constellations authenticated the generation of bit level encryption keys as per Diffie Hellman key exchange scheme. This authentication serves to mitigate impersonation attacks in a wireless network where an un-authorized node can attempt to initiate key exchange with an authentic node.

## 5.6. Conclusion

In this chapter, a novel scheme to provide security in the physical layer along with reducing the peak to average power ratio of OFDM signals through dispersion of the phases of the modulated signal has been presented. The scheme conceals the modulated constellation from eavesdroppers using symmetric encryption keys which are generated at the legitimate communication nodes exploiting the channel and non-ideal circuit characteristics over the bandwidth of interest. Bit level encryption keys are further exchanged over carriers whose modulations are concealed thereby providing immunity against impersonation attacks. It has been demonstrated that the applied encryptions can be successfully reversed at the legitimate receiver on

the experimental test bench to recover the original modulated symbols with zero bit errors. The proposed physical layer encryption technique successfully concealed both single carrier and OFDM modulated signals from a well-positioned eavesdropper and a reduction of PAPR by 4.2dB and 5.2dB respectively were achieved for an OFDM signal with 1664 QPSK modulated sub-carriers.

## 6. Bandwidth Interleaved Modulators and Transmitters

In this chapter, novel schemes to mitigate the problem of transmitting wideband complex envelope modulated signals using interleaved RF transceiver hardware of narrower bandwidths are presented. The novelties presented in this chapter correspond to items 1, 4 and 9 in the list of publications. The author's contributions to the novelties presented in this chapter are architectures for bandwidth interleaved modulators and transmitters with in-circuit and spatial combining, calibration of paths for seamless combining, experimental validation including designing the test apparatus.

### 6.1. Introduction:

Future wireless communication systems such as fifth generation mobile communications and high throughput satellites are expected to feature throughputs ranging up to several gigabits per second. This requires a proportional increase in the bandwidths for the wireless channel and the hardware involved in transmission and reception of the modulated signals. The upper limit of the bandwidth of the signal that can be generated depends on the maximum sample rate of the DACs in the modulators. The constraint of bandwidth is not just limited to generation of the modulated signal but to every part involved from generation to transmission including the filters, amplifiers and the antennas. In this chapter, published techniques to generate wideband signals using DACs of relatively narrower bandwidths are discussed and a novel technique to generate and transmit wideband signals using legacy transmitter hardware is presented.

A block diagram of a typical vector RF modulated heterodyne transmitter is shown in Fig. 6.1. A digital signal processor (DSP) generates the vector modulation symbols called basebands (BB) in accordance with the digital data meant for transmission. These digital basebands are applied to a pair of DACs to generate the equivalent in-phase (I) and quadrature (Q) analogue baseband waveforms. These waveforms are vector up-converted to the required intermediate frequency (IF) and further up-converted to the RF carrier frequency which is amplified by the RF power amplifier (PA) and transmitted. The baseband may be directly up-converted to RF in homodyne transmitters. The maximum operating bandwidth of a transmitter is

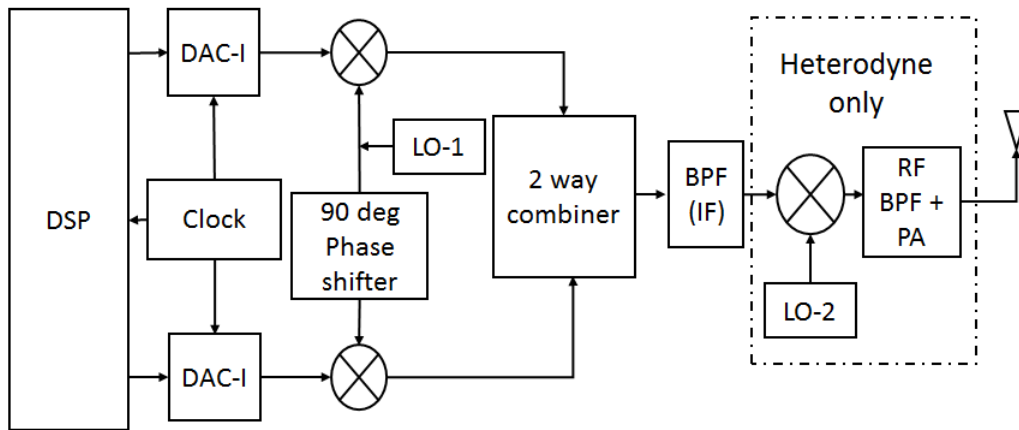


Fig. 6.1.: Generic block diagram of a wireless transmitter

constrained by the bandwidths of the individual blocks that constitute the transmitter such as the DACs, PA and passive microwave modules. The problems associated with the bandwidth in a transmitter were introduced in Chapter 2. The problems are discussed in greater detail in this section.

**Digital to Analogue Converters:** The most obvious factor that imposes an upper limit on the usable bandwidth of a DAC is its sample rate. The maximum sample rate is affected by the switching characteristics of the transistors in the current steering cells of the DAC whose slewing and settling times affect the maximum speed of operation.

Another factor that imposes an upper limit on the bandwidth of the signal that can be obtained from a DAC is the non-ideal anti-aliasing filter. An ideal anti-aliasing filter would have a brick-wall frequency response which is not practical which limits the usable bandwidth to lower than Nyquist rate.

In addition to these, DACs exhibit sinc-roll off which attenuates the signals at the Nyquist frequency by 3.9 dB. The frequency response of a DAC is of the form described by eq. 6.1 where the  $T_s$  is the sampling interval  $f$  and is the frequency of the signal. This implies that a signal component at Nyquist frequency will suffer an attenuation of 3.92dB. A concise description of impact of DAC and ADC limitations on system performance is provided in [98].

$$H(f) = \frac{\text{Sin}(\pi f T_s)}{(\pi f T_s)} \quad (6.1)$$

The role of DACs in a wireless transceiver is to generate modulated basebands for transmission with a signal to noise ratio (SNR) higher than that defined by Shannon's theorem. This parameter is constrained by number of bits 'N', non-linear

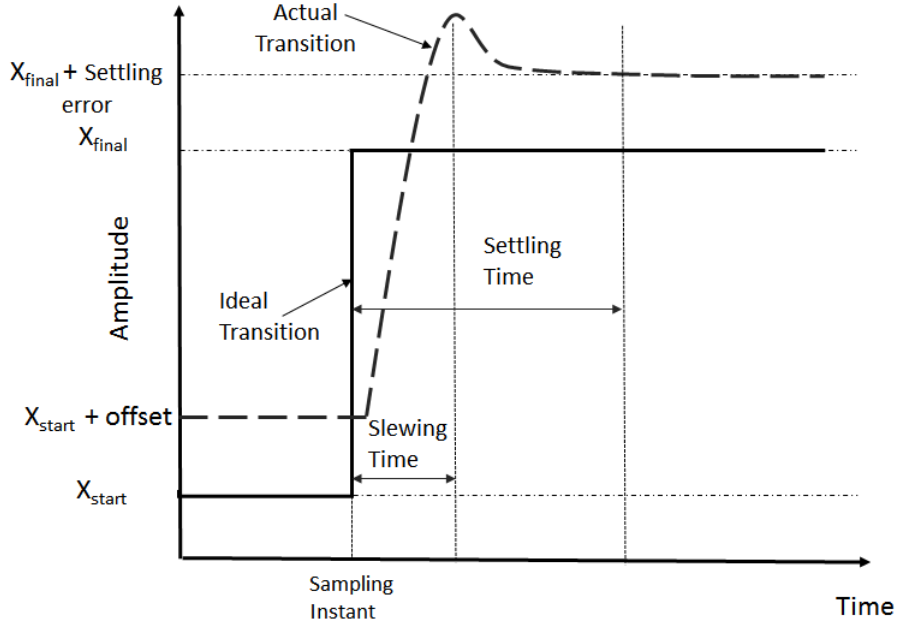


**Fig. 6.2.:** DAC slewing and settling times.

distortion and sample rate. The signals encountered in wireless communication applications such as OFDM consist of multiple tones and the time domain envelopes exhibit a high peak to average ratios (PAR). The value of SNR reduces with increasing PAR to the value computed as per eq. 6.3.

$$\text{SNR} = 6.02N + 4.77 - 20\text{Log}_{10}(\text{PAR}\sqrt{2}) + 10\text{Log}_{10}(\text{BW}/f_s) \quad (6.2)$$

$$\text{SNR}_{\text{multi}} = \text{SNR}_{\text{single}} - 20\text{Log}_{10}(\text{PAR}\sqrt{2}) \quad (6.3)$$

Further information on impairments caused by the DAC are given in Appendix 2. Another factor that reduces the SNR in DACs is the timing jitter  $T_{\text{jitter}}$  in the sampling clock. The rise in noise  $N_{\text{jitter}}$  caused by jitter is given by eq. 6.4

$$N_{\text{jitter}} = -20\text{Log}_{10}(2f_{\text{signal}}T_{\text{jitter}}) \quad (6.4)$$

It may be inferred that there is a necessity to increase the sampling rate for a DAC to increase the SNR and the operating bandwidth. This has been done by interleaving more than one DAC in time and frequency domains as discussed in the next section.

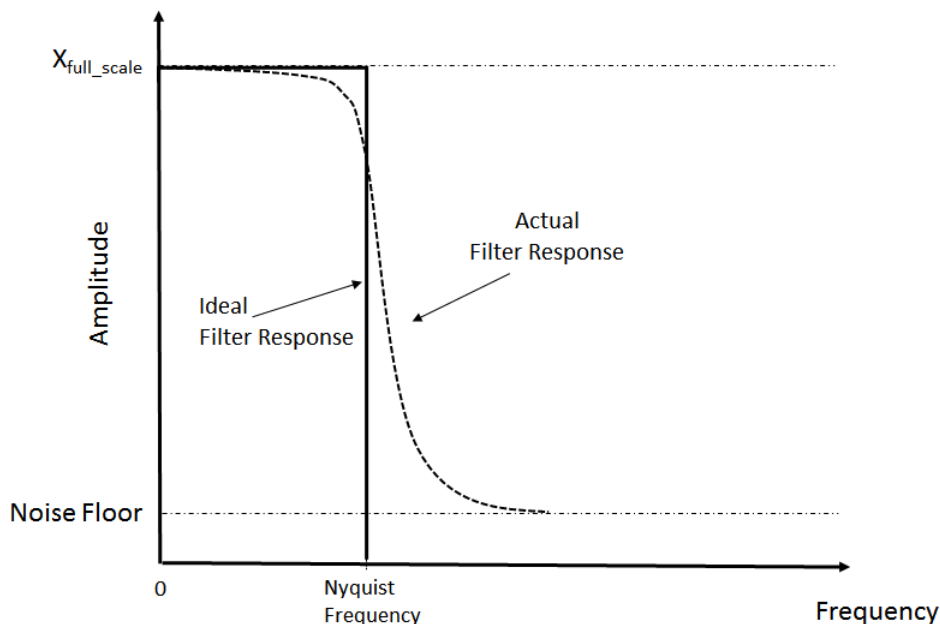


**Fig. 6.3.:** Response of Anti-Alias Filter

**RF Matching Circuits** The popularly known maximum power transfer theorem states that maximum power is transferred from source to load if their impedances are matched in a conjugate manner. It is no secret that reactance varies with frequency. Inductive reactance increases with frequency and capacitive reactance reduces with frequency. Under the maximum power transfer condition, the source and load reactances cancel out due to resonance. But this can happen at only one frequency. Mismatched load and source impedances lead to inefficiencies caused by reflections of the power from the load and therefore it is not possible to achieve perfect power transfer over a broad range of frequencies without reflections. The relation between reactive load and reflection coefficient over a specified bandwidth is provided by Bode-Fano criterion

$$\int_{\omega_1}^{\omega_2} Ln \frac{1}{|\Gamma_{\min}|} d\omega \leq \frac{\pi}{RC} \quad (6.5)$$

where  $\Gamma_{\min}$  is the magnitude of the minimum reflection coefficient,  $\omega_1$  and  $\omega_2$  are the lower and higher angular frequencies. This limits the achievable impedance matching required for effective power transfer and is particularly critical with RF power amplifiers.

**Pre-distortion of RF Power Amplifiers:** The cost and power consumption of an RF power amplifier are major contributors to cost and power budget of the

entire transmitter and it is imperative to get maximum RF output power from it. Various architectures for the RF power amplifier were discussed in Chapter 4. A limiting factor in linearization of high efficiency architectures is the bandwidth. Wider bandwidths in the modulated envelope lead to greater memory effects and pose greater computational challenges in behavioural modelling and digital pre-distortion. OFDM signals with wider bandwidths and greater number of sub-carriers exhibit larger PAPR values requiring greater linearity in power amplifiers at the cost of efficiency. Since a power amplifier is a strongly non-linear device, its higher orders of non-linearity result in parasitic bandwidth expansion and in-band AM-AM and AM-PM distortions as seen in Chapter 4. The bandwidth of the DAC needed to perform digital pre-distortion (DPD) to mitigate these impairments is proportional to the order of non-linearity. Considering a simplified behavioural model for an RF power amplifier of order 5 implies a bandwidth requirement of five times the channel bandwidth for the DACs. In addition to these, the bandwidth of the components needed to accomplish digital pre-distortion also increases. Non-linear transfer functions were introduced in Chapter 2.

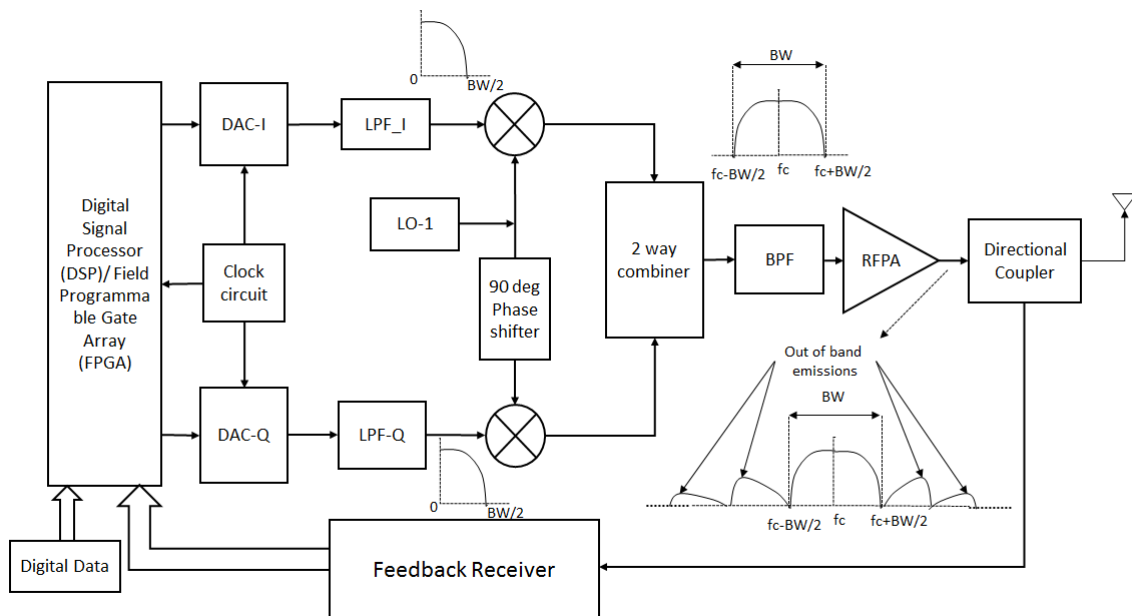


**Fig. 6.4.:** Transmitter with feedback for DPD

It may be inferred that the bandwidth in the feedback path is five times the channel bandwidth of the transmitter. Band-limited DPD techniques have been developed to avoid using ADCs in the receiver with five times the channel bandwidth but it is inevitable for the DAC. The effectiveness of DPD depends upon the accuracy of the receiver in the feedback path to sense and capture the impairments. It was observed in Chapter 2 that odd order non-linear transfer functions also result in parasitic products within the channel bandwidth which may be sensed to estimate

the coefficient values of the non-linear terms. This depends on the SNR of the ADCs which in turn depends on the bandwidth.

## 6.2. Prior Art Techniques to mitigate the problems

### 6.2.1. Digital to Analogue Converters:

The problem of generating wider bandwidth baseband signals has been accomplished by multiplexing [99, 100] and interleaving DACs in time [101, 102, 103, 104, 105] and frequency domains [106, 107, 108, 109, 110]. Time domain interleaving has been the most popular method of the three used by manufacturers for its ease of implementation in an integration circuit.

**a) Time Multiplexed DACs:** A schematic block diagram of a 2 way multiplexed DAC is shown in Fig. 6.5.

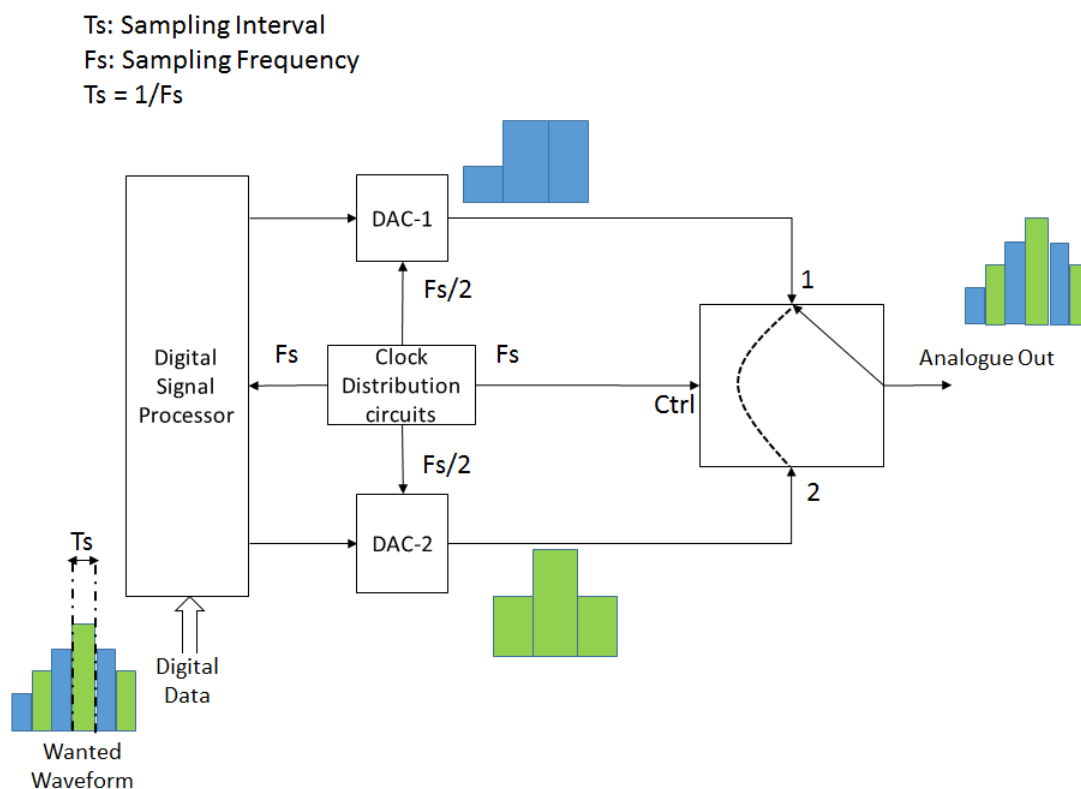


**Fig. 6.5.:** DAC Multiplexing

A multiplexer is used to select between the outputs of DACs running at half the sample rates. The number of multiplexed stages can be scaled up using a multiplexer

of higher order and faster clocking rates. The switching speed of the multiplexers and cross talk between the multiplexed paths limit the maximum sample rate. The multiplexer needs to be operated at the original sample rate  $F_s$ . The available SNR is affected by the timing jitter caused at the higher switching frequency. The quality of the signal is also affected by the mismatch in gains between the multiplexed paths and differences in the electrical lengths of the transmission lines running between the output of each DAC and the multiplexer and also the offsets in the phases of the clocks fed to each DAC. Scaling up the number of multiplexed paths needs a multiplexer of higher order along with associated circuit extensions for the address lines to control the multiplexer. The problem of mitigating the cross talk through digital pre-processing/digital pre-compensation complicates with higher number of multiplexed paths.

An analysis of degradation in signal to noise and distortion ratio (SNDR) caused by offset in the duty cycle of the clock signals fed to two multiplexed DACs. A 6-bit time two way interleaved DAC operating at 20 GSPS is presented in [103]. The authors report a spurious free dynamic range of 35 dB. This would suffice for single carrier lower order modulation scheme but would be insufficient to meet the signal quality requirements of 64-QAM or 256-QAM modulated OFDM signals with over 1200 active sub-carriers exhibiting a PAPR greater than 9 dB. In [99], the authors provide an insight of the process of multiplexing DACs, provide methods to mitigate the images in higher Nyquist zones and demonstrate the transmission of a (four levels pulse amplitude modulation) PAM-4 signal at symbol rates of 80 GBaud over an optical link. The measured BER at the output of the multiplexer was  $2.6 \times 10^{-4}$  but deteriorated to  $5.9 \times 10^{-4}$  after amplification. In [100], the authors have implemented two way multiplexed DACs with sample rates up to 52 GSPS for optical communications with baud rates up to 92 Gbaud using 16-QAM modulation schemes at a BER of  $2.63 \times 10^{-2}$ . While the speeds obtained are more than 50 times of those needed for wireless communications, the available SNR values are not suitable for transmission of higher order modulated signals such as 64-QAM encountered in wireless communications.

**b) Time Interleaved DACs:** A schematic block diagram of a 2 way interleaved DAC is shown in Fig. 6.6.

In a two way time interleaved DAC, the digital data for odd and even samples are separated and applied to the first and second DACs separately. The clock input to the second DAC is delayed by half a period relative to the first DAC and the two outputs are summed instead of being switched. This method has an advantage of cancelling images at odd Nyquist zones. However, it is critical to maintain the relative timing delay of half of the sampling period between the two paths. This complicates further as the number of interleaved stages is increased. If  $N$  stages are interleaved, the relative delay in the clock phase between successive paths should be  $T/N$  where  $T$  is the operating sampling period/interval of the DACs. Mismatches

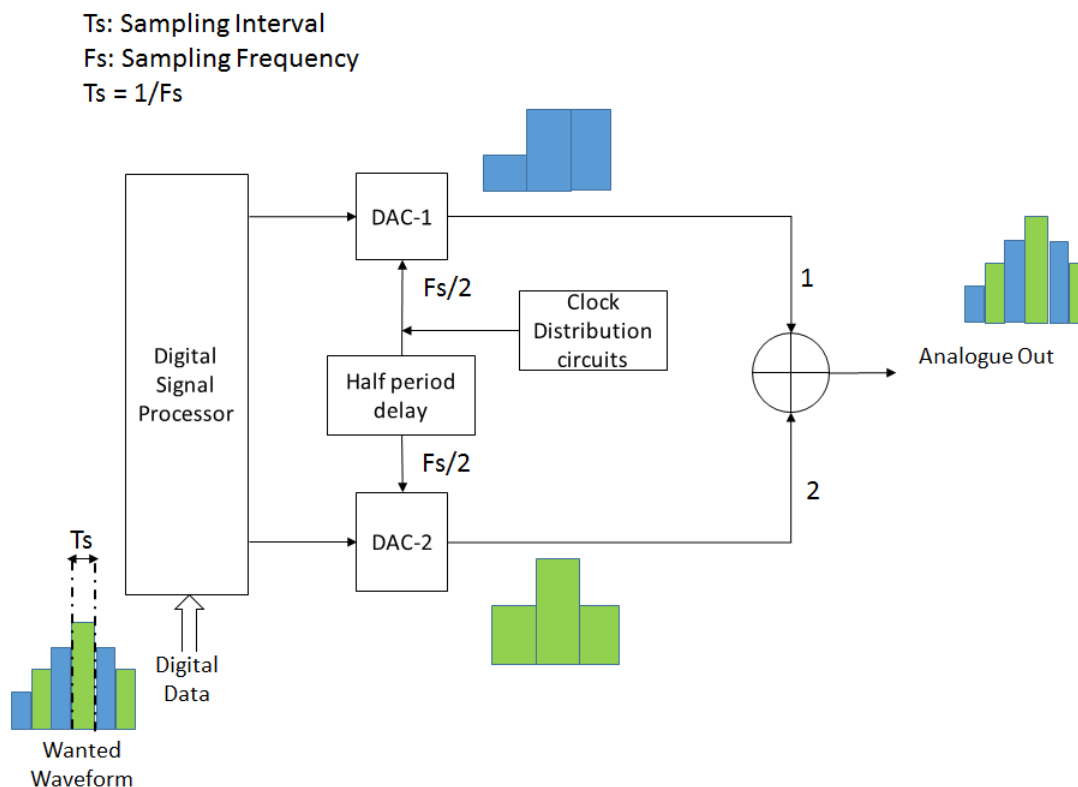


**Fig. 6.6.:** DAC Time Interleaving

in the delays between successive stages leads to glitches and interleaving spurs. The quality of the signal is also affected by the mismatch in gains between the interleaved paths and differences in the electrical lengths of the transmission lines running between the output of each DAC and the combiner.

A systematic analysis of time interleaved DACs is provided in [104]. Methodology to mitigate mismatches in time interleaved DACs is reported in [111]. In [105], the authors demonstrate the bandwidth enhancement of a delta-sigma DAC using time interleaved delta sigma modulators achieving SFDR of 42 dB at a sample rate of 30.72 MHz aimed at generation of baseband signals modulated as per LTE standards. However, this figure would deteriorate at higher sampling rates due to timing jitter. In [102], the authors demonstrate an all-digital RF transmitter for operation at a carrier frequency of 5.2 GHz with time interleaved delta-sigma DACs operating 28 GSPS. A signal to noise ratio of 49 dB is reported over a bandwidth of 219 MHz. While this is novel, implementing such a scheme for millimetre wave wireless communications is expensive and the SNR would deteriorate further due to jitter in clock signals at higher sampling rates. The available SNR would also deteriorate if the signal is up-converted to millimetre wave frequencies due to phase noise of the local oscillator.

**c) Frequency Domain Interleaved DACs:** Any signal having a finite bandwidth is made up of several sinusoidal tones of distinct amplitudes and phases. The amplitudes and phases of the constituent sinusoidal tones can be obtained by taking the Fourier transform of the signal of interest. Digital signals are discrete in nature. A digitally generated baseband signal  $m(t)$  may be represented by a series of complex sinusoids each having an amplitude  $a_n$  and phase  $\theta$  that constitute the signal in the form of discrete Fourier transform (DFT) having a total of  $N$  frequency bins in the overall bandwidth as shown eq. 6.6. The instantaneous time  $t = nT_s$  for a sampled data system where  $n$  is the sample number and  $T_s$  is the sampling interval.

$$m(nT_s) = \sum_{n=-N/2}^{N/2} a_n e^{j\theta} e^{j\omega n/T_s} \quad (6.6)$$

As each component in eq. 6.6 is characterized by a distinct amplitude, phase and frequency, it may be inferred the generation of a wide bandwidth signal can be accomplished in parts using more than one DAC with smaller bandwidths as long as the integrity of the amplitude, phase and timing of each frequency component of  $m(nT_s)$ . The concept of frequency domain interleaving in data-converters was introduced by Le-Croy in 2006. The concept was termed digital bandwidth interleaving which was applied to extend the bandwidth of oscilloscopes to 30 GHz using ADCs interleaved in frequency domain by Pulaikis [112] of Le Croy Instruments. A doctoral thesis was published on wideband signal acquisition with frequency interleaved ADCs by Steven Callender [113]. The task of frequency domain interleaving DACs poses greater challenges with signal quality than the ADC since it is necessary to combine the interleaved signals in analogue domain. This requires appropriate knowledge of the hardware characteristics to pre-compensate the interleaved signals so that they combine with appropriate amplitudes and phases. The block diagram of two DACs interleaved in frequency domain is shown in Fig. 6.7.

This arrangement may also be termed as bandwidth aggregation[107]. The signal of interest in digital domain is split into two half bandwidth signal components. The half bandwidth signal components are applied to two DACs in parallel operating at half the intended sample rate. The output of the second DAC i.e. the DAC applied with the higher half bandwidth signal components is up-converted using a local oscillator to frequency translate it to the higher band i.e. to the band adjacent to that occupied by the output of the first DAC. The frequency of the local-oscillator is set at  $F_s/4$  i.e. half of the effective sample rate. The up-converted output of the second DAC is combined with the output of the first DAC to yield the required signal. Firstly, the up-converter in the path of the second DAC in Fig. 6.7 will also yield an image component that occupies the frequency band 0 to  $F_s/4$  i.e. the band occupied by the lower half bandwidth components. This image acts as an in-band interferer which needs to be eliminated. Secondly, the signal quality in the up-converted path will also be affected by the phase noise of the LO.

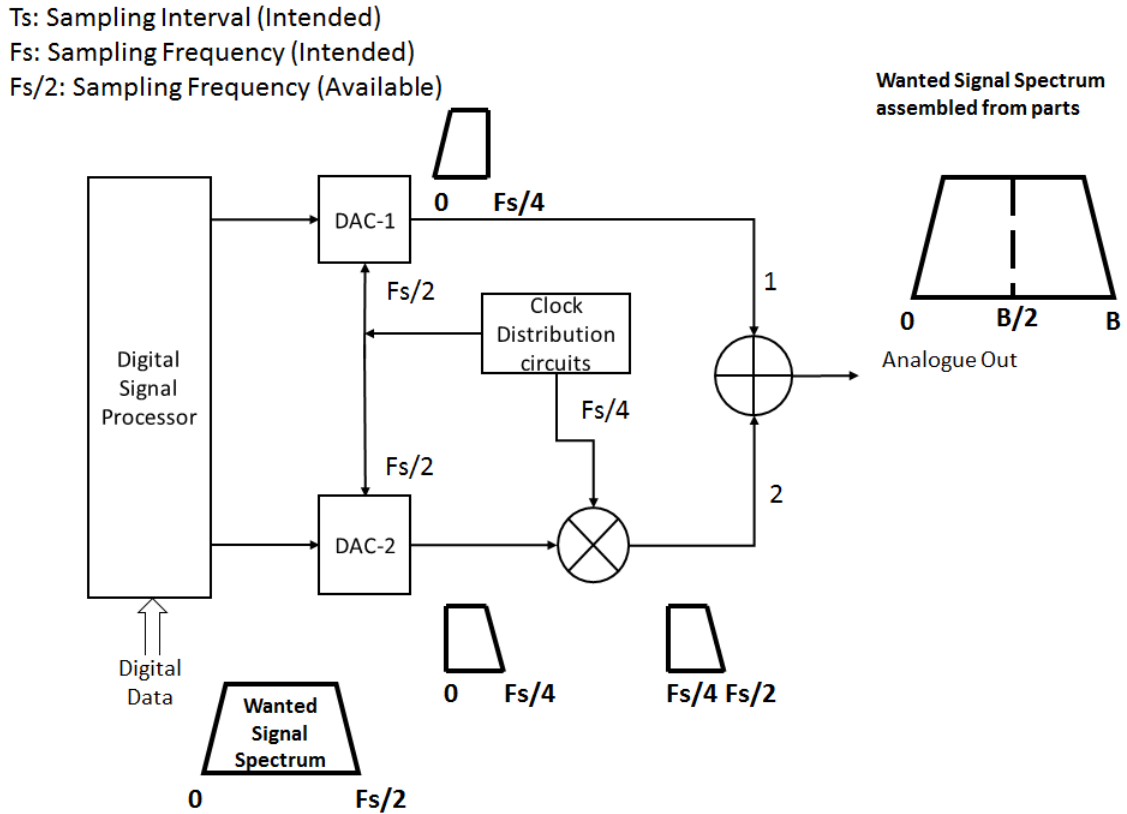
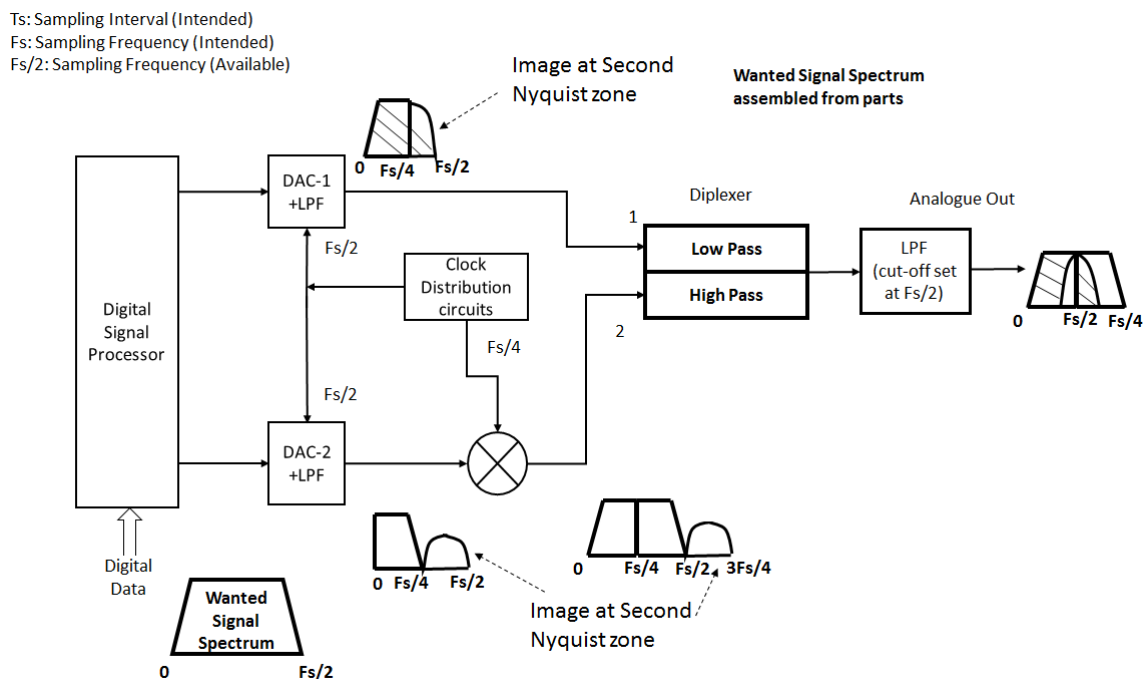


Fig. 6.7.: Interleaving DACs in frequency domain

Thirdly, the electrical lengths and circuit gains in the direct and the up-converted paths are different and hence it is necessary to balance them through calibration in order to maintain the integrity of the signal being generated. The mathematical framework for DACs interleaved in the frequency domain is presented in [106, 107] where the extent of oversampling needed for each interleaved DAC is derived. In [109], the authors present an optical transmitter with three bandwidth interleaved DACs combined with a triplexer achieving a signal bandwidth of 100 GHz bandwidth for optical communication. An SNR value of 21 dB was reported while tested with an OFDM signal with 5180 QPSK modulated sub-carriers. LO phase noise and un-compensated spurs from the mixer were found to cause the degradation in SNR. A similar system is reported in [108] for optical communications using 2-PAM and 4-PAM modulation schemes.

The up-conversion in the path of the second DAC of Fig. 6.7 would yield images in the band of frequencies occupied by the output of the DAC in the first path. Since perfect brick-wall filtering is unrealizable in hardware, there would be a presence of residual images in the adjacent channel. Similarly, the images of the signal generated by the DAC in the first path caused by frequency components in the second Nyquist zone would fall in the band of frequencies occupied by the wanted up-converted out-

put in the second path. The images therefore cause mutual interference between the two paths. A schematic diagram of signal generation with two frequency/bandwidth interleaved DACs in the presence of mutual interference discussed above is shown in Fig. 6.8. The low pass filter (LPF) at the output port attenuates the image at the second Nyquist zone of the second DAC.



**Fig. 6.8.:** Practical frequency domain interleaving DACs with images

In [110], the system of bandwidth interleaved DACs with mutual interference is modelled in the form of a MIMO system whose transfer function is represented mathematically in the form of a matrix as in eq. 6.7.

$$\begin{bmatrix} Y_1 \\ Y_2 \end{bmatrix} = \begin{bmatrix} H_{11} & H_{12} \\ H_{21} & H_{22} \end{bmatrix} \begin{bmatrix} X_1 \\ X_2 \end{bmatrix} \quad (6.7)$$

Where  $\mathbf{Y}$  is the matrix of outputs,  $\mathbf{X}$  is the matrix of inputs and  $\mathbf{H}$  is the matrix representing the MIMO transfer function. The principal diagonal elements in the matrix represent the gains for the wanted signals and the others represent mutual coupling terms. The coupling is mitigated by pre-compensating the signal applied to the respective DACs. The compensating values are obtained by inverting the MIMO transfer function.

**d: Pre-distortion of RF power amplifiers.** The concept of DPD was introduced in Chapter 4 where an input signal to an RF power amplifier is convolved

with the inverse of the amplifier's non-linear transfer function so that the output signal from the amplifier is linearized. Memory effects in RF power amplifiers were discussed in Chapter 4. A convenient representation of an RF power amplifier's transfer function is provided by Memory Polynomial as discussed in Chapter 4. The mathematical representation of Memory Polynomial in eq. 6.8 for convenience .

$$y(n) = \sum_{p=1}^N \sum_{m=0}^M C_{pm} x(n-m) |x(n-m)|^{p-1} \quad (6.8)$$

where  $y(n)$  is the  $n$ th output sample  $c_{pm}$  is the scaling factor for the non-linear term of power  $p$  and memory depth  $m$ . One of the causes for the memory effects discussed in Chapter 4 is hysteresis of inductive and capacitive components. Wider bandwidth implies greater effect of hysteresis and hence greater memory depth which in turn implies higher order of the matrix describing the behavioural model and greater computational requirements. The success of DPD operation depends on the ability to sense the non-linear components at the output of the PA and the ability to compute its inverse. In [114], the authors present a band switched feedback receiver to linearize an RF power amplifier for 5G communications with a channel bandwidth of 200 MHz at a centre frequency of 26 GHz. The receiver in the feedback path is switched to acquire the in-band and out of band emissions of the PA in parts using a narrow bandwidth ADC. Experimental validation results show an improvement in EVM by 3.3% and a reduction in out of band emissions in the adjacent channel by 25 dB. A similar approach is proposed in [115] at a centre frequency of 20 GHz with a receiver architecture similar to the one shown in Fig. 6.9 where the band to be acquired is selected by tuning the LO and a variable attenuator at the input is used to limit the RF power fed back to the spurious free dynamic range of the receiver. The technique employed is actually bandwidth interleaved reception similar to that reported in [112] and [113] but limited to acquisition of one band at a time.

### 6.3. A novel system level design approach for wideband modulators and transmitters

Bandwidth scalability is of particular importance in systems featuring adaptive bandwidth allocation such as 5G and NG-HTS. A number of published schemes to enhance the bandwidth of DACs were discussed in the previous section. To scale up or scale down the number of interleaved/multiplexed sections in a multiplexed DAC, the analogue multiplexer module needs to change along with its associated circuits for address lines and timing logic to vary the address inputs to route the signal from the appropriate multiplexed module to the output. This gets cumbersome at board/system level when encountered due to the extent of re-engineering required for inclusion of new addressing logic. To scale up or scale down the number

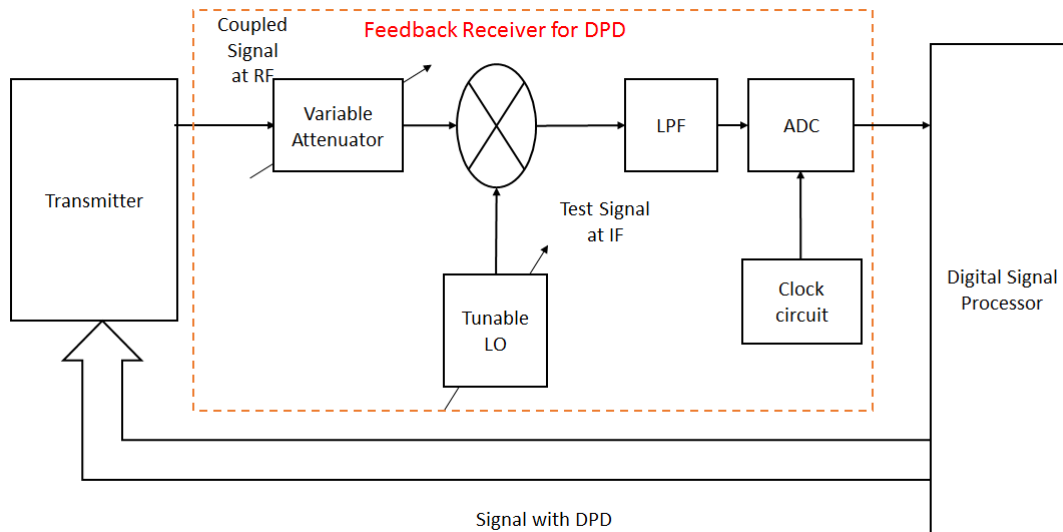


**Fig. 6.9.:** Switched band feedback receiver for DPD

of interleaved sections in a time interleaved DAC, the clock division and distribution module needs to change along with its associated circuits for maintenance of phase and duty cycle relations between the clock pulses fed to each interleaved module. To scale up or scale down the number of interleaved sections in a bandwidth/frequency interleaved DAC, the multiplex filter at the output needs to change in addition to the digital calibration image rejection and clock distribution circuits. However, the re-design of clock distribution circuits in this case is less complex compared to the case of time interleaved DACs since there is no phase shift required between them. The errors in relative phases of the clock inputs can be mitigated with relative ease by performing multipath calibration described in Chapter 3. However, the complexity of mitigating the images and the consequent mutual interference still remains.

Looking at the problem of designing wideband transmitters for a given application from a system level approach, the internal architectures of DACs or PAs are unknown. A system level design specification is provided in terms of operating band, channel bandwidth, spectrum mask, modulation scheme and EVM to the system designer and it is the responsibility of the system designer to architect a commercially viable solution with the available parts. It is also desired from a system perspective to design scalability of the system in terms of power and bandwidth along with modularity and ability to reuse legacy hardware in part or whole where possible. Considering these factors, novel scalable architectures are presented for bandwidth interleaved modulators and bandwidth interleaved transmitters whose operating bandwidths can be scaled up or down seamlessly.

### 6.3.1. Bandwidth Interleaved Modulators:

The objective of the modulator in a transmitter for wireless communications is to generate vector modulated basebands consisting of In-phase (I) and Quadrature (Q) components in phase quadrature to one another rather than generating an arbitrary signal. The presence of quadrature relation between the basebands to be generated eases the task of frequency domain interleaving. In [110], the authors proposed a novel method to mitigate the mutual interference between bandwidth interleaved DACs caused by non-ideal filtering which would leave residues of up-conversion images. The problem complicates if the number of interleaved stages increases due to a proportional increase in the rank of the matrix describing the MIMO transfer function and consequently increases mathematical computations needed to mitigate the mutual interference. In this work, a novel method that exploits the quadrature relations between the I and Q parts of the vector modulated baseband can be exploited to cancel the images in the even Nyquist zones is presented. This relaxes the specifications for the filters and also enables scalability of bandwidth with relative ease.

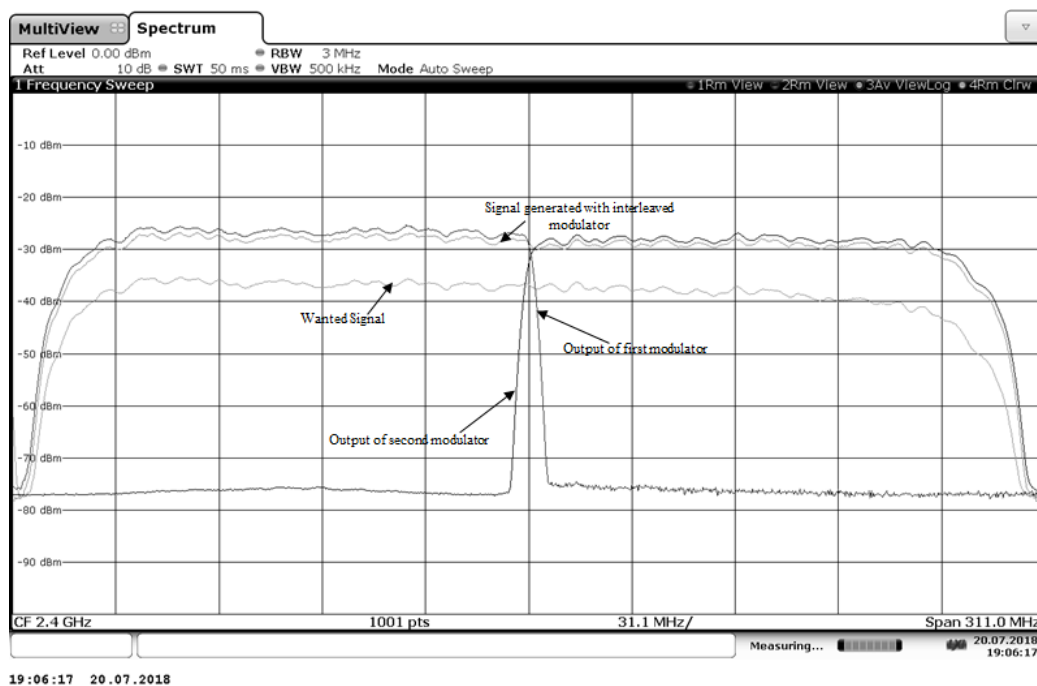
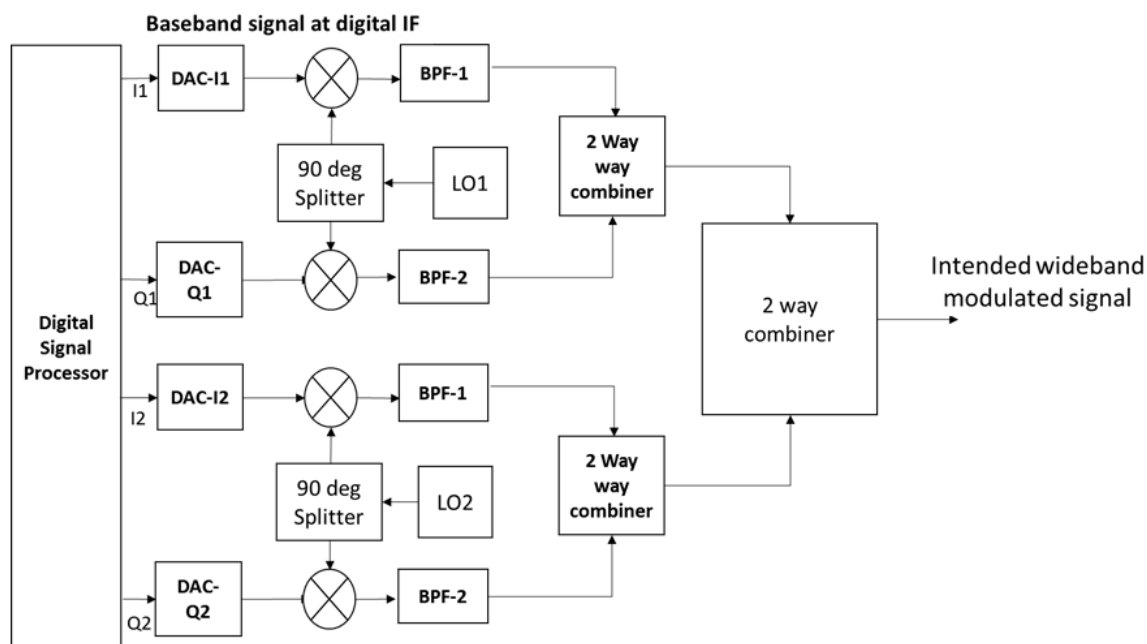


Fig. 6.10.: Wideband signal generated in parts and combined at 2.4 GHz

Considering as an example, the generation of a bandpass DVB-S2 signal which is 8-PSK modulated at a symbol rate of 250 mega samples per second (MSPS) with a root raised cosine (RRC) filtering requirement having a roll off factor  $\alpha = 0.2$  and an up-sampling factor of 3 for wave shaping. This signal will have a resultant bandwidth of 300 MHz (250 MHz X 1.2) and requires a modulator having DACs of

sample rate of 750 MSPS in the I and Q paths respectively. This signal could be generated using two bandwidth interleaved modulators clocked at half the sample rate employing the architecture depicted in Fig. 6.11. The first modulator consisting of DACs I1 and Q1 with a vector up-converter that generates lower half of the required spectrum. The second modulator consisting of DACs I2 and Q2 where the second vector up-converter generates the upper half of the required spectrum and the two parts are combined to yield the desired 8-PSK signal.



**Fig. 6.11.:** Bandwidth Interleaved Modulator

The fast Fourier transform (FFT) of a signal of bandwidth  $BW$  sampled at rate  $F_s$  would appear as shown in Fig. 6.12. Vector up-conversion of this signal with an LO at frequency  $F_{carr}$  would occupy the spectral space from  $F_{carr} - BW/2$  to  $F_{carr} + BW/2$ . Letting the baseband signal of interest  $m(t)$  be represented as

$$m(t) = I(t) + jQ(t) \quad (6.9)$$

This signal when modulated on to an RF carrier  $C(t)$  at frequency  $F_{carr}$  takes the following form:

$$C(t) = I(t)Cos(2\pi f_c t) + Q(t)Sin(2\pi f_c t) \quad (6.10)$$

The steps involved in generating the intended wideband complex envelope modulated signal using bandwidth interleaved modulators are as described below. For

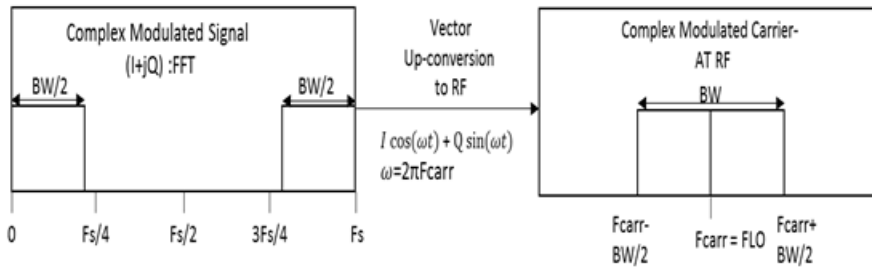


**Fig. 6.12.:** Complex baseband FFT and its output modulation spectrum

a digitally generated signal, the time variable  $t$  is discrete and takes the values of  $nT_s$  where  $n$  is the sample number and  $T_s$  is the sampling interval. Generate digital sine and cosine LO signals at an intermediate frequency  $F_{IF} = F_s/4$  sample rate  $T_s$  and length equal to that of the baseband signal. Let the two digital LO signals be designated as:

$$LO_{IFCOS} = \text{Cos}(2\pi ft) \quad (6.11)$$

$$LO_{IFSIN} = \text{Sin}(2\pi ft) \quad (6.12)$$

i) Frequency translate the digital baseband to the intermediate frequency by digital up-conversion to obtain a digitally up-converted modulated baseband  $I_{IF}$  as shown below.

$$I_{IF} = I(t) \cdot LO_{IFCOS} + Q(t) \cdot LO_{IFSIN} \quad (6.13)$$

Also obtain its Hilbert Transform  $Q_{IF}$ .

$$Q_{IF} = -Q(t) \cdot LO_{IFCOS} + I(t) \cdot LO_{IFSIN} \quad (6.14)$$

Obtain the FFT of  $I_{IF}$  and  $Q_{IF}$ .

Both these signals have the same spectral content but a phase quadrature to one another at every frequency in the spectral space they occupy. This is shown graphically in Fig. 6.13.

ii) Extract the frequency components at frequency bins from  $0$  to  $F_s/4$  and  $3F_s/4+1$

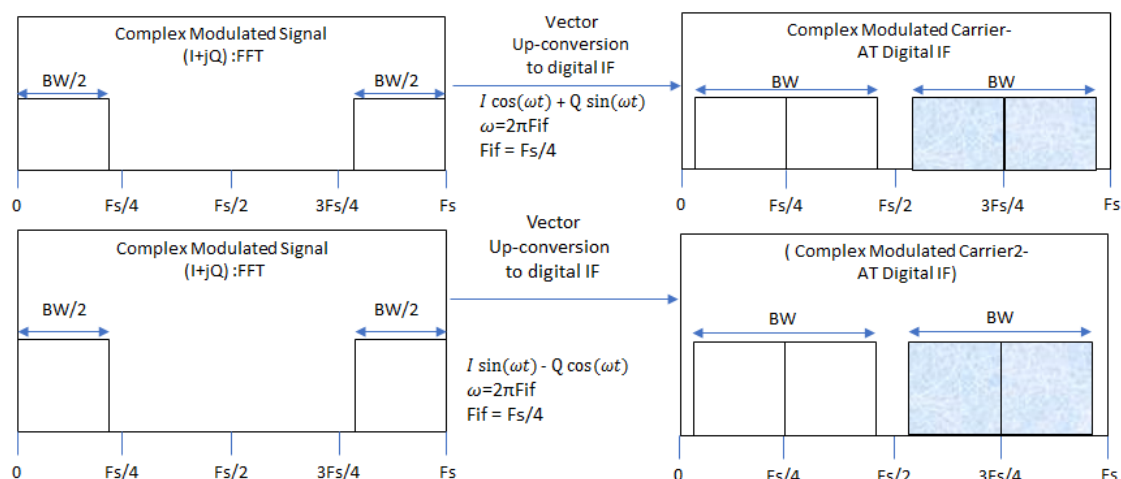


**Fig. 6.13:** . Digital up-conversion of the desired baseband to digital IFs in quadrature. The chosen digital IF is centred at  $F_s/4$

to  $F_s$  from the FFT of signals  $I_{IF}$  and  $Q_{IF}$ . These represent the lower half of the spectral content to be generated. Obtain the Inverse Fast Fourier Transform (IFFT) of the extracted frequency components. Let these signals be designated as  $I_{Low}$  and  $Q_{low}$  respectively. Add the imaginary part of  $I_{low}$  to the real part of  $Q_{low}$  to form the signal  $I_{bb1}$ . Subtract the imaginary part of  $Q_{low}$  from the real part of  $I_{low}$  to form the signal  $Q_{bb1}$ .  $I_{bb1}$  and  $Q_{bb1}$  thus generated would have the same magnitudes but quadrature phases.

iii) Extract the frequency components at frequency bins between  $F_s/4 + 1$  to  $3F_s/4$  from the FFT of signals  $I_{IF}$  and  $Q_{IF}$ . These represent the upper half of the spectral content to be generated. Obtain the inverse fast Fourier transform (IFFT) of the extracted frequency components. Let these signals be designated as  $I_{High}$  and  $Q_{High}$  respectively. Add the imaginary part of  $I_{High}$  to the real part of  $Q_{High}$  to form the signal  $I_{bb2}$ . Subtract the imaginary part of  $Q_{High}$  from the real part of  $I_{High}$  to form the signal  $Q_{bb2}$ .  $I_{bb2}$  and  $Q_{bb2}$  thus generated the signal will have the same magnitudes but quadrature phases. By the theory of Fourier analysis, each frequency component in the FFT could be represented by a sinusoid with a specific amplitude and phase.  $I_{bb1}$  and  $Q_{bb1}$  constitute a quadrature pair such that each frequency component in their FFTs is a sinusoid having the same amplitude but 90 degrees difference in phase relative to one another in the pair. This implies that the equal amplitude and phase quadrature between the frequency components that constitute the signals generated could be exploited for image rejection while up-converted to the required RF carrier frequency. The same is applicable to the pair  $I_{bb2}$  and  $Q_{bb2}$ .

iv) Apply the half bandwidth signals ' $I_{bb1}$ ,  $Q_{bb1}$ ,  $I_{bb2}$  and  $Q_{bb2}$  thus generated to DACs  $I_1$ ,  $Q_1$ ,  $I_2$  and  $Q_2$  of the interleaved modulator shown in Fig. 6.14. Clock the DACs

at sample rate  $F_s/2$  i.e. half of the original sampling frequency. Set the frequency of Local Oscillator LO2 to the intended carrier frequency  $F_{carr}$  and the frequency of Local Oscillator LO1 lower than  $F_{carr}$  by an amount equal to the IF chosen. LO1 and LO2 need to be phase locked to a common reference oscillator.

v) By virtue of single sideband up-conversion owing to quadrature relations, the up-conversion image frequency components of DACs I1 and Q1 in the band  $F_{carr} - 2IF$  to  $F_{carr} - IF$  cancel out due to destructive combination after vector up-conversion. The second Nyquist zone images of DACs I1 and Q1 which would fall in the spectral band of the second modulator (consisting of DACs I2 and Q2) also cancel out due to destructive combination after vector up-conversion.

vi) The same mechanism is applicable to the second modulator consisting of DACs I2 and Q2 whose up-conversion images of the first Nyquist zone components and the images in the second Nyquist zone cancel out after vector up-conversion. The mutual inference between the first and second bandwidth interleaved modulators caused by image components is thus eliminated. The process is shown in Fig. 6.14.

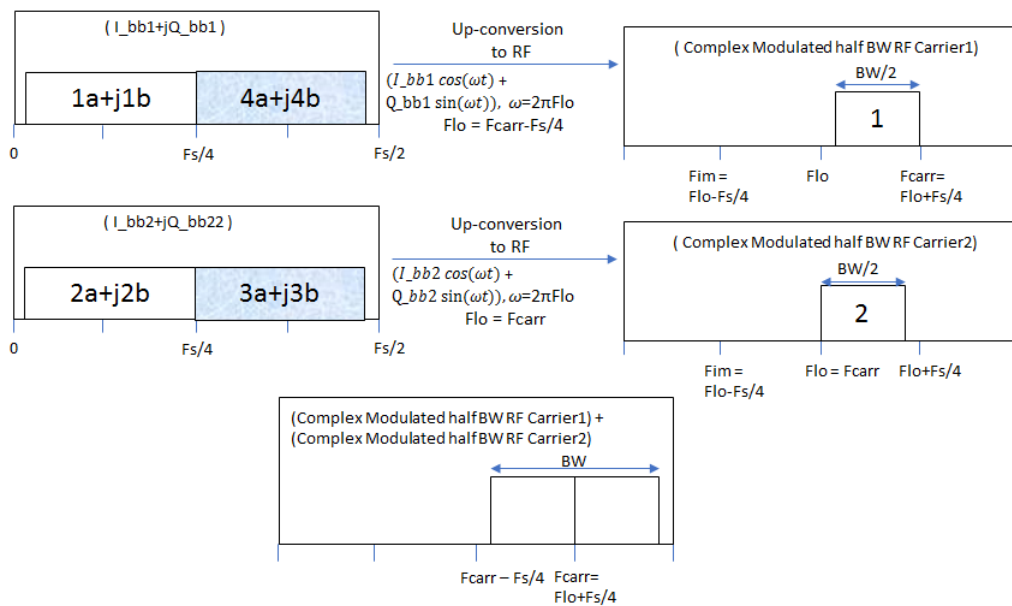


**Fig. 6.14.:** Single sideband up-conversion and combination of the interleaved basebands.

As the interleaving is performed at RF instead of baseband, an RF power combiner can be used instead of a diplexer filter due to lower fractional bandwidths relative to the RF carrier frequency. Spectrum plots of half bandwidth signals generated in two bandwidth interleaved modulators designed to produce an 8PSK modulated signal at 2.29 GHz with a bandwidth of 100 MHz is shown in Fig. 6.15.

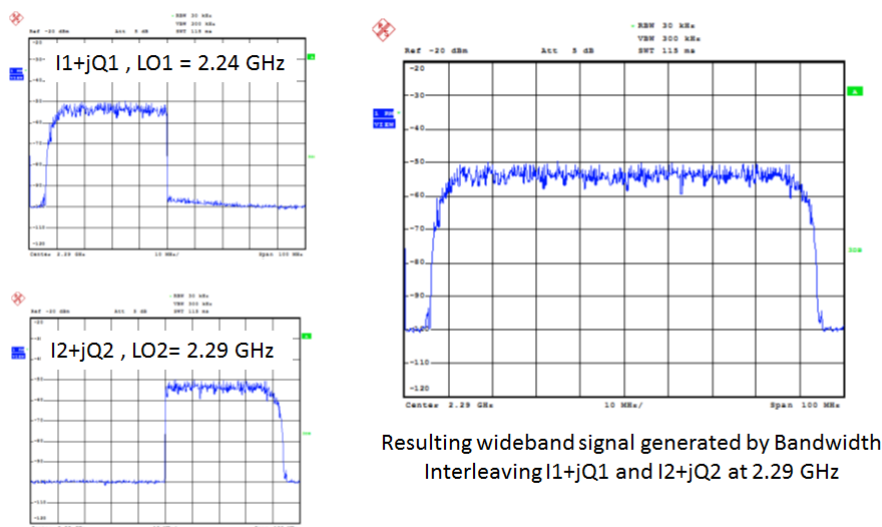


**Fig. 6.15.:** Spectrum screenshots of 96MHz DVB-S2 8PSK signal generated at 2.29 GHz with BW interleaved modulators.

### 6.3.1.1. Choice of LO .

The choice of LO frequencies depend upon the number of paths being interleaved.

- i) Considering the block diagram of Fig.6.11, the LO frequency for both the modulators can be set at the intended carrier frequency  $F_{carr}$ . This will enable using the same LO module to feed the mixers of both the modulators thereby reducing the cost of implementation. But, this arrangement is limited to interleaving just two modulators. This would require the half bandwidth signal in first modulator to be spectrally inverted so that the up-conversion yields the lower sideband i.e. the spectral space between  $F_{carr} - BW/2$  to  $F_{carr}$ . This arrangement is highly susceptible to dc offset in any of the DACs which would result in LO leak. This option was used for the experimental validation in the next section.
- ii) A second choice for the LO frequencies is to choose  $F_{carr} - BW/2$  for the first modulator and  $F_{carr}$  for the second modulator. This requires the LO frequencies to be numerically related to a common reference frequency. LO modules consist of VCOs phase locked in a loop to highly stable reference oscillators like oven controlled crystal oscillators (OCXOs).  $F_{carr} - BW/2$  and  $F_{carr}$  are required to be numerical multiples of the reference frequency in order to maintain uniform phase relations between the two modulators. This arrangement is scalable to any number of interleaved sections. This option was chosen for the experimental validations in this section. The signal generated with interleaved modulators shown

in Fig. 6.15 used this option where the LO for up-conversion of the half bandwidth signal in paths I1 Q1 was set at 2.24 GHz i.e. a value  $F_s/4$  below the intended carrier frequency of 2.29 GHz. The LO for the up-conversion of the signals in paths I2 Q2 was set at the intended carrier frequency 2.29 GHz.

- iii) Another choice for the LO frequencies is to choose  $F_{\text{carr}} - BW/2$  for the first modulator and  $F_{\text{carr}} + BW/2$  for the second modulator. This would require the half bandwidth signal in second modulator to be spectrally inverted so that the up-conversion yields the lower sideband i.e. occupies the spectral space between  $F_{\text{carr}}$  and  $F_{\text{carr}} + BW/2$ . This also requires the LO frequencies to be numerically related to a common reference frequency. LO modules consist of VCOs phase locked in a loop to highly stable reference oscillators like oven controlled crystal oscillators (OCXOs).  $F_{\text{carr}} - BW/2$  and  $F_{\text{carr}} + BW/2$  are required to be numerical multiples of the reference frequency in order to maintain uniform phase relations between the two modulators. This arrangement is scalable to any even number of interleaved sections. The cost of implementation is lower than choice ii in case of more than two interleaved sections since two adjacent sections can be fed with the same LO signal.

### 6.3.1.2. Calibration of Paths

The integrity of the signal generated with bandwidth interleaved modulators as explained above depends upon maintenance of the amplitude, phase and timing relations between the interleaved sections in order to avoid distortions and mutual interference. Mutual interference caused by up-conversion images can be avoided with appropriate quadrature calibration between the I-Q sections of each stage. This will also relax the order of filtering needed at each stage relative to prior art techniques due to inherent image cancellation. A primary source of distortion is the sinc roll-off of the DACs which results in significant attenuation of frequency components above 80% of Nyquist rate. Inverse sinc filtering procedures are provided by DAC vendors to compensate the sinc roll-off. It is also essential to calibrate and pre-compensate the non-linear phase responses and the relative gain and phase variations between the interleaved paths. The first step is to perform 2 paths wide-band calibration individually on pairs I1 Q1 and I2 Q2 of the individual modulators shown in Fig. 6.11. This will be followed by calibration of relative gain and offsets between the pairs. The proposed procedure for path calibration was introduced in Chapter 3. The bandwidth and centre frequency specifications for the stimulus need to be set in accordance with the operational requirements of the modulator. Since the interleaved modulators are fed with different LO signals, discontinuities in their oscillating phases can destroy the integrity of the final signal generated. An extra step is needed to ensure the seamless continuity in gain and phase of the final signal generated with the interleaved modulators.

**Path calibration of IQ paths in each interleaved modulator:** The bandwidth to be considered to calibrate each path should be equal to the bandwidth of the signal in the respective path. For example, if a signal of bandwidth BW originally sampled at rate  $F_s$  is generated by interleaving N number of modulators with equal bandwidths, then the bandwidth and the sample rate to be chosen for each path are  $BW/N$  and  $F_s/N$ . The proposed procedure is described here taking a case of two paths.

- i) Let  $F_{s_2} = F_s/2$ . Generate a truncated sinc or chirp stimulus of bandwidth  $f_{edge} = F_s/4$  sampled at rate  $F_{s_2}$  applying  $f = f_{edge}$  in eq. 3.8 or eq. 3.9 respectively as described in chapter 3.
- ii) Perform two path calibration on paths I1 Q1 as described in Chapter 3 subsec. 3.3.1.4 setting the frequency of LO1 depending on the choice of LO configuration selected from the options in subsec. 6.3.1.1.
- iii) Perform two path calibration on paths I2 Q2 as described in Chapter 3 subsec. 3.3.1.4 setting the frequency of LO2 depending on the choice of LO configuration selected from the options in subsec. 6.3.1.1.

The above calibration steps will ensure rejection of up-conversion images and mutual interference between the interleaved paths.

**Calibration of relative offsets between the interleaved modulators:** A signal generated with interleaved modulators should not have discontinuities in amplitude and phase. Therefore, the relative offsets in gain and phase between the modulators should be determined and pre-compensated after the successful wideband calibration of the paths in each modulator.

1. Generate a cosine wave at frequency  $F_{s_2}/4$  and apply to DACs in paths I1 and I2 at mutually exclusive intervals with LO1 and LO2 set at their designated frequencies. The up-converted outputs yield frequency components at frequencies  $LO1 + F_{s_2}/4$ ,  $LO1 - F_{s_2}/4$ ,  $LO2 + F_{s_2}/4$  and  $LO2 - F_{s_2}/4$ . But  $LO2 - F_{s_2}/4 = LO1 + F_{s_2}/4$  since  $LO2 - LO1 = F_s/4 = F_{s_2}/2$ . Therefore, the up-converted components at frequencies  $LO2 - F_{s_2}/4$  and  $F_{s_2}/4$  overlap but appear at different time instants.
2. Perform two path calibration again between paths I1 and I2 as explained in chapter 3 subsec. 3.3.1.4 but by replacing the truncated sinc stimulus with a single frequency cosine stimulus described in step 1 and considering path I1 as reference.
3. Multiply the magnitudes of the baseband signals in paths I2 Q2 with the inverse of the gain offset and rotate the phase with the inverse of the mean phase difference obtained in step 2. This finishes the calibration.

The partitioned components of the wideband signal intended for transmission are applied to the DACs in the bandwidth interleaved modulators after pre-compensating them through calibration and with the appropriate choice of the LOs.

The extent of over sampling needed for the DACs in the interleaved modulators relative to that needed by a single wideband modulator is dependent on the application, target SNR and the type of modulation in the signal being generated. Single carrier modulated schemes such as 8PSK, 32 APSK, etc. applied in satellite communications require over sampling to implement Root Raised Cosine (RRC) filtering for wave shaping. This requirement for over-sampling by a numerical value would remain irrespective of the modulator being implemented as a single wideband module or one constructed with two or more bandwidth interleaved modules. In these cases, it is enough to have a sampling factor for the original signal such that the bandwidth after raised cosine filtering is limited to half of the sampling frequency. This is because the digital IFs generated prior to separation of the components in the frequency domain need to fall within the first Nyquist zone. The up-sampling factor in case of OFDM signals can be less than 2 since only about 66% of the bandwidth available for a given sample rate is actually used to carry data in most wireless communication standards. For example an LTE signal with a sample rate of 30.72 MSPS carries data only over a bandwidth of 20 MHz. The remaining spectral space is left for guard-bands and pulse shaping. If the baseband is up-sampled by a factor of 4 and down-sampled by a factor of 3, an effective sample rate of 40.96 MSPS is achieved. The 20 MHz wide resampled complex LTE baseband if up-converted to a digital IF will occupy a bandwidth of 20 MHz in the first Nyquist zone and its image will occupy a bandwidth of 20 MHz in the second Nyquist zone. This value is sufficient to generate and transmit the signal through bandwidth interleaved modulators since the entire information contained in the signal would be available in the first Nyquist zone itself and the single sideband up-conversion at the output of the DACs will reject images by over 60 dB to nearly eliminate mutual interference.

## 6.4. Experimental Validation of Bandwidth Interleaved Modulators

The test apparatus for this validation was similar to that used in Chapter 3 subsec. 3.3.1.5 A computer (PC) running the tool MATLAB was used as a DSP, an evaluation board TSW30SH84 from Texas Instruments consisting of a quad DAC module DAC34SH84 with LVDS interface to connect to a digital interface board TSW1400EVM. A vector signal analyzer (VSA) FSQ-40 from Rohde and Schwarz was used as a reference receiver. The VSA was capable of demodulating an input modulated signal up to a bandwidth of 100 MHz. The outputs of DAC1 and DAC2 were treated as an IQ pair and connected to I and Q inputs of a vector up-converter module TRF3705 designated as UC1\_IF. The outputs of DAC3 and DAC4 were treated as the second IQ pair and connected to I and Q inputs of another vector up-converter module TRF3705 designated as UC2\_IF. The outputs from the DACs were up-converted to 2.24 GHz and the output. The reference oscillators of the on-board clock source module LMK02808 were synchronized with the reference output

of the VSA after sufficient warm up time.

An 8-PSK modulated carrier generated at 2.29 GHz at a symbol rate of 80 MSPS, bandwidth of 100 MHz generated with a single wideband modulator with DACs running at 200 MHz and that generated with bandwidth interleaved modulators using DACs at sample rate 100 MSPS are shown in Fig. 6.16. This plot was treated as reference. This signal was chosen for validation since it could be demodulated by a standard VSA available at the time of validation. Being a single carrier modulation scheme, if this signal is generated with bandwidth interleaved modulators it will be susceptible to the gain and phase mismatches and discontinuities between the interleaved modulators thereby indicating the quality of the interleaving scheme.

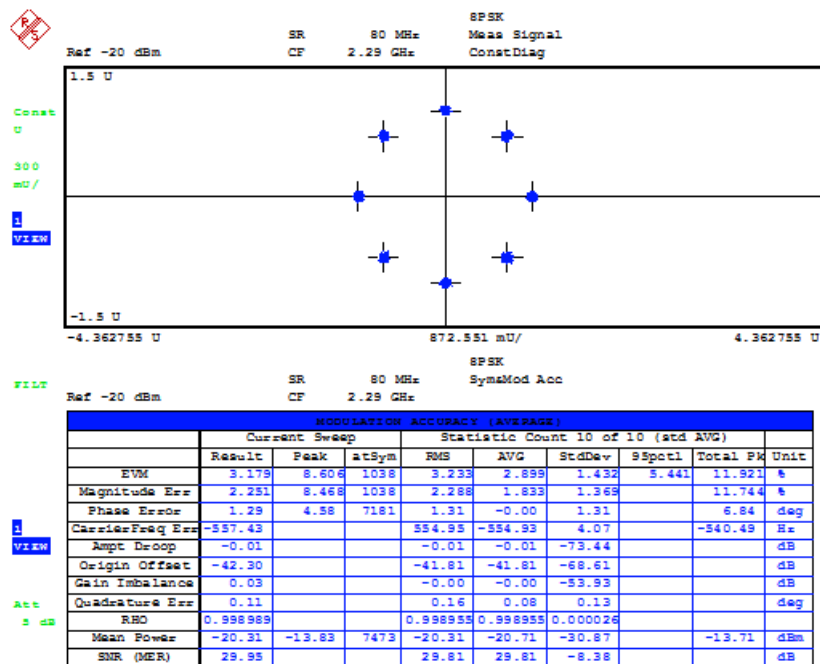


**Fig. 6.16.:** 8-PSK modulated signal generated with single wideband modulator using DACs operating at 200 MSPS

The 8-PSK signal was partitioned in frequency domain to extract two half bandwidth basebands namely I1 Q1 (lower half bandwidth baseband) and I2 Q2 (higher half bandwidth baseband) as explained in the previous section. The LO for the modulator meant for the baseband I1-Q1 was set at 2.24 GHz i.e. 50 MHz below the intended centre frequency of 2.29 GHz and the LO for the modulator meant for baseband I2-Q2 was set at the intended centre frequency 2.29 GHz. The modulators were subject to calibration using a chirp stimulus as explained in the previous section and FIR filters were synthesized to pre-compensate the basebands for gain and phase ripples, imbalances and discontinuities. The basebands I1-Q1 and I2-Q2 were convolved with the respective FIR filters for pre-compensation and applied to the respective modulators. The demodulated constellation of the signal generated through bandwidth interleaved modulators is shown in Fig. 6.17.

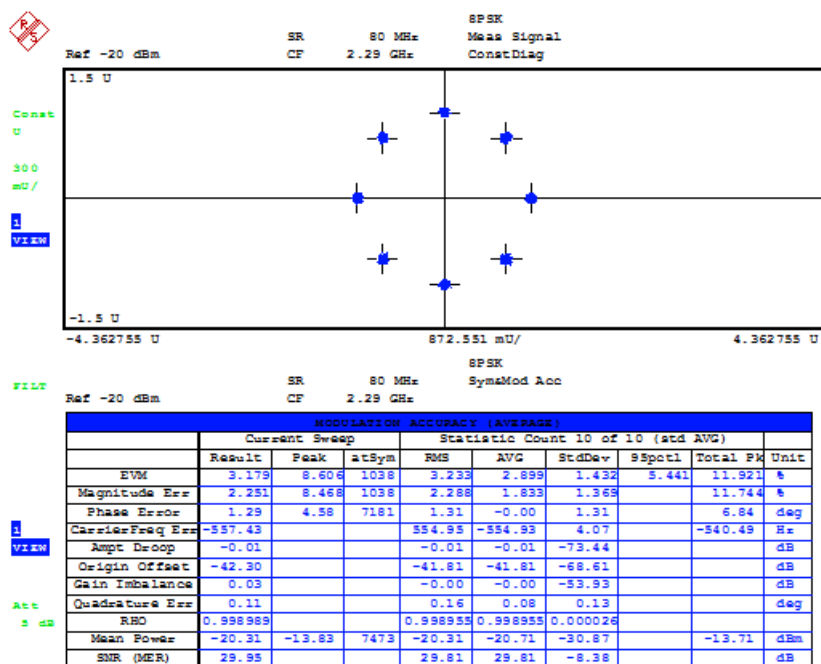


**Fig. 6.17.:** 8-PSK modulated signal generated with bandwidth interleaved modulator using DACs operating at 100 MSPS.

**Observations:** It is observed from the demodulated data that the average EVM of the signal generated by bandwidth interleaved modulators is comparable and slightly lower than that generated with a single wideband modulator.

The above validation was repeated successfully with another 8-PSK signal of bandwidth 300 MHz and a OFDM signal with 300 MHz of bandwidth. These validations formed the basis for the next section on spatially combined bandwidth interleaved transmitters.

#### 6.4.0.1. SNR analysis

The impact of jitter, sampling rate and phase noise were discussed in chapter 2. It was observed that the jitter in clock signals is the time domain manifestation of phase noise in the oscillators that generate the clock signals. A brief analysis of the impact of clock jitter on the signal generated with two bandwidth interleaved modulators is performed as an example. The original sample rate for the wideband signal was 600 MSPS. This signal was generated with two bandwidth interleaved modulators clocked at 300 MSPS. The DAC selected for this experiment was DAC34SH84, 4 channels DAC made by Texas Instruments. The DACs were clocked with the signals generated by LMK04808B, a clock generation and distribution module with internal PLLs and VCOs made by Texas Instruments. The same part was used to generate the clock signals for a single wideband modulator running at 600 MSPS and for the bandwidth interleaved modulators running at 300 MSPS. The simulated phase noise

plot of the clock signal at 600 MHz is shown in Fig. 6.18. The calculated jitter is 117.1 fs (femto seconds).

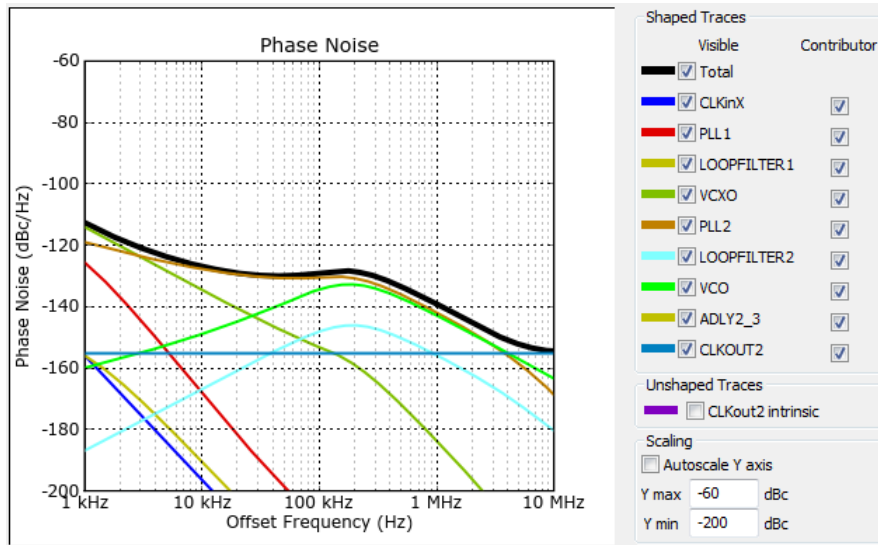


Fig. 6.18.: Phase noise of 600 MHz clock

The simulated phase noise plot of the clock signal at 300 MHz is shown in Fig. 6.19. The calculated jitter is 108.1 fs (femto seconds). The impact of jitter on SNR is tabulated in Tab. 6.1

Tab. 6.1.: SNR in the generated signals in the presence of clock jitter

Modulator Type	Modulator output Power in dBm	No. of bits	Quantization noise in dBc	RMS clock Jitter	Bandwidth 'BW' in Hz	Sampling Frequency 'fs' in Hz	DAC SNR in dB with ideal clock	SNR Available with Jitter in dB
Interleaved	1	15	90.3	1.09E-13	1.50E+08	3.00E+09	102.06	79.72
Interleaved	1	15	90.3	1.09E-13	1.50E+08	3.00E+09	102.06	79.72
Single	1	15	90.3	1.17E-13	3.00E+08	6.00E+09	102.06	73.06

The signals in the above table are up-converted to a carrier frequency  $f_{carr}$  with a local oscillator. Consider up-converting these signals for transmission at Ku Band centered at 14.15 GHz. The simulated phase noise plot of the LO is shown in Fig. 6.20.

This results in an available SNR of 49 dB after up-conversion. It may be inferred that the phase noise of the LO is a dominant factor in determining the SNR available from a transmitter. This parameter is independent of the type of signal generated in the modulator.

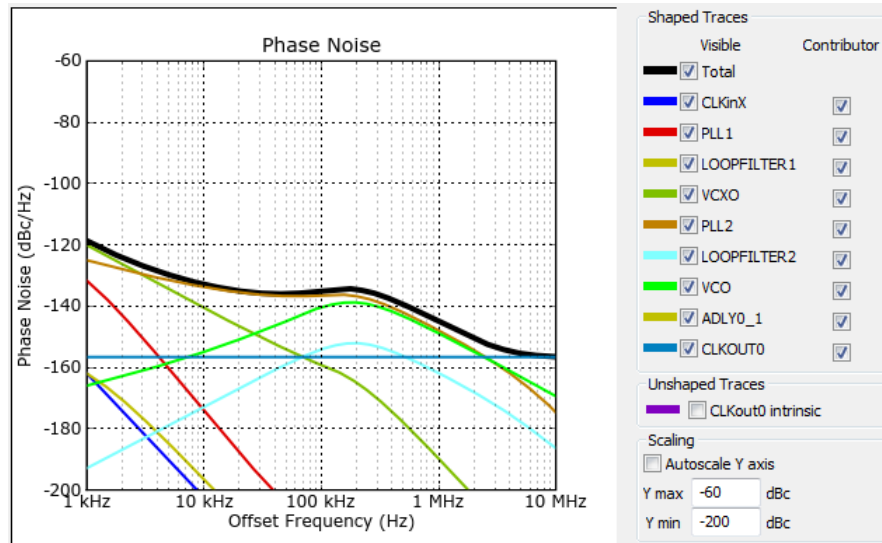


Fig. 6.19.: Phase noise of 300 MHz clock

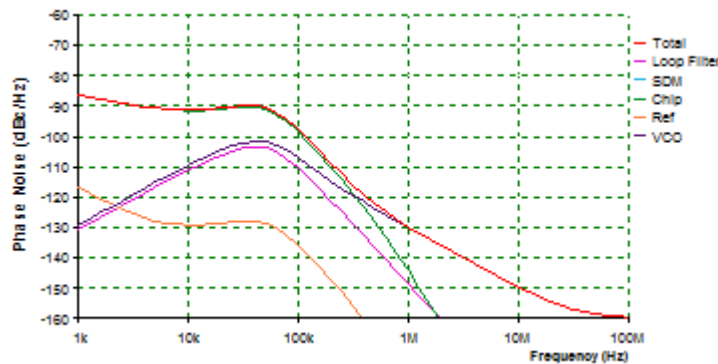


Fig. 6.20.: LO phase noise profile at Ku Band

### 6.4.1. Spatially Combined Bandwidth Interleaved Transmitters

From a wireless transmission system perspective, the problem in transmission of wide bandwidths is not limited to modulators alone. The RF up-converters and PAs are generally integrated with the outdoor units (ODUs) in satellite communication systems where it is not practically viable to implement the scheme of bandwidth interleaved modulators. PAs will be inefficient if operated in the linear region of transfer characteristics as seen in chapter 4 and earlier in this chapter. The non-linear characteristics of the PA affect the integrity of the envelope by introducing AM-AM and AM-PM distortions and also result in RF emissions outside the assigned bandwidth which would violate regulatory norms and also intrude the spectrum assigned to other users. A feedback receiver is required to accomplish DPD in a transmitter which conventionally requires a five times the channel bandwidth to

acquire the out of band (OOB) emissions. Applying this requirement to modulators alone, the extent of oversampling and calibration operations needed will complicate the process by a large extent. As seen earlier, DPD is popularly accomplished by modelling the transmitter as a non-linear system with memory using basis functions in the form of matrices. The ranks of the matrices increase in proportion to the bandwidth owing to increase in long term memory effects.

As seen earlier, the problem of wide channel bandwidths affects all stages in a transmitter. In this section we present a novel scheme to extend the concept of bandwidth interleaving to transmitters whole entities in the frequency domain and seamlessly combining their outputs spatially at the receiver to cater to wideband transmission requirements. This would enable using RF power amplifiers with gains and output power reduced by a factor equal to the number of interleaved stages. In addition, this scheme when applied to OFDM systems will reduce the PAPR of the signal encountered at each interleaved stage due to lower number of data sub-carriers per stage. The bandwidth for the feedback receiver for DPD is also reduced by a factor equal to the number of interleaved stages. A block diagram of this scheme is shown in Fig. 6.21.

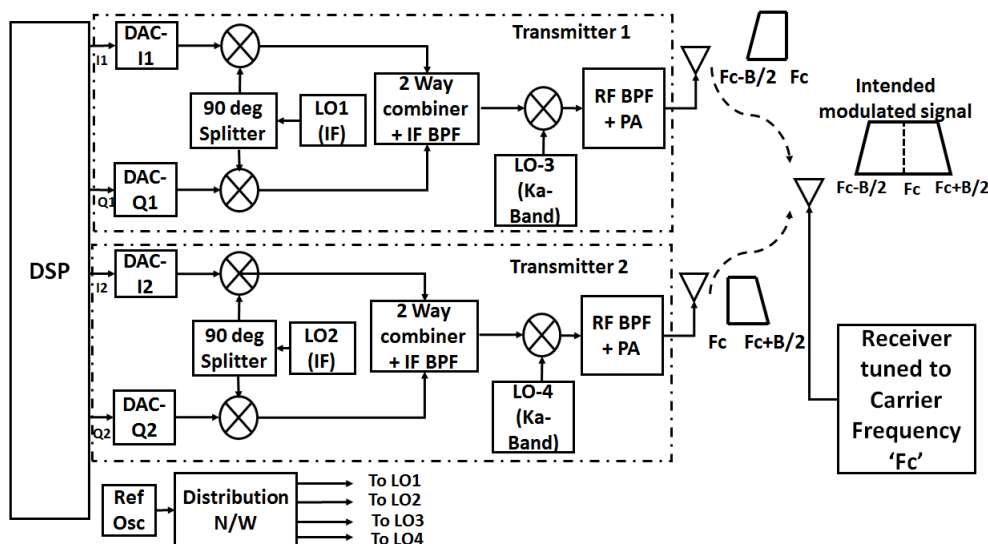
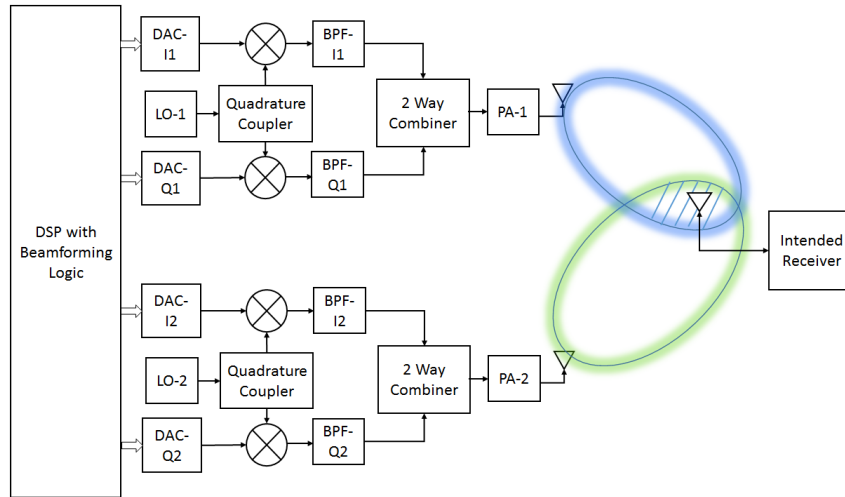


Fig. 6.21.: Spatially Combined Bandwidth Interleaved

The procedure for transmission of a wideband signal over bandwidth interleaved transmitters is similar to that explained in subsec. 6.3.1 with a difference that the outputs are combined spatially over the air at the intended point of reception. This also provides a degree of security in the physical layer. The additional steps required to accomplish this task are listed below.

- Set the boresights of the two transmitters in the direction of the intended receiver as shown in Fig. 6.22 where the signal at the receiver is a vector sum of the signals carried by each beam. This figure was introduced in Chapter 2 but

the application was deferred until now. In the present application, each beam carries a half bandwidth signal partitioned from an intended wideband signal in the frequency domain. The two half-bandwidth signals carried by each beam combine at the receiver to yield the intended wideband signal. Antennas with wide beam-widths (e.g. 120 deg sectoral beams) could also be used depending on the end application. The PAs in each transmitter are needed to transmit only half the total RF power and half the total bandwidth. A common feedback receiver with half the total bandwidth requirement can be switched between the two transmitters to accomplish DPD.



**Fig. 6.22.:** Two transmitters spatially combined

- It is a pre-requisite to calibrate and pre-compensate the RF chains in each transmitter for quadrature offsets and bandwidth dependent impairments. The integrity of the signal at the receiver depends upon the ability to maintain the integrity of amplitudes, phases and timing of the parts of the signal transmitted from the interleaved transmitters. This requires uniformity in gain and phase responses experienced by each part of the signal which could be accomplished by path calibration. It is necessary to calibrate the RF propagation paths between the transmitters and the receiver for gain and phase imbalances. A test signal with a bandwidth equal to that of the intended wideband signal such as a frequency modulated chirp signal described earlier and defined by equations eq. 3.9 and eq. 3.10 may be used, where  $y(n)$  is the value of the  $n$ th sample,  $T_s$  is the sampling interval,  $M$  is the total number of samples,  $k$  is the frequency variation parameter,  $f_{max}$  and  $f_{min}$  are the maximum and the minimum frequencies respectively.
- The calibration to be performed here is a case of the novel scheme described in Chapter 3 using chirp stimulus applied to spatially combined RF signal paths.
- This chirp signal is subject to bandwidth interleaved transmission as explained

in the previous section and received at the receiver. The FFT of the received signal is computed and the amplitudes and phases of the components received from each transmitter are compared against an ideal chirp signal. The first numerical differences of amplitude and phase spectra are computed. The height of the step at the center frequency in the amplitude and phase would indicate the gain and phase offsets between the two transmit paths respectively. The FFT values also help to train the coefficients of channel equalizer filter in the receiver as in a general case with pilot signals.

- The offsets in transmission path 2 relative to 1 thus computed may be either conveyed to Tx2 over a narrow band reverse link for offset tuning. This will enable the seamless reception of the two half bandwidth signals at the receiver which when combined would resemble the intended wideband modulated signal. A narrow band beacon signal on the reverse link will also serve to identify the relative offsets in the two transmit paths when captured by the two transmitting antennas and evaluated owing to channel reciprocity.

A predetermined OFDM signal with sub-carriers modulated at lowest order could also be used instead of chirp for path calibration. In a two-way communication system, a beacon signal at the carrier frequency can be transmitted by the receiving node which can be sensed by the receivers in the bandwidth interleaved nodes. The sensed beacon signal can be used to determine the variations in gain and phase in the paths between the interleaved transceivers and the intended receiving node.

## 6.5. Experimental Validation of spatially combined bandwidth interleaved transmitters

The transmitter and the receiver were built for transmission at carrier frequency 28.9 GHz. The transmitter followed a heterodyne architecture with the intermediate frequency (IF) selected at 800 MHz which was then up-converted to 28.9 GHz. The LO for RF up-conversion was tuned to 14.15 GHz and was multiplied in frequency by a factor of 2 owing to better phase noise performance than using an oscillator directly at 28.3 GHz to mix with the IF at 800 MHz to yield the modulated carriers at 28.9 GHz at power +2 dBm. The LO for the IF stage of the first bandwidth interleaved transmitter was set at frequency equal to  $800 \text{ MHz} - \text{BW}/2$  where BW is the bandwidth of the intended signal being transmitted. The LO for the IF stage of the second bandwidth interleaved transmitter was set at frequency equal to the intended IF i.e. 800 MHz. The receiver consisted of an RF front end with a noise figure of 3 dB which down-converted the received signal to an IF at 800 MHz. This was followed by an analog to digital converter (ADC) clocked at 4 Gbps that digitized the IF. Further down-conversion and demodulation were accomplished in the digital domain. The antennas were designed to have beam-widths of 120 degrees in the

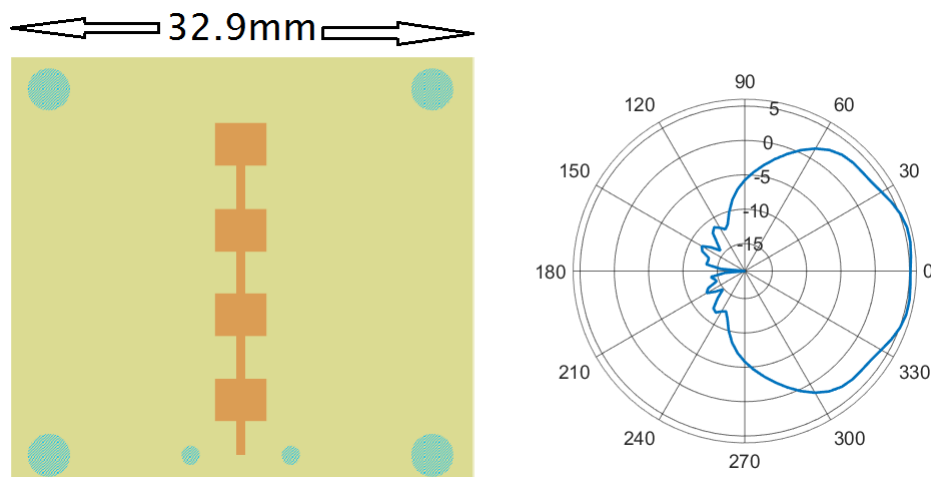


**Fig. 6.23.:** Gerber screenshot of the antenna designed and its simulated gain pattern (dBi) in azimuth plane.

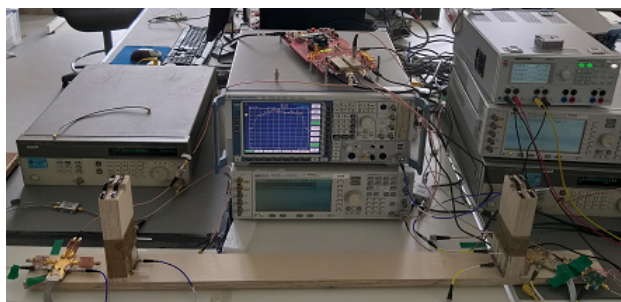


**Fig. 6.24.:** Test Bench used for validation. Receiver is on the left. The transmitters are on the right.

azimuth plane as shown in Fig. 6.23 and etched on RO3003 substrate from Rogers Corporation.

A wooden test apparatus was designed with propagation path length of a meter between its ends. This distance corresponds to 96 wavelengths at 28.9 GHz. One of the ends of the apparatus was mounted with a patch antenna and connected to a receiver consisting of a Ka-Band down-converter and a high speed ADC clocked at 4 GSPS. Two similar antennas were fabricated the same substrate for the transmitters and placed on the right side of the apparatus at a spacing of eight wavelengths with a ground plane in between them. An overall path loss of 51 dB was observed between the transmitters and the receiver. The evaluation was performed in a regular laboratory environment instead of an anechoic chamber to emulate a real use case scenario that would include multipath propagation effects. A picture of the test bench is shown in Fig. 6.24.

The physical layout of the antennas is shown in Fig. 6.25.

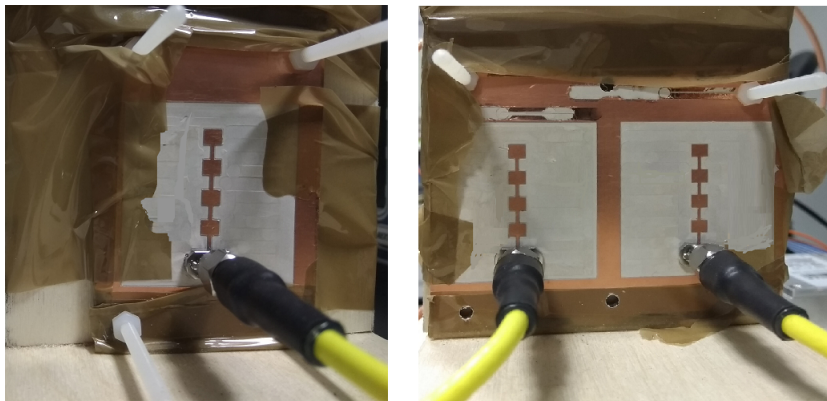


**Fig. 6.25.:** Antenna placement (Left: Receiving Antenna) (Right: Transmitting Antennas)

**Case 1: 96 MHz 8PSK signal at 28.9 GHz using two spatially combined bandwidth interleaved transmitters** As proof of concept, this scheme was first tested to generate and transmit a 96 MHz 8PSK signal at 28.9 GHz using two bandwidth interleaved transmitters. A vector signal analyzer (VSA) FSQ-40 made by Rohde and Schwarz was used as the receiver instead of a Ka-Band down-converter and a high speed ADC described in the apparatus above. The transmission distance was limited to a metre for proof of concept since the distance measured around 92 wavelengths at the chosen carrier frequency. The mentioned 8PSK signal at 96 MHz bandwidth was chosen for proof of concept since its bandwidth and modulation scheme were within the capability of the available test equipment for demodulation. Being a single carrier modulation scheme, it is highly sensitive to mismatches in gains and phases between the interleaved paths. A frequency modulated chirp signal having the same bandwidth was generated. The signal was partitioned in the frequency domain and transmitted through bandwidth interleaved transmitters each having half the required bandwidth and sample rate. The received signal was down-converted to baseband and digitized in the VSA. The digitized baseband was demodulated on MATLAB. The half bandwidth chirp signals transmitted from each transmitter were combined spatially at the receiver and analyzed for phase and gain mismatches between the two transmission paths. The discontinuity in gain and phase between the two paths manifested in the form of a step at the centre frequency in the FFT plot. An FIR filter was synthesized at the receiver to equalize the path gains applying the novel calibration procedure described in chapter 3. The chirp signal was now replaced by the intended 8PSK signal, subject partitioning in frequency domain for bandwidth interleaved transmission. Each half bandwidth signal thus generated was subject to pre-compensation filtering with the FIR filters generated in the previous step to mitigate the gain and phase imbalances between the interleaved paths and transmitted as explained in the previous section. The VSA was now used as a receiver and the received signal was demodulated. Successful demodulation of this signal certifies the reliability of the proposed scheme. The spectrum plots of

the signals received over the air from a single wideband transmitter and the spatially combined signal received from bandwidth interleaved transmitters are shown in Fig. 6.26.

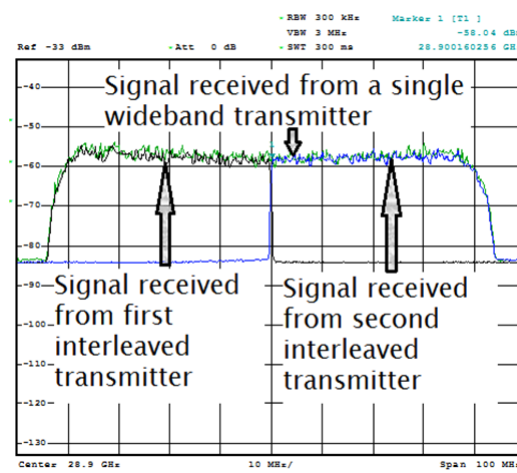


Fig. 6.26.: Received Spectrum of Bandwidth interleaved transmission

The demodulated constellations of the signals received over the air from a single wideband transmitter and the spatially combined signal received from bandwidth interleaved transmitters are shown in Fig. 6.27..

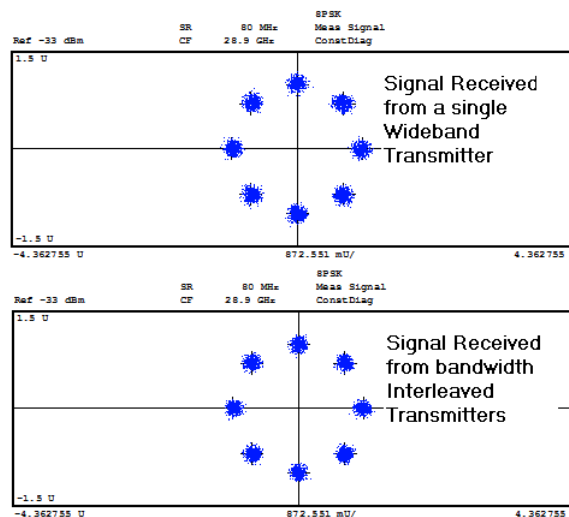


Fig. 6.27.: Comparison of constellations demodulated by VSA at 28.9GHz.

**Case 2: Validation with a 440 MHz wide 8PSK signal:** The second case chosen was also an 8PSK modulated signal but at symbol rate 400 Msps and bandwidth of 440 MHz to support transmission over next generation high throughput satellites

## 6.5 Experimental Validation of spatially combined bandwidth interleaved transmitters

(NG-HTS) expected to have bandwidths up to 500 MHz per beam as mentioned in Chapter 1. The paths were calibrated using a chirp signal as in the first case and the intended 8PSK modulated signal was subject to bandwidth interleaved transmission. The half bandwidth signals thus transmitted were combined spatially at the receiver. The received signal was subject to filtering to equalize the path mismatches and then demodulated. The mean EVM calculated over 32768 samples without equalization was 12% but resulted in no bit errors and hence the equalizer trained was not applied. The spectrum of the signal received at the receiver's antenna and the demodulated constellation are shown in Fig. 6.28 and Fig. 6.29 respectively.



**Fig. 6.28.:** Spectrum of 400MSPS 8PSK signal received from interleaved transmitters centered at 28.9GHz

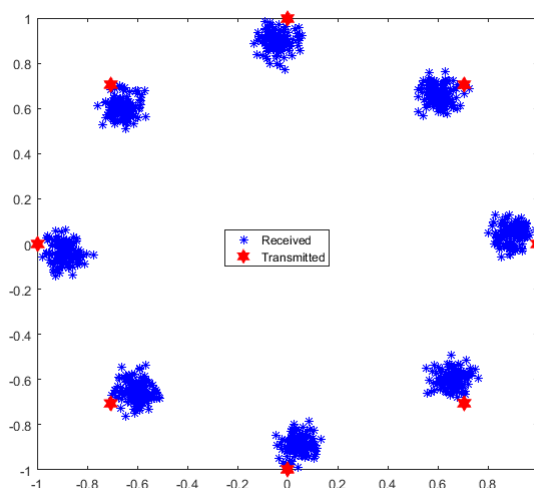


**Fig. 6.29.:** Demodulated 8PSK constellation at 400MSPS

The necessity for appropriate path calibration can be inferred from the distorted constellation shown in Fig. 6.30.

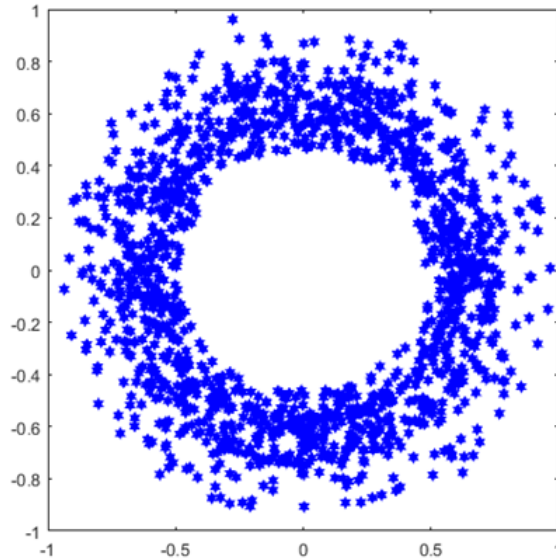


**Fig. 6.30.:** Uncalibrated case with bandwidth interleaved transmitters

### Case 3: Validation with a 400 MHz wide OFDM signal.

The bandwidth interleaved transmission scheme was then applied to transmission of a 400 MHz wide OFDM signal with 1416 data sub-carriers modulated with QAM64 constellation and 128 pilot sub-carriers. The sub-carrier spacing was set at 240 kHz, chosen in accordance with 5G-NR specifications at a sample rate of 491.52 MHz with an aim of achieving a throughput of 2.039Gbps using 1416 sub-carriers for data over an effective bandwidth of 355.2MHz. The length of the cyclic prefix was set at 128 samples. This signal was transmitted with two spatially combined bandwidth interleaved transmitters with each one transmitting half of the bandwidth as described above. The receiver consisted of an RF front end of noise figure 3dB which down-converted the received signal to an IF at 600 MHz. This was followed by an Analog to Digital Converter (ADC) clocked at 3Gbps that digitized the IF. Further down-conversion and demodulation were accomplished in the digital domain. The calculated mean EVM after equalization was 3.12% over 16992 symbols (12 OFDM frames). The spectrum of the signal received at the receiver's antenna and the demodulated constellation are as shown in Fig. 6.31 and Fig. 6.31. As each subcarrier represents 6 bits due to QAM64 modulation, a total of 1416 data sub-carriers occupying a bandwidth of 339.84MHz (240 kHz X 1416) yield an effective transmission bit rate of 2.039Gbps.

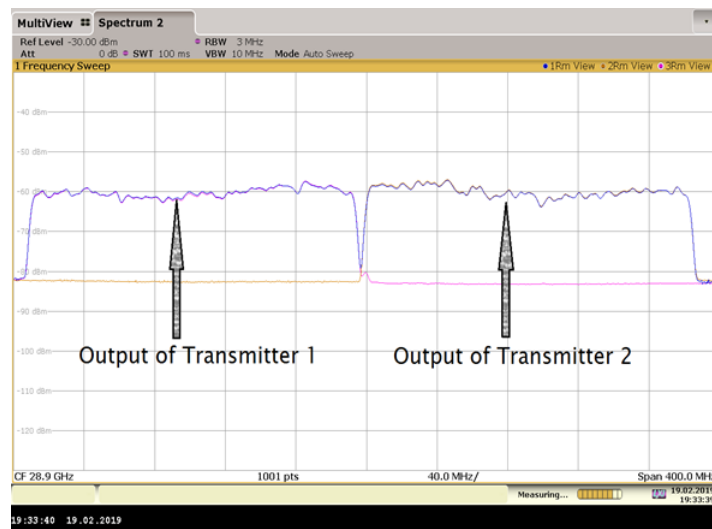


Fig. 6.31.: Spectrum of 355.2 MHz wide QAM64 modulated OFDM signal

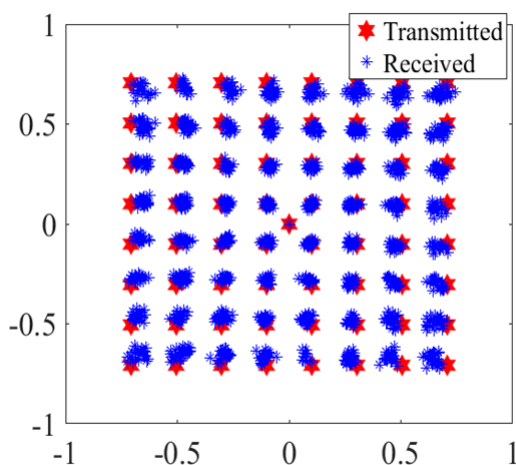
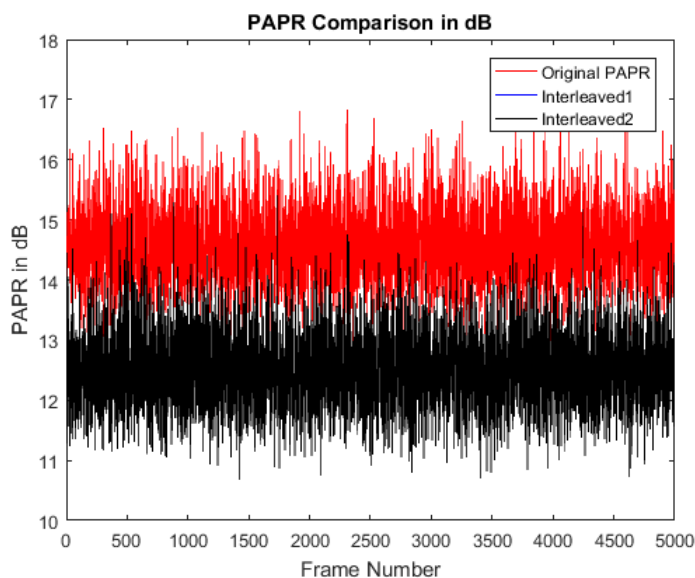


Fig. 6.32.: Demodulated constellation of QAM64 OFDM signal of bandwidth 355.2MHz

**Inference from validation:** The proposed scheme of transmitting wideband signals with spatially combined bandwidth interleaved transmitters has been proven to be a means to mitigate the problem of bandwidth in data-converters and the complete RF front end. The necessity to calibrate the RF signal paths enables a potential application to provide a tier of security in the physical layer. The proposed scheme provides the ability to reuse legacy hardware for next generation wideband wireless communications.

**Impact of bandwidth interleaving on PAPR:** With bandwidth interleaving, the requirement of EIRP to meet the link budget reduces by a factor equal to the number of interleaved paths. It is however necessary to assess the PAPR of the bandwidth interleaved signals since PAPR values higher than that of the original signal will make the interleaving scheme power in-efficient. Simulations were carried out in MATLAB for 5000 cycles of randomly generated bit streams using the same modulation and bandwidth interleaving schemes as tested above to test the impact of bandwidth interleaving on PAPR. The half bandwidth signals generated from the original wideband signal showed a reduction in PAPR by a factor of 2 dB.



**Fig. 6.33.:** Comparison of PAPR of Bandwidth Interleaved Signals against that of the original wideband signal.

## 6.6. Conclusions

In this chapter, the bandwidth limitations of the RF signal chain in a transmitter were examined from a system point of view. A key contributor to the bandwidth limitation is the DAC in the transmitter's hardware chain whose maximum sample rate and effective resolution bandwidth impose a maximum limit on the bandwidth of the modulated signal that can be generated and transmitted. The wideband impairments in the hardware elements succeeding the DACs in the signal chain such as load mismatches, bandwidth dependent impairments in a PA and bandwidth requirements for digital pre-distortion of the PA discussed in Chapter 4 were re-examined from a system point of view. Prior arts published in the domain of wide bandwidth signal generation by multiplexing and interleaving multiple DACs

in time and frequency domain were discussed. It is inferred that time domain multiplexing and interleaving requires complex clock distribution circuits running at the intended high sample rate. Scaling up the number of multiplexed stages requires re-design of the clock distribution network and address lines for the multiplexer which complicates the problem at board and system level. Scaling up the number of time interleaved stages requires re-design of the clock distribution network with appropriate clocking phase at the interleaved stages which is critical to operation. Frequency interleaved DACs require less complex clock distribution circuits between the interleaved stages but need mitigation of up-conversion images. It is inferred that scaling up the number of frequency interleaved sections requires less complex clock distribution circuits than time interleaving but requires novel designs for multiplex filters to combine the outputs. Prior arts published in the domain of digital pre-distortion of RF power amplifiers with limited bandwidth feedback receivers were discussed. It is inferred that digital pre-distortion of a wideband transmitter can be accomplished with feedback receiver of narrower bandwidths which can be switched across the band of interest acquiring a fraction of the band at a time during the learning phase of DPD. It is also inferred that the effective number of bits in high speed interleaved DACs is constrained by the jitter in clock which in turn depends on the phase noise characteristics of the oscillator that generates the clock signal. This reduces the dynamic range and hence the order of the modulation that can be supported.

A novel seamless scheme of interleaving modulators and transmitters as whole systems in frequency domain has been presented where the problem of image rejection in frequency interleaved DACs is mitigated at system level by exploiting the quadrature phase relations of the I and Q basebands. The presented scheme on bandwidth interleaved modulators relaxes the filtering requirement in the interleaved stages due to image rejection by design. This is specifically beneficial in millimeter wave communication systems. The presented scheme can be implemented independent of beam forming architectures involved in combining the signals from the interleaved transmitters spatially due to the robustness of the calibration scheme applied to mitigate the gain and phase offsets between the signal paths. Experimental validations show that comparable performance is achieved with interleaved modulators and transmitters to that of direct wide bandwidth signal modulation and transmission. It has also been demonstrated that the proposed scheme enables the use of same hardware in part or whole for both satellite and 5G terrestrial communications in Ka Band. Inherent from its architecture, the proposed scheme is scalable and adaptable to increased transmission bandwidths as it requires only the inclusion of additional interleaved stages without a theoretical upper limit and practically only constrained by the jitter and phase noise in the available Local Oscillator and clock modules. This enables the reuse of existing low bandwidth legacy transmitter hardware either in part or whole for next generation wireless transmission with wider bandwidths. The necessity to calibrate the wireless paths of the spatially combined interleaved transmitters implies that an un-authorized receiver offset from the intended point

of reception will not receive the modulated envelopes as needed for demodulation of data. This provides a degree of security in the physical layer and may be considered an extended case of directional modulation. It is also inferred that the presented scheme of bandwidth interleaved transmission reduces the effective PAPR per stage by a factor of 2 dB and the band power to be transmitted is also reduced by a factor equal to the number of interleaved stages. This also improves the overall efficiency due to reduction in linearity requirements.

# 7. Conclusions and future work

## 7.1. Summary

The motivation for this research activity undertaken is to enhance the performance of a Radio Frequency transmitter for operation in next generation millimetre wave wideband radio communications by digitally assisted means.

The features expected from next generation terrestrial wireless and satellite communications were discussed in Chapter 1. It was inferred that the expectation for user data rates over wireless data links is in the order of several giga bits per second enabled by novel technological advances such as carrier aggregation, wide modulation bandwidths and massive MIMO.

In Chapter 2, the key parameters of wireless transceivers and performance limitations in their building blocks were discussed. The impact of the block level limitations and impairments on the overall system performance was analysed. Technical areas of focus to mitigate the limitations and enhance performance by digitally assisted means were presented.

In Chapter 3, the system level impacts of wideband signal distortions in RF signal paths along with the impact of gain and phase imbalances between them were discussed. Prior arts in the domain of calibration of I and Q signal paths in RF transceivers and calibration of signal propagation paths in a beam forming system were discussed. It was inferred that the prior art schemes were mostly iterative in their approach whose complexity and efforts involved increased with number of paths to be calibrated. Novel system level schemes were proposed to perform the task of calibration over  $N$  paths independent of the architecture in a non-iterative manner where only one measurement cycle with a reference receiver was needed.

In Chapter 4, an overview of RF power amplifiers, their key parameters, classes of operation, topologies, behaviour modelling and digital pre-distortion was presented. Novel methods were presented to design  $N$  way Doherty power amplifiers, to model the behaviour of asymmetric Doherty amplifiers, model the non-linearity in outphasing amplifiers caused by amplitude imbalances in Chireix combiners and a phase-only digital pre-distortion technique for outphasing amplifiers were presented.

In Chapter 5, an overview of physical layer security and PAPR reduction techniques published in prior arts were discussed. A novel technique to accomplish both these tasks together by means of encryption using unique channel and hardware responses

between two authentic nodes in a wireless network over the bandwidth of interest was presented.

In Chapter 6, an overview of schemes published in prior arts to generate wideband modulated signals by interleaving DACs of narrower bandwidths was presented and the associated challenges in the implementation of those schemes were discussed. A novel scheme of bandwidth interleaved modulators and transmitters was presented where the limitations in generating and transmitting wideband complex envelope modulated signals were mitigated at system level in a seamless and scalable manner.

## 7.2. Contributions

### 7.2.1. Primary Contributions

- Chapter 3: A novel non-iterative to mitigate the wideband impairments in the signals paths of an RF transmitter was presented to calibrate roll offs and ripples in their pass band gain and phase responses and the imbalances between them across multiple RF signal paths. The calibration techniques presented are applicable to both circuit and spatially combined signal paths with ease. The effectiveness of the technique was demonstrated by calibrating the four signal paths in a digital outphasing transmitter in chapter 4 and in a spatially combined bandwidth interleaved transmitter presented in Chapter 6. Inherent from design, the presented scheme can be scaled up to calibrate any number of RF signal paths with relative ease. A patent application bearing the number PCT/EP2019/052125 has also been filed with the World Intellectual Property Organization (WIPO) with elaborate details of the implementation.
- Chapter 6: A novel scheme to generate wide bandwidth complex envelope modulated signals in parts by interleaving multiple modulators of narrower bandwidths in frequency domain has been presented where the bandwidths can be scaled up with reduced hardware changes in comparison with prior arts. This scheme has been extended to another novel scheme of interleaving entire transmitters as whole entities in frequency domain and combining their outputs spatially at the intended point of reception. Comparable performance is achieved to that of direct wide bandwidth signal modulation and transmission. The presented method can be implemented independent of the internal architecture of the building blocks. Experimental validations show that the presented techniques are applicable to both single carrier and OFDM modulated wireless transmitters. This makes the presented techniques suitable for application in multi-standard transmitters for operation in heterogeneous networks. The scheme of spatially combined bandwidth interleaved transmitters has shown the potential to reuse legacy hardware of narrower bandwidths for application in next generation wideband transmitters with the need for major hardware changes such as inclusion of additional switching and filtering

circuits. This is particularly beneficial where high data rate DACs and wideband RF front end modules are prohibitively expensive or not available. The scheme has also shown reduction in PAPR of the reduced bandwidth OFDM signals relative to a single wideband OFDM signal. The power transmission requirement per interleaved transmitter is reduced by a factor of the number of interleaved paths. If by link budget calculations it is necessary to transmit a wideband complex modulated signal with an EIRP of 10 Watts for reception at the specified distance and SNR, transmission of the same signal with the presented interleaved transmitters will only require 5 Watts of EIRP per transmitter. This feature combined with reduced PAPR in the interleaved transmitters improve the efficiency transmission power efficiency and also require lower power drives per path thereby reducing the cost of implementation. These features come handy in applications involving adaptive bandwidth allocation and adaptive modulation and coding schemes. Inherent by design, the proposed system is scalable to accommodate any number of interleaved transmitters. The upper limit of bandwidth is only constrained by the available signal to noise ratio in the presence of phase noise in the local oscillators. A potential to enhance the overall power efficiency has also been observed due to reduced PAPR and hence lower linearity requirements for the power amplifiers in the interleaved stages.

- Chapter 5: A novel scheme to jointly accomplish physical layer security along with reduction of peak to average power ratio (PAPR) up to 5dB without the necessity to transmit additional information has been presented. Popularly used data encryption schemes such as Diffie Hellman require key generation data to be exchanged over a public network. While the keys generated in Diffie Hellman are asymmetric and the size of the keys are long enough to guard against brute force attacks, it is also essential to ensure that the key agreement does not take place with an impersonating node. A novel scheme to encrypt the phases of the complex modulated signals used for communications over a wireless link is presented. The scheme exploits the impact of the parameter group delay on the integrity of single carrier modulated symbols where a dispersive filter with non-linear phase response in the frequency domain with variation in group delay comparable to the symbol duration is used to encrypt the signal intended to be transmitted. The process is undone at the receiver using a recovery filter having a phase response equal to the inverse of that of the encrypting filter. The presence of encryption in the modulated constellation authenticates the Diffie Hellman key agreement process between legitimate nodes. The encrypting phases are generated using the convolved channel and hardware responses that are unique to the two legitimate nodes. An eavesdropper is obfuscated due to difference in the channel and hardware responses observed at its end thereby increasing immunity to impersonation attacks. In case of OFDM signals, the encrypting phases are directly added to the phases of the modulated sub-carriers to randomize them. This reduces

the effective PAPR of the signal similar to the principle behind SLM technique but without the need to transmit additional information to the receiver for undoing the encryption prior to demodulation. The scheme thus provides PAPR reduction and security in the physical layer of the wireless link.

### 7.2.2. Contributions As Co-author

- Chapter 2: Another novel non-iterative method based on vector positioning of constellation symbols of a specially designed 64-QAM modulated signal that can calibrate RF path impairments was presented. It uses a modulated waveform that closely resembles a current standard communication signal format and is able to alleviate both frequency and power dependent impairments such as amplitude ripple-tilt, group-delay, AM-AM and AM-PM conversion in linear, weakly non-linear and strongly non-linear systems. The contributions here were co-design of the calibration process, design verification, experimental validation and drafting literature for publication.
- Chapter 4: A design to implement an N-way Doherty power amplifier for Ku band applications was presented. With the emergence of low-earth orbit satellite constellations where a large power output is not a requirement, the presented design provides a viable option for ground station transmission as shown by its performance within spectral mask limits for satellites communications. The presented method helps to optimize efficiency while amplifying signals of varying envelopes with a given PAPR due to the advantage of several peaking stages which can be scaled up further depending on the application. The contributions here were design verification and drafting literature for publication.
- Chapter 4: A comparison of behavioural models for asymmetric Doherty power amplifiers has been made and inferred that Vector Switched Volterra models estimate the performance closest to the measured results. This eases the task of digital pre-distortion since selection of the most appropriate behavioural model is critical to quality. The contributions here were design verification, experimental validation and drafting literature for publication.
- Chapter 4: The non-linear transfer function of an outphasing transmitter cannot be modelled in a straight forward manner using conventional Volterra and Memory Polynomials since the source of non-linearity lies in the amplitude and gain imbalances between the outphasing branches. This problem complicates further by the use of Class E amplifiers in the branches since they operate in switching mode where amplitude correction won't yield useful outcomes. A concise standalone model for the Chireix power combiner in an outphasing transmitter under amplitude imbalance was presented based on the analysis of its nonlinear behaviour. A phase only pre-distortion technique was presented for Outphasing transmitters with Class E amplifiers which would

simplify the task of mitigating its impairments with relative ease. The contributions here were design verification and drafting literature for publication.

### 7.3. Future Work

As with the work carried out in this thesis, there are potential extensions that have been planned for future work.

- **Spatially Combined Bandwidth Interleaved Transceivers:** The concept of spatially combined bandwidth interleaving can also be extended to include receivers in a similar manner thereby deriving architectures for spatially combined bandwidth interleaved transceivers. Such a scheme will provide the benefit of configuring a set of transceivers for a given bandwidth and given modulation scheme in wireless communication systems featuring adaptive bandwidth allocation and in RF test and measurement equipment for evaluating wireless transceiver modules for next generation wireless communications.
- **Enhanced Security In The Physical Layer And Further PAPR Reduction Through Phase Encrypted Bandwidth Interleaving:** It can be inferred from Chapter 6 that appropriate calibration of RF signal paths is essential to maintain the integrity of signals transmitted by spatially combined bandwidth interleaved modulators at the intended point of reception. This itself provides a degree of security in the physical layer. It was also observed that the bandwidth interleaving reduces the PAPR by a factor of 2 dB which helps to relax the linearity requirements in the interleaved transmitters proportionally. This if combined with the phase randomization based joint PAPR reduction and physical layer security scheme, the combination has the potential to improve efficiency and security further.
- **Bandwidth Interleaved Transceivers with Phase Noise Compensation:** One of the parameters that can impose a hard limit on the carrier to noise ratio in bandwidth interleaved transceivers is the phase noise of the local oscillators. Digital compensation of the phase noise can help improve the signal to noise ratio in bandwidth interleaved transmitters.

### 7.4. Conclusions

The work carried out in this thesis enhances the performance of radio transmitter for application next generation wireless communications by digitally assisted means. Novel methods identified and validated in this work have resulted in mitigation of bandwidth dependent impairments in the building blocks of a transmitter, combining multiple transmitters of relatively narrow bandwidths in a seamless manner to

operate as a single wideband system and jointly provide security of communications with improvement in power efficiency in transmitters. These methods have been shown by experimental validation to be viable solutions to the problems of bandwidth dependent hurdles in architecting wide bandwidth OFDM and single carrier transmitters.

# Acknowledgments

I would like to take this time to thank Dr. John Dooley, and Prof. Ronan Farrell for providing me with opportunity to conduct research challenging and interesting field and their valuable guidance and advice throughout my candidature. I would like to thank my mother, wife, son and entire family for their unrelenting support and co-operation without which it would not have been possible to pursue this doctoral research. None of this work would have occurred with the funding provided by the Science Foundation of Ireland and European Regional Development Fund under Grant Number 13/RC/2077 which I am extremely grateful. I would like to thank colleagues and friends at NUI Maynooth for mentoring me and providing valuable support throughout my tenure as a doctoral researcher. I consider myself very lucky to have such good mentors, colleagues and most importantly great friends.



# A. Appendix Impact of oscillator phase noise on SNR, timing jitter.

The LO and clock signals in a wireless transceiver are synthesized from a reference oscillator by means of a phase locked loop (PLL). The basic block diagram of a PLL based frequency synthesizer is shown in Fig. A.1

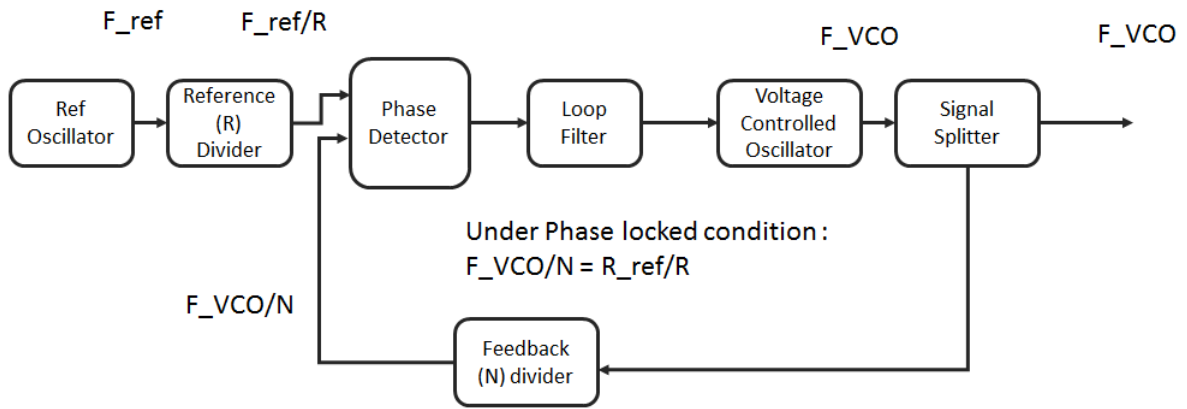


Fig. A.1.: Phase Locked Loop based Local Oscillator

The objective of a PLL is to lock the phase of an RF signal generated by a voltage controlled oscillator to that of a highly stable reference oscillator thereby ensuring stability in output frequency and phase. An oven controlled crystal oscillator or a GPS disciplined voltage controlled reference oscillator is used as a reference frequency source. The frequency of the reference oscillator  $F_{ref}$  is divided by the reference frequency divider by a factor  $R$  to yield a phase comparison frequency  $F_{ref}/R$ . The output of the VCO operates at the intended RF frequency or a sub-harmonic of it.

The circuit schematic of a VCO designed for operation between 13 GHz and 15 GHz is shown in Fig. A.2. The output of the oscillator is ideally supposed to oscillate at a single frequency but is modulated by parasitic noise and exhibits sidebands close to the centre frequency. This parasitic noise is termed as phase noise which is a figure of merit for an oscillator. Phase noise is measured and quantified in terms of power of the sideband relative to power of the intended oscillation at offsets from the centre frequency. The effective phase noise depends upon the noise figure of the active device used in the oscillator, quality factor of the resonator, purity of the tuning

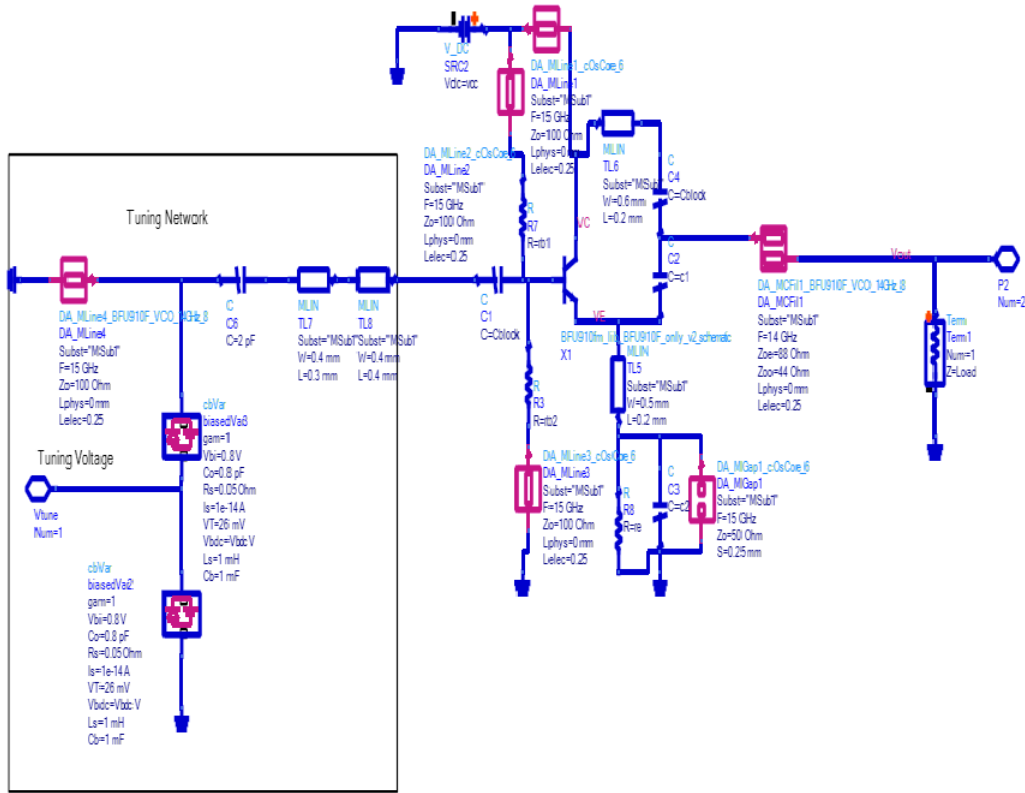


Fig. A.2.: VCO schematic

voltage and bias voltage applied. More information about phase noise is available in the application note [15] and [16]. The phase noise at a frequency offset  $f_m$  from the centre or carrier frequency  $f_o$  of an individual oscillator may be calculated using Leeson's formula given in eq. A.1.

$$L(f_m) = 10 \text{Log} \left[ \frac{1}{2} \left( \left( \frac{f_o}{2Q_1 f_m} \right)^2 + 1 \right) \left( \frac{f_c}{f_m} + 1 \right) \left( \frac{FkT}{P_s} \right) \right] \quad (\text{A.1})$$

where  $Q_1$  is the quality factor of the resonator,  $F$  is the noise figure of the transistor,  $P_s$  is the power to the transistor's input port,  $f_o$  is the resonant or centre frequency of the oscillator and  $f_c$  is the flicker noise corner frequency of the transistor.

The phase noise in the oscillator reduces the available SNR over the bandwidth of interest and can also cause inter-channel interference by reciprocal mixing with signals in the adjacent channel. The phase resultant noise simulated with the VCO at 14.5 GHz in Fig. A.2 phase locked to a reference oscillator with a loop bandwidth of 500kHz using a PLL module ADF4159 from Analog Devices is shown in Fig. A.3.

The phase noise when integrated over a bandwidth of 10MHz results in an available SNR of just around 49dB.

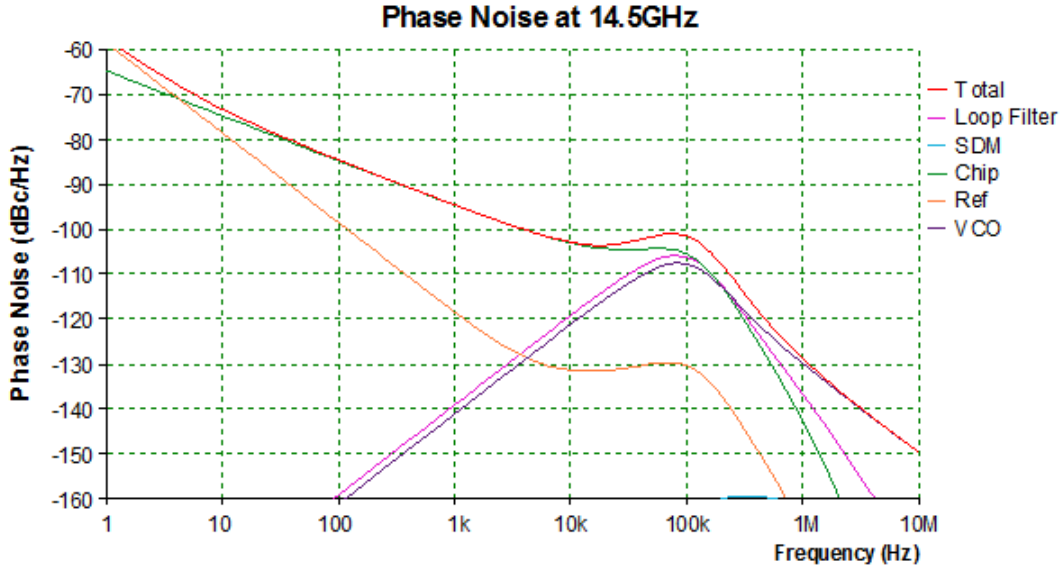


Fig. A.3.: LO phase noise profile at Ku Band

## A.1. Timing Jitter and Phase Noise

The phase noise of an oscillator used to generate the clock signals for the data converters manifests in the form of jitter in the time domain. Jitter is the extent of uncertainty in the occurrence of the rising and falling edges of the clock. The impact of jitter on the SNR of the signal generated or sensed by a data converter is to reduce its SNR proportionally. If the area under curve of the phase noise plot is ‘A’, the timing jitter  $T_{jrad}$  in radians is mathematically equal to

$$T_{jrad} = \sqrt{2XA^{A/10}} \quad (A.2)$$

$$T_{jsec} = \frac{T_{jrad}}{2\pi f_{clock}} \quad (A.3)$$

The resulting decrease in SNR  $N_{jitter}$  of a signal at frequency  $f_{signal}$  generated by the DAC running with the jittery clock is mathematically equal to

$$N_{jitter} = -20\text{Log}_{10}(2f_{signal}T_{jitter}) \quad (A.4)$$

It may be inferred from eq. A.4 that higher frequency components in the signal generated or sensed by a data-converter suffer more degradation in SNR due to jitter. The lowest noise figure that can be obtained in an active device termed as  $F_{min}$  depends on the semiconductor technology used and increases with frequency. The quality factor of the resonator used in the tuning circuits of a VCO also reduces with frequency owing to dielectric, ohmic and inductive losses. The problem of phase noise in LO modules is mitigated by using oscillator circuits at sub-harmonic frequencies and using frequency multiplier circuits using non-linear devices such as step recovery diodes. However, the same principle won't be directly applicable to generation of clock circuits since a clock signal needs to ideally represent a square wave which requires Schmitt Trigger circuits with high slew rates to produce a signal with the required clock pulse shape. This limits the maximum speed at which data converters can be operated. Mitigation of this problem is primary objective of the work described in this thesis whose details are presented in chapter3.

## B. Impairments in data converters

- a) Settling Errors in Data Converters: If the input to a DAC is varied from a starting value  $X_{start}$  to the final value  $X_{final}$ , it takes a finite amount of time for the analogue output voltage to rise and settle to a value close to  $X_{final}$  for pre-determined accuracy (example within 0.1% of  $X_{final}$ ). The time taken to settle is termed as settling time and designated as 'Ts', the time taken to rise is termed as slew time 'Tslew' and the difference in the final settled value and the desired final value  $X_{final}$  is the settling error. A brief graphical description of this error mechanism is shown in Fig 2.5. This parameter affects the maximum speed at which the DAC can be operated and is affected by the slew rate of the current switches involved in the biasing the DAC. The impact of settling errors increases with bandwidth of the signal. Difference in settling errors between the data converters used in the I and Q paths affects the EVM of the modulated or demodulated signal by introducing IQ imbalance.
- b) Sampling time uncertainty: Jitter in the sampling clock causes a variation in the time interval between adjacent samples. Jitter is caused by noise in the oscillator that generates the clock signal. The average power of this error  $P_{delta}$  caused by timing error  $T_{delta}$  with intended sampling interval  $T_s$  and step size  $X_{delta}$  is given by eq. B.1. Differences in sampling uncertainties between the data converters used in the I and Q paths cause parasitic phase modulation which would corrupt the intended modulation.

$$P_{\delta} = \frac{X_{\delta}}{T_{\delta}} \quad (B.1)$$

c) Sinc Roll off: The frequency response of a data converter rolls off in the form of Sinc function due to zero order hold characteristic of its analogue circuits. The frequency response of a DAC is of the form

$$H(f) = \frac{T_s \text{Sin}(\pi f T_s)}{(\pi f T_s)} \quad (B.2)$$

The response is plotted in Fig. Fig. B.1. This implies that the amplitude of the frequency component at  $0.4/$  in the output of the DAC is reduced to a value of 75.6% of the ideal amplitude. This behaviour impacts the spectral flatness of the modulated signal generated by the DAC in wideband systems. This is behaviour

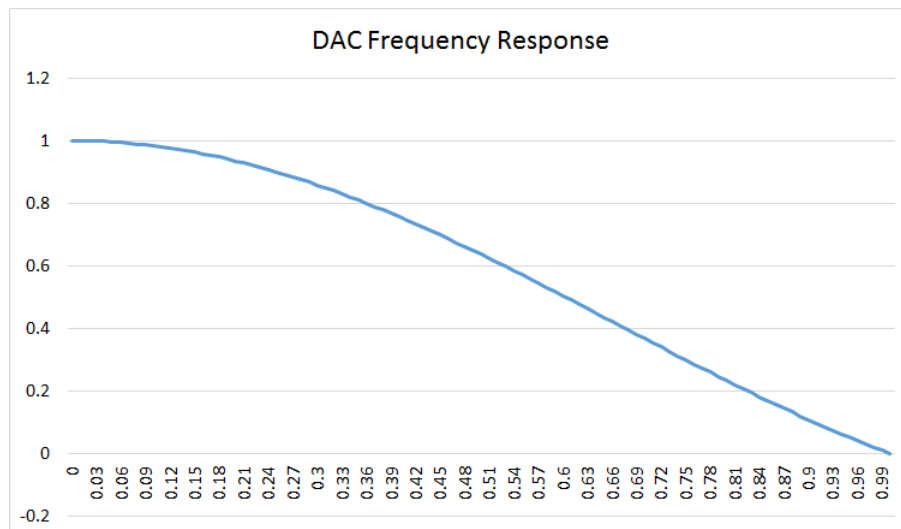


**Fig. B.1.:** Sinc Roll-off

would specifically affect OFDM based systems since the integrity of the modulation on the sub-carriers would be compromised.

d) Quantization Noise: Since DAC's output is actually in discrete steps and not continuous, the extent of error in the output analogue value relative to an ideal analogue signal manifests in the form of noise thereby affecting the SNR of the output signal being generated. This has an impact on the quality of the modulated signal generated in the modulation stage of an RF transmitter. The effective SNR in dB available in the output signal of bandwidth  $B$  in the presence of quantization noise [14] is given by the mathematical relation

$$SNR_{dB} = 6.02N + 1.76 + 10\text{Log}_{10}(f_s/2B) \quad (\text{B.3})$$

Where  $N$  is the bit resolution,  $B$  is the bandwidth of the signal in Hz and  $f_s$  is the sampling frequency.  $f_s = 1/T_s$ . A similar effect is observed in the receiver where analogue variations smaller than the step size cannot be sensed by the ADC. The signals encountered in wireless communication applications such as OFDM consist of multiple tones and the time domain envelopes exhibit a high peak to average ratios. The value of SNR reduces in the presence of PAR to

$$SNR = 6.02N + 4.77 - 20\text{Log}_{10}(\text{PAR}\sqrt{2}) + 10\text{Log}_{10}(BW/f_s) \quad (\text{B.4})$$

$$SNR_{multi} = SNR_{single} - 20\text{Log}_{10}(\text{PAR}\sqrt{2}) \quad (\text{B.5})$$

e) Effective Number of Bits (ENOB): The resolution of a data converter can be N bits but its effectiveness reduces due to the combined impact of quantization and distortion. ENOB in the presence of a finite Signal to Noise and Distortion Ratio (SNDR) is mathematically computed as:

$$ENOB = \frac{SNDR - 1.76}{6.02} \tag{B.6}$$

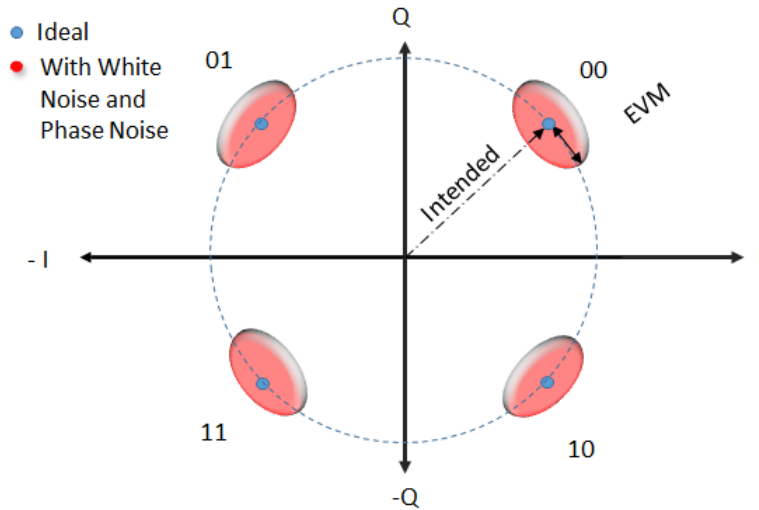


**Fig. B.2.:** Constellation Dispersion due to Noise and Jitter

b) Effective Resolution Bandwidth (ERB): It was observed in eq. B.5 and eq. B.4 that SNR of the signal generated or sensed by a data converter is dependent on its frequency and hence the value of ENOB reduces with frequency. The frequency of the tone at which ENOB reduces by 3 dB is termed at the Effective Resolution Bandwidth (ERB). This is a parameter that indicates the usable bandwidth of data-converter for a given SNDR requirement.



# Bibliography

- [1] B. Timus, M. Fallgren, A. Uusitalo, F. Osseiran, M. Boccardi, V. Tullberg, K. Vraun, H. Kusume, P. Taoka, M. Marsch, O. Maternia, H. Queseth, M. Schellmann, and H. Schotten, “Scenarios for 5G mobile and wireless communications: The vision of the METIS project scenarios for the 5G mobile and wireless communications :,” *IEEE Communications Magazine*, vol. 52, no. 1, pp. 26–35, 2014.
- [2] A. Osseiran, V. Braun, and T. Hidekazu, “The foundation of the mobile and wireless communications system for 2020 and beyond,” *Proc. IEEE Veh. Tech. ...*, pp. 1–5, 2013. [Online]. Available: <http://ieeexplore.ieee.org/lpdocs/epic03/wrapper.htm?arnumber=6692781>{%}5Cn<https://www.metis2020.com/wp-content/uploads/publications/VTC{ }2013{ }Oss{ }et{ }al{ }MobileSystem2020.pdf>
- [3] ETSI ISG-mWT, “5G Wireless Backhaul/X-Haul,” vol. 1, pp. 1–24, 2018.
- [4] Qualcomm, “Making 5G NR a reality,” no. December, 2016.
- [5] Y. Vasavada, R. Gopal, C. Ravishankar, G. Zakaria, and N. BenAmmar, “Architectures for next generation high throughput satellite systems,” *International Journal of Satellite Communications and Networking*, vol. 34, no. 4, pp. 523–546, 2016. [Online]. Available: <https://doi.org/10.1002/sat.1175>
- [6] S. K. Sharma, S. Chatzinotas, and B. Ottersten, “Satellite cognitive communications: Interference modeling and techniques selection,” *2012 6th Advanced Satellite Multimedia Systems Conference, ASMS 2012 and 12th Signal Processing for Space Communications Workshop, SPSC 2012*, pp. 111–118, 2012.
- [7] O. Vidal, G. Verelst, J. Lacan, E. Albery, J. Radzik, and M. Bousquet, “Next generation high throughput satellite system,” *Proceedings - 2012 IEEE 1st AESS European Conference on Satellite Telecommunications, ESTEL 2012*, pp. 1–7, 2012.
- [8] “The 5G Future and the Role of Satellite,” Tech. Rep.
- [9] “SaT5G Project - Sat 5G.” [Online]. Available: <https://www.sat5g-project.eu/>
- [10] S. Bhad, P. Gulhane, and A. Hiwale, “PAPR Reduction Scheme for OFDM,” *Procedia Technology*, 2012.
- [11] WiFi pineapple. [Online]. Available: <https://www.wifipineapple.com>

- 
- [12] B. Z. Katz, C. Sahin, and K. R. Dandekar, "Real-time wireless physical layer encryption," in *2016 IEEE 17th Annual Wireless and Microwave Technology Conference (WAMICON)*, April 2016, pp. 1–4.
- [13] "Data Converter Requirements for Communications," in *CMOS Data Converter for Communications*. Kluwer Academic Publishers, dec 2005, pp. 27–59.
- [14] W. Kester, "MT-001 TUTORIAL Taking the Mystery out of the Infamous Formula, "SNR =  $6.02N + 1.76\text{dB}$ ," and Why You Should Care," Tech. Rep.
- [15] "MT-086 TUTORIAL Fundamentals of Phase Locked Loops (PLLs)," Tech. Rep.
- [16] G. D. Vendelin, A. M. Pavio, and U. L. Rohde, *Microwave Circuit Design Using Linear and Nonlinear Techniques: Second Edition*. John Wiley and Sons, jan 2005.
- [17] "5G-The Microwave Perspective | Analog Devices." [Online]. Available: <https://www.analog.com/en/technical-articles/5g-the-microwave-perspective.html>
- [18] A. Hakkarainen, J. Werner, and M. Valkama, "RF imperfections in antenna arrays: Response analysis and widely-linear digital beamforming," in *IEEE Radio and Wireless Symposium, RWS*, 2013, pp. 187–189.
- [19] X. Zhang, M. Matthaiou, M. Coldrey, and E. Björnson, "Impact of residual transmit RF impairments on training-based MIMO systems," in *IEEE Transactions on Communications*, vol. 63, no. 8. Institute of Electrical and Electronics Engineers Inc., aug 2015, pp. 2899–2911.
- [20] C. Fulton, M. Yeary, D. Thompson, J. Lake, and A. Mitchell, "Digital Phased Arrays: Challenges and Opportunities," *Proceedings of the IEEE*, vol. 104, no. 3, pp. 487–503, mar 2016.
- [21] E. Nash, "Correcting Imperfections in IQ Modulators to Improve RF Signal Fidelity," *Application Note*, pp. 1–8, 2009.
- [22] M. Longbrake, L. L. Liou, D. M. Lin, P. Buxa, J. McCann, T. Pemberton, T. Dalrymple, and S. Hary, "Wideband phased array calibration method for digital beamforming," in *National Aerospace and Electronics Conference, Proceedings of the IEEE*, 2013, pp. 11–17.
- [23] A. Khandelwal and A. Verma, "A novel gain, phase and offset calibration scheme for wideband direct-conversion transmitters," in *IEEE Vehicular Technology Conference*, vol. 2015. Institute of Electrical and Electronics Engineers Inc., jul 2015.
- [24] "Keysight Technologies Enhancing Measurement Performance for the Testing of Wideband MIMO Signals White Paper How to generate and apply magnitude and phase corrections for multichannel baseband IQ measurements when using the Keysight M9703A AXIe digitizer," Tech. Rep.

- [25] A. Rezola, J. F. Sevillano, I. Gurutzeaga, D. Del Rio, R. Berenguer, and I. Velez, "Built-in-Self-Calibration for I/Q Imbalance in Wideband Millimeter-Wave Gigabit Transmitters," *IEEE Transactions on Microwave Theory and Techniques*, vol. 65, no. 11, pp. 4758–4769, nov 2017.
- [26] Z. Zhu and X. Huang, "An iterative calibration technique for LINC transmitter," in *Midwest Symposium on Circuits and Systems*, 2013, pp. 384–387.
- [27] K. Technologies, "Keysight Technologies Calibration Techniques for Improved MIMO and Beamsteering Characterization," Tech. Rep.
- [28] B. Kang, J. Yim, T. Kim, S. Ko, W. Ko, H. Shin, I. Ryu, S. G. Yang, J. D. Bae, and H. Park, "Design and analysis of an ultra-wideband automatic self-calibrating upconverter in 65-nm CMOS," *IEEE Transactions on Microwave Theory and Techniques*, vol. 60, no. 7, pp. 2178–2191, 2012.
- [29] S. Kawai, T. Yamagishi, Y. Hagiwara, S. Saigusa, I. Seto, S. Otaka, and S. Ito, "A 1024-QAM capable WLAN receiver with self-calibration technique," in *2017 IEEE International Symposium on Circuits and Systems (ISCAS)*. IEEE, may 2017, pp. 1–4. [Online]. Available: <http://ieeexplore.ieee.org/document/8050600/>
- [30] "US Patent for Wideband IQ mismatch correction for direct down-conversion receiver Patent (Patent # 9,647,867 issued May 9, 2017) - Justia Patents Search." [Online]. Available: <https://patents.justia.com/patent/9647867>
- [31] "US Patent for Coefficient estimation for digital IQ calibration Patent (Patent # 9,431,962 issued August 30, 2016) - Justia Patents Search." [Online]. Available: <https://patents.justia.com/patent/9431962>
- [32] S. Jo, "Calibrating an RF transmitter," vol. 1, no. 19, 2004. [Online]. Available: <https://patents.google.com/patent/US20050059361>
- [33] "US Patent for Receiver with multi-tone wideband I/Q mismatch calibration and method therefor Patent (Patent # US7962113B2 issued Jun 14, 2011) - Google Patents." [Online]. Available: <https://patents.google.com/patent/US7962113>
- [34] "US Patent for Systems and methods to provide wideband magnitude and phase imbalance calibration and compensation in quadrature receivers Patent (Patent # 7,158,586 issued January 2, 2007) - Justia Patents Search." [Online]. Available: <https://patents.justia.com/patent/7158586>
- [35] "US Patent for On-chip IQ imbalance and LO leakage calibration for transceivers Patent (Patent # 8,559,488 issued October 15, 2013) - Justia Patents Search." [Online]. Available: <https://patents.justia.com/patent/8559488>
- [36] "US Patent for Transceiver IQ calibration system and associated method Patent (Patent # 9,025,645 issued May 5, 2015) - Justia Patents Search." [Online]. Available: <https://patents.justia.com/patent/9025645>

- [37] W. Li, Y. Zhang, L. K. Huang, J. Cosmas, C. Maple, and J. Xiong, "Self-IQ-Demodulation Based Compensation Scheme of Frequency-Dependent IQ Imbalance for Wideband Direct-Conversion Transmitters," *IEEE Transactions on Broadcasting*, vol. 61, no. 4, pp. 666–673, dec 2015.
- [38] "US Patent for Frequency domain estimation of IQ imbalance in a wireless OFDM direct conversion receiver using loopback connection Patent (Patent # 7,184,714 issued February 27, 2007) - Justia Patents Search." [Online]. Available: <https://patents.justia.com/patent/7184714>
- [39] "permn - File Exchange - MATLAB Central." [Online]. Available: <https://uk.mathworks.com/matlabcentral/fileexchange/7147-permn>
- [40] K. El-Akhdar, S. Ahmed, G. Neveux, D. Barataud, and J. Nebus, "Calibrated rf time-domain measurement of non-linear devices in digital polar transmitter architecture," in *2013 European Microwave Conference*, Oct 2013, pp. 452–455.
- [41] K. K. Johnson, "Residual BER Prediction Predicting Residual BER II "Measurements for Lowering Radio Cost" Predicting Residual BER II "Measurements for Lowering Radio Cost"," Tech. Rep., 2002.
- [42] T. H. Lee, *THE DESIGN OF CMOS INTEGRATED CIRCUITS SECOND EDITION*.
- [43] Y. Tsvividis, Y. Tsvividis, R. T. Stone, H. M. Berlin, W. L. Engl, C. Galupontoro, C. G. Fonstad, W. Liu, and K. R. Laker, "[16] Operation and Modeling of the MOS Transistor , 2011 , 723 pages , Yannis Tsvividis ,," 2011.
- [44] B. Razavi, *RF microelectronics*. Prentice Hall, 2012.
- [45] G. Gonzalez, *Microwave Transistor Amplifier: Analysis and Design Second Edition*, 1996.
- [46] O. Kiel, "Aalborg Universitet Self-heating and memory effects in RF power amplifiers explained through electro-thermal." [Online]. Available: <https://doi.org/10.1109/NORCHIP.2013.6702015>
- [47] N. B. Carvalho, C. Pedro, P. Martins, and P. M. Cabral, "Power Amplifier Memory Origins and Impact on Intermodulation Distortion Workshop on Memory Effects In Power Amplifiers IMS-San Francisco 2006," Tech. Rep.
- [48] S. A. Maas and S. A. Maas, *Nonlinear microwave and RF circuits*. Artech House, 2003.
- [49] F. M. Ghannouchi, *Behavioral modelling and predistortion of wideband wireless transmitters*.
- [50] S. C. Cripps, *RF power amplifiers for wireless communications*.
- [51] —, *RF Power Amplifiers for Wireless Communications, Second Edition (Artech House Microwave Library (Hardcover))*, 2nd ed. Norwood, MA, USA: Artech House, Inc., 2006.

- [52] H. Chireix, "High power outphasing modulation," *Proceedings of the Institute of Radio Engineers*, vol. 23, no. 11, pp. 1370–1392, Nov 1935.
- [53] F. Raab, "Efficiency of outphasing RF power-amplifier systems," vol. 33, no. 10, pp. 1094–1099, October 1985.
- [54] A. Birafane and A. B. Kouki, "On the linearity and efficiency of outphasing microwave amplifiers," vol. 52, no. 7, pp. 1702–1708, July 2004.
- [55] W. H. Doherty, "Technical Papers: A New High Efficiency Power Amplifier for Modulated Waves," *Proceedings of the Institute of Radio Engineers*, vol. 24, no. 9, pp. 1163–1182, 1936.
- [56] P. Colantonio, F. Giannini, and E. Limiti, *High Efficiency RF and Microwave Solid State Power Amplifiers*. John Wiley and Sons, sep 2009.
- [57] P. Colantonio, F. Giannini, R. Giofre, and L. Piazzo, "The Doherty Power Amplifier," in *Advanced Microwave Circuits and Systems*. In-Tech, apr 2010. [Online]. Available: <http://www.intechopen.com/books/advanced-microwave-circuits-and-systems/the-doherty-power-amplifier>
- [58] P. Colantonio, F. Giannini, and E. Limiti, "High Efficiency PA Design Theory," in *High Efficiency RF and Microwave Solid State Power Amplifiers*. John Wiley & Sons, Ltd, sep 2009, pp. 177–222.
- [59] A. Grebennikov and S. Bulja, "High-efficiency doherty power amplifiers: Historical aspect and modern trends," pp. 3190–3219, 2012.
- [60] "US Patent for Integrated 3-way Doherty amplifier Patent (Patent # 10,038,407 issued July 31, 2018) - Justia Patents Search." [Online]. Available: <https://patents.justia.com/patent/10038407>
- [61] F. H. Raab, P. Asbeck, S. Cripps, P. B. Kenington, Z. B. Popovic, N. Pothecary, J. F. Sevic, and N. O. Sokal, "Power Amplifiers and Transmitters for RF and Microwave," Tech. Rep. 3, 2002.
- [62] A. Grebennikov and S. Bulja, "High-efficiency doherty power amplifiers: Historical aspect and modern trends," pp. 3190–3219, 2012.
- [63] M. J. Pelk, W. C. Neo, J. R. Gajadharsing, R. S. Pengelly, and L. C. De Vreede, "A high-efficiency 100-W GaN three-way Doherty amplifier for base-station applications," *IEEE Transactions on Microwave Theory and Techniques*, vol. 56, no. 7, pp. 1582–1591, jul 2008.
- [64] R. Darraji and F. M. Ghannouchi, "Digital doherty amplifier with enhanced efficiency and extended range," *IEEE Transactions on Microwave Theory and Techniques*, vol. 59, no. 11, pp. 2898–2909, nov 2011.
- [65] R. Darraji, F. M. Ghannouchi, and O. Hammi, "A dual-input digitally driven doherty amplifier architecture for performance enhancement of Doherty transmitters," in *IEEE Transactions on Microwave Theory and Techniques*, vol. 59, no. 5, may 2011, pp. 1284–1293.

- 
- [66] C. F. Campbell, “A Fully Integrated Ku-Band Doherty Amplifier MMIC,” *IEEE Microwave and Guided Wave Letters*, vol. 9, no. 3, pp. 114–116, 1999.
- [67] “US Patent for Multi-way doherty amplifier Patent (Patent # 9,325,280 issued April 26, 2016) - Justia Patents Search.” [Online]. Available: <https://patents.justia.com/patent/9325280>
- [68] C. Sahin, B. Katz, and K. R. Dandekar, “Secure and robust symmetric key generation using physical layer techniques under various wireless environments,” in *2016 IEEE Radio and Wireless Symposium (RWS)*, Jan 2016, pp. 211–214.
- [69] J. Hua, S. Jiang, W. Lu, Z. Xu, and F. Li, “A novel physical layer encryption algorithm based on statistical characteristics of time-selective channels,” *IEEE Access*, vol. 6, pp. 38 225–38 233, 2018.
- [70] L. Cheng, L. Zhou, B.-C. Seet, W. li, D. Ma, and J. Wei, “Efficient physical-layer secret key generation and authentication schemes based on wireless channel-phase,” *Mobile Information Systems*, vol. 2017, pp. 1–13, 07 2017.
- [71] X. Wu and Z. Yang, “Physical-layer authentication for multi-carrier transmission,” *IEEE Communications Letters*, vol. 19, no. 1, pp. 74–77, Jan 2015.
- [72] S. Mathur, W. Trappe, N. Mandayam, C. Ye, and A. Reznik, “Radio-telepathy: Extracting a secret key from an unauthenticated wireless channel,” in *Proceedings of the 14th ACM International Conference on Mobile Computing and Networking*, ser. MobiCom ’08. New York, NY, USA: ACM, 2008, pp. 128–139. [Online]. Available: <http://doi.acm.org/10.1145/1409944.1409960>
- [73] W. Hou, X. Wang, J. Chouinard, and A. Refaey, “Physical layer authentication for mobile systems with time-varying carrier frequency offsets,” *IEEE Transactions on Communications*, vol. 62, no. 5, pp. 1658–1667, May 2014.
- [74] X. Du, D. Shan, K. Zeng, and L. Huie, “Physical layer challenge-response authentication in wireless networks with relay,” in *IEEE INFOCOM 2014 - IEEE Conference on Computer Communications*, April 2014, pp. 1276–1284.
- [75] Gao Baojian, Luo Yongling, Hou Aiqin, Zhao Xiaoning, and Wu Qian, “New physical layer encryption algorithm based on dft-s-ofdm system,” in *Proceedings 2013 International Conference on Mechatronic Sciences, Electric Engineering and Computer (MEC)*, Dec 2013, pp. 2018–2022.
- [76] Y. Ding and V. F. Fusco, “A vector approach for the analysis and synthesis of directional modulation transmitters,” *IEEE Transactions on Antennas and Propagation*, vol. 62, no. 1, pp. 361–370, Jan 2014.
- [77] Y. Ding and V. Fusco, “Improved physical layer secure wireless communications using a directional modulation enhanced retrodirective array,” in *2014 XXXIth URSI General Assembly and Scientific Symposium (URSI GASS)*, Aug 2014, pp. 1–4.

- [78] M. P. Daly, E. L. Daly, and J. T. Bernhard, "Demonstration of directional modulation using a phased array," *IEEE Transactions on Antennas and Propagation*, vol. 58, no. 5, pp. 1545–1550, May 2010.
- [79] Y. Shiu, S. Y. Chang, H. Wu, S. C. . Huang, and H. Chen, "Physical layer security in wireless networks: a tutorial," *IEEE Wireless Communications*, vol. 18, no. 2, pp. 66–74, April 2011.
- [80] M. Bisht and A. Joshi, "Various Techniques to Reduce PAPR in OFDM Systems: A Survey," *International Journal of Signal Processing*, vol. 8, no. 11, pp. 195–206, 2015. [Online]. Available: <http://dx.doi.org/10.14257/ijcip.2015.8.11.18>
- [81] R. K. Singh and M. Fidele, "An efficient PAPR reduction scheme for OFDM system using peak windowing and clipping," *Proceedings of 2015 3rd International Conference on Image Information Processing, ICIIP 2015*, pp. 491–495, 2016.
- [82] N. Jacklin and Z. Ding, "A linear programming based tone injection algorithm for papr reduction of ofdm and linearly precoded systems," *IEEE Transactions on Circuits and Systems I: Regular Papers*, vol. 60, no. 7, pp. 1937–1945, July 2013.
- [83] S. Vangala and S. Anuradha, "Hybrid PAPR reduction scheme with selective mapping and tone reservation for FBMC/OQAM," *2015 3rd International Conference on Signal Processing, Communication and Networking, ICSCN 2015*, no. 3, pp. 1–5, 2015.
- [84] J. Wang, X. Lv, and W. Wu, "SCR-Based Tone Reservation Schemes with Fast Convergence for PAPR Reduction in OFDM System," *IEEE Wireless Communications Letters*, vol. 8, no. 2, pp. 624–627, 2019.
- [85] W. Zhang, C. Zhang, C. Chen, W. Jin, and K. Qiu, "Joint papr reduction and physical layer security enhancement in ofdma-pon," *IEEE Photonics Technology Letters*, vol. 28, no. 9, pp. 998–1001, May 2016.
- [86] V. Sudha, B. Anilkumar, and D. Sriramkumar, "Low-complexity modified SLM method for PAPR reduction in OFDM systems," *2nd International Conference on Electronics and Communication Systems, ICECS 2015*, no. Icecs, pp. 1324–1328, 2015.
- [87] K. Mhatre and U. P. Khot, "Efficient Selective Mapping PAPR reduction technique," *Procedia Computer Science*, vol. 45, no. C, pp. 620–627, 2015. [Online]. Available: <http://dx.doi.org/10.1016/j.procs.2015.03.117>
- [88] V. Sudha and D. S. Kumar, "PAPR reduction of OFDM system using PTS method with different modulation techniques," *2014 International Conference on Electronics and Communication Systems, ICECS 2014*, no. X, pp. 1–5, 2014.

- 
- [89] G. Rashwan, S. Kenshi, and M. Matin, "Analysis of PAPR hybrid reduction technique based on PTS and SLM," *2017 IEEE 7th Annual Computing and Communication Workshop and Conference, CCWC 2017*, no. Ici, pp. 1–4, 2017.
- [90] P. Cheng, Y. Xiao, L. Dan, and S. Li, "Improved SLM for PAPR reduction in OFDM system," in *2007 IEEE 18th International Symposium on Personal, Indoor and Mobile Radio Communications*, Sep. 2007, pp. 1–5.
- [91] X. Zhang, B. Zhang, and D. Guo, "Physical layer secure transmission based on fast dual polarization hopping in fixed satellite communication," *IEEE Access*, vol. 5, pp. 11 782–11 790, 2017.
- [92] S. Mishra and A. Agarwal, "Peak to average power ratio reduction in sub-carrier Index modulated OFDM using selective mapping," *2017 International Conference on Computer, Communications and Electronics, COMPTELIX 2017*, vol. 1, no. 2, pp. 168–171, 2017.
- [93] A. D. Jayalath and C. Tellambura, "Adaptive PTS approach for reduction of peak-to-average power ratio of OFDM signal," *Electronics Letters*, vol. 36, no. 14, pp. 1226–1228, jul 2000.
- [94] M. Hosseinzadeh Aghdam and A. A. Sharifi, "PAPR reduction in OFDM systems: An efficient PTS approach based on particle swarm optimization," 2018.
- [95] W. Diffie and M. Hellman, "New directions in cryptography," *IEEE Transactions on Information Theory*, vol. 22, no. 6, pp. 644–654, November 1976.
- [96] A. Azizzadeh and L. Mohammadi, "Degradation of ber by group delay in digital phase modulation," in *2008 Fourth Advanced International Conference on Telecommunications*, June 2008, pp. 350–354.
- [97] S. Jose, "Synchronization in the Mobile standards," *Wsts*, pp. 1–20, 2013.
- [98] K. Technologies, "Keysight Technologies Demystifying the Impact of ADCs and DACs on Test Instrument Specifications."
- [99] H. Yamazaki, M. Nagatani, S. Kanazawa, H. Nosaka, T. Hashimoto, A. Sano, and Y. Miyamoto, "Digital-Preprocessed Analog-Multiplexed DAC for Ultra-wideband Multilevel Transmitter," *Journal of Lightwave Technology*, vol. 34, no. 7, pp. 1579–1584, 2016.
- [100] H. Yamazaki, M. Nagatani, F. Hamaoka, K. Horikoshi, M. Nakamura, A. Matsushita, S. Kanazawa, T. Hashimoto, H. Nosaka, and Y. Miyamoto, "Ultra-high-speed optical transmission using digital-preprocessed analog-multiplexed DAC," *Optics Communications*, vol. 409, no. June 2017, pp. 66–71, 2018. [Online]. Available: <http://dx.doi.org/10.1016/j.optcom.2017.06.100>
- [101] B. Li, L. Zhao, J. Wu, and Y. Cheng, "Duty Cycle Distortion in Half-rate Nyquist DACs with Limited Output Bandwidth," *Proceedings - IEEE International Symposium on Circuits and Systems*, vol. 2018-May, pp. 1–4, 2018.

- [102] M. Tanio, S. Hori, N. Tawa, T. Yamase, and K. Kunihiro, "An FPGA-based all-digital transmitter with 28-GHz time-interleaved delta-sigma modulation," *IEEE MTT-S International Microwave Symposium Digest*, vol. 2016-Augus, pp. 1–4, 2016.
- [103] S. N. Kim, W. C. Kim, M. J. Seo, and S. T. Ryu, "A 65-nm CMOS 6-Bit 20 GS/s Time-Interleaved DAC with Full-Binary Sub-DACs," *IEEE Transactions on Circuits and Systems II: Express Briefs*, vol. 65, no. 9, pp. 1154–1158, 2018.
- [104] S. Balasubramanian, G. Creech, J. Wilson, S. M. Yoder, J. J. McCue, M. Verhelst, and W. Khalil, "Systematic analysis of interleaved digital-to-analog converters," *IEEE Transactions on Circuits and Systems II: Express Briefs*, vol. 58, no. 12, pp. 882–886, 2011.
- [105] N. E. Majd, H. Ghafoorifard, and A. Mohammadi, "Bandwidth enhancement in delta sigma modulator transmitter using low complexity time-interleaved parallel delta sigma modulator," *AEU - International Journal of Electronics and Communications*, vol. 69, no. 7, pp. 1032–1038, 2015. [Online]. Available: <http://dx.doi.org/10.1016/j.aeue.2015.04.001>
- [106] C. Schmidt, V. H. Tanzil, C. Kottke, R. Freund, and V. Jungnickel, "Digital signal splitting among multiple DACs for analog bandwidth interleaving (ABI)," *2016 IEEE International Conference on Electronics, Circuits and Systems, ICECS 2016*, pp. 245–248, 2017.
- [107] C. Schmidt, C. Kottke, V. H. Tanzil, R. Freund, V. Jungnickel, and F. Gerfers, "Digital-to-Analog Converters Using Frequency Interleaving: Mathematical Framework and Experimental Verification," *Circuits, Systems, and Signal Processing*, vol. 37, no. 11, pp. 4929–4954, 2018. [Online]. Available: <https://doi.org/10.1007/s00034-018-0791-y>
- [108] X. Chen, S. Chandrasekhar, P. Winzer, P. Pupalais, I. Ashiq, A. Khanna, A. Steffan, and A. Umbach, "180-GBaud nyquist shaped optical QPSK generation based on a 240-GSa/s 100-GHz analog bandwidth DAC," *Optics InfoBase Conference Papers*, pp. 12–14, 2014.
- [109] X. Chen, S. Chandrasekhar, S. Randel, G. Raybon, A. Adamiecki, P. Pupalais, and P. J. Winzer, "All-Electronic 100-GHz Bandwidth Digital-to-Analog Converter Generating PAM Signals up to 190 GBaud," *Journal of Lightwave Technology*, vol. 35, no. 3, pp. 411–417, 2017.
- [110] R. Freund, C. Schmidt, C. Kottke, V. Jungnickel, and R. Freund, "Enhancing the Bandwidth of DACs by Analog Bandwidth Interleaving Enhancing the Bandwidth of DACs by Analog Bandwidth Interleaving," no. April, p. 9, 2016.
- [111] M. Soudan and R. Farrell, "Methodology for mismatch reduction in time-interleaved ADCs," *European Conference on Circuit Theory and Design 2007, ECCTD 2007*, pp. 352–355, 2008.
- [112] P. Pupalais, "Digital Bandwidth Interleaving," pp. 1–4, 2010.

- [113] S. Callender, “Wideband Signal Acquisition via Frequency-Interleaved Sampling,” p. 2014, 2014.
- [114] S. Deb, M. Tanio, S. Hori, N. Tawa, Y. Wada, and K. Kunihiro, “Band-Limited Digital Predistortion with Band-Switching Feedback Architecture for 5G mmWave Power Amplifiers,” *2018 48th European Microwave Conference, EuMC 2018*, no. 3, pp. 9–12, 2018.
- [115] Q. Zhang and W. Chen, “Digital predistortion for 5G wideband power amplifiers using multiple band-limited feedback signals,” *89th ARFTG Microwave Measurement Conference: Advanced Technologies for Communications, ARFTG 2017*, pp. 1–4, 2017.